Application of engineering methodologies to address patient-specific clinical questions in congenital heart disease

Daria Cosentino

Submitted for the degree of Doctor of Philosophy
University College London

London, January 2014

Talent wins games, but teamwork and intelligence win championships.

Michael Jordan

DECLARATION OF ORIGINALITY

I, Daria Cosentino, confirm that the contents of this thesis are my own work. Where information has been derived from other sources, I confirm that this has been indicated in the thesis.

In particular, the optical stereo-photogrammetry images acquisitions and post-processing discussed in Chapter 4 have been carried out by Iwona Zwierzak from the University of Sheffield. The statistical analysis presented in Chapter 5 has been performed in collaboration with Michael Quail. The mock circuit built in Chapter 6 and the MR acquisitions have been executed together with Dr Giovanni Biglino and Dr Jennifer Steeden.

ABSTRACT

The recent advances in medical imaging and in computer technologies have improved the prediction capabilities of biomechanical models.

In order to replicate physiological, pathological or surgically corrected portions of the cardiovascular system, several engineering methodologies and their combinations can be adopted. Specifically, in this thesis, 3D reconstructions of patient-specific implanted devices and cardiovascular anatomies have been realised using both volumetric and biplanar visualisation methods, such as CT, MR, 4D-MR Flow and fluoroscopy. Finite Element techniques have been used to computationally deploy cardiovascular endoprosthesis, such as stents and percutaneous pulmonary valve devices, under patient-specific boundary conditions. To analyse pressure and velocity fields occurring in patient-specific vessel anatomies under patient-specific conditions, Lumped Parameter Networks and Computational Fluid Dynamics simulations have been employed.

In this thesis, the above mentioned engineering tools have been applied to address three clinical topics:

1 - Percutaneous pulmonary valve implantation (PPVI)

Nowadays, more than 5,000 patients with pulmonary valve dysfunctions have been treated successfully with a percutaneous device, consisting in a bovine jugular venous valve sewn inside a balloon expandable stent. However, 25% of the treated patients experienced stent fracture. Using a novel methodological patient-specific approach that combines 3D reconstructions of the implanted stent from patients' biplane fluoroscopy images and FE analyses, I carried out a risk stratification for stent fracture prediction.

2 - Transposition of the Great Arteries (TGA)

Patients born with the congenital heart defect TGA need a surgical correction, which however, is associated with long term complications: the enlargement of the aortic root, and the development of a unilateral pulmonary stenosis. These may originate a complex hemodynamics that I tried to investigate by using patient-specific LPN and CFD models.

3 - Aortic Coarctation (CoA)

Finally, combinations of FE and CFD-LPN models have been used to plan treatment in a patient with CoA and aberrant right subclavian.

ACKNOWLEDGEMENTS

This research has been funded by the European Commission, through the MeDDiCA Initial Training Network (www.meddica.eu, PITNGA-2009-239113), Marie Curie actions under FP7, People Progamme.

I would like to truly acknowledge Dr. Silvia Schievano, Dr. Vanessa Diaz, and Dr. Andrew M. Taylor for their constant supervision, their advices, their willingness and their encouragement throughout my PhD.

I am particularly grateful to Prof. Giancarlo Pennati and Prof. Francesco Migliavacca for their valuable collaborations, support, and wise suggestions over the years.

This work would have not been possible without the help of the people that accompanied my working days in the office, with whom I shared scientific opinions, non-scientific lunches, and all the rest: Claudio, Giorgia, Giovanni, Jan, Hopewell, Paolo, Lollo, Rosso, Alessandra, Gianmarco, Tobias, Jenny, Greg, Catriona, Michael.

I would like to acknowledge my “MeDDiCa community”, spread around Europe, and particularly Iwona and Dr. Andrew Narracott for our successful collaboration.

Special thanks go to my UCwhat?? basketball team: it’s also for the hours spent with you on and off the court, not thinking about my research, that my thesis arrived to completion.

“Grazie” to my inseparable university friends, biocosi that were always behind my computer and my mobile phone ready to cheer me up and/or to tease me: Ita, Catto, Mikel, Mirky, Chiara, Pavel, Ngi, Nozza, Carolaccia, Bedetta, amico Guido, Ramius.

A big thank you to Zappalorto for transmitting me the passion for London, with a foot and the stomach always in Abruzzo; to Eleonora because we shared together the joys of being young and PhD students; to Carlo, for that part of the road that we walked together.

Finally, the most sincere thank you goes to my family, source of unconditional support.

Daria

CONTENTS

CHAPTER 8 **197**

CHAPTER 9 **226**

LIST OF FIGURES

LIST OF TABLES

LIST OF ABBREVIATIONS

0D – Zero Dimensional
2D – Two Dimensional
3D – Three Dimensional
4D – Four Dimensional
AA – Ascending Aorta
AO – Aorta
AP – Antero-Posterior
ARSA – Aberrant Right Subclavian Artery
ASD – Atrial Septal Defect
ASO – Arterial Switch Operation
BAV – Bicuspid Aortic Stenosed Valve
BCPA – Bidirectional Cavopulmonary Anastomosis
BiB – Balloon-in-ballon
BMS – Bare Metal Stent
BPS – Bilateral Pulmonary Stenosis
CAD – Computer Aided Design
CFD – Computational Fluid Dynamics
CHD – Congenital Heart Disease
CI – Confidence Interval
CoA – Coarctation of the Aorta
CT – Computed Tomography
CTDIvol – Volume CT Dose Index
DA – Descending Aorta
DIV – Double Inlet Ventricle
d-TGA – Dextro-Transposition of the Great Arteries

ECG- Electrocardiography
F – Fluoroscopy
FE – Finite Element
FEM – Finite Element Method
FSI – Fluid-Structure Interaction
FVM – Finite Volume Method
*h*CT – High Dose Computed Tomography
HLSH – Hypoplastic Left Heart Syndrome
HR – Heart Rate
IVC – Inferior Vena Cava
LA – Left Atrium
*l*CT – Low Dose Computed Tomography
LPA – Left Pulmonary Artery
LPN – Lumped Parameter Network
l-TGA – Levo-Transposition of the Great Arteries
LV – Left Ventricle
MR – Magnetic Resonance
MRA – Magnetic Resonance Angiography
MRI – Magnetic Resonance Imaging
NS – Navier-Stokes
ODE – Ordinary Differential Equation
OP – Optical Stereo-Photogrammetry
OR – Odds Ratio
PA – Pulmonary Artery
PC – Phase Contrast
PPVI – Percutaneous Pulmonary Valve Implantation
PT – Pulmonary Trunk
PVR – Pulmonary Vascular Resistance
RA – Right Atrium
RPA – Right Pulmonary Artery
RV – Right Ventricle
RVOT – Right Ventricular Outflow Tract

SNR –Signal-Noise-Ratio

SSFP – Steady-State Free Precession

STL – Standard Triangulated Language

SV – Stroke Volume

TAVI – Transcatheter Aortic Valve Implantation

TGA – Transposition of the Great Arteries

TKE – Turbulent Kinetic Energy

VA – Ventriculo-Arterial

VSD – Ventricular Septal Defect

WSS – Wall Shear Stress

μCT – Micro-Computed Tomography

CHAPTER 1

INTRODUCTION

1.1 INTRODUCTION

The primary goal of medical care is the increase of life expectancy and quality of life, through the development of preventive and curative measures, the minimisation of poor living conditions associated with chronic diseases, and the rescue of lives in life-threatening emergencies. In the last century, a marked improvement of the medical care has largely contributed to the partial achievement of these never-fulfilled aims, and a significant role in such improvement has been played by the science of biomedical engineering.

Biomedical engineering is an interdisciplinary field that aims to reduce the gap between engineering and medicine to advance healthcare treatment. Indeed, it integrates the technological background and problem solving skills of the former, with the medical and biological knowledge of the latter. Several scientific branches are involved in the understanding and modelling of the physical processes of the living system under both physiological and pathological conditions, and to implement devices, tools and machines to be used by doctors for diagnosis, monitoring and therapeutic purposes. The fields of mechanics, informatics, electronics, material science, signal processing are only some of the included subjects.

The development and the broadening of this relatively new science has acquired increasing importance on the medical care achievements, not only in terms of treatments, but also in terms of discovering causes of diseases, analysing consequences of palliative and surgical choices, and providing didactic platforms for the clinicians to practice their skills.

The recognised utility of biomedical products favoured the financing of research projects in this area, with increasing interests and money being invested in several sectors of the bioengineering. Between the others, the cardiovascular field covers a large slice of the market; this being easily explained considering that cardiovascular diseases are the leading cause of death worldwide, accounting for approximately 40% of deaths in Europe. The European Commission allocated over €600 million to the Framework 7th HEALTH Programme (2007-2013) aiming at improving the health of European citizens and strengthen competitiveness of European health-related industries; the area of cardiovascular disease was considered a priority.

It is in the context of this Framework 7th HEALTH that my PhD was funded. In particular, the research presented in this Thesis is part of the Marie Curie Initial Training Network (MC ITN) project MeDDiCA, focused on Cardiovascular Engineering and Medical Devices. Being based in the Cardiorespiratory Unit of the Great Ormond Street Hospital for Children, the focus of my research was specifically on congenital heart disease. The groundwork of this Thesis is the collaboration between clinicians and engineers for the development of computational models able to provide answers to specific clinical questions.

1.2 AIMS OF THE THESIS

The main aim of the research presented in this Thesis was to use conventional engineering methodologies as a tool to answer specific clinical questions in the sphere of personalised medicine.

The objectives of this research were to develop and validate a framework based on routinely clinically acquired data in order to:

- Predict stent fracture in each individual undergoing CP (NuMed Inc, Hopkinton, NY, USA) stent implantation
- Characterise and quantify proximal and peripheral resistances that develop in the presence of pulmonary artery stenosis to help plan each patient’s treatment strategy
- Define the optimal treatment in a case study of aortic re-coarctation.

1.3 OUTLINE OF THE THESIS

The following Chapters, 2 and 3, provide a general clinical and engineering introduction to the Thesis. Chapter 2 illustrates the physiology of the cardiovascular system in the adult and in the fetus, to show how an abnormal development of the heart and circulatory system gives rise to congenital heart disease. A brief summary on the most common congenital heart defects and the current options for repair or palliation is provided, with specific focus on the clinical problems addressed in this Thesis. Chapter 3 reviews the concept of modelling in bioengineering and particularly of patient-specific modelling. The principal engineering methodologies exploited in this Thesis for the implementation and validation of patient-specific cardiovascular models are discussed, from medical data acquisition to computational and experimental tools. An overview of the imaging methods and the in-vivo pressure acquisitions is presented, followed by the definition of finite element (FE) method and finite volume method (FVM), lumped parameter networks (LPN) and multi-domain simulations. Hints on the rapid-prototyping technique and its applications, and on the components used in mock-circulatory loops follow.

After the overview of the general methodologies applied in this Thesis, Chapters 4 to 8 explain how these tools were employed during my PhD to study specific clinical cases.

Chapters 4 and 5 focus on the percutaneous pulmonary valve implantation (PPVI) device and outcomes, with the first chapter describing the methodology implementation and validation, followed by the second chapter related to the patient-specific clinical application. PPVI is nowadays an established technique to treat pulmonary valve dysfunction which, however, still presents high incidence of stent fracture (25%). Chapter 4 presents a quantitative assessment of uncertainty for the 3D reconstruction of stents using available imaging techniques. The shape of an in-vitro deformed PPVI stent was reconstructed from micro-computed tomography (CT) acquisitions, CT images with two different radiation doses, an experimental optical technique, and biplane fluoroscopy images. Geometric parameters were used to evaluate the accuracy and the repeatability of each technique along with variation to micro-CT data, assumed to represent the gold standard imaging method. The aim of this chapter was the validation of the stent reconstruction method from fluoroscopy acquisitions that was then used for the study presented in Chapter 5 focused on PPVI stent fracture prediction. In this chapter, I created a statistical model, based also on FE simulation results, able to predict fracture/no fracture of the device after implantation in a specific patient using only procedural fluoroscopy acquisitions data as input.

The clinical subject of Chapter 6 and 7 is transposition of the great arteries (TGA). Patients born with such defect undergo surgical correction, which, however, is associated with long term complications: the enlargement of the neoaortic root, and the development of a unilateral pulmonary stenosis amongst others. These may translate in both sites in complex hemodynamics conditions which I investigated in this Thesis using patient-specific computational models. Chapter 6 shows the creation of a computational fluid dynamic (CFD) multi-domain model of the neoaorta following arterial switch operation (ASO) in a patient born with TGA, validated with in-vitro data generated by an experimental set-up and acquired through 4D magnetic resonance (MR) Flow imaging method. In Chapter 7, this validated multi-domain approach coupled with a LPN simplified methodology was applied to study the flow distribution in the pulmonary artery bifurcation in the presence of unilateral stenosis in patients born with TGA and treated with ASO.

Chapter 8 presents the combination of CFD, LPN and structural patient-specific realistic models to plan treatment in a patient with aortic re-coarctation and aberrant right subclavian artery.

Finally, Chapter 9 summarises the results of this Thesis and outlines a number of remaining research issues, which have been identified as areas for future work.

In terms of engineering methodologies, the different imaging techniques employed in this Thesis are described mainly in Chapter 4: 3D reconstructions of patient-specific implanted devices and cardiovascular anatomies were realised using both volumetric and biplanar visualisation methods, such as CT, MR, and fluoroscopy. Chapter 5 introduces FE structural simulations which are utilised also in Chapter 7 and 8 to computationally deploy cardiovascular stents, under patient-specific boundary conditions. Chapter 6 introduces the first fluid dynamic problem where CFD and multi-domain analyses were used together with an experimental mock circuit to analyse pressure and velocity fields occurring in patient-specific vessel anatomies under patient-specific conditions. CFD coupled with LPN and multi-domain modelling were the methodologies adopted also in Chapter 7. Finally, Chapter 8 presents a case study in which all the previously described, implemented and validated structural and fluid dynamics techniques were applied.

CHAPTER 2

CLINICAL PROBLEMS

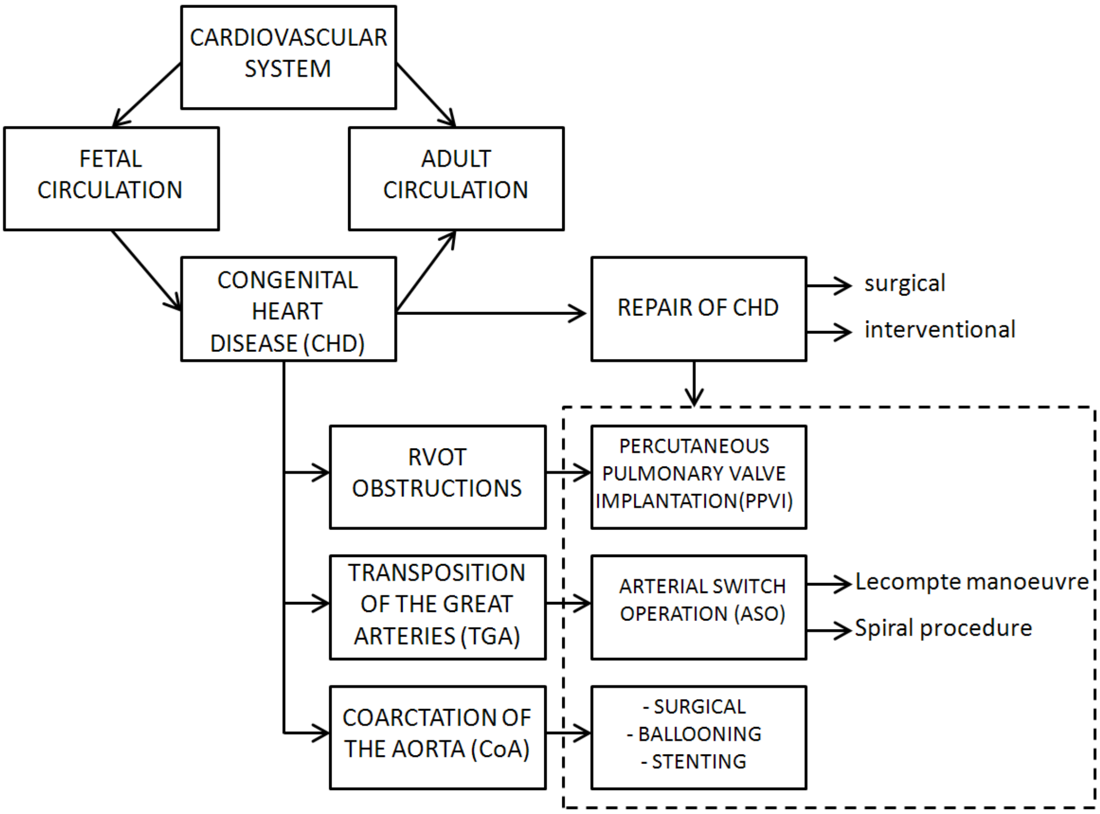

2.1 INTRODUCTION

In this chapter, the physiological adult and fetal cardiovascular system are briefly introduced followed by some of the defects that can affect heart and circulation in the newborns. Particular focus will be given to those congenital heart defects treated in the remainder of this Thesis: Section 2.4 described right ventricular outflow tract (RVOT) obstruction and relative treatments with particular emphasis on the percutaneous repair. Section 2.5 provides information on transposition of the great arteries, surgical correction and long-term complications both in the systemic and pulmonary side. The chapter concludes with the description of aortic coarctation and the options currently available for its treatment (Section 2.6).

2.2 NORMAL CIRCULATION

2.2.1 Adult circulation

The main components of the human cardiovascular system are blood, vessels and heart. Through the flowing of the blood into the vessels' network, the cardiovascular system provides the tissues with nutrients, delivers oxygen, transports hormones, removes metabolic waste, stabilises body temperature and pH, and maintains homeostasis.

The heart is the pulsatile pump that permits the blood to circulate in all body. It is a hollow muscular organ composed anatomically by four chambers (Figure 2.1): two upper chambers called atria (right and left) and two lower chambers called ventricles (right and left). The right and left sides of the heart are divided through two muscular walls, the atrial and the ventricular septum. The upper and lower chambers of each side are in communication through two non-return valves: the tricuspid valve on the right, and the mitral valve on the left. Blood is transferred from the atria to the ventricles when the atrio-ventricular valves are open; while, when they are closed, their function is to avoid blood regurgitation from the ventricles.

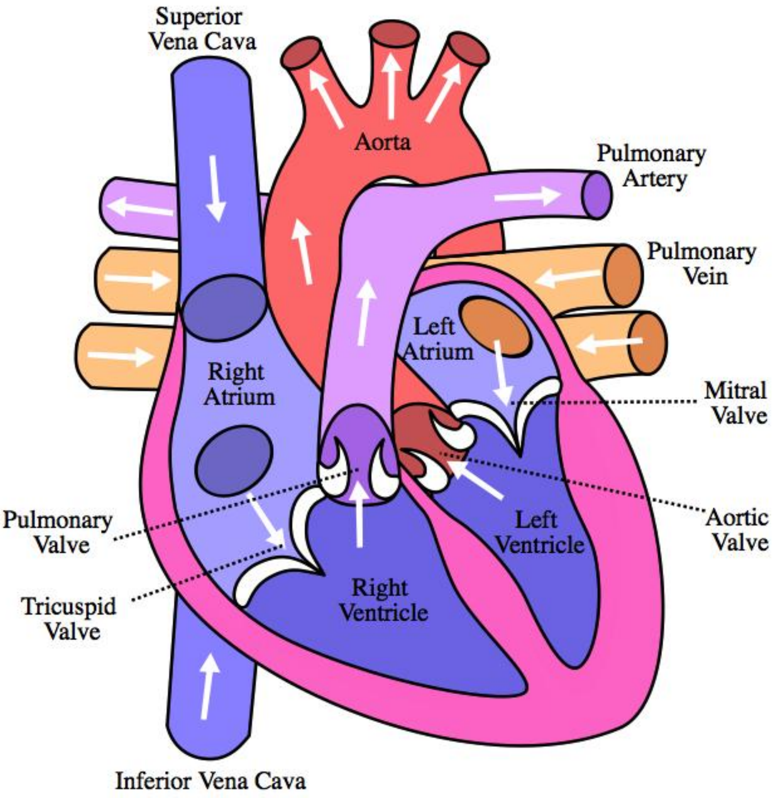

Figure 2.1 - Graphic representation of a physiological human heart with its valves, atria and ventricles, and the arteries/veins attached to them. Image taken from Wapcaplet (http://upload.wikimedia.org/wikipedia/commons/e/e5/Diagram_of_the_human_heart_%28cropped%29.svg).

Two other non-return cardiac valves are present at both outlets of the heart: the pulmonary valve that puts in communication the right ventricle with the main pulmonary artery, and the aortic valve located between the left ventricle and the aorta. The right heart receives deoxygenated blood from the body and pumps it towards the lungs, where carbon dioxide is released and oxygen is absorbed. Deoxygenated blood coming from the upper and lower body enters the right atrium through the superior and inferior vena cava, respectively; while blood resulting from the myocardium irroration is conveyed here through the coronary sinus. The left heart receives oxygenated blood from the pulmonary veins and pumps it to the systemic circulation, where the oxygen supply is delivered to the tissues through the capillary network (Figure 2.2). Both cardiac halves function as two flanked pumps in series, with a synchronised contraction that affects the oscillations of flows and pressures in the vessels directly connected with the outlet chambers, such as aorta and pulmonary artery.

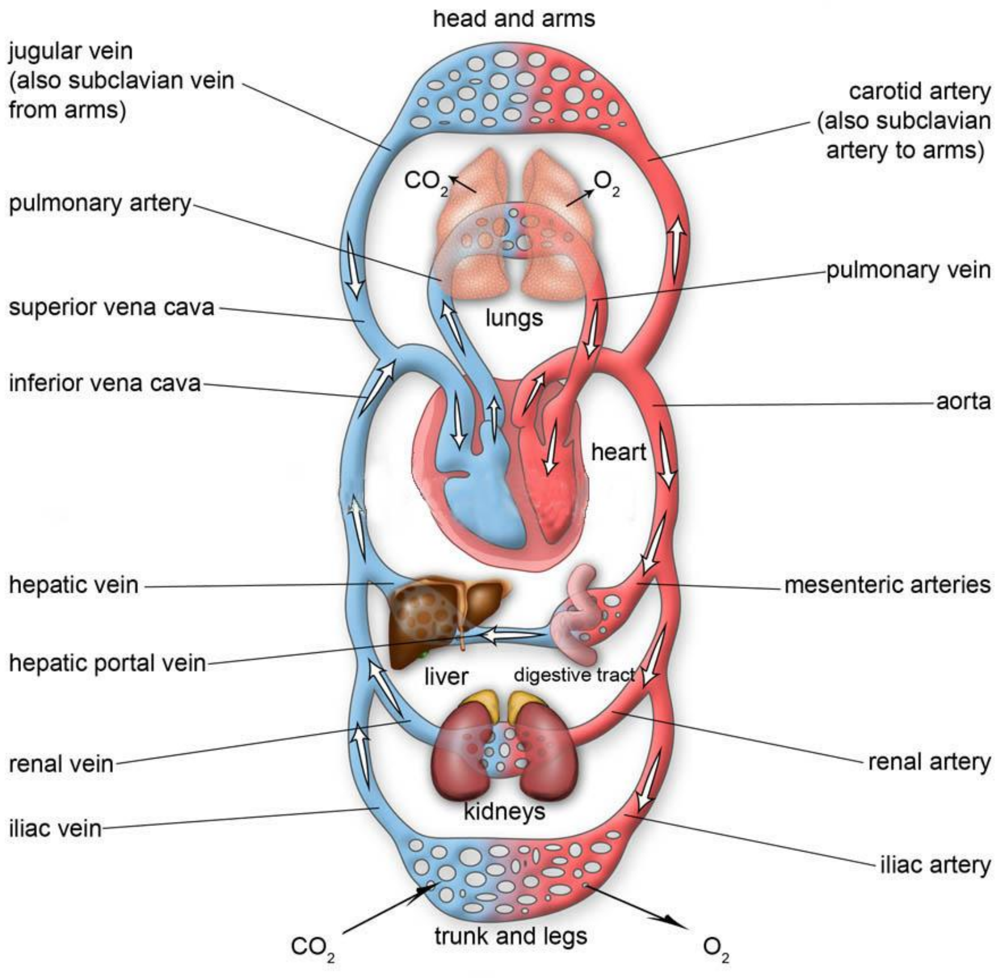

Figure 2.2 - The physiological human circulatory system. In red the vessels perfused by blood rich in oxygen, in blue those with deoxygenated blood. Image adjusted from http://www.medicalook.com/human_anatomy/organs/Routes_of_Circulation.html.

The aorta is the main systemic vessel, and it arises from the upper part of the left ventricle (Figure 2.1). Its first tract ascends for about 5 cm and then arches backward and to the left side. The aortic valve delineates its origin with three small dilatations, each corresponding to one of the three leaflets, called the sinuses of Valsalva or aortic sinuses. The only vessels departing from the ascending aorta are the left and right coronary arteries originating at the level of the aortic root (Figure 2.3), from the left and right aortic sinuses respectively.

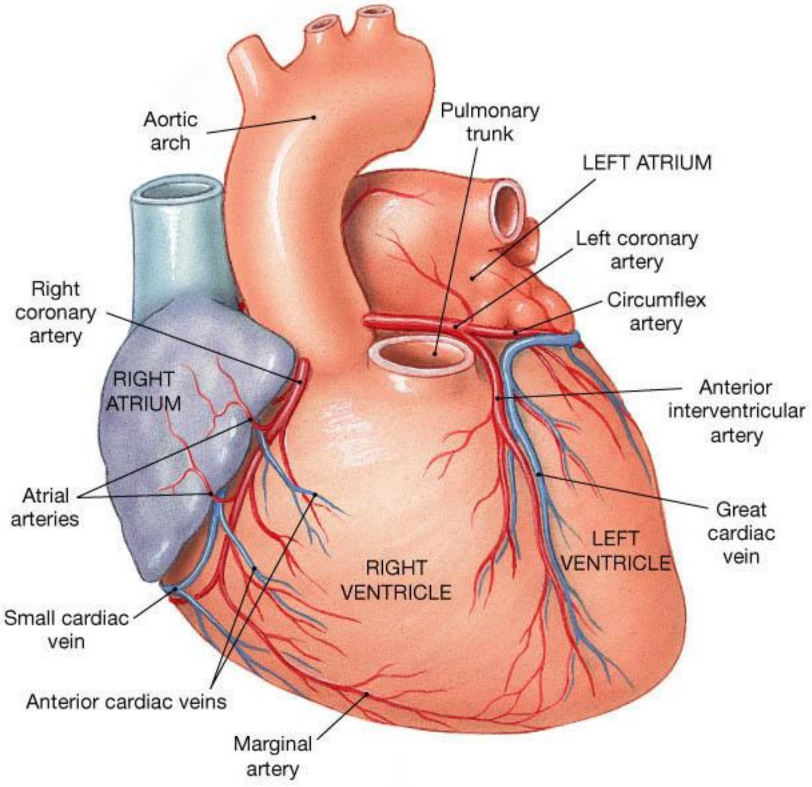

Figure 2.3 - Image of the physiological human heart with the coronaries departing from the ascending tract of the aorta. Image taken from http://droualb.faculty.mjc.edu/Lecture%20Notes/Unit%204/FG21_09a.jpg.

The calibre of the aorta increases at the level of the aortic arch, where a bulging outward of its right wall is present. Usually, three branches depart from the highest part of the arch: the innominate artery, the left common carotid, and the left subclavian.

Finally, the descending part of the aorta can be divided into two portions: the thoracic and the abdominal. The former does not present a considerable diminishment in size, the latter shows a marked reduction in size as further branches bifurcate.

The main pulmonary artery, or pulmonary trunk, originates from the right ventricle and it extends obliquely upward and backward passing in front of the first tract of the ascending aorta (Figure 2.1). Its dimensions are about 5 cm in length and 3 cm in diameter. It then divides into two horizontal branches, the right and the left pulmonary arteries. The right branch is longer and larger than the left branch and runs behind the ascending aorta to the root of the right lung. The left branch passes in front of the descending aorta to the root of the left lung.

The pulmonary valve is a semilunar valve made of three leaflets or cusps, with a diameter of 2-3 cm at its annulus. It lies in a plane slightly antero-superior to the aortic valve, at the superior end of the right ventricle.

2.2.2 Fetal circulation

The fetal circulation (Figure 2.4) is a shunt-dependent circulation as it relies on the presence of intra-cardiac and extra-cardiac shunts for the exchange of oxygenated and deoxygenated blood. In fact, gas exchange does not take place in the lungs, but it occurs at the level of the placenta: it collects deoxygenated blood from the fetus via the umbilical arteries, and returns oxygenated blood taken from the mother circulation through the umbilical veins (ductus venosus). The fetal cardiovascular system is designed in order to deliver the most highly oxygenated blood to myocardium and brain: 50-60% of the placental flow saturated with oxygen bypasses the hepatic circulation via the ductus venosus streaming to the inferior vena cava and then to the right atrium. In the inferior vena cava (IVC), this blood tends to keep separated from the systemic venous blood returning from the lower body. Also, a tissue flap (Eustachian valve) located where the IVC connects to the right atrium contributes in directing the more oxygenated blood directly to the left atrium, through the foramen ovale (a flap of tissue pushed open between the atria). Then, from the left ventricle, this blood is pushed into the ascending aorta, and it preferentially perfuses brain and coronary circulation. On the other hand, the desaturated blood coming from the upper body and the heart muscle perfusion arrives in the right atrium through the superior vena cava where it mixes with the part of desaturated blood streaming from the lower body through the IVC. From the right atrium, it goes to the right ventricle, and because of the considerable pulmonary vascular resistances characterising the undeveloped pulmonary fetal circulation, only about 12% of this blood enters the pulmonary arteries for the nourishment. The remaining 88% accesses the descending aorta through a shunt connecting the aorta to the pulmonary arteries, called ductus arteriosus.

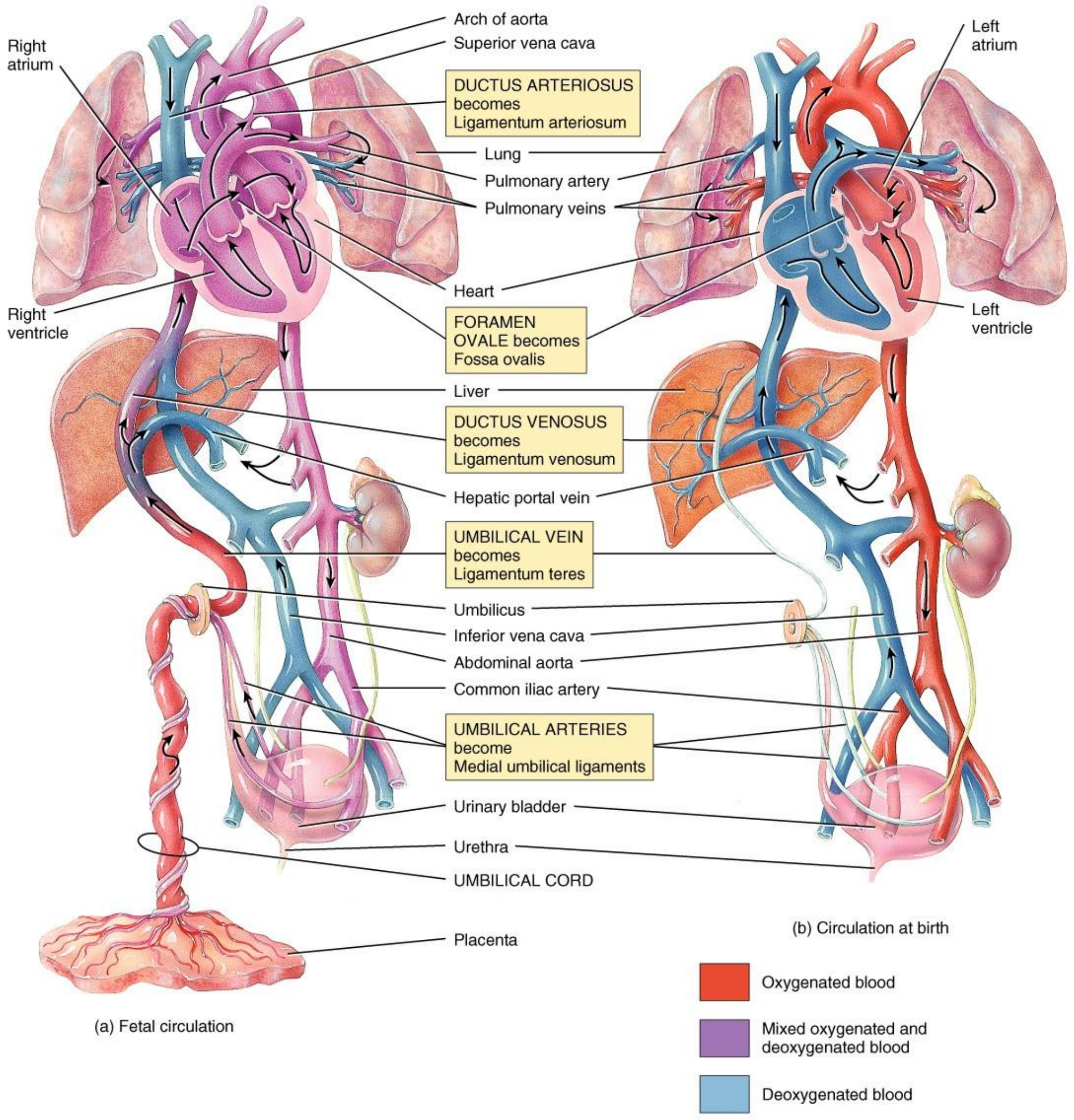

Figure 2.4 - A schematic representation of the fetal circulation (on the left), and of the circulation at birth (on the right). The intra-cardiac and extra-cardiac shunts proper of these circulations are highlighted in the picture. Image taken from http://scientificillustration.tumblr.com/post/44638068025/obligatory-anatomy-diagram-of-the-day-fetal-and.

The transitional phase from the fetal circulation to the post-natal life (Figure 2.4) requires several cardiopulmonary adaptations. First of all, the blood oxygenation has to be transferred from the placenta to the lungs. Once the umbilical vessels are closed, the ductus venosus will stop being perfused, thus interrupting the flow towards the IVC, and in 3 to 10 days after birth it will passively seal. During the last period of gestation, the pulmonary vascular resistances progressively start reducing, and a dramatic fall is finally experienced at birth after the lungs' expansion. The consequent increment of pulmonary blood flow increases the pulmonary venous return to the left atrium. This, combined with the decreased venous return to the right atrium, leads the two atrial pressures to equalise bringing the foramen ovale to its closure within minutes to hours from birth. The last of the described shunts, the ductus arteriosus, closes around 4 days after the delivery.

In case the conversion from fetal to neonatal circulation does not progress physiologically, several abnormalities in the heart or in the blood vessels can arise, known under the name of congenital heart disease (CHD).

2.3 CONGENITAL HEART DISEASE

Congenital heart defects include all the malformations affecting the heart originating in the fetus during gestation. They represent the major cause of infant morbidity in the Western world, with a mortality incidence of 20% (**1**). Only in the USA, nearly one out of 100 infants is born with one or more congenital heart diseases every year. The causes are thought to be mainly genetic, and due to mutations in the regulators of the heart development, but epidemiological analyses showed that also environmental factors are associated to the genesis of CHD. In recent studies, the genetic basis for some defects has been disclosed, and the increasing interest on the subject is bringing new insights on the genetic dysregulations leading to heart diseases (**2**).

In general, CHD can be classified in two categories: those boosting a blood overload towards the pulmonary circulation, and those causing an insufficient pulmonary perfusion. The first category is composed by those congenital malformations inducing oxygenated blood to re-circulate across the lungs before the oxygen is delivered to the tissues through the systemic circulation. In the second group, on the other hand, the tissues are not perfused by sufficiently oxygenated blood, causing cyanosis in the child. Finally, a combination of different defects could coexist, further complicating the cardiovascular system.

A list of common and less common congenital heart diseases with a brief description is presented below. Transposition of the great arteries and coarctation of the aorta will be extensively illustrated in Section 2.5 and 2.6 respectively, as patients affected by these defects will be further studied in the research presented in this Thesis.

- Atrial septal defect (ASD): the foramen ovale typical of the fetal circulation does not close at birth, thus leaving the communication between atria open.
- Ventricular septal defect (VSD): orifice of various dimensions and localizations between the left and right ventricle, often associated to other abnormalities.
- Tricuspid valve atresia: absence of the tricuspid orifice and consequent right ventricle hypoplasia. This condition is always associated with the ASD to permit the life of the newborn by allowing the mixing between oxygenated and deoxygenated blood coming from the pulmonary veins and from the venae cavae respectively.
- Aortic stenosis: valvular, subvalvular of supravalvular narrowing of the aorta. According to the location it can cause insufficiency or coronary artery abnormalities, while left ventricular hypertrophy is always present. Associated CHD are usually patent ductus arteriosus and coarctation of the aorta.
- Hypoplastic left heart syndrome (HLHS): CHD with an undeveloped left heart, including ventricle, valves and aorta. Two other defects are necessary for the life of the newborn affected by HLHS: a communication between the atria and a patent ductus arteriosus.

The next group of CHDs shares RVOT obstructions or pulmonary valve complications.

- Pulmonary atresia: the pulmonary valve does not become patent, thus this condition is usually associated with hypoplastic right ventricle and triscuspid valve.
- Pulmonary stenosis: it consists in a narrowing of the pulmonary valve opening and/or the RVOT. Its position can be: supravalvular, compromising the patency of the main pulmonary artery, or of the branch pulmonary arteries; valvular, with the leaflets of the pulmonary valve abnormally thickened not permitting the full opening; subvalvular, restricting the diameter of the RVOT.
- Absent pulmonary valve: rare defect characterised by underdeveloped pulmonary leaflets and thus significant pulmonary insufficiency.
- Truncus arteriosus: the embryological structure of the truncus arteriosus, which is an arterial trunk originating from both ventricles, fails to divide into aorta and main pulmonary artery before birth. It is always associated with VSD to allow the systemic and pulmonary blood to mix in the ventricles.

- Double outlet right ventricle: in such rare disease, associated with VSD, both aorta and main pulmonary artery originate from the right ventricle.
- Tetralogy of Fallot: this malformation presents four pathological conditions: i) valvular or subvalvular pulmonary stenosis, ii) VSD, iii) right ventricle hypertrophy, and iv) misposition of the aorta above the VSD.

2.3.1 Repair of CHD

Surgical repair is usually needed to correct the CHDs described in the previous paragraph, from days to months after birth.

The survival of children born with congenital heart disease has remarkably increased since the introduction of cardiac surgery (**3**). In the last decades, surgical corrections evolved and improved, showing encouraging mid-term and long-term clinical outcomes. An important role in this success has been played by improvements in early diagnosis, due to the advances of fetal echocardiography (**4**).

The optimisation of surgical techniques has recently become particularly craved, because of a larger inclination to perform the surgical intervention earlier in the life of the sick newborn. In the past, the majority of the techniques used were multiple-step-procedures: usually a palliative intervention was performed soon after birth, and once the baby was stable, a later surgery was following to correct finally the defect. However, such temporary palliations, as the systemic-to-pulmonary shunts, or the pulmonary artery bandings, bear risks of damaging the patient’s circulation causing a noteworthy overload to the pulmonary system and a pressure increase in the right ventricle. In addition, eventual distortions or interruptions caused to a pulmonary branch during the palliation, or shunts and bandings themselves, could make the patient not suitable for undergoing the following surgery.

For these reasons, cardiac-surgeons have abandoned the palliative choice for the better perspective offered by one complete repair intervention. Although it needs to be advanced in time, exposing the child to a demanding surgery soon after he is born, it is able to reduce the mortality associated with the CHD and, at the same time, it can prevent damages to the circulation growth and development (**5**). Though, it must be considered that, in the long-term prospective, surgery in infants often remain pure palliative, as the allometric growth will inevitably change the relationship between the cardiac structures and the implanted device or conduit. And, also those cases planned to be definitive will probably present complications such as cardiac arrhythmia, valve dysfunction and heart failure (**6**) because of the debilitating and invasive approach used on neonates.

In recent years, as the number of tools and devices has markedly grown, an alternative to surgery for the treatment of CHD over time has been found in interventional cardiology techniques, able to safely delay the need for surgery. One example of percutaneous approach to treat RVOT dysfunction resulting from initial surgical repair of CHD – percutaneous pulmonary valve implantation – is reported in Section 2.4.

2.4 RVOT OBSTRUCTION and PPVI

As briefly described in Section 2.3, some CHD are directly associated with obstruction of the RVOT. The obstruction is corrected at birth by surgically reconstructing the RVOT with a patch or a conduit, which often leaves the patient with no valve or a malfunctioning one. Furthermore, the biological or synthetic materials these patches and conduits are made of are prone to degradation and calcification, causing morphological and/or functional changes of the new RVOT over time. Therefore, the patient will require revision of the first repair. The classic approach to this problem is repeated surgical repair. Surgical intervention on cardiac valves is nowadays accomplished with low mortality rates. However, it still bears several pitfalls: first of all, the necessity of sternotomy and the nature of the intervention which rise the risk of infections; then, the use of the heart-lung machine which requires blood anticoagulation drugs, thus increasing haemolytic dangers (**7**); lastly, the economical aspect that cannot be neglected due to the high costs related to the heart-lung machine components, the intensive post-operative treatments required for the patients, and the long hospital stay (**8**).

More recently, an innovative percutaneous technique has been developed that allows for a minimally-invasive approach to pulmonary valve replacement: PPVI.

Transcatheter valves were first introduced in 1992 by two research groups, who performed studies on animals. Pavcnik and co-workers proved the feasibility of transcatheter positioning of a prosthetic caged-ball aortic valve in dogs (**9**), while Andersen succeeded in implanting transluminally a porcine aortic valve in closed-chest pigs (**7**). During the 1990s and at the beginning of the XXI century, further experiences in animals were carried on (**10**– chronic study in lambs; **11**– acute study in pigs; **12**– acute study in lambs; **13**– study in sheep), encouraging the development of this procedure.

The first successful transcatheter valve implantation in man was realised in 2000 by Bonhoeffer and colleagues, who created an innovative system to replace the pulmonary valve (**14**). The device used for this procedure (Melody™, Medtronic Inc, Minneapolis, MN, USA) was developed from commercially available products: a Contegra conduit (Medtronic Inc, Minneapolis, MN, USA) (Figure 2.5) – a segment of bovine jugular vein with a native valve in the centre – was sutured to a CP stent – a Platinum-10%Iridium balloon-expandable stent. The procedure was performed under fluoroscopy guidance in a 12 year-old boy with stenotic RVOT/pulmonary artery after tetralogy of Fallot repair. The valved stent was crimped onto a balloon-in-balloon catheter (Figure 2.5b), and through femoral access, was guided to the RVOT. Once in place, first the inner balloon, second the outer balloon, were inflated to deploy the device into the patient's implantation site.

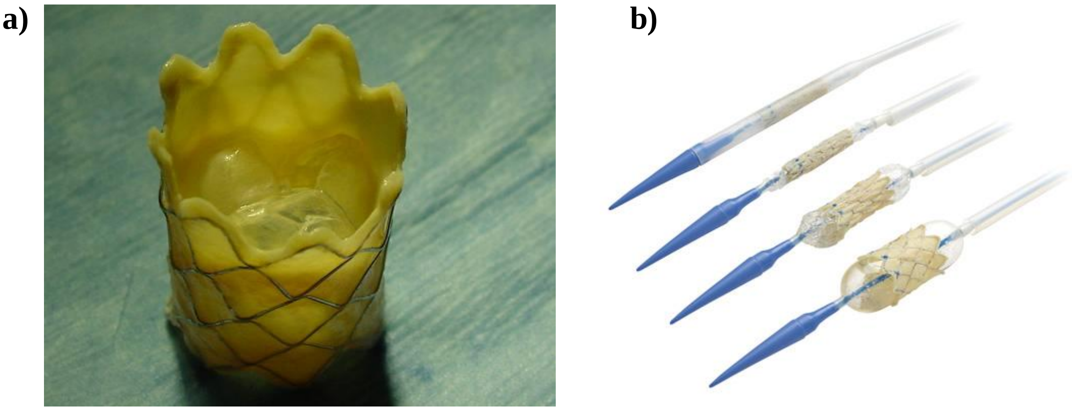

Figure 2.5 - Melody™ device in expanded configuration (a), and during the deployment procedure (b).

Following the success of this first-in-man percutaneous valve implantation, in 2002, Cribier and co-workers performed the first clinical transcatheter aortic valve implantation (TAVI) (**7**) to treat a patient for whom open-heart surgery was judged prohibitive. The device, consisting of 3 bovine pericardial leaflets sewn inside a balloon expandable stainless steel stent (Figure 2.6), was positioned and deployed inside the patient's native stenotic heart valve, without obstructing the coronary flows, neither the mitral valve function. The achieved satisfactory results confirmed the practicability of TAVI (**15**).

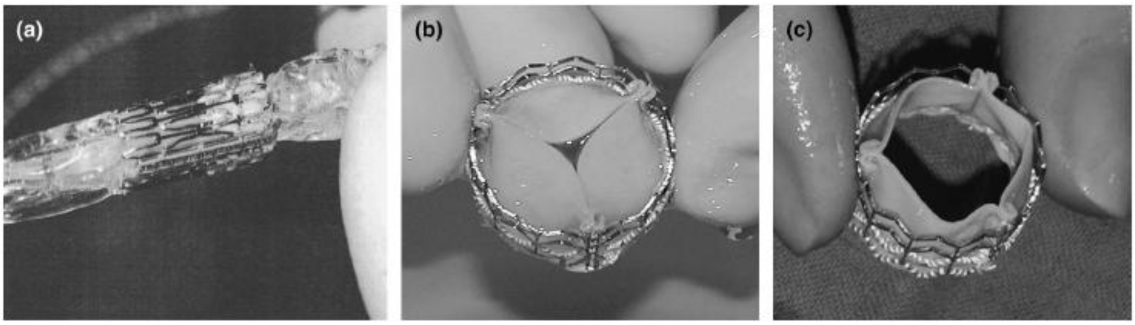

*Figure 2.6 - Cribier transcatheter aortic valve: a) valved stent crimped onto the balloon catheter; b) valve leaflets in closed position; c) valve leaflets in open position (**16**).*

In the last decade, percutaneous valve technology and applications have grown exponentially in the aortic, pulmonary and tricuspid position, with several prostheses currently under development especially for TAVI applications. In PPVI, two devices are clinically available: Melody™ (Medtronic, MN, USA), which received CE approval in 2006 and FDA approval in 2010, and Edwards Sapien™ Pulmonic Transcatheter Heart Valve (Edwards Lifesciences, Irvine, CA, USA). The PPVI population studied in this Thesis has been treated with Melody™ which therefore will be the PPVI device considered in the reminder of this Thesis.

2.4.1.1 PPVI devices in this Thesis

Melody™ is constructed with a valve from a bovine jugular vein, sewn into a balloon-expandable CP stent. This stent is manufactured from heat-tempered 90%platinum-10%iridium, 0.33 mm wires with excellent radiopacity that make it easy to visualise with x-rays. The wires are formed in a 8 zig pattern, wrapped around a cylinder to create a ring and welded at the crown points to other wires to form a cylindrical structure (**17**). The CP stent with a 6 ring configuration is the frame of the PPVI Melody™ device (Figure 2.5a). Since the platinum welds were prone to fracture, this component of the PPVI was modified during the early clinical experience by introducing a gold braising process to reinforce the crowns. The bovine vein is attached to the stent by sutures around the proximal and distal rings and at each strut intersection. Bovine jugular venous valves are available only up to 22 mm of diameter, thus limiting the use of this minimally-invasive technique to those patients (15%) who have a small implantation site. A second generation device is currently under development (**18**) to treat patients with large RVOTs who are unsuitable for PPVI with Melody™. This new device consists of 6 nitinol rings interwoven with a polyester graft (Figure 2.7) and a pericardial valve. The proximal and distal ends of the stent-graft are larger (up to 40 mm diameter) than the central portion (22 mm diameter) which holds the valve, to ensure safe anchoring of the device to the implantation site (**18**). The material of choice for the stent, nitinol, is characterised by large, fully recoverable deformations and high fracture resistance. Therefore, the design of this new PPVI device should allow minimally-invasive treatment in patients with larger and more dynamic outflow tracts, with low risk of stent fracture.

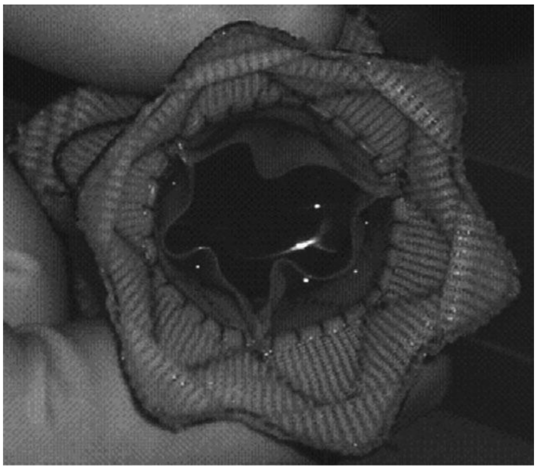

*Figure 2.7 - Second generation PPVI device (**18**).*

In 2009, a successful first-in-man implantation of this new PPVI device was undertaken in a 42-year-old man with congenital heart disease, a previous medical history of four open heart surgeries and two additional thoracic procedures. Surgical replacement of the severely insufficient pulmonary valve was considered too high risk, whereas PPVI with the Melody™ device was prevented by the anatomical dimensions and highly dynamic characteristics of the native outflow tract (**19**). The device is currently undergoing preclinical trial in the US and Canada.

2.4.1.2 PPVI procedure

During the procedure in the catheterisation laboratory, the Melody™ valved stent assembly is hand-crimped from 18 mm diameter to a size of 6 mm onto a custom made delivery system, before being re-expanded inside the patient's implantation site up to 22 mm. The delivery system (Ensemble™, Medtronic) comprises a balloon-in-balloon (BiB) deployment design with three available outer balloon diameters: 18 mm, 20 mm and 22 mm. The inner balloon sizes are half of the outer balloon diameters, and they are 1.0 cm shorter than the outer balloon lengths. BiB catheters allow the insertion of the device in a two-stage process: the inner balloon is the first to be inflated, semi-expanding the stent into an even cylindrical configuration. This allows (i) a fine positioning of the device in the RVOT, before the outer balloon is inflated for the final expansion; (ii) and to avoid any wall injuries caused by the dogboning effect during the stent inflation. Also, each balloon is provided with two markers, increasing the visibility of the delivery system, and permitting the measurements of the functional length accurately along the process.

Over the last 13 years, PPVI with Melody™ has shown a marked learning curve with safety and efficacy improvements that have led to successful worldwide clinical use of this procedure (>5,000 implants to date).

Despite the success of this technique, a major technical issue still remains: stent fracture. During the preclinical testing phase of this device, stent fracture was not identified as a potential problem: the device was mounted inside a cylindrical compliant conduit in a mock circuit, and the cardiac pulsatile loading conditions were replicated exposing the device to millions of cycles, as requested by standard testing regulations. In this set-up, at the end of the testing, the valve showed some tears and became sometimes incompetent, while the stent presented no signs of mechanical failure: exactly the opposite of what happens in the clinical experience. Finite element analysis of the device tested with the same loading conditions for long-term mechanical performance (fatigue analysis) gave the same results: no risk of stent fractures. This suggests that the preclinical tests simulated incorrectly the in-vivo loading conditions, not taking into account the specificity of patients' anatomies and dynamics.

PPVI stent fracture occurs in approximately 25% of the treated patients (**20**), but luckily does not cause highly risky hemodynamic or clinical complications because in most of the cases the stent does not lose its structural integrity. When this does happen, and the patient becomes symptomatic again, a second PPVI stent can be safely implanted in the first (**21**). In order to minimise the risk of stent fracture, a pre-stenting strategy has been developed with the implantation of one or several bare stents before the valved device. This technique is feasible and safe, and has been shown to help in relieving eventual RVOT obstruction and reducing the risk of developing fractures because it creates a reinforced scaffold for the PPVI device (**22**). However, despite the bare metal stent, Melody™ stent fracture remains a problem and close clinical follow-up is required (**23**). Chapter 5 of this Thesis will analyse the problem of PPVI stent fracture in our patient population by using engineering tools.

2.5 TRANSPOSITION OF THE GREAT ARTERIES AND COMPLICATIONS FOLLOWING THE ARTERIAL SWITCH OPERATION

2.5.1 TGA

Transposition of the Great Arteries is the most common cyanotic congenital heart disease in neonates (**24**). The incidence of the disease is estimated at 20-30 cases per 100,000 live births every year, with a 60-70% male predominance (**25**).

Although the aetiology of this congenital disease is still unknown, some risk factors have been identified:

- Mother's age > 40 years
- Alcoholism
- Diabetes
- Poor nutrition during pregnancy
- Rubella or other viral illness during pregnancy.

The hallmark of TGA is ventriculo-arterial (VA) discordance, whereby the aorta arises from the right ventricle and the pulmonary artery (PA) arises from the left ventricle (Figure 2.8b) (**26**).

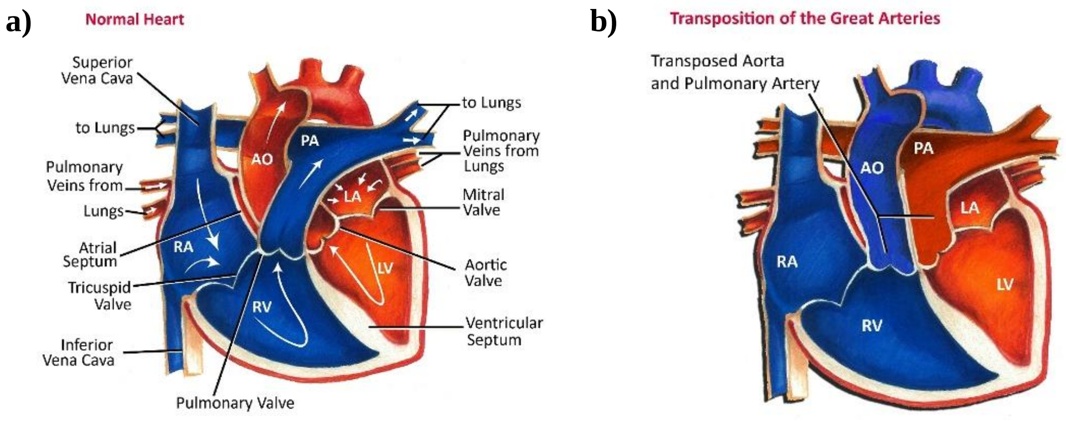

Figure 2.8 - Schematic representation of the normal heart (a) opposed to the TGA heart (b).RA, RV, LA, LV indicates respectively the right and left atrium and right and left ventricle. The incorrect origin of the aorta (AO) and the pulmonary artery (PA) are highlighted in the picture on the right. Image taken from http://pediatricheartspecialists.com/articles/detail/transposition_of_the_great_arteries.

This anatomical arrangement impacts on the way blood circulates throughout the body; in fact, the pulmonary and systemic circulations function in parallel rather than in series.

Oxygenated pulmonary venous blood returns to the left atrium and left ventricle, but it is re-circulated to the pulmonary vascular bed via the abnormal pulmonary arterial connection to the left ventricle. Deoxygenated systemic venous blood returns to the right atrium and right ventricle where it is pumped to the systemic circulation, effectively bypassing the lungs.

This parallel circulation results in insufficient oxygen supply to the tissues and excessive right and left ventricular workload (**27**). It is incompatible with prolonged survival unless oxygenated and deoxygenated blood are mixed at some anatomic level, such as in the presence of atrial or ventricular septal defects acting as left-to-right shunts (**28**). If the pathology is left untreated, the mortality rate is approximately 30% in the first week of life, rising to 50% in the first month, and to 90% by the end of the first year. On the other hand, early diagnosis and treatment allow the overall short-term and mid-term survival rate to exceed 90% (**27**).

The most common causes of postoperative mid-term mortality are mainly arrhythmia, right ventricle dysfunction and mechanical complications at the level of the intra atrial baffle surgically created to treat the defect (emedicine.medscape.com).

In approximately 60% of patients, the aorta is anterior and to the right of the pulmonary artery, while a subset of patients presents the aorta located in front and to the left of the pulmonary artery. These two types of configurations are referred to as dextro-transposition of the great arteries (d-TGA) and levo-transposition of the great arteries (l-TGA).

In addition, most TGA patients (regardless of the spatial orientation of the great arteries) exhibit a subaortic infundibulum, absence of subpulmonary infundibulum, and fibrous continuity between the mitral valve and the pulmonary valve (**29**). However, several exceptions have been observed and cannot be placed in the above classifications (**27**).

With regard to ventricular morphology, the patient's ventricles have normal shape and thickness in presence of atrial-septal defect at birth; otherwise the right ventricular wall is considerably thickened, with such thickening increasing with growth. Within few weeks, the right ventricle often becomes enlarged and hypertrophied. The wall of the left ventricle, instead, becomes thinner and compressed (**28**).

The aortic valve plane is rightward and anterior relative to the pulmonary trunk. The fibrous continuity of the leaflets of the atrio-ventricular and the ventriculo-arterial valves is located on the right side rather than on the left side (**28**).

Coronary arterial anatomy in TGA patients is not only significantly different from the normal circulatory arrangement, but it can also vary substantially within this patients' group. In most cases, the coronary arteries originate from the aortic sinuses contiguous to the pulmonary trunk and run directly toward the atrio-ventricular groove following a normal course. In other cases, they originate from different sinuses and have an intramural course, or can be characterised by abnormal looping around the vessels (**28**).

Another anatomical consideration concerns the pulmonary trunk, which can be larger than the descending aorta, particularly in those cases presenting a ventricular septal defect. Either isthmic coarctation or interrupted aortic arch are very common in hearts with ventricular septal defect (**28**).

Following from these considerations, TGA clearly results in a complex anatomical and physiological arrangement that requires surgical correction.

2.5.2 Surgical Repair of TGA: the Arterial Switch Operation

Repair of TGA has been attempted since the 1950s. The most successful procedures were introduced in 1958 by A. Senning (**30**) and in 1963 by W.T. Mustard (**31**). Both approaches consisted in redirecting blood flow within the atria: the former has the advantage of not using foreign material (i.e. atrial patch), the latter of being simpler to manage post-operatively (**32**). The Senning or Mustard procedures represent an 'atrial switch' and have been used to palliate TGA until a new procedure, referred to as 'arterial switch', was introduced in 1980. The first successful arterial switch operation (ASO) was reported by Jatene (**33**), and it proved to be more beneficial than the atrial correction (**28**), as it avoids arrhythmias and dysfunctions of the systemic ventricle. This Thesis will focus solely on TGA patients who underwent ASO procedure, as described below.

In the first day of life, the primary step undertaken to treat a newborn with TGA defect is to perform a Rashkind balloon atrial septostomy (**26**). This minimally-invasive procedure uses a balloon catheter to enlarge the foramen ovale (i.e. the hole allowing communication between the atria in the fetal circulation) in order to prevent its sealing, otherwise naturally occurring soon after birth. This facilitates blood mixing and increases oxygen saturation (Figure 2.9), bridging the patient to the surgery.

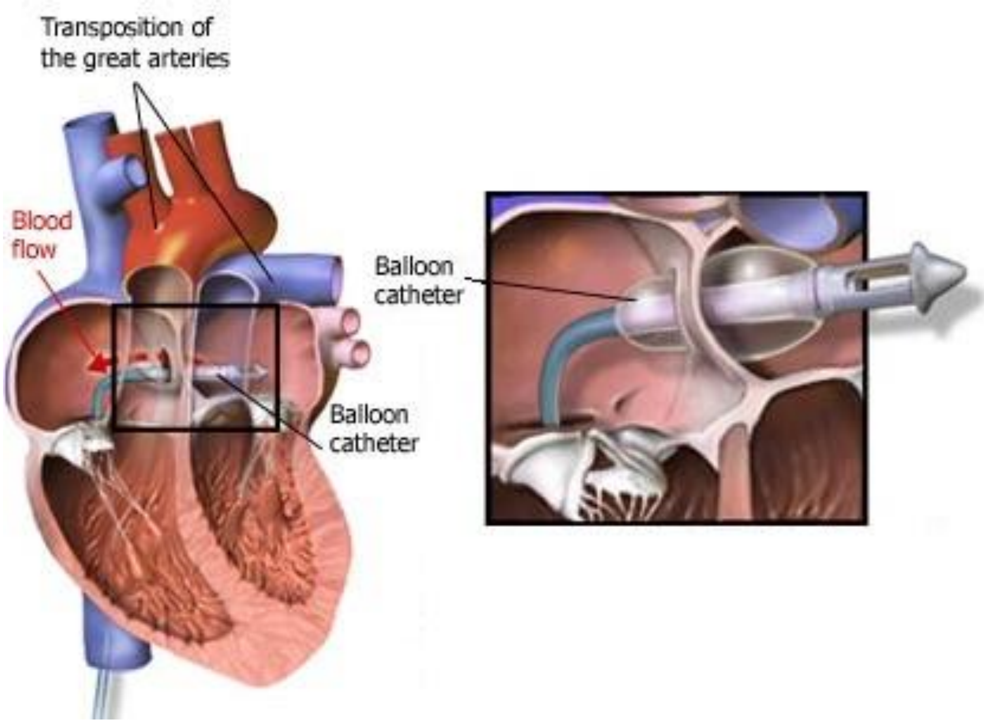

Figure 2.9 - Rashkind procedure: the balloon catheter is inserted into the septal defect and inflated. After inflation, the catheter is pulled back through the hole (http://www.hakeem-sy.com).

After 10-15 days, the aorta and main pulmonary artery can be surgically repositioned (Figure 2.10) performing the actual arterial switch, which requires cardiopulmonary bypass and aortic cross clamping.

One particularly challenging feature of ASO is the relocation of the coronary arteries, in order to avoid cardiac hypoxemia and ischemia of the myocardium. The left and right coronary arteries ostia are visualised and excised from the aortic root, with adjacent aortic wall, as "buttons". In abnormal looping course the dissection of the coronary trunk is extended, in order to avoid any stretch or kink during the relocation. The coronary artery buttons are then shifted posteriorly and implanted into the facing sinuses of the main pulmonary artery root. The left coronary artery is allocated in a low position and the right coronary artery in a high position, in order to reduce the risk of distortion. A lateral relocation could prevent compression by the pulmonary bifurcation.

The aorta is transected in the middle of the ascending portion, in order to lessen the amount of reconstructed aorta posteriorly below the transferred pulmonary artery bifurcation. The pulmonary trunk is transected 5–10 mm below its bifurcation. Next, the main pulmonary artery and its branches are brought forward with a practice that goes under the name of Lecompte manoeuvre, and the distal aorta is moved posteriorly (**28**). A termino-terminal anastomosis is then realised between the distal aorta and the root of the pulmonary valve. Using a patch of cryopreserved pulmonary artery homograft, the pulmonary artery is then reconstructed, and finally the atrial septal defect closure completes the arterial switch repair (**28**).

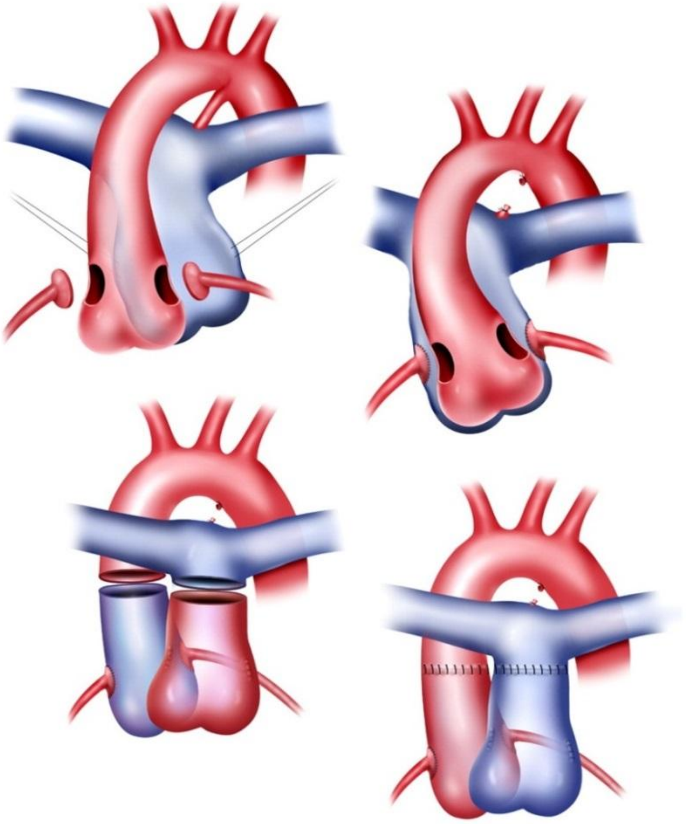

Figure 2.10 - Schematic representation of the arterial switch operation, including relocation of coronary buttons (http://radiology.rsna.org).

2.5.3 Postoperative complications

Although arterial switch restores normal blood flow with mixing of oxygenated and deoxygenated blood, and 90% 10-year survival has been reported to date, indicating the success of the surgery (**26**), several long-term complications can arise. It should be noted that since this procedure has been performed for only approximately 30 years, there are no long-term survivors so far, and the possible extent of long-term complications cannot be fully appreciated yet (**34**).

2.5.3.1 Systemic side

Aortic wall abnormalities in surgically repaired TGA are likely due to anomalous aorticopulmonary septation, damage to the vasa vasorum, and surgical manipulations during ASO. Vasa vasorum transections during the procedure, with consequent blood flow inhibition, can induce necrosis followed by dilatation. This can lead to impaired distensibility of the neoaorta, reported by both invasive and image-based studies (**35**). Kinking of the coronary arteries could also occur, because of the spatial arrangement of the vessels, which does not respect the physiological one. Moreover, the length of the vessels sometimes is not adequate to easily relocate them, thus they need to be stretched. As a result, the coronaries are prone to stenosis, and the occlusion of the coronary arteries is not an uncommon event in the follow-up of TGA patients (**36**).

Physical manipulations during ASO, such as the reimplantation of the coronary arteries and suturing of the two main vessels, can also lead to scarring and changes in the neoaortic root wall, resulting in progressive aortic dilatation. Aneurysm formation and aortic dissection have also been attributed to the ASO surgical handlings (**37**).

After ASO, the neoaortic wall (the former pulmonary artery) is exposed to higher systemic pressures. Concern has been raised about the ability of the pulmonary root to adapt to a systemic pressure load. A study by Co-Vu and colleagues discussed the risk for the native pulmonary root to dilate when implanted in the aortic position, because of the histological differences inherent to the vessel walls of the pulmonary and aortic arteries. Also, no evidence of stabilization in the root dimensions has been observed yet, around 15-20 years postoperatively (**38**).

Both aortic distensibility and aortic dimensions are crucial parameters affecting aortic valve dynamics. Decreased distensibility of the aortic root increases stress and strain on the neoaortic valve leaflets, therefore predisposing for aortic valve dysfunction (**37**). In addition, the risk for neoaortic valve regurgitation appeared to increase with length of time after the operation, which parallels the risk for neoaortic root dilation (**38**).

Furthermore, the relocation of the ascending aorta onto the pulmonary valve might create an abnormally acute angulation of the aortic arch (Figure 2.11) as a consequence of the Lecompte manoeuvre.

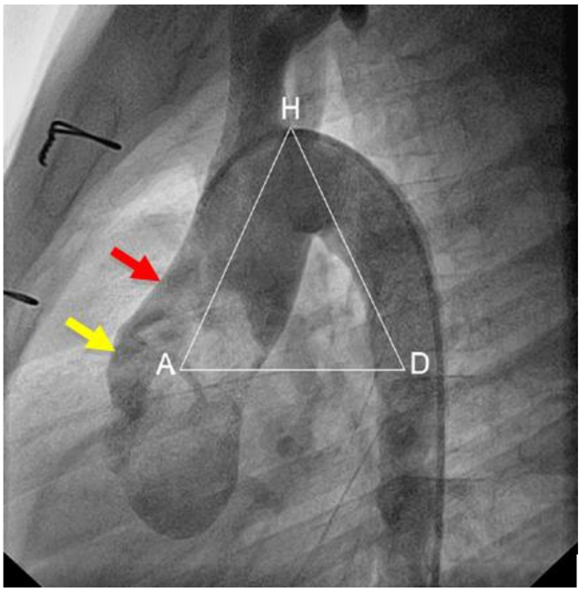

*Figure 2.11 - Fluoroscopy visualisation of an acute aortic arch, or gothic arch, as a result of arterial switch operation. The enlarged aortic root (indicated by the yellow arrow) and the indentation resulting from repositioning of the pulmonary arteries following the Lecompte procedure (red arrow) can also be appreciated. Image modified from (**39**).*

This postoperative morphological feature has been suggested to induce enhanced systolic wave reflection and consequent ascending aortic dilatation (**39**). The acute angulation of the aortic arch, also referred to as “gothic” arch, has been associated with compromised exercise capacity in these patients (**40**). Furthermore, the increased impedance due to a stiffer and abnormally shaped aortic arch is likely to impinge on the VA coupling, as recently indicated by Biglino and co-workers. Thus, it has been suggested that TGA repair by ASO can also have consequences on pumping efficiency and energetics (**41**).

2.5.3.2 Pulmonary side

Complications on the pulmonary side are mainly identified with the development of pulmonary artery unilateral stenosis. Indeed, during the Lecompte maneuver, the operation of moving the pulmonary artery in front of the aorta causes a relevant stretching of the left pulmonary artery. In addition, it has been observed that the presence of a portion of ductal tissue can cause the so-called coarctation of the left pulmonary artery. Here, the LPA narrows where the ductus arteriosus inserts between the two arteries, and when relocated during the Lecompte maneuver this can create a significant stenosis and flow asymmetry (**42**). This issue has been reported to occur in 7 to 28% of ASO cases (**43**).

If the asymmetry of the flow is considered to be detrimental for the patient, the most common solution for this problem is either stenosis ballooning or stenting. However, some cases have been reported with the ballooning not considered as optimal solution (**36**). The percentage success of balloon dilation was assessed around 50% and inversely proportional to the age of the patient (**43**). Dilatation was indicated as not very efficient but beneficial in terms of decreased right ventricular pressure, given that it allows postponing the surgical approach. On the other hand, it has been demonstrated that stenting is a more effective strategy, since the conduit remains patent for a longer time (**44**).

In some patients, a controversial occurrence was noticed: although a severe unilateral pulmonary stenosis was diagnosed from MR examination, no asymmetric flow distribution between left and right pulmonary arteries was observed. This phenomenon has not been explained yet, and it is likely connected with a change (remodelling) in the distal pulmonary vascular resistances that allows for balanced flow-split despite the presence of the stenosis.

2.5.3.3 Remodelling of the pulmonary resistances

In general, the human organism is able to respond to and partly compensate mismatches in order to restore physiological conditions. In the context of variations of pulmonary resistance, remodelling can be defined as the ability of vessels to change their structure without changing their volume (**45**). Remodelling can be classified as *inward* or *outward*: the former leads to a reduction of the lumen, the latter is associated with an increase of the lumen. Furthermore, a sub-classification based on the amount of tissue belonging to the arterial wall refers to the remodelling as hypotrophic, hypertrophic and eutrophic, respectively for a decrease, increase or no change (**46**) in tissue quantity.

Remodelling in case of hypertension has been widely studied and discussed in literature. Several in-vitro experiments confirmed that an increment in the relaxation of the peripheral resistances and in the wall-lumen ratio in hypertensive patients (inward eutrophic remodelling) was not associated with any increase in the total cross sectional area of the vessel, at least in the minor vessels. In the great arteries, remodelling brings to a wall-lumen ratio rise that always leads to tissue growth (**46**).

Hypertension is not the only possible reason for remodelling. Altered blood flow can lead to vascular remodelling, influencing vascular tone and attracting inflammatory cells (**47**). This scenario is more representative for the cases here discussed, as the TGA patients analysed in this Thesis research did not present any sign of pulmonary hypertension. In general, cardiologists accept that pulmonary hypertension occurs where pulmonary pressure is greater than 50% of systemic pressure (**48**), while in the analysed cases the pulmonary pressures were in the physiological range.

Remodelling in small vessels can be due to various reasons. Inflammation or presence in the blood stream of certain proteins, growth factors, nitride oxide or enzymes can facilitate the onset of vascular remodelling (**47**). Furthermore, arteries show inward remodelling after a reduction in blood flow. The lumen of a vessel shrinks if the flow is reduced. Experiments with murine mesenteric artery showed the effect of surgically modified blood flow on the arterial diameter. The average in-vivo diameter before flow alteration was 193±9 μm. After two hours in un-physiological state, the arteries with low flow registered a decrease in diameter of 17±5%, while arteries with high flow measured an increase of 17±7% (**47**; **49**).

Changes in the pulsatility of the flow can also be responsible for the remodelling of the vasculature, as shown in patients with Fontan circulation (**50**).

2.5.4 Surgical Repair of TGA: an alternative operation

In a normal anatomy, the aorta and the main pulmonary artery present a spiral spatial arrangement, while the ASO with Lecompte manoeuvre, as described in Section 2.5.2, does not maintain the spiral relationship of the great arteries. This has been indicated as one of the main causes for some of the clinical complications in repaired TGA (**51**). For this reason, a modified ASO by a so-called "spiral reconstruction" (Figure 2.12) has been advocated by one group in Taiwan to potentially help in avoiding coronary kinking.

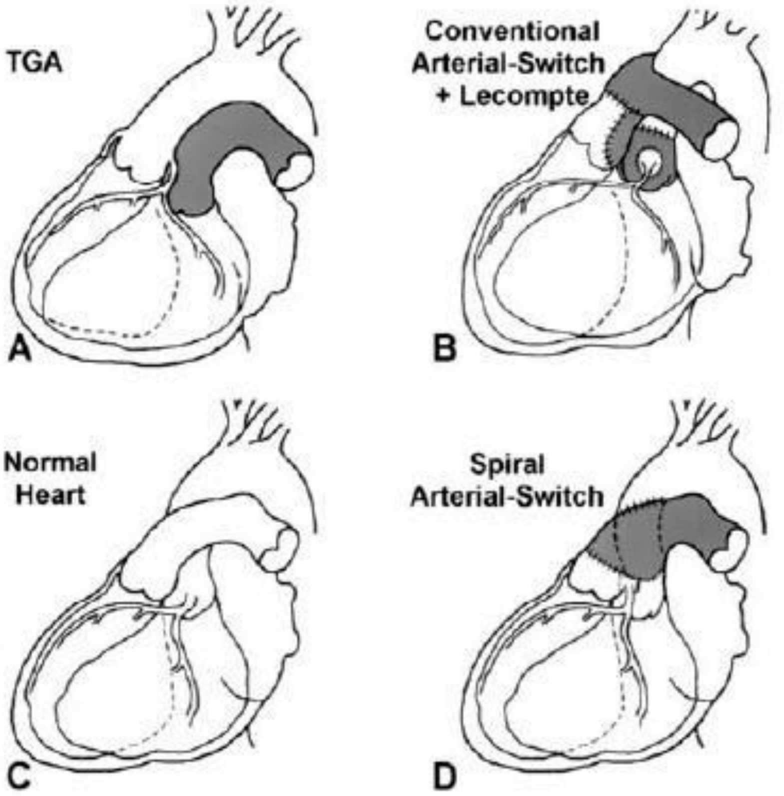

Figure 2.12 - Comparison between normal heart (C), TGA (A), ASO with Lecompte (B) and spiral ASO (D). It is possible to appreciate how the spiral procedure restores a more physiological anatomy than the traditional arterial switch operation (image from ***51****).*

The three main differences of the spiral procedure with respect to the previous technique have been described by the group who introduced it as follows: (1) the aorta is amputated obliquely so that a larger left lip can be used as the floor of the pulmonary pathway; (2) the right posterior part of the pulmonary trunk is divided to make a larger flap to be everted to the left and a more leftward pulmonary pathway after neoaortic anastomosis and posterior attachment (suturing the caudal edge of the right pulmonary artery to the posterior neoaorta) accordingly; (3) the posterior attachment site is ascertained after release of the aortic cross-clamp, as in the previous technique (Figure 2.10). However, to facilitate exposure, the aorta is cross-clamped again distal to the deepest site of attachment and then stitched from the right (**51**).

Therefore, this procedure restores the high-pressure ascending aorta to its natural location, reducing the acute angulation of the aortic arch due to the Lecompte manoeuvre and all the resulting issues, such as arch hypoplasia and neocoarctation.

2.6 AORTIC COARCTATION AND TREATMENTS

2.6.1 CoA

Coarctation of the aorta (CoA) is a narrowing of the aorta typically occurring just distal to the head and neck vessels, in the region adjacent to the ductus arteriosus (Figure 2.13).

The incidence of such a disease is estimated to be around 0.1% of newborns (**52**), and can be found isolated or in association with other heart defects, such as bicuspid aortic stenosed valve (BAV), tricuspid aortic stenosis (**53**; **54**), ventricular septal defect, patent ductus arteriosus, mitral stenosis or regurgitation, aneurysm of the circle of Willis (**53**).

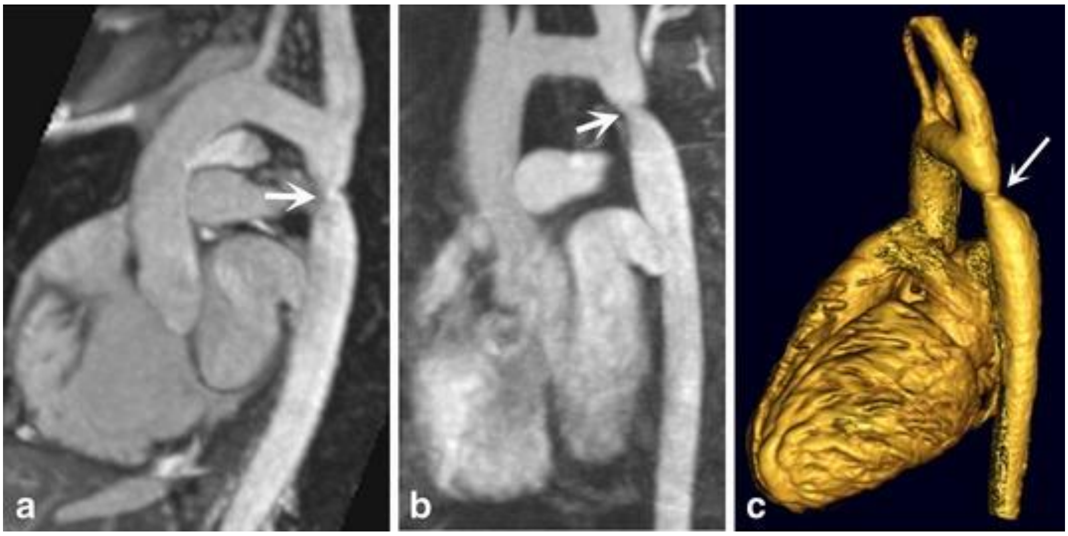

Figure 2.13 - Patient with CoA imaged through unenhanced 3D SSFP magnetic resonance angiography (MRA) (a) and contrast enhanced MRA (b). Three-dimensional volume rendering of the heart and the aorta with coarctation (c) indicated by the arrow. Image taken from ***55****.*

This condition entails hypertension in the arms, development of an extensive collateral arterial circulation connected to the descending aorta and its branches (Figure 2.14a) (**53**), left ventricular failure and aortic dissection (**56**). Also, the narrowed portion of the aorta creates a significant pressure gradient and a flow jet with high velocity (Figure 2.14b) that can compromise hemodynamic parameters such as pulse blood pressure, aortic capacitance and wall shear stress (**57**).

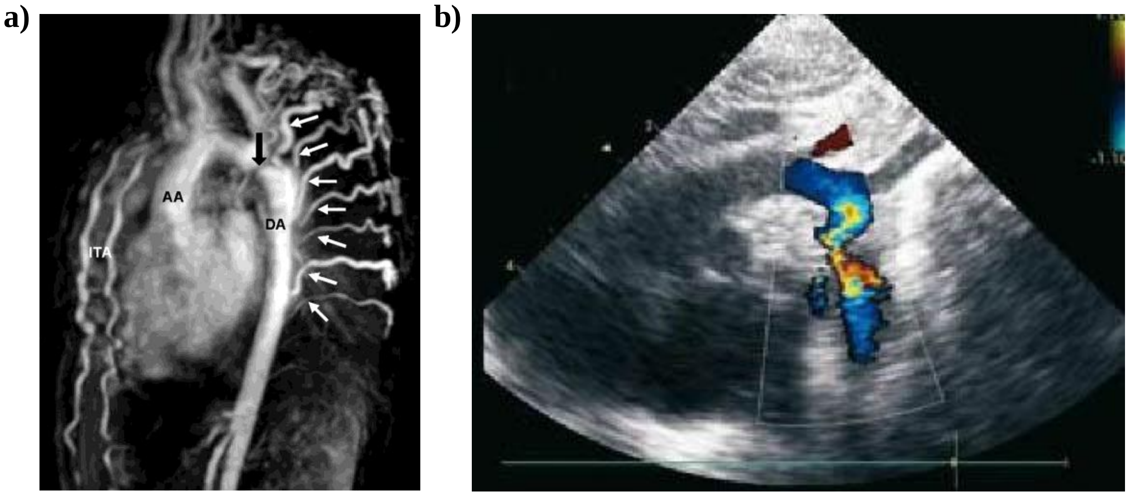

Figure 2.14 - a) Magnetic resonance angiography of a CoA, with intercostals collateral arteries indicated by the white arrows (AA=ascending aorta, DA=descending aorta). Image taken from Ijland and Tanke, 2009; b) Echocardiography in an aortic arch with coarctation, showing a high velocity jet through the narrowing. Image taken from ***58****.*

Native CoA is usually detected during the investigation for systemic hypertension. Adults with CoA could be asymptomatic or present symptoms typically associated with hypertension. Non-invasive functional assessment consists in the measurement of the cuff pressure difference between arms and legs, peak gradient estimation by Doppler echocardiography, and flow measurement through 2D or 3D Phase-Contrast MRI (**59**). However, Doppler echocardiography could be obtained only in patients with a favourable location of the descending aorta, and usually overestimates the pressure gradient (**60**), while the upper-lower body pressure difference was proven not to be a reliable estimate for the pressure loss across the CoA (**61**). Invasively, the exam used for a pre-operative evaluation and a post-operative assessment is pressure measurement by cardiac catheterisation. The anatomy is usually determined through MRI, CT, or contrast aortography.

2.6.2 Treatments

No treatment modality has been widely accepted as optimal. Among the options there are various surgical techniques, percutaneous balloon angioplasty, stenting and implantation of a covered stent.

Surgery is generally performed in patients with a pressure gradient across the stenosis larger than 30 mmHg (**56**), using end-to-end resection, patch repair or tube grafts. For years, it has been considered the standard treatment, but, due to the technical difficulties, related risks (paraplegia, higher perioperative mortality) and long term issues (recurrence of residual CoA, late aneurysm, persistent hypertension) (**62**) is no longer routinely performed (**63**).

In 1982, percutaneous balloon angioplasty was first tested to relieve the surgically created CoA in newborn lambs (**64**), and then introduced as a successful treatment in humans. However, not all CoA are suitable for balloon dilatation, and also high risk of re-coarctation, aneurysm formation and dissection are associated with such minimally-invasive procedure (**62**). Stenting (Figure 2.15) has been introduced in the last decade as a successful alternative to surgery (**65**), but without eliminating the risks presented by ballooning of aneurysm formation, damage to the aortic wall and vessel obstruction (**66**).

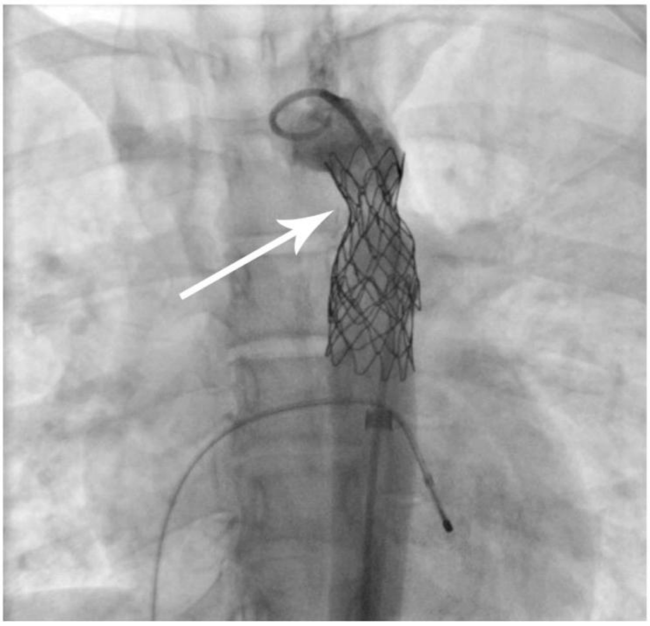

Figure 2.15 - Fluoroscopy images of a CoA treated with stent implantation. Image taken from ***67****.*

In 2011, a multicentre observational study tried to compare the three presented options (surgical, balloon angioplasty and stenting) for the treatment of native CoA in terms of immediate, short-term and intermediate outcomes. The cohort included 350 children between 6 and 12 years old from 36 centres. Lower immediate complications were observed in the stented patients that together with the surgical patients presented superior hemodynamics and imaging outcomes at short-term and intermediate follow-up. However, stented patients more likely required a planned re-intervention (**68**).

The final alternative consists in implanting covered stents. Results from a single centre have shown that covered CP stents, although still bearing with aortic wall complications, can be a safer alternative to conventional stenting, also allowing further secure later re-dilatation (**62**).

Among the potential disadvantages of the covered CP stent are the eventual graft ruptures due to balloon re-dilation, the needs of large sheath, and the potential occlusion of aortic side branches (**62**).

The technological and scientific advancements of the last decades have made available an increasing number of tools that can help facilitate the diagnosis and guide the treatment for several of the CHD and issues described above. In particular, the application of engineering methodologies to study the physiology and the pathology of the cardiovascular system has provided precious insights and additional directions for the treatment of heart diseases. In the next chapter, some of these engineering tools will be described.

CHAPTER 3

ENGINEERING METHODOLOGIES

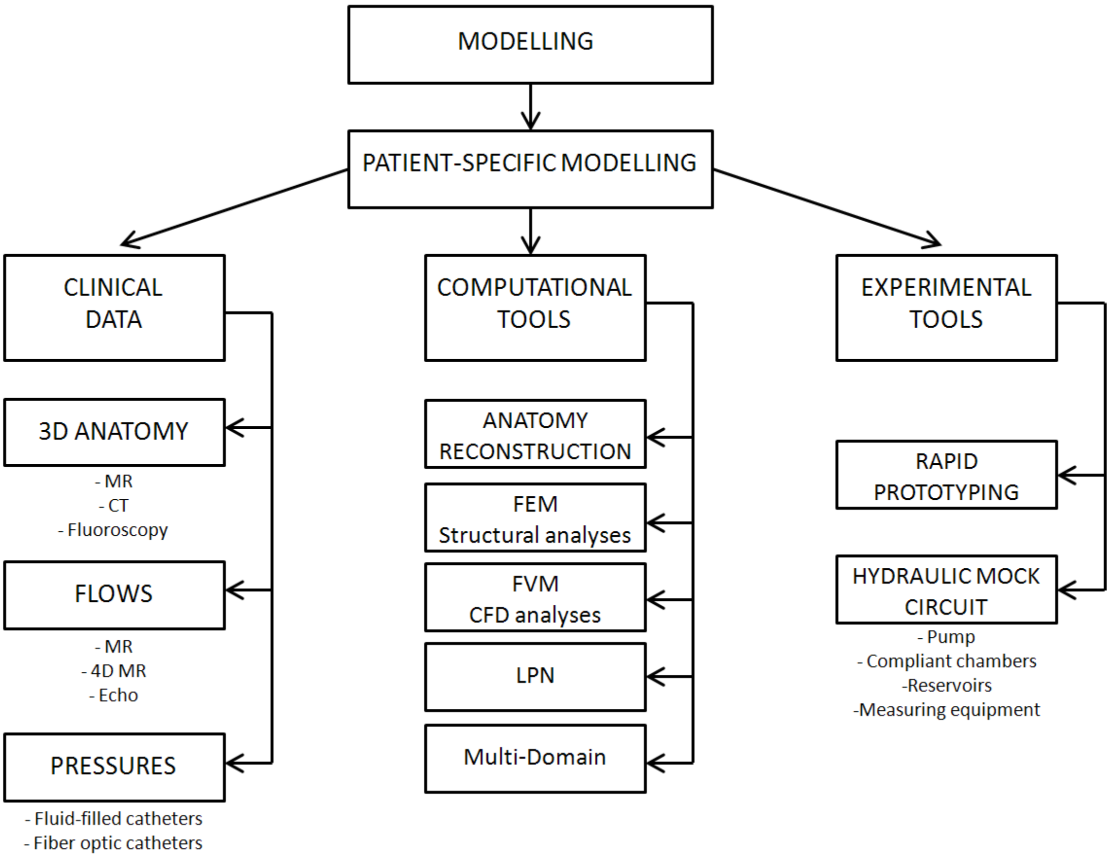

3.1 INTRODUCTION

The central idea of a scientific model is the representation of a complex system through the identification of its target features, and the reduction of its complexities by means of simplifications and discretisation in problems of smaller size. Scientific models are used to better understand and explore unknown organised structures, and to predict their reactions once a precise action is executed on them. The human body is one of the most elaborate and dynamic systems, and its modelling has been largely attempted with increasing level of detail, for different purposes.

The concept of modelling in bioengineering and particularly of patient-specific modelling is revised at the beginning this chapter. All the steps undertaken for a cardiovascular patient-specific model implementation are tackled in the following sections: from clinical data collection and acquisition modality (Section 3.4), to numerical tools at the basis of the models (Section 3.5), to experimental tools mainly used for validation purposes (Section 3.6).

3.2 MODELLING

"Model: a simplified description, especially a mathematical one, of a system or process, to assist calculations and predictions" (Oxford dictionary).

"A model is a substitute for a real system. Models are used when it is easier to work with a substitute than with the actual system" (**69**).

"Models are of central importance in many scientific contexts.... Models are one of the principal instruments of modern science.... There are a variety of things that are commonly referred to as models: physical objects, fictional objects, set-theoretic structures, descriptions, equations, or combinations of some of these" (**70**).

"A scientific model seeks to represent empirical objects, phenomena, and physical processes in a logical and objective way. All models are *in simulacra,* that is, simplified reflections of reality, but, despite their inherent falsity, they are nevertheless extremely useful." (**71**).

"Models are a mentally visual way of linking theory with experiment, and they guide research by being simplified representations of an imagined reality that enable predictions to be developed and tested by experiment" (**72**).

Four are the main concepts inferable from the above definitions:

- A model is a simplification of a physical reality
- A model is representative of a system
- A model is used to withdraw information on unknown variables
- A model can assume different shapes.

The importance scientific modelling has reached in our society is also reflected by the interest on the topic from other disciplines. As an example, researchers belonging to the field of philosophy of science tried to categorise models on the basis of their representational style. Thus, models can be classified as:

- Scale models: down-sized or enlarged representations of the chosen target system (**73**).
- Idealised models: simplification of a complex reality with the aim of making it more governable and understandable. Such a classification can be also broken down into a sub-classification: Aristotelian models, in which all the properties irrelevant to the aim of the model are withdrawn (for example the mechanical model of the planetary system, with all the planets represented by only mass and shape); Galilean models, implicating distortions from the reality to simplify too convoluted issues to deal with (for example the model of a point mass moving on a frictionless plane).
- Analogical models: models based on shared properties, i.e. models that are interpretations of the same formal calculus (analogy between sound and light in the fact they are both described by the same wave's mathematical formulation).
- Phenomenological models: representations of observable properties of their targets, leaving off unknown mechanisms. These are models not strictly based on theories, but that incorporate principles and laws associated with theories.

In this Thesis, all the above defined types of models have been used, with different modalities, to try and answer specific clinical questions.

In a biomedical environment, models are usually classified as *in-vivo*, *in-vitro* and *in-silico*. *In-vivo* models use a living organism in their normal state as substrate for an experimental testing; animal testing and clinical trials belong to this category. *In-vitro* models employ experimental controlled and isolated environments to replicate the target system, such as mock circuits composed of a pump and connected pipes trying to duplicate parts of the cardiovascular system. Finally, *in-silico* models are those implemented via computer simulations. These have been recently considered constituting a new scientific paradigm with extreme practical significance. Indeed, they are the only tool that we have to learn and explore complex dynamical models when standard methods fail (**70**). However, their trustworthiness needs to be questioned through two important inquiries: the verification and the validation of such models. The verification ensures the model to be respectful of the assumptions and the specifications, confirming the model implementation is correct and the computational solution is accurate enough. The validation assesses whether the model is really representative of the target system for the chosen purpose and application.

Usually, validation of biomedical computational models happens through the comparison of the results generated in-silico and those achieved with an experimental set-up representative of the same reality. In case of patient-specific models (whose concept will be discussed below), the validation occurs against those data of the patients that have not been input into the model as boundary conditions.

3.3 PATIENT-SPECIFIC MODELLING

Patient-specific modelling is a new field of biomedical engineering, recently experiencing remarkable advancements. It consists in developing computational or experimental models replicating the patho-physiology of a single individual. Its utility could be found in clinical environments, with the final aim of becoming a standard of care. Indeed, such models could be used to improve diagnosis, to tailor specific surgeries or treatments for an individual patient and to train clinicians regarding a particular surgical/interventional case. Also, they could help in the estimation of valuable predictors of diseases that are not directly measurable, such as stresses experienced by a vessel's wall due to specific fluid dynamic conditions or to the implantation of percutaneous devices.

A simple search in the *Pubmed* database with the key-word "patient-specific" produces the following histogram (Figure 3.1) for the number of publication by year, testifying the increasing importance given to single individual patient cases (total number of publications found almost 400,000).

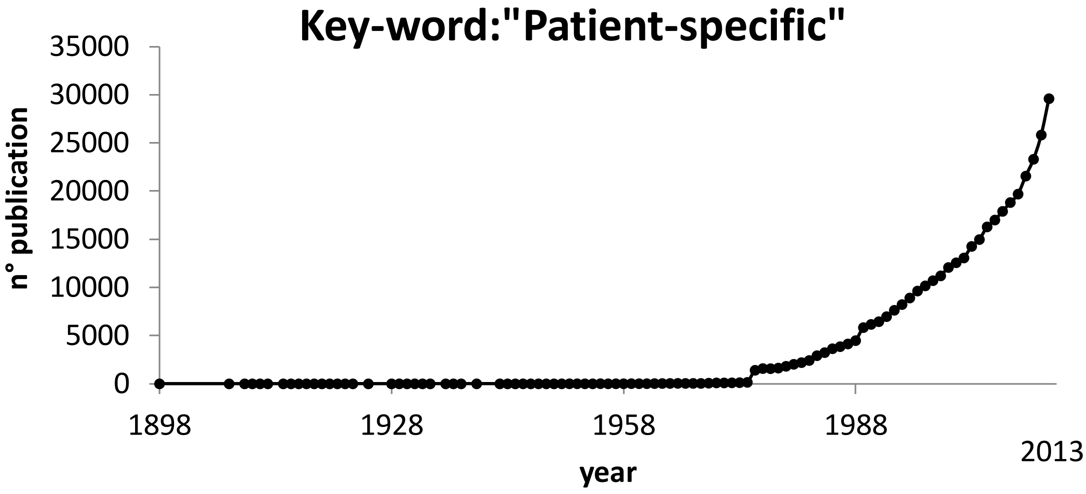

Figure 3.1 - Results from the Pubmed search with the key-word "patient-specific" illustrating the progress in this field over the years.

Combining the search with the additional key-word "model", a similar exponential trend is noticeable, with a total of almost 26,000 titles found (Figure 3.2). Obviously, not all publications are related to the cardiovascular field, nor to the more general biomedical field, but it is expected that every research area is developing its own tools to the benefit of the individual patients.

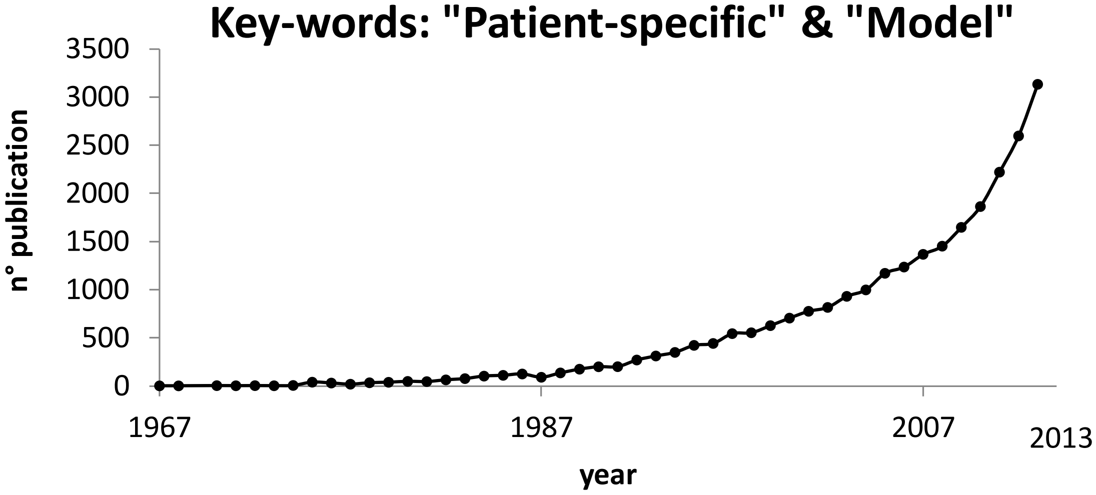

Figure 3.2 - Results from the Pubmed search with the key-words "patient-specific" and "model" illustrating the progress in this field over the years.

In the clinical arena, patient-specific models usually employ a 3D reconstruction of the anatomy of interest, typically built using image clinical data. Boundary conditions for these models are set using the outcomes of clinical exams, such as flows from MR and echo, and pressures from catheterism. For computational applications, the numerical methods at the base of modelling include finite volume method, finite element method and ordinary differential equations (ODE) methods. For experimental studies, 3D hard printing methods, such as the rapid prototyping technique, are adopted to recreate the physical anatomy of the patient, while the experimental tools used to run the experiment vary according to the application.

In the cardiovascular field, two main types of problems are modelled: fluid dynamics problems and structural problems. The aim of the first category is to replicate the physics of the blood flowing into the vessels and the heart, and the principal variables of these problems are flows and pressures. The objective of the second category is to represent the cardiovascular structures subjected to specific loads and displacements, for example after the implantation of a cardiovascular prosthesis.

When fluid dynamic and structural problems are combined together, a fluid-structure interaction (FSI) case arises. In FSI simulations, the movements of the cardiac structures are the driving forces for the fluid to flow, and vice-versa, the pressure field generated by the flow dynamics is imposed to the solid structures.

In general, the process for the implementation of a patient-specific model occurs as depicted in the graph reported by Neal and Kerchoffs in their publication (Figure 3.3) (**74**).

The key points of such process can be identified in:

- Data collection
- 3D anatomy reconstruction
- Set-up of the numerical equations or of the experimental mock circuit
- Model validation
- Model application to clinical practice.

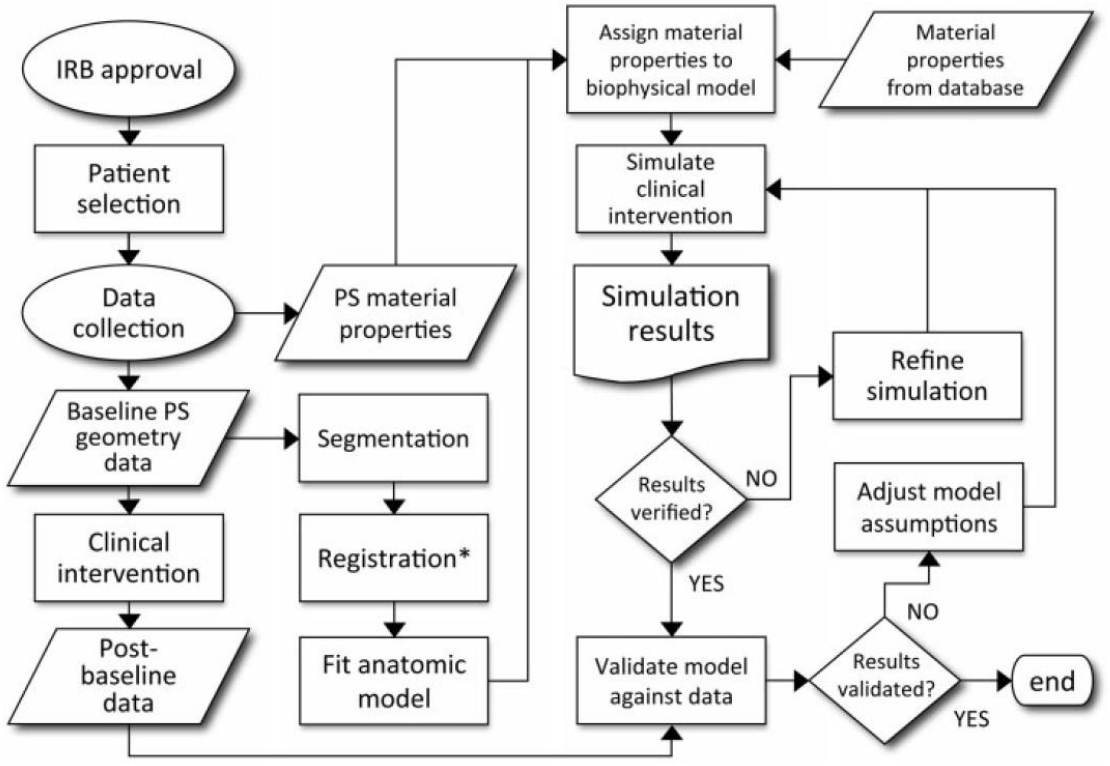

Figure 3.3 - General workflow for the creation and validation of a patient-specific (PS) model. IRB = institutional review board. Image taken from ***74****.*

3.4 CLINICAL DATA

The clinical data used for the implementation of patient-specific models are mainly the results of imaging exams and pressure measurements.

All patients' data used in the research presented in this Thesis were acquired as part of ethically approved studies (Local Research Ethics Committee Institutional approved at all hospitals) and following informed consent from patients and/or parents/guardians.

In the following paragraphs, a brief description of the imaging methods and pressure acquisitions used in this Thesis is reported.

3.4.1 Imaging methods

Tremendous advances in the field of medical imaging in the past decades have allowed for fine anatomical details to be obtained when performing routine diagnostic exams in most radiology departments. Such improvements gave a boost to the development of modelling techniques, especially in the context of patient-specific applications. In the cardiovascular setting, 3D visualisation techniques provide details on the vessel anatomies and cardiac structures, while 2D modalities supply data on flow fields. A brief analysis of the imaging techniques employed in this Thesis is presented below.

3.4.1.1 Magnetic Resonance Imaging

Magnetic resonance has become an important imaging technique for the assessment of cardiovascular disease in both congenital and acquired heart conditions (**75**; **76**). It produces high quality anatomical images of the inside of the human body, as well as being able to provide functional information non-invasively through the measurement of blood flows, ventricular volumes, stroke volumes and ejection fractions.

Cardiac motion and function over several cardiac cycles are usually imaged through a 3D whole-heart sequence, performed with electrocardiographic (ECG) gating. Data-sets of heart and great vessels are acquired using balanced steady-state free precession (SSFP) (**77**; **78**) that provides good contrast between myocardium and blood (**79**). Image quality can be enhanced using contrast agents, such as Gadolinium (**80**).

MR imaging of flow is accomplished using methods that resolve spatial dimensions (2D) in individual slices. Quantitative flow assessment through this method offers the advantage of a sequential acquisition of flow data in different vessels with individually adjusted velocity encodings (**81**). However, the 2D methods requires repeated planning and acquisition at each vessel site which can be time-consuming and limits retrospective data analysis only to those vessel sections that were targeted when planning the scan.

Recently, a new technique has been developed, i.e. 4D magnetic resonance imaging flow acquisition (4D MR flow), which allows for acquisition of 3D morphological information as well as blood flow velocities in 3 directions for each voxel at each measured time point of the cardiac cycle. It provides not only detailed quantitative flow and vessel wall parameters, with complete vascular coverage, but also additional measurements of derived hemodynamic parameters, such as shear stresses, vortex formations, and pressure fields. (**82**). This technique becomes a resourceful tool in the diagnostic work-up of complex CHD that require multiple quantitative flow acquisitions in arterial and venous vessels with normal and abnormal flow patterns (**81**). 4D flow acquisition in these cases may reduce scan time, eliminating the need for planning and acquisition of multiple 2D flows, thus making the protocol less time expensive and demanding for the patient. Furthermore, retrospective data analysis in 4D sequences is not limited to the acquired single predefined 2D image plane, thus avoiding incomplete or falsely registered datasets (**81**).

4D flow represents a unique source of data to validate in-silico results from CFD simulations as this MR sequence return the same information as CFD analysis in terms of 3D velocity components over time. However, conventional 4D flow sequences still require long acquisition time, in the order of 15 minutes, thus limiting their use in patients' routine scans.

The main limitation of MR imaging is its suitability to patients with implanted metallic devices. Presence of stents or mechanical valves can cause significant signal loss in the treated area, creating artifacts and disturbing flow acquisition in the closest regions.

In this Thesis, cardiovascular MR imaging was performed with a 1.5T scanner (Symphony Maestro Series or Avanto, Siemens Medical Systems, Erlangen, Germany) based at our Centre and with a 4-element body phased array coil. A 3D gradient echo sequence after the administration of Gadolinium was used to extract the anatomy of the RVOT of the patient selected from the PPVI population as described in Chapter 5 and of the aorta of the TGA patient selected for the study reported in Chapter 6. A 3D whole-heart sequence was employed to analyse the pulmonary artery vessels of Chapter 7. 2D-MR methods were used to extract functional information on the flows which was then inputted in the CFD analyses of Chapters 6, 7 and 8. Finally, a 4D MR flow sequence was tested and exploited in the in-vitro experiment described in Chapter 6, to compare and validate in-silico results against in-vitro results that replicated a patient-specific TGA aortic anatomy and hemodynamic conditions.

3.4.1.2 Computed tomography

Computed tomography is a volumetric imaging technique that has become one of the principal methods for cardiac visualisation since it allows 3D anatomy acquisition in about 5-10 seconds. This quick examination time presents invaluable advantages especially in the assessment of babies and young children who then may not require sedation. However, this imaging method employs ionising radiations which carry long-term risks for the patients (i.e. development of late cancers). CT uses computer-processed x-rays to generate 2D tomographic images of the patient's anatomy acquired around a single axis of rotation. The back projection of such images allows the 3D reconstruction of the volume of interest. CT images are endowed with high resolution and less image artifacts than MR images. With the introduction of 64-slice CT scanners, versus the early 4-slice scanners, the tomographic section thickness decreased from 1.25 mm to about 0.5 mm, and the temporal resolution increased from about 250 ms to 83 ms or less (**83**). This improvement also allowed a better dynamic evaluation of the cardiac structure throughout the cardiac cycle by using the so-called 4D-CT.

Unlike MR imaging, metal implants are not a contraindication for CT examination which allows visualisation of metallic devices, and therefore is used also to assess potential stent fractures and in-stent restenosis (**83**; **84**).

In this Thesis, CT was performed using a 64-slice Dual-source multidetector system (SOMATOM Definition, Siemens, Germany). CT pulmonary and aortic angiography with retrospective ECG-gating was used to acquire patient anatomies for the studies described in Chapters 4 and 8, where both patients had previously implanted stents to treat pulmonary dysfunction and aortic coarctation respectively. In addition, CT accuracy in assessing stent geometry and deformations was compared to the accuracy of other imaging methods, such as fluoroscopy and optical imaging techniques, as explained in Chapter 4. A similar imaging technique, albeit not used in the clinical practice, was employed in the comparison study just mentioned, micro-CT. Micro-CT, performed for this research at the Royal Hallamshire Hospital, Sheffield, UK with a Skyscan 1172 ex-vivo cone-beam scanner (Bruker, Belgium), is based on the same principles of CT, but has an extremely large ionising dose radiation which is irradiated over a long acquisition time (a few hours). In addition, in micro-CT the object is placed on a rotating plate, while the source of x-rays and the detectors are fixed in space. This technique is generally used in experimental studies to produce the computational reconstruction of objects with high resolution, to the extent that it is considered the gold standard among volumetric imaging methods. However, it is not suitable for patients' examination due to the extremely high radiation dose.

3.4.1.3 Fluoroscopy

Fluoroscopy is a 2D intra-operative imaging technique routinely used by cardiologists to assess not only the cardiac anatomy of the patient, but also the position of balloons and devices during interventional procedures. A fluoroscope is composed by an x-rays source and a fluorescent screen, each positioned at the opposite sides of the patient. An image intensifier converts the x-rays into visible radiations forming moving images of the interior of the patient, generally broadcasted on a screen in the operating room for the doctor to be visualised real-time. Fluoroscopy can be used both with and without contrast medium. The contrast is usually employed to check the patency or the size of a vessel, and when used, the exam is referred to as angiography.

Biplane fluoroscopy images for this Thesis were acquired at the Catheterisation Laboratory of our Institution, equipped with Axiom Artis Flat Detector system (Siemens, Germany), an innovative system that eliminates distortions associated with conventional image intensifier technology. This provides excellent image quality (high spatial and contrast resolution) and accuracy at minimum radiation dose. Biplane fluoroscopy images of a CP stent were acquired for the imaging technique testing of Chapter 4. In addition, cine images of PPVI procedures were used to reconstruct the 3D geometry and deformations of PPVI stents in-situ as explained in Chapter 4 and 5 in a patient treated with the next generation PPVI device and several patients treated with Melody™. Procedural protocol required that fluoroscopy was performed with the biplane arms catheter positioned in the antero-posterior and perpendicular–lateral projections, so that the resulting images were projections of the anatomy and device in two orthogonal planes.

3.4.1.4 Echocardiography

Echocardiography is an imaging technique based on Doppler ultrasound, able to visualise slices of the heart from different angulations, thus allowing clinicians to evaluate the heart shape, dimensions, wall and valves. It is a non-invasive technique, routinely used in clinical practice to diagnose and follow-up heart diseases. Other than anatomical data, it can provide functional information such as estimation of cardiac output, ejection fraction and blood velocity through the heart. It can show eventual abnormal communications between atria and ventricles, and valvular regurgitations or stenosis.

In this Thesis, echocardiography data were used to measure blood velocity in the aortic coarctation in the patient case described in Chapter 8.

3.4.2 Pressure measurements

In-vivo intravascular pressures are registered during cardiac catheterisation via pressure catheters placed in the vessel of interest. Pressure catheters can be of 2 different types:

fibre optic catheters, which are high-fidelity factory-calibrated catheters, whose transducer technology is based on a pressure sensitive optical interferometer. The sensor element is usually mounted at the tip of an optical fibre; and fluid-filled catheters which are based on the principle that a fluid drives the pressure waveform from the catheter tip, positioned where the pressure has to be measured, to the other end of the catheter that is where the pressure transducer is located, outside of the patient's body. For safety reasons, these catheters are usually filled with heparinised saline, a fluid with anticoagulant properties. Fluid-filled catheters are cheaper than the fibre optic version, but lack in high precision, due to the fact that the pressure information is easily affected by the transition from inside to outside the body.

Non-invasive but less accurate central pressure assessment can be obtained from cuff pressure measurement.

In this Thesis, intravascular pressure information was acquired in one of the TGA patients studied in Chapter 7 and in the coarctation patient during the re-stenting catheter procedure (Chapter 8).

3.5 COMPUTATIONAL TOOLS

Patients' data gathered from clinical exams need to be post-processed to become useful in model implementation. First of all, the 3D anatomy of the region of interest has to be created; then, numerical or experimental tools are used to set-up the model.

3.5.1 Anatomy reconstruction

The 3D reconstruction of the cardiovascular structures was performed in this Thesis using the commercial software Mimics (Materialise, Leuven, Belgium) for image post-processing. Raw DICOM images from MR or CT were imported into Mimics where they could be visualised in three projection planes: the transverse, coronal and sagittal section. To isolate the region of interest in the images, a segmentation mask was created by defining the upper and lower thresholds of greyscale values to be included in the mask. A region-growing algorithm was then applied to eliminate those pixels not connected to the desired selected area. Next, manual editing functions (i.e. pixel drawing and erasing) were used to obtain a clear region of interest in all the 2D views, free from eventual noise or unwanted contours. At this point, the software generated the

3D model using the three bi-dimensional views, and smoothing operations were finally performed to refine the contours of the 3D volume, adjusting surface irregularities. The accuracy of the reconstructed anatomy strongly depends on the resolution of the inputted medical images.

The generated model was saved as a triangulated surface – file extension STL (Standard Triangulated Language) – and exported either in a meshing software for computational model generation, or in the controlling software of a rapid prototyping machine, for the creation of a physical 3D phantom.

3.5.2 Numerical methods

3.5.2.1 Finite Element Method and Finite Volume Method

Solid mechanics, as well as fluid mechanics and the other engineering sciences, generally use partial differential equations to characterise the complexity of physical systems. Indeed, the physics of the continuum mechanics, both solid and fluid, is governed by three fundamental principles, generally expressed in the form of partial differential equations, and referred to as conservation laws:

- Conservation of mass
- Conservation of momentum (Newton’s second law F=m a)
- Conservation of energy.

The different behaviour between fluids and solids is then accounted for through the use of different constitutive equations (**85**).

Most of the time, it is not possible to obtain an exact solution of these partial differential equations. Thus, it is necessary to fall back on approximations: the continuum problems are therefore approached and resolved by representing the infinite set of values proper of the continuum by a finite set of values through the concept of discretisation.

The Finite Element method and the Finite Volume method consist in the transformation of these partial differential equations into algebraic equations for steady problems and ordinary differential equations for transient problems, by using simple approximations of unknown variables. The more the number of discrete variables used, the more exact the solution will be.

Both FEM and FVM can deal with complex geometries in multi-dimensional problems, as the integral formulations they are based on do not depend on any specific mesh structure (**85**), unlike their predecessor for the solution of partial differential equations, the Finite Difference Method, which is developed upon the differential formulation.

The main difference between FEM and FVM regards the way the domain is treated: the FEM divides the whole domain into elements with finite area and the discretisation is based upon a piecewise representation of the solution in terms of specified basis functions that can be linear or quadratic polynomial. The dependant values are stored at the nodes of the elements, and the solution is considerable continuous up to a point. Structural mechanics problems are commonly solved by using this numerical method.

The FVM divides the whole domain into boxes with finite volume, that are the regions of integration, and the dependant values are stored in the centre of the finite volume. It provides discrete solutions, and its approach is conservative, as the flux leaving a volume is equal to the flux entering the adjacent volume. Thus, this method allows an intuitive representation of the fluid dynamics, and it is mainly used for CFD applications.

FEM for structural analyses

Dhatt and colleagues in their book "Finite Element Method" (**86**) conveyed that FEM is the result of three disciplines: engineering science, numerical methods, and computer science. Engineering science describes the physical laws through partial differential equations, then elaborated and solved through numerical methods. Finally, computing tools are needed to perform the necessary calculations to obtain the solution. The same concept regards also the FVM.

The first time the term "Finite Element Method" appeared was in the 1960s, in a study by Clough and colleagues about the calculation of a plane stress in a Delta airplane wing. Further research on FE allowed the method to largely improve, and increasing applications were found also in other fields of mechanics (**87**; **88**). In the 1970s, commercial FE software appeared on the market (Abaqus, Adina, Ansys), and since then the rapid development in computer technologies and in programming languages made the FE technique increasingly appealing (**89**).

Finite element analysis is now considered a valuable method to evaluate the mechanical performance of intravascular devices and to quantify stresses and deformations due to external loads and boundary conditions that cannot otherwise be readily measured (**90**). Indeed, FDA guidance for computational preclinical testing of intravascular stents recommends durability tests under estimated in-vivo loading conditions. A fatigue life analysis method, such as the Goodman criterion, is also requested to provide an evaluation of the combined effects of mean and alternating stresses on the device fatigue life (**91**).

In this Thesis, FE analyses were used to solve structural mechanics problems associated with intravascular stents in Chapters 5, 7 and 8. The FE software chosen for the implementation and the solution of analysed models is Abaqus (Abaqus/Simulia Inc, Providence, RN, USA). A standard formulation was used in those cases where static and low-speed dynamic events were represented and where the stresses needed a high accurate solution (Chapter 5); while an explicit dynamic formulation was used in those cases where large models had to be solved with relatively short dynamic response times characterised by largely discontinuous events or processes and that require the use of contact algorithms (Chapter 7 and 8). Here, the code applies a large-deformation theory, so that the modelled part can undergo large rotations and large deformations.

FVM for CFD analyses

The computational fluid dynamic problems discussed in this Thesis were solved using a FVM solver. Computational fluid dynamics has been defined as “the art of replacing the governing partial differential equations of fluid flow with numbers, and advancing these numbers in space and/or time to obtain a final numerical description of the complete flow field of interest” (**92**). As explained by Dr Anderson in his book, the result of CFD simulations is a collection of numbers (i.e. a quantitative description of the analysed problem) (**92**). The recent advances in computer technologies have speeded up the repetitive manipulation and storage of millions of numbers, remarkably increasing the use of computational studies and the complexity of the treated problems.

The main advantage of CFD simulations lies in a complete 3D representation of the flow properties and in the possibility of reproducing the anatomies with high degrees of freedom. Also, possessing the flow solution in the whole domain, parameters of interest such as flow distribution, pressure gradients and power losses are obtainable at any moment without previous planning needed as during experimental tests. Finally, the cost of computational simulation is lower than that of experimental set-ups, being only related to computer capabilities and software purchase.

In this Thesis, the software used for the solution of CFD problems was Fluent (Ansys v.14, Fluent Inc. ©, Lebanon, NH). This code was adopted to study the fluid dynamics in the aorta of the TGA patient presented in Chapter 6, in the main pulmonary artery and bifurcations of patients from Chapter 7 and finally in the aortic coarctation study of Chapter 8.

The CFD method is based on the solution of the Navier Stokes (NS) equations and of the mass balance equation in each volume of the grid in which the 3D domain is divided. The 3D NS equations are:

$$\rho\left\{\left(\frac{\partial v_i}{\partial t}\right)+v_i\frac{\partial v_i}{\partial x}+v_j\frac{\partial v_j}{\partial y}+v_k\frac{\partial v_k}{\partial z}\right\}=F_i-\frac{\partial p}{\partial x_i}+\mu\nabla^2 v_i$$

where ρ is the fluid density, v_i is the component of the velocity vector in the specified Cartesian direction ($i = x, y, z$), t is the time, F_i is the vector of the external body forces operating on the fluid, p is the pressure and μ is the fluid viscosity.

The continuity equation is shown below:

$$\frac{\partial \rho}{\partial t}+\rho\nabla\cdot\boldsymbol{v}=0$$

and becomes as follows:

$$\nabla\cdot\boldsymbol{v}=0$$

for incompressible fluids (constant density ρ).

In the simulations of this Thesis, with Ansys Fluent, the Navier-Stokes momentum equations were solved with an upwind scheme of the second order. Upwind schemes use a solution-sensitive finite difference method to account for the direction in which information are propagated in a flow field. Also, they introduce stability in problems with high Reynolds numbers, thus facilitating the convergence of the solution. However, its accuracy is lower than other schemes, for example the central differencing scheme; for this reason, it is preferable to use orders higher than the first to increase the spatial accuracy. A standard spatial discretisation was chosen for the pressure, and an implicit least-square-cell-based discretisation for the gradient. A SIMPLE (Semi-Implicit Method for Pressure Linked Equations) pressure-velocity coupling algorithm was exploited. The first order implicit transient formulation was chosen to discretise the NS equation in the temporal domain, with a time-step Δt of 10^{-4} s. In all CFD simulations, the absolute convergence criterion was the residuals of mass and momentum conservation equations to be less than 10^{-4}. Also, vessels with rigid properties were assumed in all the simulations, and a no-slip condition was imposed at the walls.

Two are the key factors for obtaining detailed and reliable descriptions of the fluid dynamics in any specific case: the boundary conditions and the representation of the 3D domain. In cardiovascular applications, the boundary conditions to be prescribed at the boundary faces of the 3D model are typically values or tracings of pressure, velocity and flow-split derived from medical exams such as catheterism, MR scans and echo measurements. Regarding the 3D volume, it is possible to mimic complicated patient-specific geometries, obtained by advanced medical imaging techniques, such as MR and CT (**93**).

Hence, in order to computationally reproduce patient-specific fluid dynamics, medical images with high resolution and time-varying boundary conditions are required for achieving adequate accuracy and reliable outcomes.

3.5.2.2 Lumped parameter networks

Lumped parameter networks are electric analogue models that can be used to represent complex hydraulic circuits. In particular, pressure and volumetric flow-rate are identified with electric tension and current, while the vascular wall's compliance, the viscosity and the inertial properties of the fluid flowing in the circuit are described by capacitance, resistance and inductance components respectively.

This approach represents a valuable tool for calculating pressure drops and flow distribution in the network, whether realistic values for all components of the LPN are available. However, it does not allow assessment of local information, such as shear stresses, velocity and pressure fields. The vascular system can be easily represented using this approach which allows modelling of the different portions of the circulation with different numbers of lumped blocks according to needs.

The hemodynamic in each compartment is described through a set of ordinary differential equations, derived from the Navier-Stokes model, after opportune assumptions and simplifications:

- The contribution of the convective terms of the NS equation is discarded
- The fluid is considered as incompressible and viscous

- Velocities are not treated by means of their distribution on the cross-section, or their variation along the conduit, but rather using the corresponding cross sectional average velocity.

A deformable vascular conduit with reduced length can be modelled using three lumped parameters: a capacitance C, an inductance L, and a resistance R. According to the available boundary conditions, one of the following four configurations can be chosen: L network, inverted-L network, T network and π network (Figure 3.4).

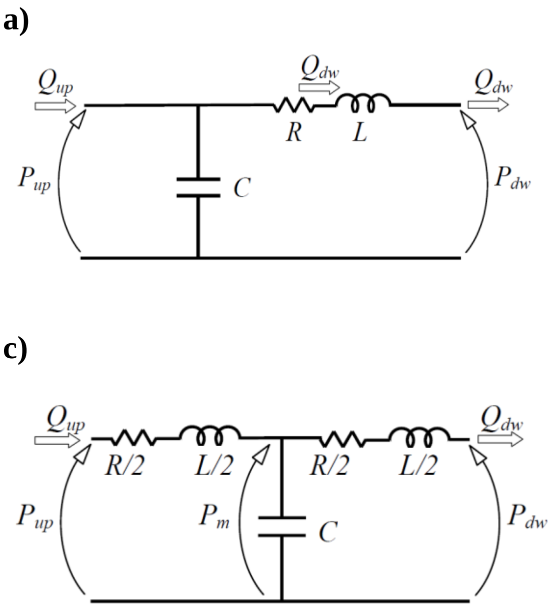

*Figure 3.4 - Four possible configurations to represent a deformable vascular conduit through a LPN block: a) L network, b) inverted-L network, c) T network and d) π network (**94**).*

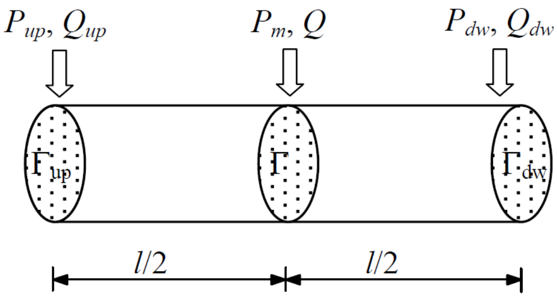

*Figure 3.5 - Scheme of a deformable vascular conduit. Pressures and flows are indicated through P and Q respectively. The upstream and downstream sections of the conduit are indicated as up and dw (**94**).*

The mean pressure and the mean flow-rate at the inlet section Γ_{up} are identified in Figure 3.5 as P_{up} and Q_{up}, while P_{dw} and Q_{dw} are those at the outlet section Γ_{dw}. The subscript *m* is instead used for the internal section Γ.

The physical network is mathematically represented through a system of ordinary differential equations, with appropriate boundary conditions. The equations representative of the generic scheme shown in Figure 3.5 are the following:

$$\begin{cases} L\dfrac{dQ}{dt} + RQ = P_{up} - P_{dw} \\ C\dfrac{dP_{in}}{dt} = Q_{up} - Q_{dw} \end{cases}$$

where:

$$R = \frac{8\mu l}{\pi R_0^4} \qquad L = \frac{\rho l}{\pi R_0^2} \qquad C = \frac{3\pi R_0^3(1-\upsilon^2)l}{2Eh}$$

with υ, E, l, R_0 and h the Poisson modulus, the Young modulus, the conduit length, its undeformed radius and the wall thickness, respectively. Viscosity and density of the fluid are indicated with μ and ρ. In the ODE system the variables are P_{dw}, Q_{up}, Q_{dw}, P_{in}. The state variables are the pressures where a C is present and the flow-rates where the equation is written for an L component (**94**).

The major advantage of such a method is the reduced computational cost and time: simulations last up to a few minutes on a personal computer. In addition, once a network representing a particular district or the overall circulation has been developed, it can be easily adapted to represent different patients or different pathological scenarios just by changing the values of the interested parameters (R, L, C). Indeed, in most cases, the mathematical skeleton of the LPN represented by the algebraic and differential equations is left unvaried.

In this Thesis, the LPN equations were written in the programming code C, and worked out with the compiler Bloodshed Dev C++ (Free Software Foundation, Inc., Cambridge, MA, USA). The ordinary differential equations in the LPN were solved with the explicit Euler time forward scheme, using a time-step Δt of 10^{-4} s:

$$f(t) = f(t-\Delta t) + \Delta t \cdot f^*(t)$$

where $f^*(t)$ is the approximation of the function at the current time-step.

LPNs were set up in the studies presented in Chapter 7 and 8 to take advantage of this technique fast response. In the first case, several simulations had to be carried out to characterise the pulmonary circulation of 15 TGA patients. This would have required many months using a traditional 3D CFD approach with the currently accessible calculation power. In the second case, LPN represented a fast tool to help cardiologists decide the optimal treatment for a patient with aortic re-coarctation in a timely manner.

3.5.2.3 Multi-Domain simulations

As for other engineering problems, also in the biomedical field a problem can show peculiar behaviours at different scales. One of the major difficulties is to identify the correct scale to approach the problem: if the scale is too big, there is the possibility to neglect some significant events occurring at the microscale, while if the scale is too small, evaluation of macroscopic phenomena may be inaccurate.

The attempt to simulate all the relevant dimensions of a problem with common numerical techniques would be far too complex to be solved, requiring a high number of variables and also of computer power. A possible solution could be to neglect the less influent scales, such as for instance the microscale. However, this is not always permitted, as sometimes the non-linearities present at smaller scales significantly influence the solution of the problem (**95**).

Often in cardiovascular models, details of the local fluid dynamics inside a vessel have the same importance as the influence exerted by the global impedance of the arterial bed. To represent local and global fluid dynamics at the same time, a multi-domain approach should be used: it consists in coupling a 3D geometry of the district of interest (local fluid dynamics), solved with the CFD methods, with a LPN reproducing a section of the vascular tree (global fluid dynamics).

The coupling between the CFD model and the LPN can be implemented through pressure and flow information exchanged in correspondence of the boundary faces (**96**). In order to have a coherent transfer of information it is important to convert the exchanged data in the scale of the receiving model. To move from the 3D domain to the 0D (of the LPN) domain there is a loss of spatial information, thus the data exchanged have to be integrated on the considered section. The opposite transfer, on the other hand, requires the amplification of a defective knowledge, being scalar. This difficulty can be overcome by arbitrarily defining a profile on the boundary face for the exchanged variables, and, in this Thesis, a uniform profile was adopted. In particular, the pressures elaborated from the network were fed into the 3D model, and the flows calculated from the CFD software were imposed as inlet to the LPN.

The equations translating this concept are reported below. The time-dependent pressure applied to the generic outlet boundary section *j* of the 3D domain is calculated as:

$$P_{tot,k}(t) = P_{h,j}(t)$$

where *k* is the generic cell face belonging to the face *j*, and $P_{h,j}(t)$ is the instantaneous hydrostatic pressure of the j^{th} interface calculated by the LPN. The flows computed by the CFD solver are passed to the LPN according to the following equation:

$$Q_j(t) = \int_{\Gamma_j} \bar{v}_i(t) \cdot \bar{n}_j \, d\gamma$$

where Γ_j is the surface of the 3D model outlet section, and $\bar{n}$ is the outward versor normal to the j^{th} interface.

The general equations for the mass and momentum conservation laws for each compartment of the LPN are the following:

$$Q_{in}(t) - Q_{out}(t) = C \frac{dP_{out}(t)}{dt}$$

$$P_{in}(t) - P_{out}(t) = R \cdot Q_{in}(t) \qquad \textit{in case of linear resistance}$$

$$P_{in}(t) - P_{out}(t) = a \cdot Q_{in}^2(t) + b \cdot Q_{in}(t) \qquad \textit{in case of non-linear resistance}$$

where $Q_{in}(t)$, $P_{in}(t)$ indicate the instantaneous volumetric flow rate and pressure at the inlet of the compartment, while $Q_{out}(t)$, $P_{out}(t)$ are flows and pressure at the outlet.

The ordinary differential equations are resolved through the explicit Euler numerical method, using a time-step Δt of 10^{-4} s (as done in case of pure LPN, Section 3.5.2.2).

Basically, the multi-domain approach provides the 3D geometry with realistic time-varying boundary conditions, allowing the CFD calculation to be influenced and influence the solution of the LPN.

The major drawback of multi-domain simulations consists in the significant computational time and power required to run the simulations. Usually, four cardiac cycles with a CFD model of about 800,000 volumes and a LPN of about 10 ODEs require 4-5 days on a personal computer with 4 CPUs.

Multi-domain simulations were carried out in this Thesis to validate the results of the simplified LPN representing the pulmonary circulations of TGA patients in Chapter 7.

3.6 EXPERIMENTAL TOOLS

The complexity of an experimental setup varies according to the problem at hand, and depends on the purposes of the study, influencing the choice of model (e.g. pure resistance, lumped parameter model, distributed, linear model or distributed, non-linear model) (**97**).

Experimental setups for hydrodynamic testing can take the form of mock circulatory loops, whereby a network of tubing and lumped resistive and compliant elements are assembled to reproduce a part or the whole of the circulatory system. Such mock loops can include a detailed anatomical element if a specific morphology is deemed important or is being investigated. Anatomical elements can be either idealised (**98**) or patient-specific (**99**). An arrangement including a detailed 3D component and lumped elements representing the remainder of the circulation can be broadly defined as "multi-scale" or multi-domain (**100**).

3.6.1 Rapid Prototyping technique

The rapid prototyping technique known as PolyJet technology (**101**) is the process of making 3D physical phantoms of digital models. It can be used to manufacture 3D rigid or compliant parts suitable for insertion in a mock circulatory loop.

Application of such a technique to the field of patient-specific modelling are evident: 3D digital anatomies reconstructed from MR\CT data, as explained in Section 3.5.1, can be exported as an STL file compatible with 3D printing. Materials with different properties can be used for the printing process: transparent or opaque, rigid or compliant. Rigid models, admittedly not reproducing realistic vessel wall distensibility and the associated recoil effect, have been used in several studies in the literature for investigating vascular anatomies (**99**), providing valuable hemodynamic data. It should be noted that they serve the purpose of collecting validation data for a computational study where the 3D models in the CFD study also present rigid walls. Regarding the transparency of the resin, its advantages could be the visualisation of air bubbles in the circuit (thus facilitating de-airing operations), and of eventual pressure catheters (to control the correct positioning).

In this Thesis, 3D printing was used in three cases for different purposes. In Chapter 4, it was employed for the production of a deformable opaque mould representative of the

RVOT of a patient, to be used as a support for a PPVI stent apposition for experimental imaging purposes. In Chapter 6, a transparent and robust resin was chosen to print the aorta of a patient, later integrated in a mock circuit to conduct a fluid dynamic in-vitro study. Finally, in Chapter 8, the peculiar anatomy of a patient with stented coarctation of the aorta was printed with rigid materials for didactic and visualisation reasons.

3.6.2 Hydraulic circuit components

Hydraulic circuits with the aim of representing the patient's cardiovascular system are generally formed by a pump, compliance chambers, valves, reservoirs and measuring equipments. The components selected for the experimental set-up of Chapter 6 that replicated the circulation of a TGA patient are described in the following paragraphs.

A pulsatile mechanical pump (Harvard Apparatus Inc., Natick, MA) simulated the ventricular pumping action through silicone rubber-covered heart-type ball valves. This pump has an adjustable stroke volume range between 15 and 100 ml and a frequency range between 10 and 100 bmp.

Arterial compliance was simulated using Windkessel (= "air chamber" in German) elements, according to the theory of compliant air element. In particular, compliance chambers were here reproduced through Perspex cylinders with a 3-way valve fitted at the top in order to control the amount of air to regulate the stiffness of the circuit.

Increasing the stiffness of the whole system rises the amplitude of the pressure waveform. The compliance value is calculated as:

$$C = \frac{dV}{dP} = \frac{V}{P_m + P_{atm}}$$

in which V is the volume of air in each cylinder, P_m is the mean pressure and P_{atm} the atmospheric pressure (760 mmHg).

Metered needle-pinch valves were used to simulate the resistance of downstream districts of the circulation. Such taps have the advantage of being easily adjustable with reproducible settings, allowing for simple regulation of the mean pressure in the circuit. However, they are strongly flow-dependent and thus implement a non-linear resistance.

Each tap resistance was characterised using a simplified steady flow circuit. A known flow was imposed with a continuous pump (Q), and the pressure drop (ΔP) across the tap (R) was measured with two pressure catheters ($\Delta P = R \cdot Q$), respectively positioned just before the tap and 5 cm downstream, to allow for pressure recovery.

An ‘atrial reservoir’ was implemented through a chamber filled with fluid up to a certain level to guarantee the chosen atrial pressure, given by the hydraulic head.

Pressures in the circuit were measured with high-fidelity factory-calibrated fiber optic catheters (Samba Preclin Samba sensors AB; Vastra Frolunda, Sweden). The transducer technology is based on a pressure sensitive optical interferometer (Fabry-Perot manufactured in silicon). The sensor element (0.36-0.42 mm of diameter) is mounted on the tip of an optical fiber (0.25-0.40 mm of diameter). The pressure catheter was calibrated prior to the experiment with the methods of “column of water”, associating the console’s read-out in Volts with known heights of water implementing known hydrostatic pressure values (1 mmHg = 1.36 cmH_2O). Thus, a correlation between pressure read in Volts by the catheter and the corresponding mmHg value was established (Figure 3.6).

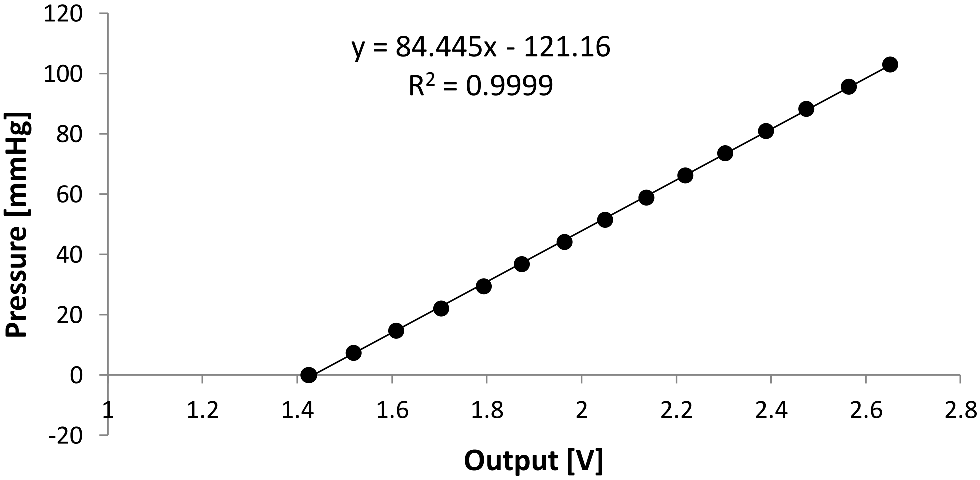

Figure 3.6 - Catheter calibration: on the x-axis the output of the console and on the y-axis the associated pressure in mmHg.

A Transonic 400-Series Multi-Channel Flowmeter Consoles & Modules for Laboratory Research was used to monitor flows. It consists in four transducers (piezoelectric crystals) that alternately emit sound rays to form an ultrasound beam. As the beam transverses a vessel, each ray undergoes a phase shift in transit time proportional to the average velocity of the liquid times the path length over which this velocity is encountered. With wide-beam ultrasonic illumination the receiving transducers integrate these velocity and yields volume flow. The probe was calibrated before the experiments using the method of “timed collection”, whereby increasing steady flows were set with a continuous pump (Sicce Multifunction Pump 2500), and the amount of water gathered in ml was quantified using a measuring cylinder; these values where then compared with the respective Volts measured by the probe.

During the experiments, a data acquisition System (BIOPAC System Inc., Goleta, CA, USA) was used to record pressure and flow output gathered from the catheter and the probe. Data were acquired at 250 Hz (AcqKnowledge 4.1.1, BIOPAC System Inc.).

The engineering and clinical tools described in this chapter were employed in the research of this Thesis for patient-specific modelling in CHD cases. As previously discussed, a computational model, to be used in clinical practice, requires verification and validation. Therefore, the patient-specific complex models presented in the following chapters will be preceded by the validation of the developed and implemented methodology, starting from the image analysis of PPVI stent fractures (Chapters 4 and 5).

CHAPTER 4

STENT IMAGING TECHNIQUES

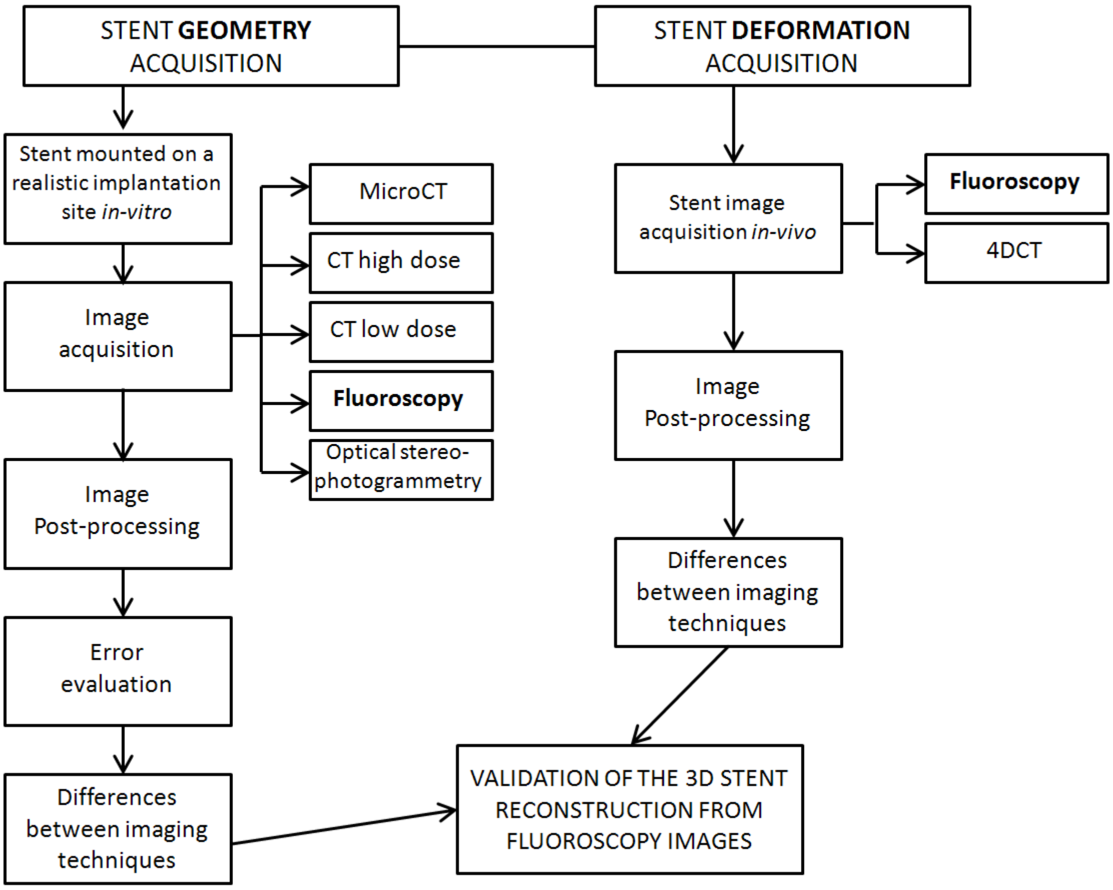

The content of this chapter is the result of a collaboration within the MeDDiCA network with the University of Sheffield, and in particular with Iwona Zwierzak and Dr. Andrew Narracott. Part of the work presented in this chapter is currently under 2nd review with the Journal "Medical Engineering & Physics".

4.1 INTRODUCTION

Imaging techniques can be used to assess stents statically and dynamically both in-vivo and in-vitro to evaluate device performance. Assessment of the accuracy of the imaging methods adopted is important, particularly in the context of data used to inform numerical analyses of device behaviour. The aim of this chapter is to assess the ability of fluoroscopy in describing PPVI stent geometry and dynamics. A set of fluoroscopy images is available for each patient who undergoes PPVI since these images are used to guide device delivery. Therefore, if accurate, they could be used to help predict stent fracture, important for example in the PPVI Melody™ stent where the incidence of such event is >25%.

The chapter is divided in two parts: accuracy and reproducibility of the stent geometry reconstruction process using biplane fluoroscopy static images was studied by comparison with micro-CT, considered the gold standard technique for stent imaging, in the first part (Section 4.2). Also in this part, an extensive comparison with other available imaging techniques was performed, including conventional CT with two different radiation doses and optical stereo-photogrammetry. The stent investigated in this first study is the CP stent used to treat several congenital heart disease cases, but also importantly as the frame housing the biological valve in the PPVI Melody™ device (Section 2.4.1.1).

In the second part, I compared the performance of dynamic biplane fluoroscopy acquisitions against 4DCT imaging technique in assessing 3D stent deformations (Section 4.4). For this part, the analysed images were from a patient who underwent PPVI with the next generation device. The validation process consisted in the comparison of some geometrical parameters derived when imaging the same stent with the different imaging techniques. The reconstruction errors associated with each imaging method and their differences were analysed. Section 4.4.2 presents the results obtained in terms of the spatial resolution of each technique, the errors associated with repeatability and post-processing and the relative accuracy of each technique.

4.2 STENT GEOMETRY ACQUISITION

A number of two-dimensional (2D) or three-dimensional (3D) imaging techniques have been employed both in-vivo and in-vitro to assess stent geometry in the past. 2D methods include conventional angiography/fluoroscopy, which are currently used to assist the interventional cardiologist in accurate stent placement, and static x-rays for follow-up examination (**20**; **102**). Also, radiology-based imaging techniques have been employed in-vitro to assess the expanded shape of different stents in idealised (**103**; **104**), and patient-specific vessel geometries (**105**). Extension of imaging to 3D in-vivo has been achieved using CT to assess the anatomy of implantation sites prior to stent deployment (**106**), during follow-up for stent fracture investigation (**84**) and in the assessment of in-stent restenosis (**83**). More recently, my research group started working on 3D reconstructions from biplane fluoroscopy images to assess the in-vivo geometry of the PPVI Melody™ stent (**79**), but no thorough analysis of this reconstruction methodology has been carried out. In the bench setting, x-ray micro-tomography or micro-CT allows high resolution visualisation of metallic devices at spatial resolution in the range 9-17 μm (**107**). In-vitro studies demonstrated micro-CT to be suitable for the imaging of small metallic stents for coronary and carotid applications deployed in latex or silicone mock stenotic arteries (**108**). In addition, a stereo-photogrammetric optical imaging method was found to be robust for assessment of coronary stent expansion (**109**). At larger scales, similar techniques have been used for tracking transcatheter aortic valve implantation stent deformation in translucent artificial vessel phantoms (**110**) including comparison with assessment using micro-CT.

Despite this interest in the application of imaging techniques to the study of stent geometry, there are few reports of quantitative evaluation to determine the optimum imaging method for stent visualisation. At small scales, Lim et al. compared the capability of CT angiography and fluoroscopy to identify strut fractures of three coronary stents designs deployed both in-vivo and in-vitro, concluding that CT angiography is preferable. In this case, quantitative assessment of the maximum bending experienced by the stents and the maximum inter-strut distances was reported (**84**). At larger scales, Nordmeyer et al. proposed an in-vitro study to evaluate the diagnostic performance of different MR imaging sequences, CT and conventional angiography to image three different great vessel stents (nitinol, platinum-iridium and stainless steel stents). They found the diagnostic accuracy of CT comparable to conventional angiography, and particular MR sequences, despite image artefacts, were proven reliable for stent stenosis assessment. However, as this study focussed on the visualisation of lumen patency and not the geometry of the deployed stent, only stent lumen diameters were measured in each image (**81**).

A quantitative comparison of outcomes of different imaging modalities to evaluate the best method for the assessment of local geometric features of stents in-vivo and in-vitro has not been undertaken. Thus, the first aim of this chapter is the evaluation of the variance in geometric measurements of the same great vessel stent when imaged with different static techniques (including established volumetric methods and two methods for reconstruction of 3D geometries from stereo planar views). In view of the following chapter, considering micro-CT as the gold standard, the error associated with the biplane fluoroscopy reconstruction technique will be assessed, together with the error associated with the other methods.

4.2.1 Materials and Methods

In order to evaluate the relative accuracy of a number of imaging techniques for the assessment of 3D stent geometry, each imaging technique was applied to the same deployed stent geometry to provide a direct comparison. The stent investigated in the first part of the study was the CP stent, employed in the PPVI Melody™ device (Section 2.4.1.1).

4.2.1.1 Stent mounted on a realistic implantation site model

A realistic implantation site geometry – RVOT of a PPVI patient – was reconstructed from MR images using Mimics as explained in Section 3.5.1 to ensure a realistic anatomy of the stent is represented in the imaging assessment.

The surface of the reconstructed RVOT was extruded internally with a 3 mm thickness (Figure 4.1a) and a 3D compliant mould of the obtained volume was produced as described in Section 3.6.1 with a flexible elastomeric material (TangoPlus Full-Cure® 930 compound, Objet Ltd, Rehovot, Israel) (Figure 4.1b). The CP stent was mounted onto this implantation site model by compressing the mould inside the semi-expanded CP stent. Once the stent was correctly positioned, the mould was re-shaped to the implantation site geometry, thus deforming the stent to the geometry of the underlying vessel. Six metallic spherical markers were glued in a number of positions on the RVOT model around the stent to provide reference points as shown in Figure 4.1c.

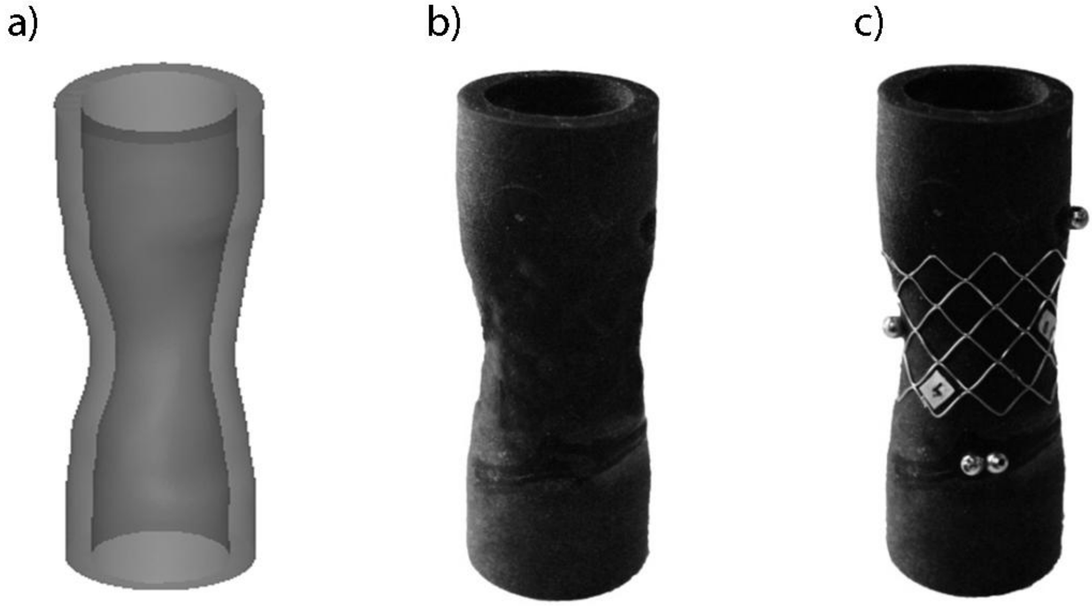

Figure 4.1 - Reconstructed (a) and printed (b) RVOT model. Valve stent deployed on the model with markers (c).

4.2.1.2 Image acquisition

The stent mounted on the realistic implantation site geometry was imaged using micro computed tomography (μCT), conventional CT, biplane fluoroscopy and optical stereo-photogrammetry techniques (Figure 4.2). Representative images obtained using each of these techniques are shown in Figure 4.3, along with an image obtained during in-vivo assessment of a PPVI device.

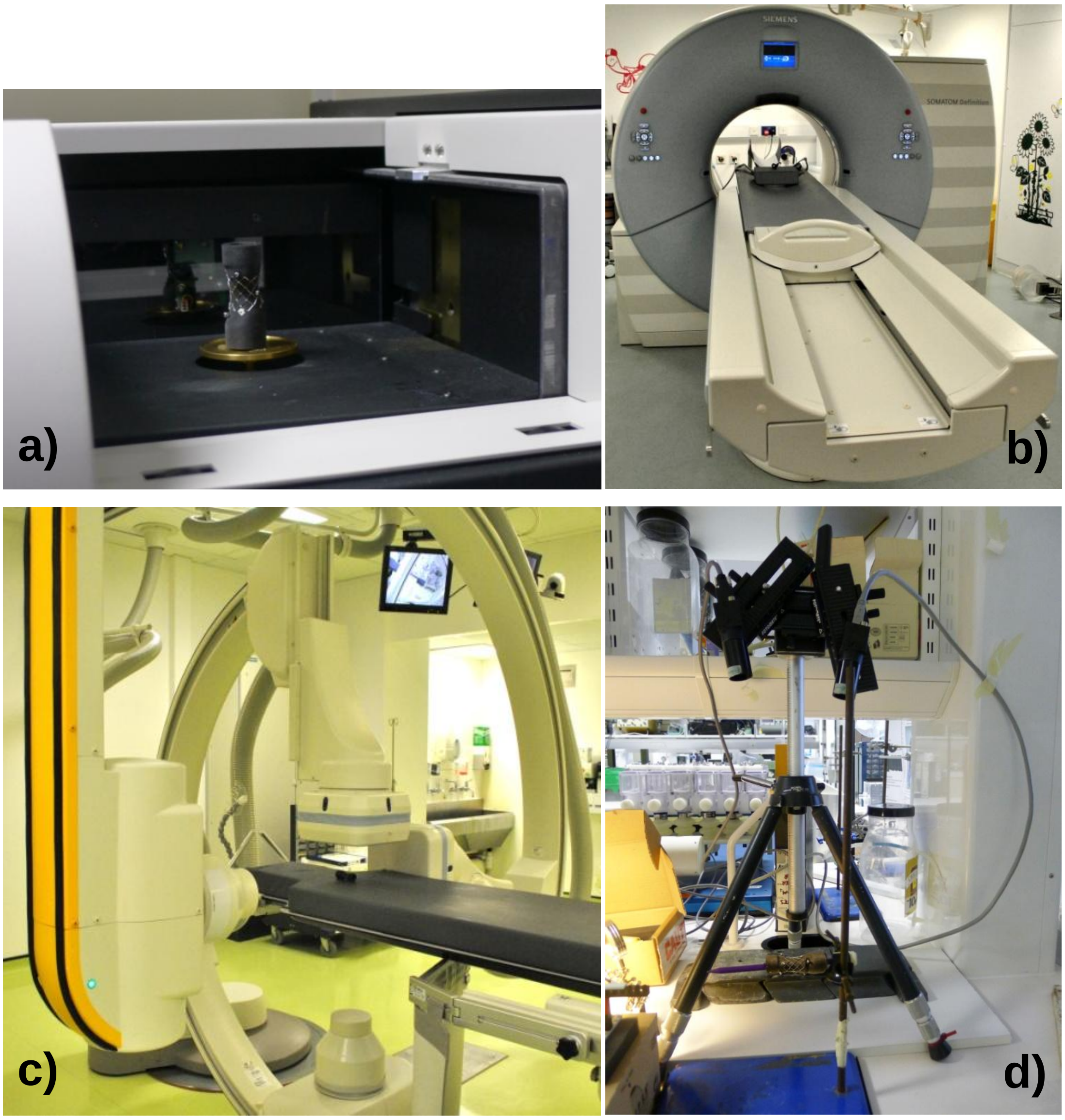

Figure 4.2 - Imaging systems used to acquire the geometry of the stent mounted on the realistic implantation site: a) micro-CT, b) CT, c) fluoroscopy, d) optical stereo-photogrammetry.

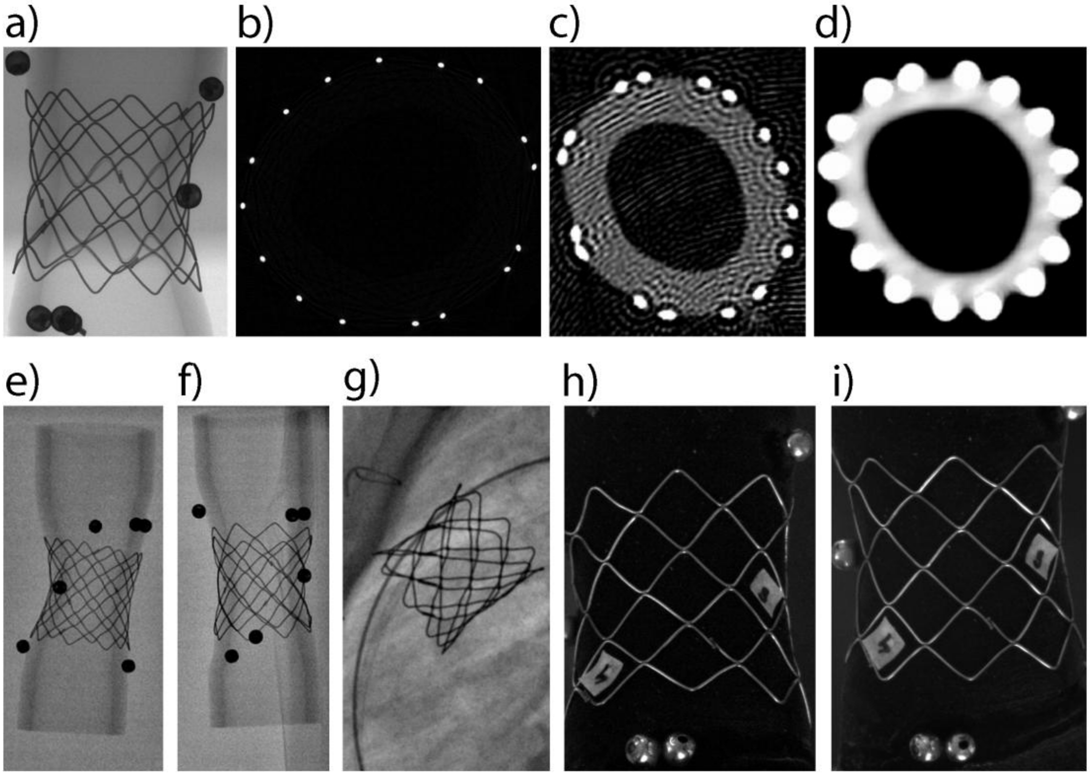

Figure 4.3 - Representative images from each imaging technique (a) Single projection image from uCT, prior to volume reconstruction and (b) cross-sectional image after volume reconstruction. (c) High-dose and (d) Low-dose clinical CT cross-sectional image. (e,f) Biplanar fluoroscopy images in vitro in two orthogonal projections. (g) In vivo fluoroscopy image of a deployed stent in a patient during PPVI. (h,i) Stereo optical images for a single stent position.

<u>Micro-CT (µCT)</u>: The model with deployed stent was placed vertically in the scanner mounted on a metal plate secured with hot melt adhesive (ethylene vinyl acetate copolymers) to ensure model stability during scanning process (Section 3.4.1.2). The voxel size was 17.2µm x 17.2µm x 17.2µm with scanning parameters: 100kV, 100 µA, Aluminium/copper filter, 360° rotation with a 0.7° rotation step resulting in 514 projection images. The stent was scanned as a 3 part oversized scan.

<u>CT</u>: Two sets of images were acquired: one with high dose of radiation and one with low dose of radiation relative to the standard cardiac protocol used in patients. The CT acquisition parameters were as follows:

- CT high dose <u>(*h*CT)</u>: collimation 16×0.6 mm, rotation time 1.0 s, pitch 0.8, 120 kVp, 250 effective mAs per rotation;

- CT low dose (*l*CT): collimation 64×0.6 mm, rotation time 0.5 s, pitch 1.0, 80 kVp, 60 mAs per rotation (effective mAs 16 using tube current modulation).

Fluoroscopy (F): Biplane orthogonal fluoroscopy images were acquired according to the protocol described in Section 3.4.1.3 with the arms of the fluoroscopy system positioned in the antero-posterior (AP) and lateral view. The acquisition was repeated three additional times by rotating both fluoroscopy arms of 22.5°, 45° and 67.5° in order to assess the influence of their orientation with respect to the imaged object.

Optical stereo-photogrammetry (OP): Acquisitions were carried out at the Royal Hallamshire Hospital, Sheffield, UK with a purpose-built stereo camera rig with camera separation of 45°. Two Flea2 fire-wire cameras were controlled using FlyCap2 software (Point Grey, Canada). A checkerboard grid pattern containing 28 squares (2x2 mm each) was captured in seven different orientations to calibrate cameras with the Bouguet Calibration Toolbox (**111**; **112**) for Matlab (The MathWorks Inc., Natick, MA, 2000). A checkerboard grid (27 x 21 mm) control object was imaged to assess calibration and reconstruction accuracy by reconstructing a reference distance (the 3 mm length of the internal grid). The optical system was designed to provide a field of view of around 30 mm along the maximum image dimension and to ensure adequate depth of field of 20 mm to maintain focus over the stent geometry. To characterise the entire stent geometry the stent was imaged in eight positions, rotating the stent in increments of 45°.

4.2.1.3 Image post-processing

µCT, *h*CT and *l*CT: The 3D volumetric image data were post-processed using Mimics (Figure 4.4) (Section 3.5.1).

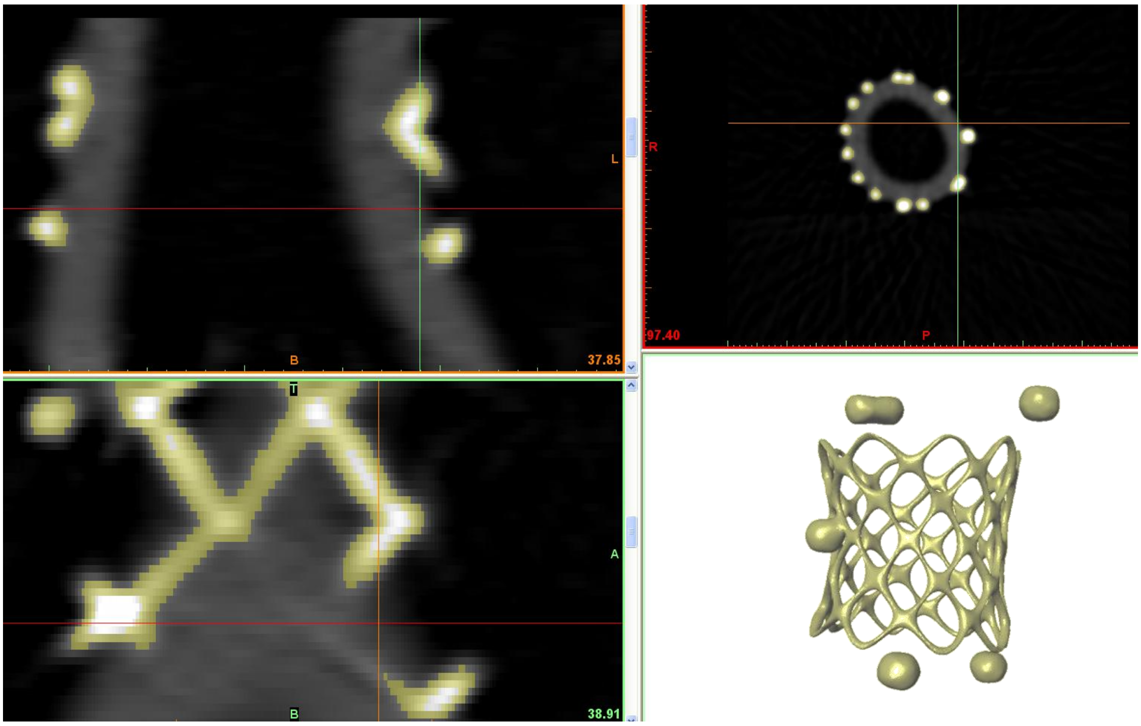

Figure 4.4 - 3D volumetric image data post-processed with the software Mmimics.

3D volumes were computed using two different smoothing factors (S1 and S2) to assess the potential distortions on the 3D volume reconstruction (S1 and S2 both employed a smoothing factor of 1.0 using 2 and 4 iterations respectively). This resulted in two 3D models for each imaging method, hereby referred to as [μ-*h*-*l*]CT-S1 and [μ-*h*-*l*]CT-S2. STL files of the reconstructed stents were then exported into the computer aided design (CAD) software Rhinoceros (McNeel, USA). The centre of each crown weld was identified by selecting four points around the circumference of the weld and taking the mean value of these points, as shown in Figure 4.5a. Three estimates of the weld centre position were obtained, one with smoothing factor S1 and two with smoothing factor S2 (named [μ-*h*-*l*]CT-S2-P1 and [μ-*h*-*l*]CT-S2-P2), to assess the repeatability of this process. The centres of the welds were connected with straight segments to represent the 3D stent geometry as a wireframe, as shown in Figure 4.5b.

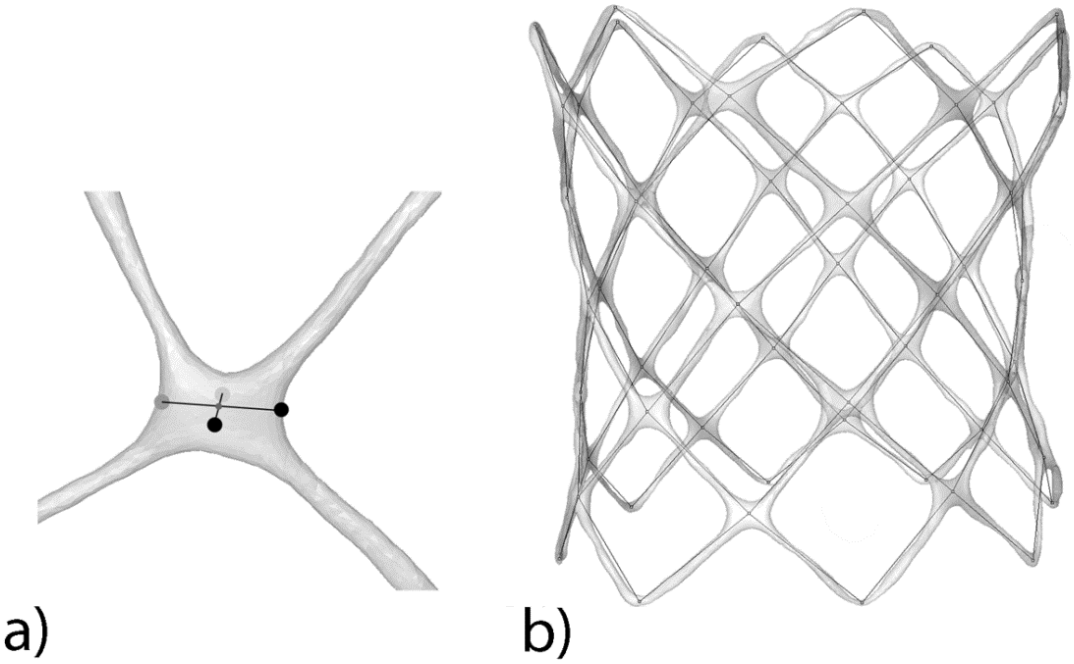

Figure 4.5 - (a) Surface points used to determine the centre of the strut weld from volumetric CT data. (b) Wire-frame representation of stent geometry superimposed to the volumetric CT reconstruction.

<u>Fluoroscopy:</u> The biplane fluoroscopy image pairs were post-processed to reconstruct the 3D stent shape as follows: the crown points of the struts forming the stent were identified in both fluoroscopy images and back-projected into the 3D space by tracing parallel rays from the orthogonal projections (CAD software Rhinoceros). The ray intersection determines the position of the strut welds in 3D space (Figure 4.6). As for the volumetric data, these points were joined with straight segments to define the struts of the device reconstructing the full stent geometry. The scaling factor for image calibration was based on the distance between reference markers as calculated from the μCT reconstruction. To assess the repeatability of the procedure, the stent geometry was reconstructed 3 times from the same image pair obtained with the arms in AP and lateral position.

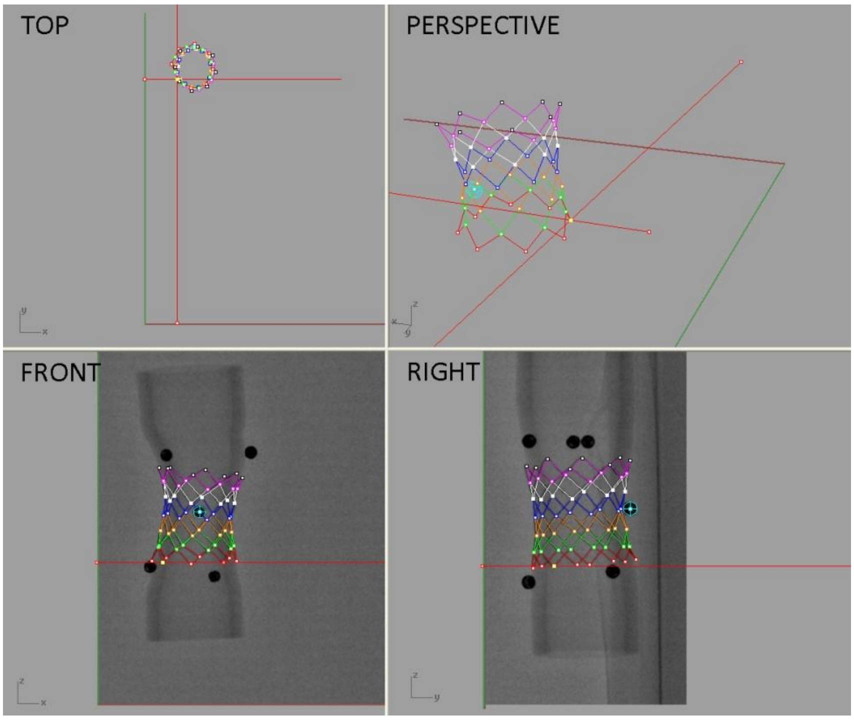

Figure 4.6 - 3D stent reconstruction process using biplane fluoroscopy images imported in the CAD software Rhinoceros.

Optical stereo-photogrammetry: For each stent position, points at the centre of each crown weld of the stent in the left and right 2D camera images were identified (Figure 4.7). The 3D coordinate of each weld centre point was obtained by triangulation using the camera calibration data and the 2D position from left and right images (**113**). The identification of the weld centre was repeated three times using the same image pair to test the repeatability of this process.

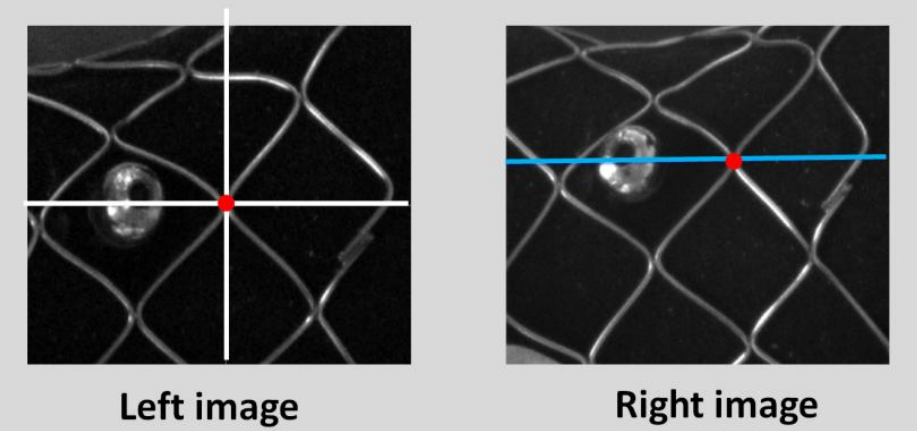

Figure 4.7 - Post-processing of the pictures obtained from the optical stereo-photogrammetry technique.

4.2.1.4 Comparison parameters

The following parameters were defined and calculated for each reconstructed stent geometry in order to compare both the repeatability of results obtained using a single imaging technique and the agreement between each of the imaging techniques:

- Strut length L (n = 96 per stent) evaluated as the distance between the two weld centre points (x_1, y_1, z_1) and (x_2, y_2, z_2) defining the end of each strut (Figure 4.8a):

$$L = \sqrt{(x_2 - x_1)^2 + (y_2 - y_1)^2 + (z_2 - z_1)^2}$$

- Strut angle β (n = 96 per stent) evaluated using the Law of cosines from the dimensions of the triangle to which the investigated angle belongs (Figure 4.8b):

$$\beta = acos\left(\frac{-b^2 + a^2 + c^2}{2ac}\right)$$

- Stent cell asymmetry C_a (n = 40 per stent) calculated as the ratio between the cell longitudinal dl and circumferential dc diagonals (Figure 4.8a):

$$C_a = \frac{dl}{dc}$$

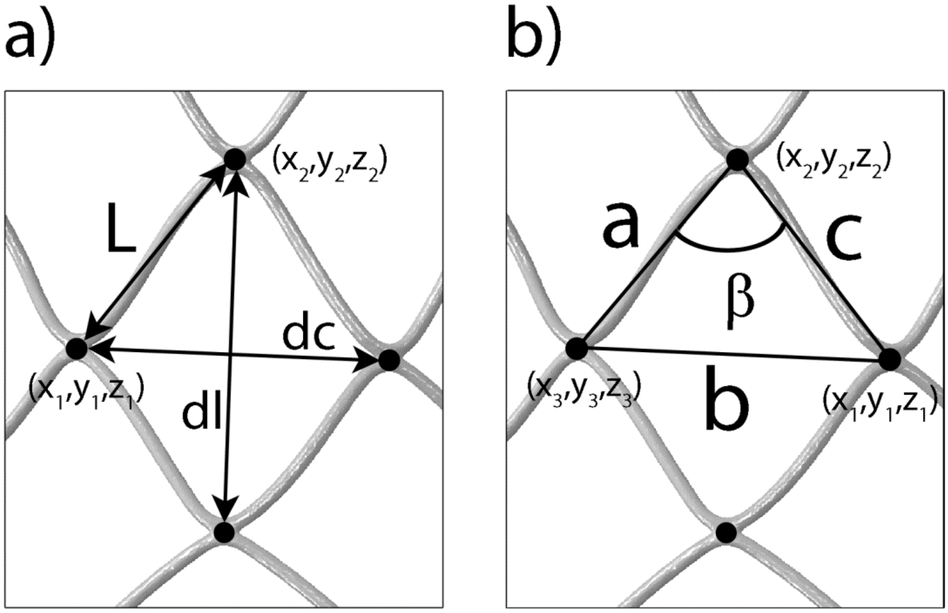

Figure 4.8 - Stent parameters used for comparing the different imaging techniques: strut length L, circumferential asymmetry C_a = dl/dc, and strut angle β.

4.2.1.5 Error evaluation of each image technique

For each technique the geometric parameters were calculated for multiple reconstructions of stent geometry. The repeatability error was assessed by calculating the standard deviation, σ_p, of the parameter values and the maximum percentage difference, ΔP_{max}, from the average parameter value, P, over all reconstructions, as follows:

$$\bar{P} = \sum_{i=1}^{n} \frac{P_i}{n}$$

$$\sigma_p = \sqrt{\sum_{i=1}^{n} \frac{(P_i - \bar{P})^2}{n-1}}$$

$$\Delta P_{max} = max \left| \frac{(P_i - \bar{P})}{\bar{P}} \right|$$

resulting in N values of standard deviation and maximum percentage difference for each parameter (N = 96 for strut length, N = 96 for strut angle, N = 40 for stent cell asymmetry). For the biplanar methods (fluoroscopy and optical), averaging was calculated from three reconstructions (n = 3); for the volumetric methods (μCT, *h*CT and *l*CT), averaging was calculated from two reconstructions (n = 2).

In addition, for the μCT, *h*CT and *l*CT volumetric data, the difference between the stent geometry obtained using S1 and S2 smoothing was assessed, again using the standard deviation and the maximum percentage difference of each parameter between the two reconstructed geometries. Moreover, for the fluoroscopy images, the influence of the imaging orientation was evaluated using the standard deviation and the maximum percentage difference of each parameter between the reconstructed geometry from each of the four rotation angles.

The maximum and mean of the N values of standard deviation and maximum percentage difference are reported in Section 4.2.2.2 as an estimation of the reconstruction error associated with each imaging technique.

4.2.1.6 Differences between image techniques

The averaged parameter value (L, β, C_a) computed from the two μCT reconstructions was used as a gold standard. For all other imaging techniques the averaged parameter values computed from the multiple reconstructions were compared with the µCT data. Pearson’s correlation coefficient was calculated between the µCT data and each other imaging technique, for all three parameters. For each parameter and for each imaging technique a Bland-Altman plot was produced using the µCT data as the comparative method in all cases.

4.2.2 Results and Discussion

4.2.2.1 Image acquisition and post-processing

The voxels of the µCT scan were isotropic with a spatial resolution of 17 µm. For the conventional CT scans, the volume CT dose index ($CTDI_{vol}$) was 0.242 mGy for the low dose sequence and 50.938 mGy for the high dose sequence. The images were reconstructed with a pixel size of 127 µm x 127 µm and slice increment of 299 µm (slice thickness of 600 µm) for the low dose scan, and with a pixel size of 123 µm x 123 µm and a slice increment of 299 µm (slice thickness of 600 µm) for the high dose scan. Acquisitions with the fluoroscopy scanner resulted in an Image Area Dose Product of 0.01 $Gy{\cdot}cm^2$ and a pixel spacing of 279 µm x 279 µm.

The resolution of the optical images was 1288 x 964 pixels with a sensor size of 3.75 x 3.75 µm per pixel. A lens of focal length 40 mm was used, positioned approximately 44 mm from the camera sensor, resulting in a magnification of 0.1. This magnification results in a field of view of 46 x 38 mm and a spatial resolution of approximately 35 µm. Calibration and reconstruction of a control object of a known size suggest measurement accuracy of the order 25 µm.

4.2.2.2 Error evaluation

Table 4.1 reports the variation in the computed parameter values for each technique with repeated reconstruction of the stent geometry. For the volumetric methods, the results demonstrate that the uncertainty in the computation of all parameters increases from µCT to *h*CT to *l*CT. For the 2D reconstruction methods, the uncertainty increases from the optical stereo-photogrammetry results to the biplanar fluoroscopy results.

Table 4.1 - Maximum standard deviations and maximum % differences (with respect to average values for each technique) in the strut lengths (L), strut angles (β) and circumferential asymmetries (Ca) between repeated point selections and smoothing factors.

	MAX (MEAN) STANDARD DEVIATION		**MAX (MEAN) % DIFFERENCE**	
	Point selection	**Smoothing**	**Point selection**	**Smoothing**
L [mm]				
μCT	0.082 (0.021)	0.078 (0.018)	2.07 (0.52)	1.97 (0.45)
*h*CT	0.136 (0.042)	0.137 (0.040)	3.51 (1.01)	3.25 (0.86)
*l*CT	0.237 (0.068)	0.228 (0.066)	6.11 (1.75)	6.25 (1.68)
OP	0.065 (0.020)	N/A	2.90 (0.35)	N/A
F	0.198 (0.063)	N/A	3.79 (0.92)	N/A
β [º]				
μCT	1.175 (0.275)	0.977 (0.288)	1.59 (0.43)	1.29 (0.35)
*h*CT	2.048(0.487)	1.512 (0.526)	2.71 (0.76)	2.01 (0.69)
*l*CT	3.472 (1.024)	4.354 (1.233)	5.57 (1.64)	4.53 (1.22)
OP	1.055 (0.356)	N/A	1.98 (0.31)	N/A
F	2.934 (0.883)	N/A	3.60 (0.81)	N/A
Ca [-]				
μCT	0.009 (0.003)	0.011 (0.003)	1.21 (0.44)	1.57 (0.45)
*h*CT	0.017 (0.006)	0.020 (0.006)	2.58 (0.85)	2.47 (0.86)
*l*CT	0.047 (0.013)	0.028 (0.009)	5.76 (1.77)	3.44 (1.20)
OP	0.009 (0.004)	N/A	1.18 (0.29)	N/A
F	0.024 (0.011)	N/A	2.78 (0.71)	N/A

These results are in line with expectations as the μCT data is obtained at the highest spatial resolution and the performance of the low dose CT imaging is expected to be worse than that of the high dose CT. The uncertainty of the optical stereo results is of similar magnitude to that of the μCT data and the uncertainty of the biplanar fluoroscopy results is of similar magnitude to that of the high dose CT. This relationship between the results of the 2D and 3D methods is in line with the variation in the spatial resolution of each technique.

The uncertainty in stent reconstruction introduced by variation of the smoothing factor used to reconstruct the stent geometry for the volumetric methods is of similar magnitude to the uncertainty associated with the repeatability in geometry reconstruction. These results suggest that the nature of post-processing of the 3D volumetric data is unlikely to significantly influence derived geometric parameters.

Finally, the max (mean) standard deviation and max (mean) % difference between the stent reconstructions from the four different fluoroscopy arm positions were equal to 0.228 mm (0.090 mm) and 4.46% (1.24%) for L, 2.357° (1.100°) and 3.71% (0.99%) for β, and 0.034 (0.016) and 4.85% (1.28%) for Ca. Therefore, the uncertainty in stent reconstruction due to the orientation of the fluoroscopy arms with respect to the stent/RVOT object is also comparable with the repeatability errors of this technique.

4.2.2.3 Differences between image techniques

The calculated values of the stent parameters (L, β, Ca) measured using each imaging technique were correlated with the corresponding values measured using μCT. Pearson's correlation coefficients were calculated for each parameter and each imaging technique and are reported in Table 4.2 and in Figure 4.9.

Table 4.2 - Values of linear correlation coefficient between values of each parameter calculated using μCT and each of the four other imaging techniques.

	***l*CT**	***h*CT**	**OP**	**F**
L	0.657	0.542	0.906	0.541
β	0.981	0.993	0.993	0.989
Ca	0.988	0.993	0.995	0.988

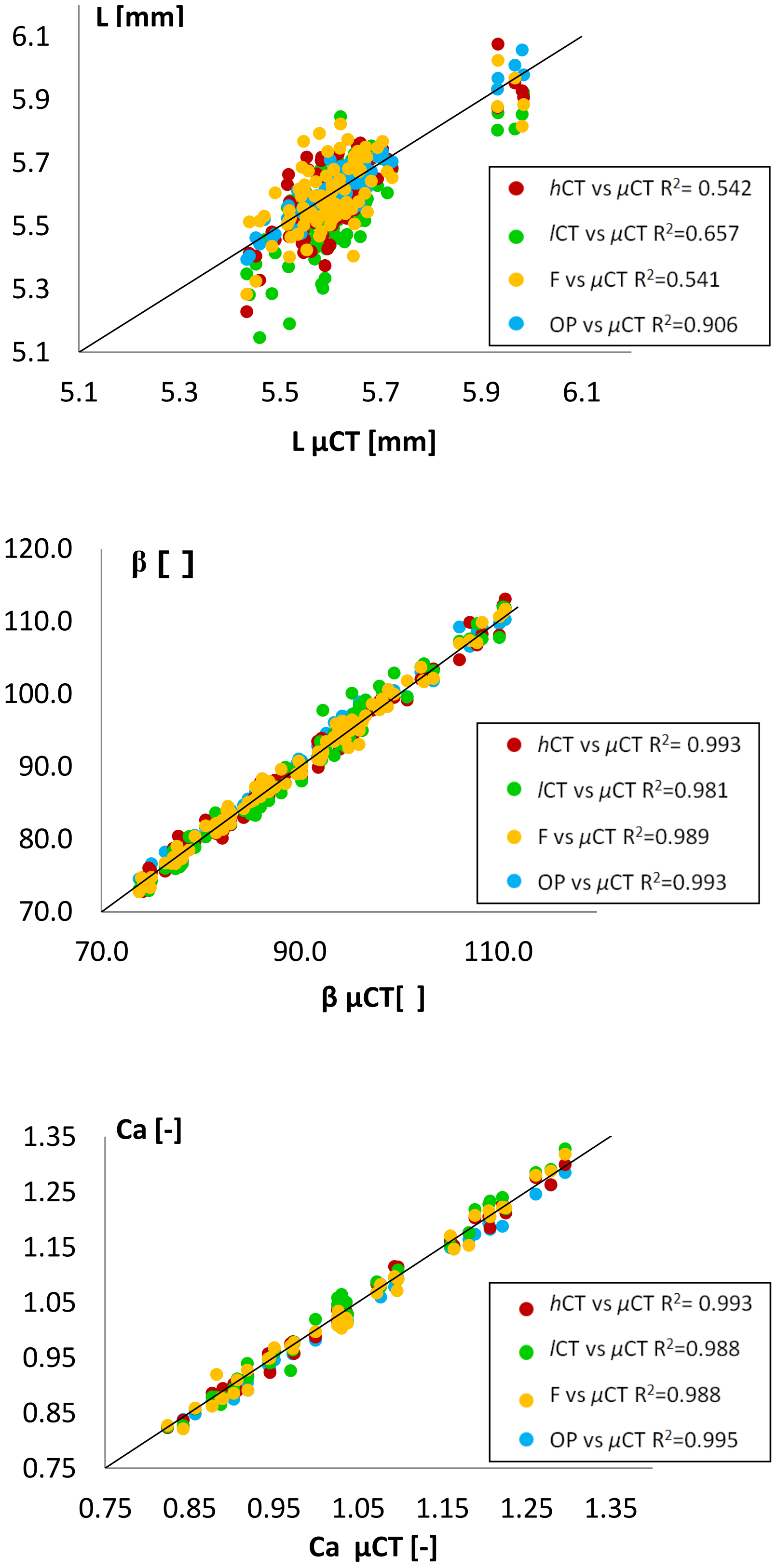

Figure 4.9 - Pearson's correlation plots calculated for L, β and Ca for each image technique against the gold standard technique, the micro-CT.

The Bland-Altman plots that compare each imaging technique with the μCT results for all parameters are shown in Figure 4.11.

The best linear correlation was observed for the optical stereo method for all three parameters analysed (L, β, Ca). Greater variance was observed in the correlation of strut length between the methods which may be explained by the clustering of the strut length parameter within two distinct ranges, observed in the distribution of values along the horizontal axis of the Bland-Altman plots. This clustering demonstrates the relative accuracy of all methods in determining stent geometry, as inspection of the stent design in these regions confirms that greater strut length parameters are consistent with stent fabrication. Indeed, longer stent struts are measured where a weld is used to close the extremities of each ring (Figure 4.10). The Bland-Altman plots support observations that the closest agreement with μCT data is obtained using the optical stereo method.

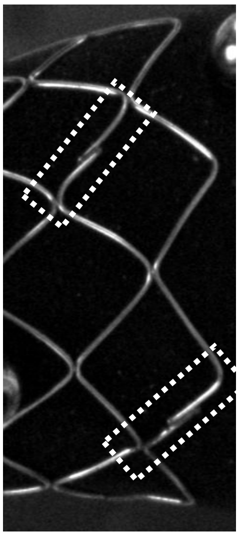

Figure 4.10 - Zoom on the stent highlighting the longer struts in correspondence of the welds used to close the extremities of each ring.

The results presented in Table 4.1 and Figure 4.11 demonstrate consistently that the performance of biplanar reconstruction methods is comparable with the performance of the clinical volumetric CT scans in evaluating 3D stent geometry. Whilst the stereo optical method demonstrates higher accuracy than the biplanar fluoroscopy results, the increase in the maximum and mean percentage error, reported in Table 4.3, is relatively small when compared with the effective spatial resolution of each technique, reported in Section 4.2.2.1. These results suggest that consistency in identification of strut landmark points is the dominant factor in determining reconstruction accuracy, independent of the spatial resolution of the imaging technique.

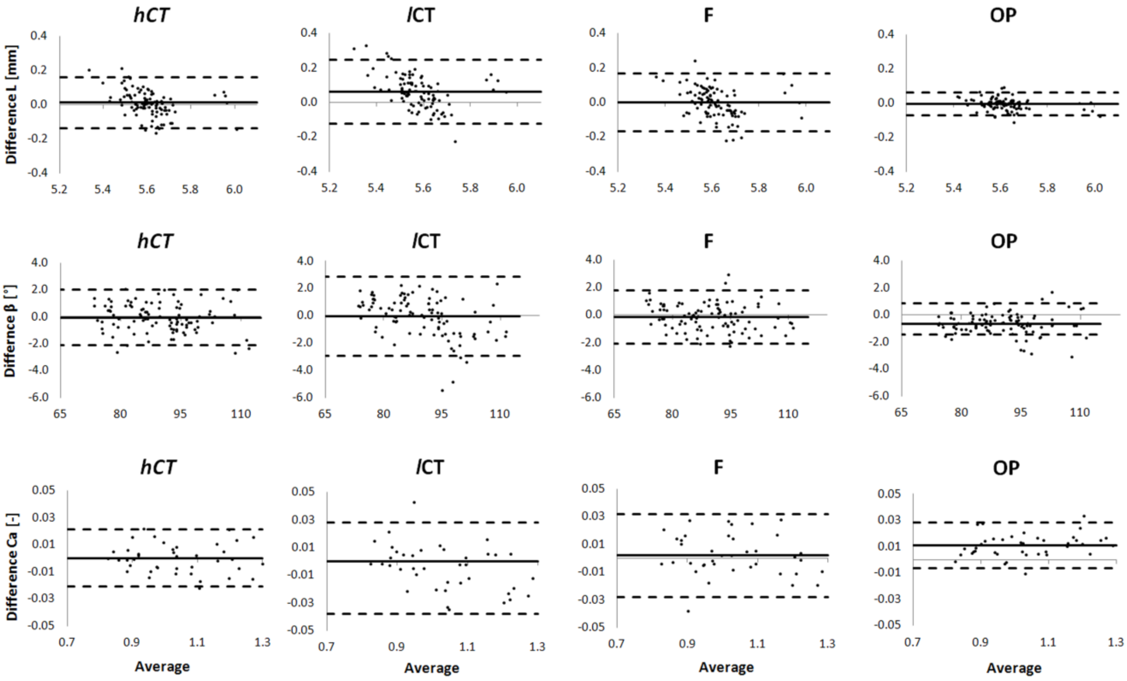

Figure 4.11 - Bland-Altman plots for each parameter (length L, angle β and circumferential asymmetry Ca) showing the differences in the values measured with the micro-CT (μCT) technique and the other techniques (high dose CT hCT, low dose CT lCT, fluoroscopy F, and stereo-photogrammetry OP). The thick line represents the mean difference between the value of the parameter measured with the considered technique and with μCT. The two dotted lines represent +1.96 and -1.96 standard deviations of the differences between the two considered methods.

Table 4.3 - Comparison of hCT, lCT, fluoroscopy and optical stereo-photogrammetry techniques: maximum (mean) % differences of all the parameters calculated with respect to μCT.

MAX (MEAN) % DIFFERENCES	***h*CT**	***l*CT**	**F**	**OP**
L [%]	3.84 (1.04)	5.94 (1.58)	4.26 (1.22)	1.97 (0.18)
β [%]	3.40 (0.96)	5.87 (1.30)	3.07 (0.89)	3.00 (0.89)
Ca [%]	2.32 (0.83)	4.43 (1.30)	4.31 (1.18)	3.02 (1.12)

4.3 Implications for in-vitro and in-vivo assessment of 3D device geometry

This first part of the study has demonstrated that, if simultaneous acquisition from two biplanar views is possible, 3D reconstruction of stent geometry is feasible. For the imaging parameters used in this study, chosen to represent those used during clinical assessment of PPVI geometry, the uncertainty on the evaluation of strut length, separation angle and cell asymmetry using biplanar fluoroscopy is of the order +/- 0.2 mm, 3° and 0.03 respectively.

Comparison between biplanar fluoroscopy and stereo photogrammetry in this study demonstrates the improvements in accuracy that can be obtained using high resolution optical systems, which maintain the advantage of high temporal resolution in contrast with volumetric methods. Whilst optical techniques cannot be employed to evaluate in-vivo device performance, these techniques may be preferred for the assessment of stent geometry at smaller length scales, such as the assessment of coronary stent implantation (**114**).

The variations observed in image quality between the micro-CT and clinical modalities are similar to those reported by Ionescu et al. (**107**) who evaluated the effectiveness of Multislice-CT, C-arm flat detector-CT and flat panel-CT for imaging a Cypher stent of 3 mm diameter. At these length scales accurate assessment of local stent features with clinical modalities is challenging, with over-estimation of strut thickness and under-estimation of lumen diameter reported of the order 300% and 30% respectively.

It is acknowledged that the imaging protocols in this study cannot fully capture the results expected during in-vivo assessment of PPVI geometry due to the absence of image attenuation from the surrounding tissues. However, qualitative comparison of in-vitro and in-vivo fluoroscopy of implanted PPVI geometry (Figure 4.3f and Figure 4.3g respectively) suggests that the protocols used within this study provide a good representation of images obtained in-vivo.

The protocol here developed has not attempted to directly evaluate dynamic changes in stent geometry over a cardiac cycle as this cannot be assessed with micro-CT, which is captured over timescales of the order 5 – 10 minutes. This study provides an accurate estimation of the accuracy of biplanar methods for dynamic assessment of stent geometry provided that the device motion is insignificant during the image acquisition period and the temporal offset between the acquisitions of each of the stereo images is minimised. However, for the assessment of PPVI stents, this is not the case as significant motion of the implanted stent is observed during the cardiac cycle (**79**). To overcome this limitation, another protocol was designed to assess the accuracy of biplane fluoroscopy in evaluating stent deformation, as discussed in the following paragraphs.

4.4 STENT DEFORMATION ACQUISITIONS

Numerical studies and simulations are often used to examine stent behaviour during implantation and to predict the influence of stent design and deployment characteristics on the solid and fluid mechanics of the vascular environment (**115**; **116**). Computational approaches can describe stent deployment at spatial and temporal resolutions that cannot be achieved with clinical or experimental studies. However, as the application of simulation to medical device design has evolved from the consideration of idealised behaviour (**117**) to a focus on predictions in patient-specific anatomies (**118**), the results of simulations are becoming increasingly dependent on the quality of the data used to describe the patient anatomy and device configuration.

In-vivo and in-vitro application of 2D and 3D imaging techniques have the potential to provide the appropriate data to both inform and validate numerical models of stent behaviour. However, to fully characterise device performance, such methods are required to reproduce 3D device geometry as a function of time. To ensure accurate assessment of stent placement, deployment, final geometry and function, high quality visualisation methods are crucial.

Characterisation of stent dynamic behaviour in patients can be achieved with 4DCT which also provides information regarding the cardiac conditions of the individual. However, CT investigations of device dynamic behaviour require high radiation dose, and as such are undesirable if alternative methods are available which provide comparable accuracy.

To evaluate whether the biplanar 2D fluoroscopy technique previously introduced is able to capture stent deformations during the cardiac cycle, a quantitative comparison against 4DCT was performed in a patient’s case.

4.4.1 Materials and Methods

The stent here investigated was the new PPVI device described in Section 2.4.1.1 (Figure 4.12) and implanted in one case under compassionate use (**119**).

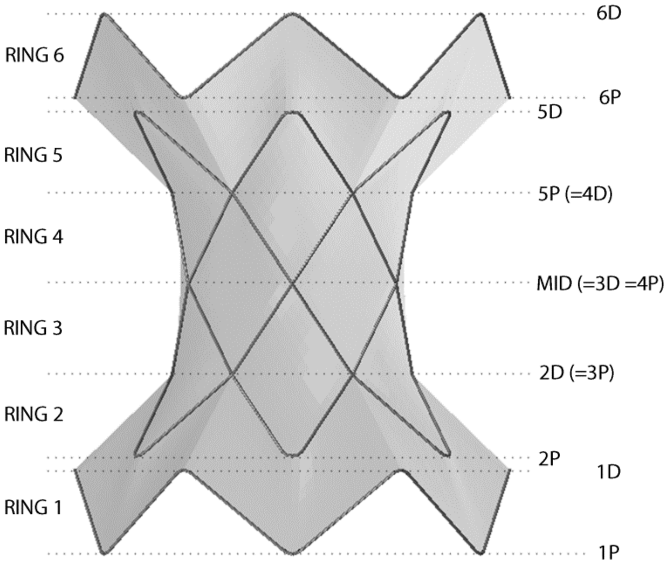

Figure 4.12 - New PPVI device design: lateral view with the nomenclature adopted for the rings on the left (RING 1 to 6) and the sections on the right (1P to 6D), P and D being proximal and distal respectively.

Following the procedure, due to the large dynamics of the patient's implantation site, great interest has been directed towards the analysis of stent deformation, in particular to monitor for potential strut fractures. Over a 4 year period, volumetric 4DCT and biplanar fluoroscopy images were acquired at a number of time points including acquisition of both 4DCT and fluoroscopy images during the same session 3 months after the procedure (**19**).

Using these data, 3D geometry and deformations of the stent in-situ acquired with the two different imaging modalities were analysed and compared to assess qualitative and quantitative differences.

4.4.1.1 Image acquisition and post-processing

4DCT acquisition parameters were as follows: collimation 2 x 32 x 0.6 mm, rotation time 0.33 s, pitch 0.2, kVp 100, effective mAs 273, using tube current modulation. Effective x-ray dose was 14.54 mSv, calculated as k*DLP, where k depends on body region and is given in the European Guidelines on Quality Criteria for CT [EUR 16262 EN, May 1999; for the chest k = 0.017 mSv mGy^{-1} cm^{-1}], and DLP = dose length product = CTDIvol * scan length, calculated by the scanner (**120**). The 4DCT dataset was divided into 10 independent phases during the cardiac cycle and the stent 3D volume was reconstructed for each frame using Mimics (Figure 4.13).

Figure 4.13 - 3D stent reconstructed from 4DCT data at one frame of the cardiac cycle, superimposed on the 4DCT image.

Centrelines of the six stent wires were extracted and imported into CAD software (Rhinoceros, McNeel, USA) for further measurement.

During follow-up, simultaneous biplanar fluoroscopy images of the stent were acquired in the AP and lateral projection at 15 frames per second. Twelve frames per cardiac cycle were acquired for more than 3 complete cycles. In Rhinoceros, back projection of stent strut landmark points from the stereo orthogonal image pairs of 12 consecutive frames allowed 3D reconstruction of the stent geometry over a complete cycle (Section 4.2.1.3) (Figure 4.14).

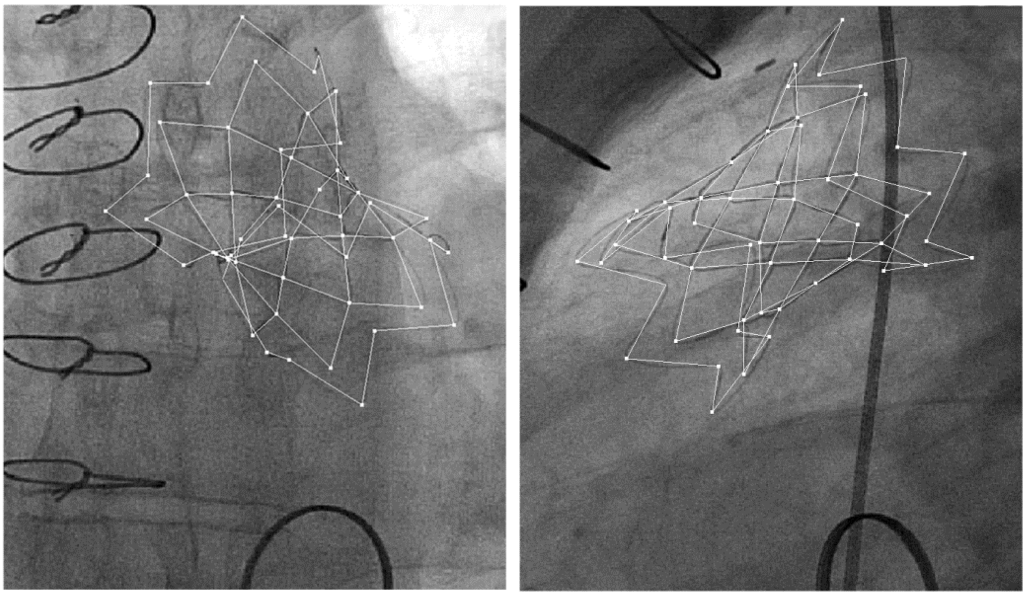

Figure 4.14 - Stent reconstructed from the antero-posterior and lateral fluoroscopy images at one frame of the cardiac cycle.

The diameter of a previously implanted prosthetic mitral valve visible in both fluoroscopic planes was used for calibration purposes. The stent landmark points corresponding to the apices of the strut wires were manually identified in both 4DCT and fluoroscopy 3D reconstructions. Three distal (D) and 3 proximal (P) diameters were calculated for the first and sixth ring. For the central portion of the stent/graft, 3 diameters for each of the 5 sections highlighted in Figure 4.12 (2P, 2D, MID, 5P, 5D) were measured. It should be noted that the data obtained with each imaging technique was derived from distinct cardiac cycles.

For each measured diameter, the maximum (D_{max}) and minimum (D_{min}) values over the cardiac cycle were identified, and the percentage compression was calculated as $100*(D_{max} - D_{min})/ D_{max}$. The diameter values were used to compare the outcomes of 4DCT and fluoroscopy data (Pearson’s correlation coefficient and Bland Altman plots using 4DCT as a reference). The percentage compression calculated by each method was used to evaluate the deformation of the device during the cardiac cycle and the potential risk of fracture.

4.4.2 Results

3D reconstruction of the stent was feasible for all frames of the fluoroscopy and 4DCT images. The cusps of the stent struts were identifiable using both image modalities but the selection process was easier for fluoroscopy than for 4DCT images due to the artefacts caused by the metal stent struts in the CT scanner. In particular, identification of the distal and proximal rings was more difficult as they are made of thinner wires.

Figure 4.15 shows the maximum and minimum diameter during the cardiac cycle from 4DCT and fluoroscopy reconstructions (top and middle panel) and the percentage of compression calculated with both methods (bottom panel). The largest difference between the compression values was measured for a diameter in the distal section of Ring 1 (7.02% vs 3.48%). Good correlation (R^2=0.9957) was observed between the diameters calculated from the two image method reconstructions. The Bland-Altman plot revealed a small systematic bias suggesting that fluoroscopy underestimates the 4DCT diameter by <1 mm (Figure 4.16). The proximal and distal rings (1P, 6D), originally designed with circular shape and 40 mm diameter sections, once released inside the patient’s implantation site, assumed elliptical profiles, and experienced the largest deformations during the cardiac cycle. The central portion of the stent (2D-5D), which holds the valve (not in direct contact with the arterial wall), maintained a circular shape and experienced less deformation than the distal and proximal rings (ring 1 and 6). The largest compression of the stent measured by each method during the cardiac cycle was 6.98% (fluoroscopy) and 7.92% (4DCT), both measured in the most distal ring (section 6D). Both methods reported an average diameter during the cardiac cycle in this section of 27 mm which is ~70% of its original dimension.

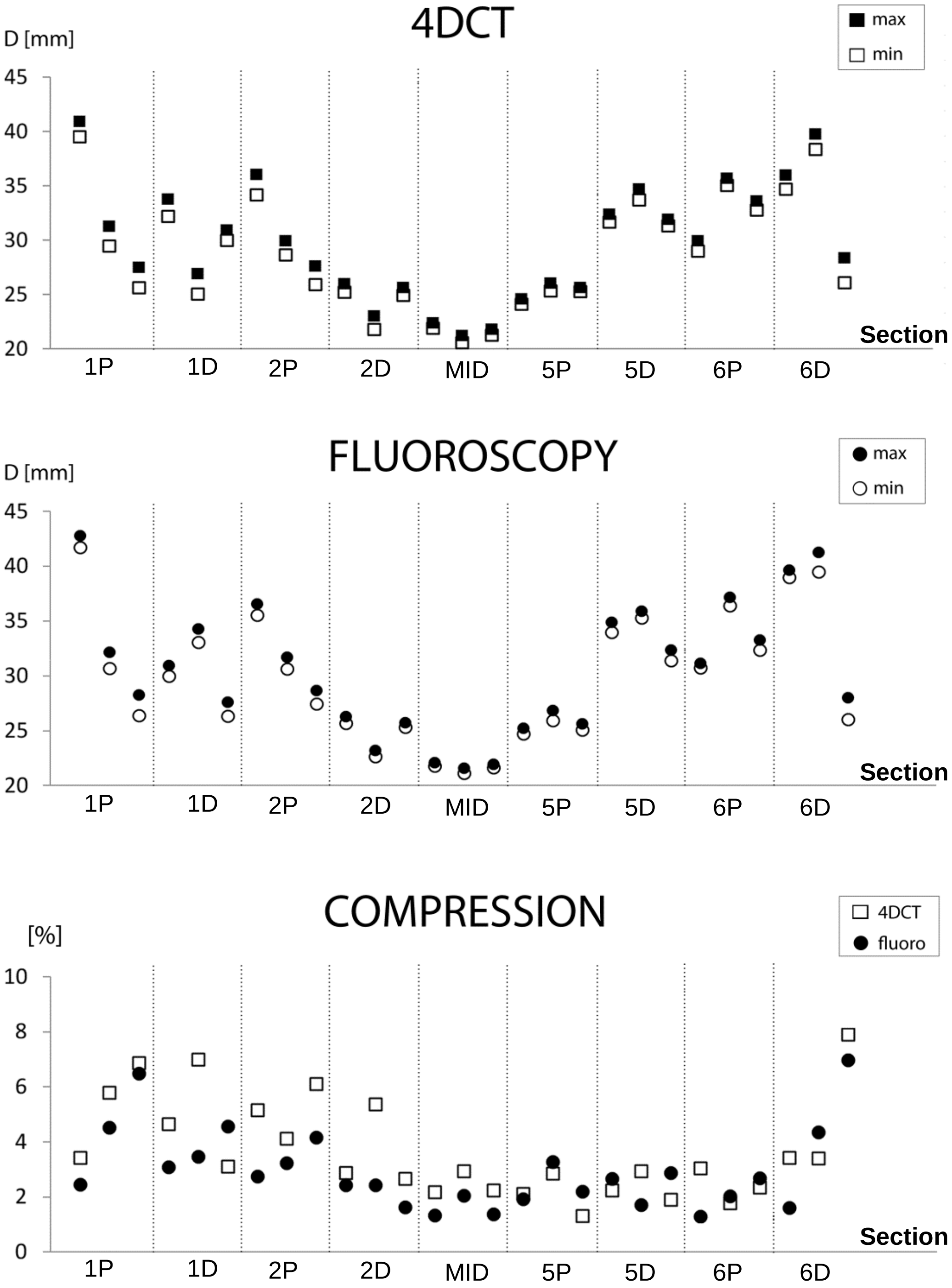

Figure 4.15 - Maximum and minimum diameter measured for the three diameters of each section (from 1P to 6D) from 4DCT (top panel) and fluoroscopy data (middle panel). Percentage of compression for the same diameters during the cardiac cycle evaluated from the stent reconstructions with both image techniques (bottom panel).

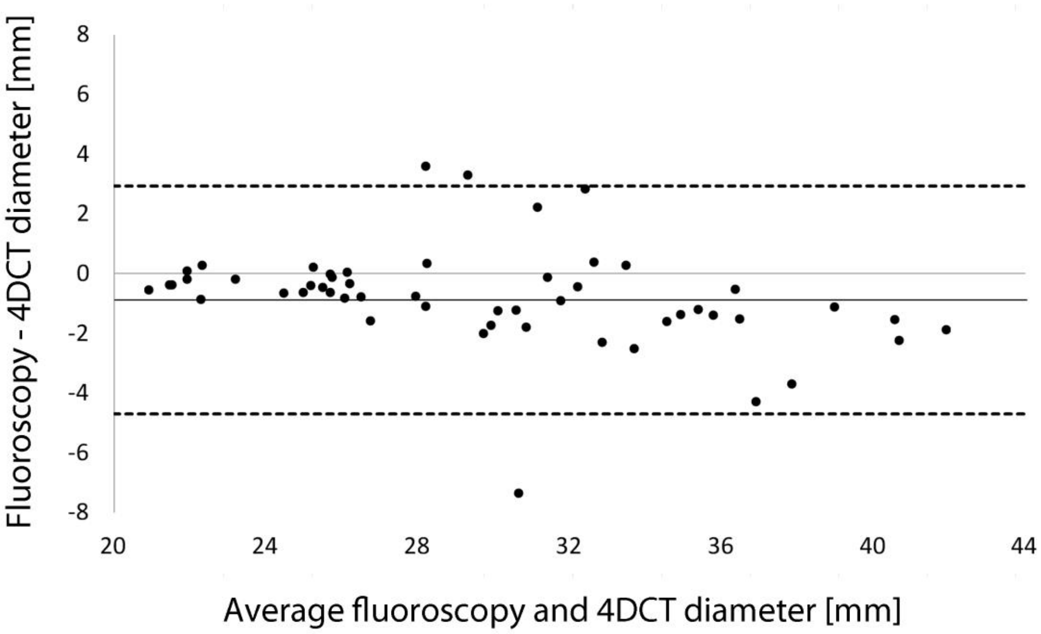

Figure 4.16 - Bland-Altman plot of the differences in diameter values (maximum and minimum) measured between 4DCT and fluoroscopy stent reconstructions. The thick line represents the mean difference between the value of the parameter measured with the 4DCT and with the fluoroscopy. The two dotted lines represent +1.96 and -1.96 standard deviations of the differences between the two methods.

4.4.3 Discussion

In this second part of the study, it has been shown that the stent compression during the cardiac cycle measured from 3D reconstructions of simultaneously acquired biplane fluoroscopy images is comparable with that measured from 4DCT data. In this case, definitive quantification of differences between the techniques could not be carried out as the data represent two different cardiac cycles, acquired within 10 minutes.

Reconstruction of 3D geometry from biplane fluoroscopy provided valuable data on both stent deformation during the cardiac cycle and interaction between the stent and the implantation site in terms of device anchoring and stability.

Detailed geometry characterisation at smaller scales is likely to be less successful (**121**) limiting this methodology to stents used in congenital heart disease treatments or heart valve replacements (**122**). In the PPVI case, the temporal resolution of 4DCT and fluoroscopy acquisition was different (10 vs 12 frames per cardiac cycle respectively). Additionally, the 4DCT scan was gated with the ECG of the patient, while the ECG was not monitored during fluoroscopy image acquisition. However, the errors introduced by these different acquisitions are expected to be of smaller magnitude than the variation between cardiac cycles.

4.5 CONCLUSIONS

In conclusion, this chapter has demonstrated that the performance of biplanar reconstruction methods is comparable with the performance of volumetric CT scans in evaluating 3D stent geometry and deformation.

In particular, biplanar fluoroscopy has been shown to be effective in the measurement of strut length, separation angle and cell asymmetry. These results support the use of biplanar fluoroscopy for the generation of 3D models of stent geometry for assessment of stent fracture risk using numerical simulation and provide a quantitative assessment of the magnitude of uncertainty in the measurement of geometric parameters derived from 3D stent geometry.

Furthermore, it has been demonstrated that biplanar 2D image techniques can provide accuracy of the same order as 3D image modalities to assess not only the geometry but also the deformation of stents in-vivo. Also, as a result of its low radiation dosage, the biplanar fluoroscopy method may have significant advantages in the measurement of dynamic 3D stent deformation.

These results are promising for the application of biplanar fluoroscopy in-vivo as a tool to assess stent geometry and 3D deformation during cardiac cycle. Very importantly, these parameters could help predict the risk of stent fracture, which, in the next chapter, are demonstrated to be related to variation in stent geometry during the cardiac cycle.

CHAPTER 5

PPVI STENT FRACTURE RISK STRATIFICATION

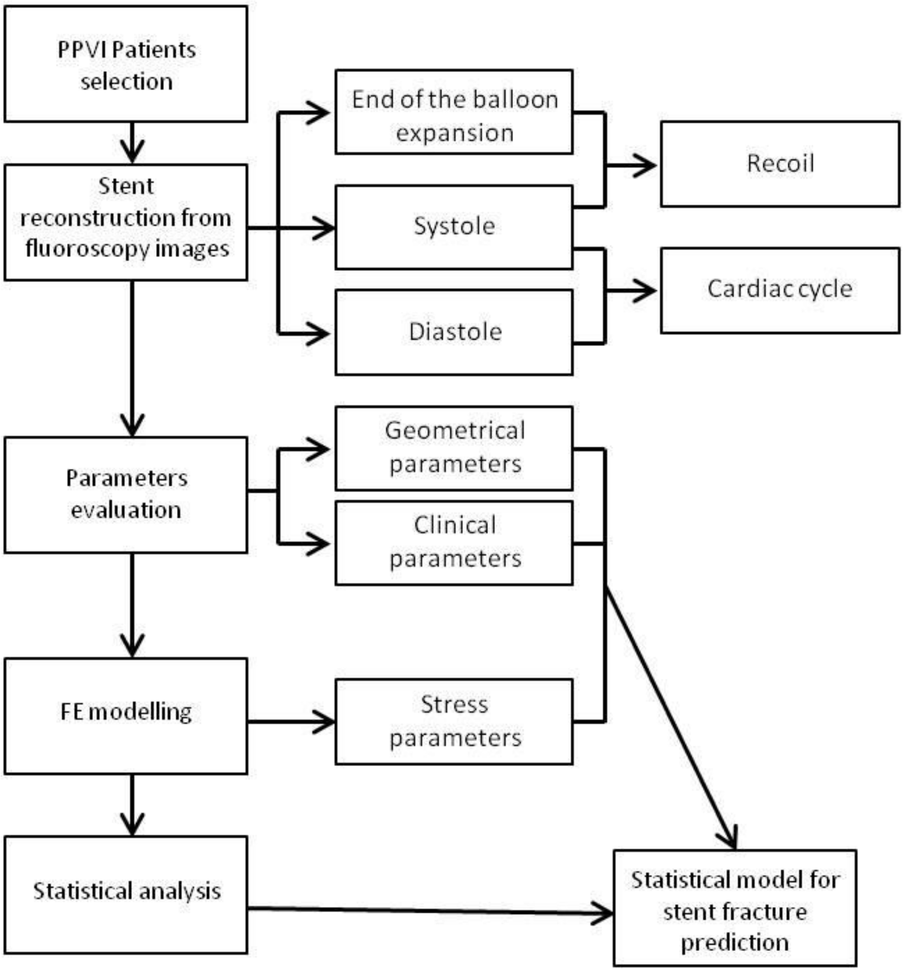

Part of the work presented in this chapter is currently under 2nd review with the Journal "Circulation: Cardiovascular Interventions".

5.1 INTRODUCTION

In the previous chapter, the biplanar fluoroscopy has been demonstrated to be an accurate tool for assessing in-vivo stent shape and shape variations during the cardiac cycle. In this chapter, such a tool will be used to analyse different geometries and deformations the PPVI device stent has to cope with in a patient population. Aim of this geometrical analysis, supported also by patient-specific FE simulations, was the individuation of those parameters responsible for stent fracture.

Indeed, despite careful patient selection and implantation of one or several bare metal stents to create a scaffold for PPVI, stent fracture remains a problem in the Melody™ device (Figure 5.1) and close clinical follow-up of the patients is required (**23**).

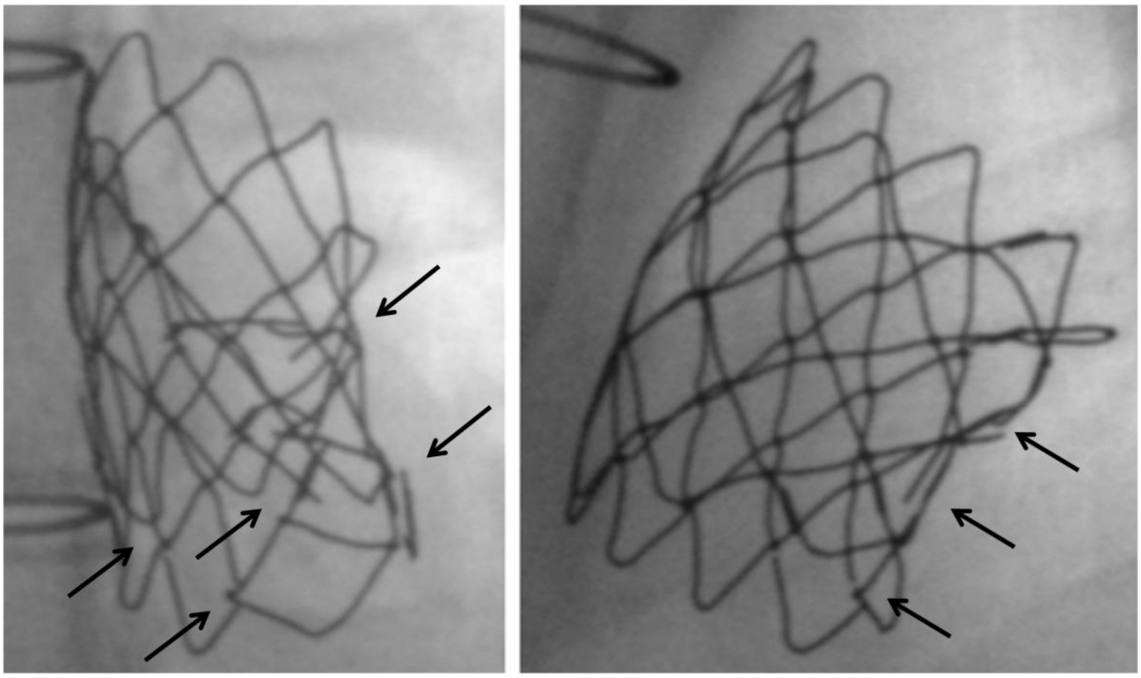

Figure 5.1 - Fluoroscopy AP and lateral projections of a Melody™ device implanted in a patient that underwent several strut fractures.

Fracture mechanics indicates two possible types of material fracture: a static fracture and a fatigue fracture. The former happens when the stress in the material exceed the ultimate tensile strength limit of the material; the latter occurs when a combination of mean and alternate stress exceeds the endurance strength limit of the material, caused by a cyclic solicitation. Fractured detected in the PPVI stent are included in the fatigue type, and the parameters influencing this adverse event can be traced back to the geometry of the stent after the implantation and to the geometry variations during the implantation phase and the cardiac cycle. Additional parameters that could be identified as potential factors for fracture, though they cannot easily assessed and quantified are:

- Asymmetry in the manual crimping before PPVI
- Initial asymmetry of the stent after the inflation of the inner balloon
- Number of balloon inflations duting PPVI
- Unexpected events after PPVI
- Bio-corrosion (even though, to my knowledge, in literature events of Melody™ stent fracture for bio-corrosion have not been reported).

Studies by Nordmeyer and McElhinney (**20**; **102**) used 2D images from procedural and follow-up angiograms and x-rays to identify risk factors associated with stent fracture, which include: PPVI in a native RVOT and/or in a non-calcified RVOT; the presence of PPVI recoil during balloon deflation; high ratio between AP and lateral PPVI diameter, at the proximal level of the stent; severe RVOT obstruction; younger age; elevated pre- and post-procedural RVOT gradient; reduced conduit diameter; smaller ratio of the measured/original conduit diameter; dynamic compression of the deployed valve and substantial apposition to the chest wall. These data indicate that mechanical factors related to the implant environment appear to play an important role in the stent fracture during and after device deployment.

The extreme morphological variability of PPVI implantation sites (**123**) often results in asymmetrical expansion of the Melody™ device (**79**), and combined with the complex 3D deformations experienced by the stent during both deployment and cardiac cycle, form the basis of stent mechanical failure. Therefore, a thorough analysis of these parameters may facilitate prediction of stent fracture with greater accuracy and precision.

In this study, the in-situ stent geometry and shape changes of the Melody™ during implantation and the subsequent cardiac cycle were analysed using the fluoroscopy methodology described and validated in the previous chapter. This data were also used to enhance the patient-specific modelling of PPVI loading conditions as a 3D patient-specific FE analysis was performed for each patient, simulating device deployment and cyclical deformations during the cardiac cycle to identify parameters associated with stent fracture. Combining geometric information derived from in-situ stent reconstructions, and patient-specific FE modelling of the patient's stent deformation, a risk stratification for stent fracture prediction was performed.

5.2 METHODS

5.2.1 Patients' selection

PPVI patients treated in our Centre were retrospectively selected for this study (n=42, Table 5.2) if the fluoroscopy images acquired during the PPVI procedure were in AP and lateral projections and available throughout the stent implantation phases from end of balloon inflation to at least one full cardiac cycle.

Two groups of patients were identified: the first (n=10) experienced fractures in the 1st year following successful PPVI; the second (n=32) had no adverse events in the same timeframe.

Stent fractures and their location were detected and assessed using routine x-ray images acquired post-PPVI. In our Centre, PPVI patients are routinely followed-up at 1 and 6 months after the implantation, and if no problems are detected, at 1 year and on a yearly basis thereafter.

5.2.2 Reconstruction from fluoroscopy data

The orthogonal biplane fluoroscopy images of the device acquired during the procedure were post-processed to reconstruct the in-situ 3D stent geometry for every patient as described in Section 4.2.1.3 (Figure 5.2a).

Calibration of the fluoroscopy images was achieved by identifying the straightest strut of the stent in both projections and by scaling the images so that the reconstructed length (Figure 5.3a and Figure 5.3b) of this strut (L_{rec}) was equal to the real length (L_{undef}=5.78 mm) of the undeformed stent struts. In 16 patients who underwent PPVI stent post-dilatation, calibration was also further assessed using the markers of the Mullins balloon (NuMed Inc, Hopkinton, NY, US).

Using this methodology, the in-situ stent configuration was reconstructed for each patient at three instants including the end of the final balloon inflation (hereafter referred to as pre-recoil), early systole and diastole (Figure 5.2b). The pre-recoil was selected from the fluoroscopy images in the frame at the beginning of balloon deflation, while the systolic and the diastolic frames were identified according to the ECG tracing synchronised with the fluoroscopy acquisitions.

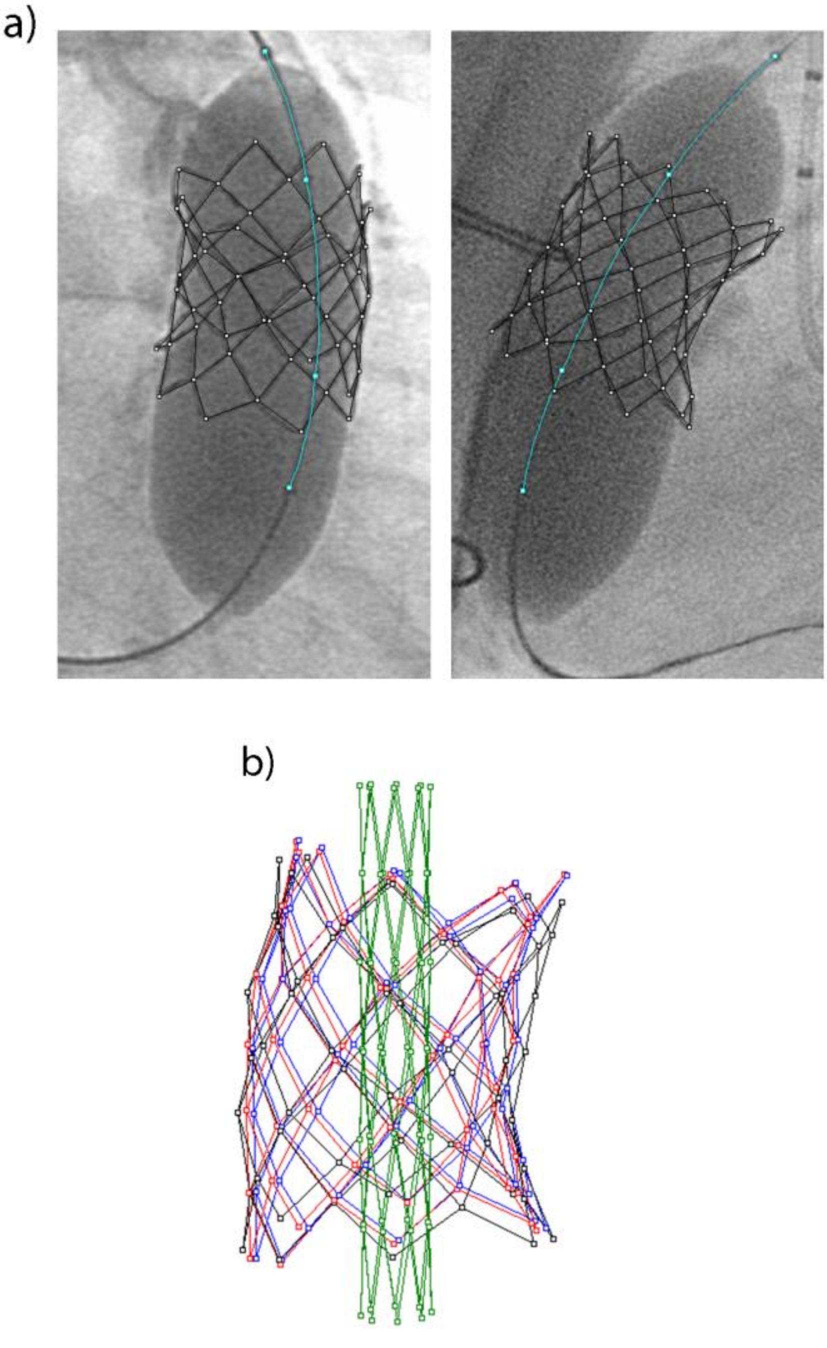

Figure 5.2 - a) Stent 3D reconstruction using orthogonal biplane fluoroscopy images for one patient at the end of balloon expansion: AP and lateral projections. The markers of the post-PPVI dilatation balloon are reconstructed in light-blue. b) 3D Stent geometry reconstructed from fluoroscopy images at the end of balloon expansion (black), systole (red) and diastole (blue) superimposed with the stent at its initial crimped configuration (green).

For this patient population, the systolic and diastolic frames corresponded to the instants of maximum and minimum diameters during the cardiac cycle. The recoil process between the end of balloon inflation and end of balloon deflation includes not only the intrinsic elastic recoil of the metal stent, but also the recoil related to the arterial wall and surrounding tissues.

5.2.3 Geometrical parameters

3D stent shape and geometrical variations after balloon deflation and during the cardiac cycle were compared between fractured and non-fractured patient groups.

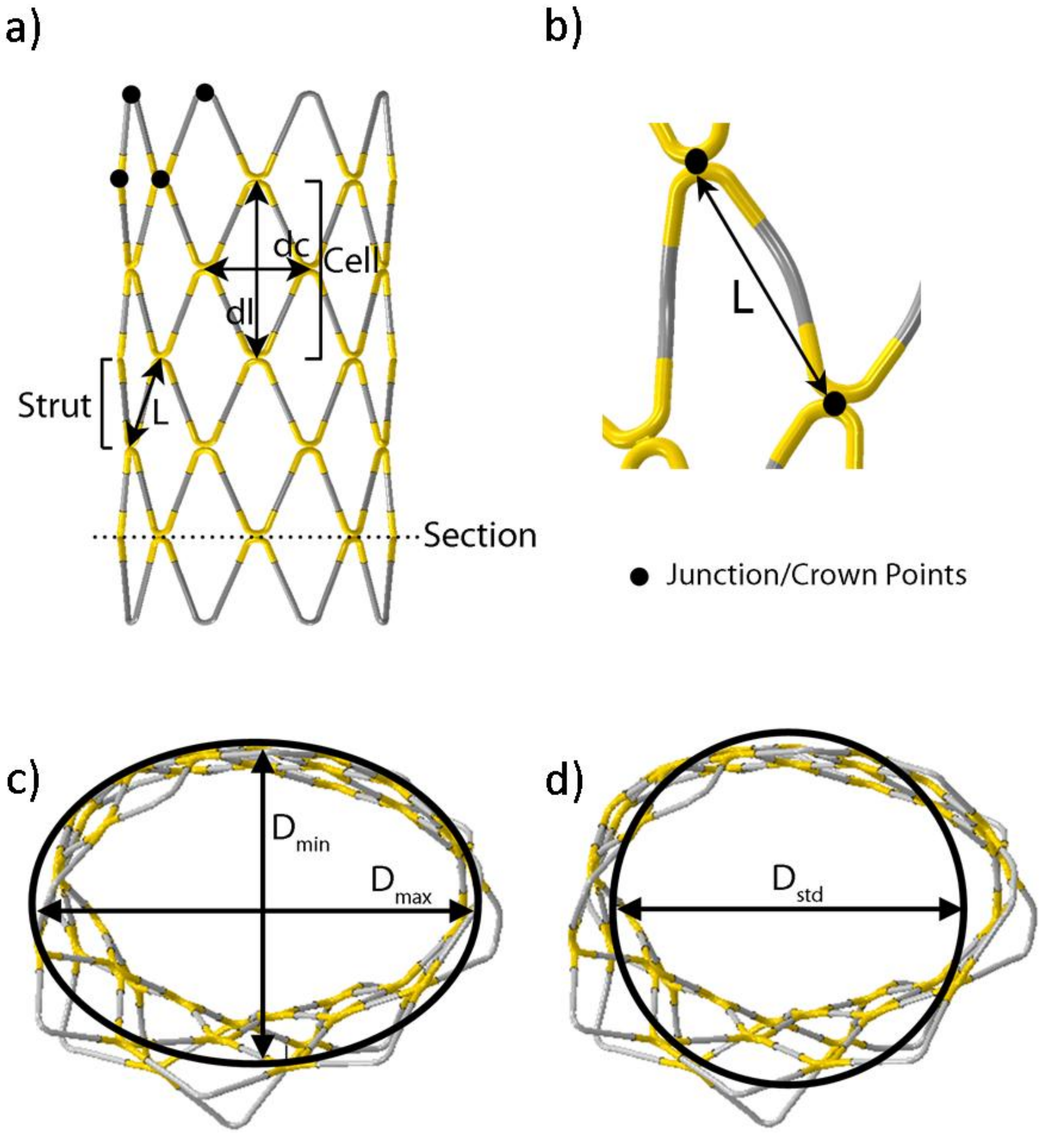

Figure 5.3 - Stent levels and parameters identified for the 3D geometrical analysis: strut length (L), cell longitudinal (dl) and circumferential (dc) diagonals, maximum (Dmax), minimum (Dmin) and standard diameter (Dstd).

Four levels were identified in the stent geometry (strut, cell, section and stent level), and a total of 22 parameters belonging to these different levels were considered per stent (Figure 5.3a):

- Strut level (96 struts per stent):
    - Strut length, L = distance between two junction points belonging to the same strut (Figure 5.3a and Figure 5.3b)
- Cell level (40 cells per stent):
    - Circumferential asymmetry ratio, C_a = ratio between cell longitudinal, dl, and circumferential, dc, diagonals (Figure 5.3a)
    - Circumferential asymmetry absolute difference, C_a* = difference between dl and dc (Figure 5.3a)
- Section level (7 sections per stent):
    - Maximum section diameter, D_{max} (Figure 5.3b)
    - Minimum section diameter, D_{min} (Figure 5.3b)
    - Standard diameter, D_{std} = diameter of the section if considered a circle with same section perimeter (Figure 5.3c)
    - Radial asymmetry ratio, R_a = ratio between D_{max} and D_{min}
    - Radial asymmetry absolute difference, R_a* = difference between D_{max} and D_{min}
- Stent level (1 per stent):
    - Longitudinal asymmetry ratio, L_a = ratio between maximum and minimum section D_{std}
    - Longitudinal asymmetry absolute difference, L_a* = difference between maximum and minimum section D_{std}
    - Maximum, minimum, average R_a
    - Maximum, minimum, average R_a*

- Maximum, minimum, average C_a
- Maximum, minimum, average C_a*

All parameters were measured for each of the 3 reconstructed stent geometries per patient (pre-recoil, systole, diastole). Moreover, percentage variations of such parameters during balloon deflation as $100\frac{\text{pre}-\text{recoil}-\text{systole}}{\text{pre}-\text{recoil}}$ and during cardiac cycle as $100\frac{\text{systole}-\text{diastole}}{\text{systole}}$were calculated – named in the text as Δ“parameter”.

5.2.4 Clinical and Radiographic parameters

The following parameters, which have previously been associated with the risk of fracture were recorded: valve compression, apposition to chest wall, dynamic compression, site calcification, PPVI recoil, pre-stenting, implant indication (stenosis, regurgitation or both), gender and age.

5.2.5 Finite element modelling

The stent geometries reconstructed from the fluoroscopy images were used to implement a patient-specific PPVI FE model for each case. The reconstructed stents from the 3 instants (pre-recoil, systole, diastole) were superimposed to the stent geometry in its initial configuration, while still crimped onto the balloon catheter (Figure 5.2b) using a partial Procrustes analysis. This allowed us to measure the displacements of every junction point from its initial position to the pre-recoil state, and to systole and diastole reducing stent rigid displacements due to heart beating and respiration motions. Such displacements were used as boundary conditions to computationally deploy the FE model of the PPVI stent. The stent geometry for FE analysis was reproduced in the initial crimped status of the device into the catheter (Figure 5.7d). The presence of the biological valve sewn inside the stent was not taken into account in this study, as it is unlikely that it affect stent fracture. The geometry of the stent was drawn from a previous study by Schievano and co-workers (**79**; **120**), who obtained the measurements by means of calliper and optic microscope measurements. Geometrical and material properties are listed in Table 5.1. Six wires of 0.33 mm in diameter were joined together through central parallelepiped links of 0.31 x 1.67 x 0.08

mm in correspondence of every central crown weld. The golden coverings were reproduced by means of an additional layer of elements of 0.025 mm of thickness around the crown weldings. The platinum-iridium alloy was assumed to have isotropic properties, and a Von Mises plasticity model was adopted, along with an isotropic hardening law. Handbook properties were selected to define the mechanical behaviour of the golden reinforcements.

Table 5.1 - Stent geometrical and material properties.

Wire diameter	0.33 mm
Initial internal diameter	4.0 mm
Initial overall length	34.32 mm
Central zigzags segment length	5.78 mm
Terminal zigzags segment length	5.62 mm
Gold sleeve thickness	0.025 mm
PLATINUM (**120**)	
Young modulus	224 GPa
Poisson ratio	0.37
Yield stress	285 MPa
Ultimate strength, S_{ult}	875 MPa
Fatigue endurance strength, S_e	263 MPa
GOLD	
Young modulus	80 GPa
Poisson ratio	0.42

5.2.5.1 Mesh sensitivity analysis

A mesh sensitivity analysis was performed on a circular cantilever beam, with the same diameter as the stent wires (0.33 mm) and with the same length as an internal strut of the stent (5.78 mm).

Seven different structured hexahedral meshes were created, with 6x4, 6x6, 8x8, 8x10, 10x10, 12x12 and 16x16 elements on the sections respectively (Figure 5.4).

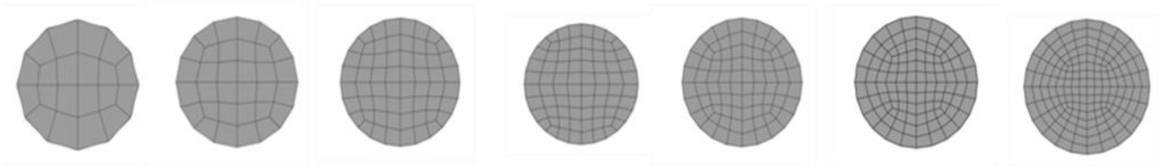

6x4 6x6 8x8 8x10 10x10 12x12 16x16

Figure 5.4 - Meshes used for the sensitivity analysis: elements on the section of the beam.

The cantilever beam was constrained at one side, fixing the translational and rotational degrees of freedom (Figure 5.5). A concentrated force of 0.16 N, to remain in the material elastic field, and directed as the *z*-axis was applied to the central node of the beam section on the opposite side. The same simulation was performed for every mesh, using solid elements with 8 points of integration (C3D8) and solid reduced elements, with only 1 point of integration (C3D8R).

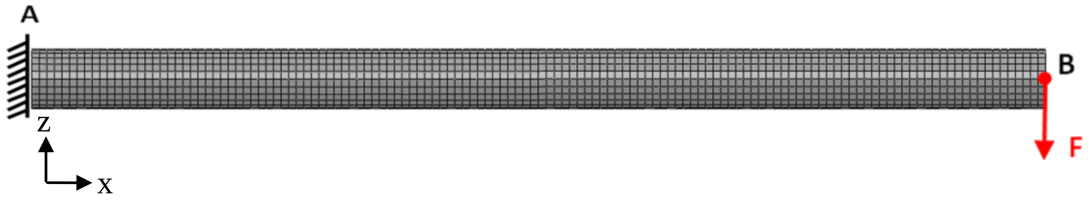

Figure 5.5 - Cantilever beam FE model, constrained at the left side (A), and with a force F applied on B, at the central node of the free section.

The results, obtained in terms of stress and displacement, were compared with the analytic solution, where a force of 0.16 N corresponded to a displacement of 0.08 mm and a stress of 264.98 MPa.

To analyse the behaviour of the beam in the material plastic field, an additional set of simulation was performed with the same meshes as described before and applying a higher concentrated force of 0.5 N. In this case, the results of the simulations were compared with the displacements and stresses obtained from the simulation with the finest mesh of C3D8 and C3D8R respectively.

After mesh sensitivity analysis on the beam, 2 different structured hexahedral meshes were used for a mesh sensitivity analysis on the whole stent FE model: a coarser mesh with 155,680 elements, and a finer mesh of 792,640 elements. The former used 6x4 elements on the section (for a total of 20 elements), the latter used 8x8 elements (for a total of 60 elements). As for the longitudinal development of the mesh, the former used 10 elements to cover 1 mm, the latter used 19 elements on 1 mm (Figure 5.6).

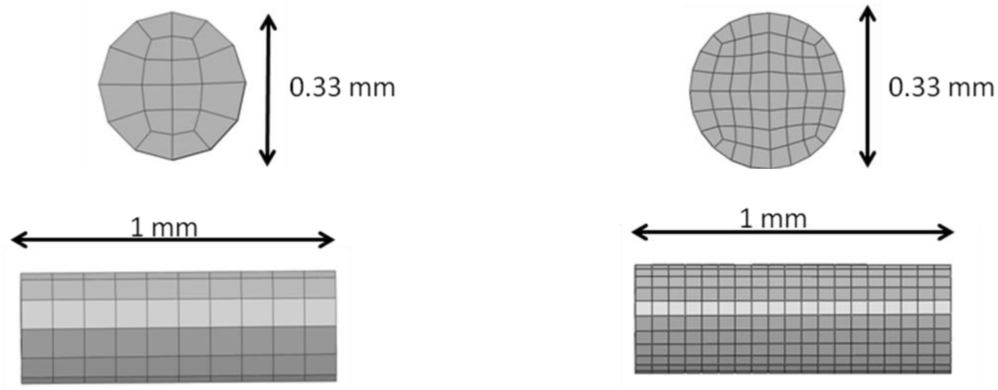

Figure 5.6 - Comparison between the 2 meshes: details of the coarser mesh on the left, and of the finer mesh on the right.

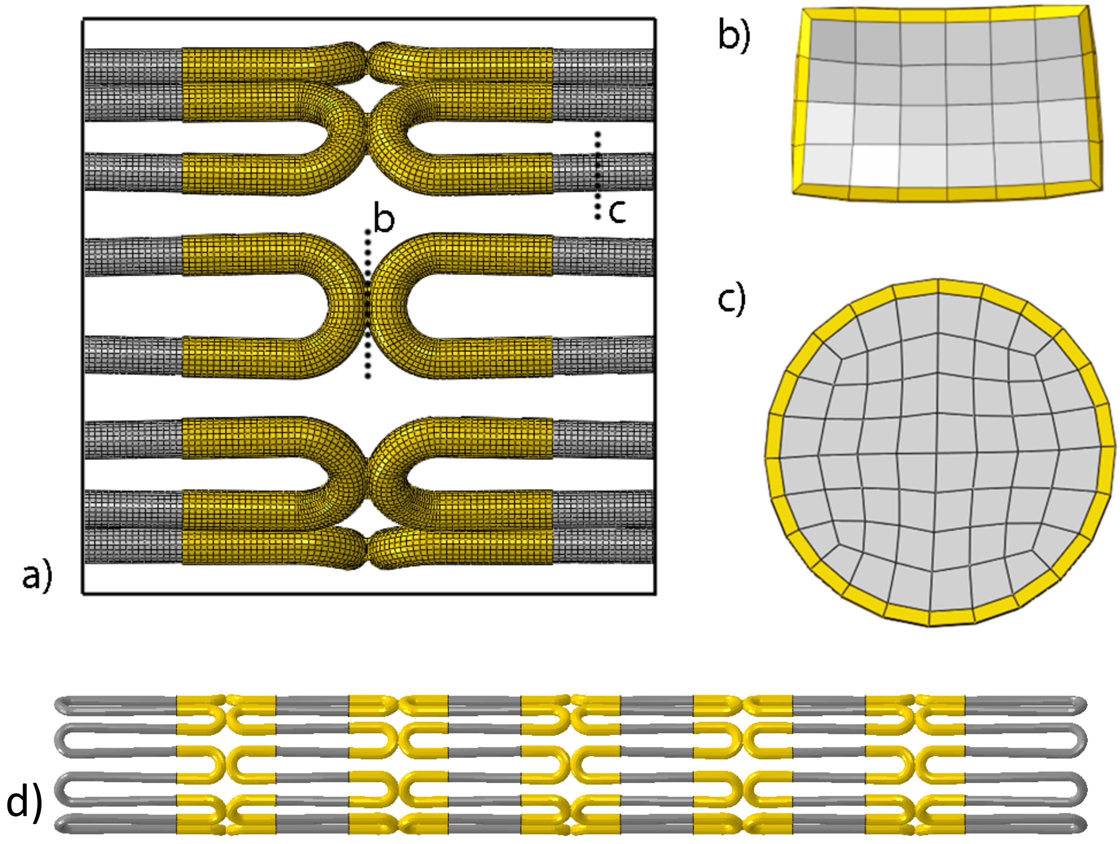

Figure 5.7 - FE model of the Melody™ device (d): details of the finest structured hexahedral mesh (a), and mesh features at the welding links (b) and at the wire section (c).

A symmetric initial stress condition formerly calculated was assigned to the stent model to account for residual stresses caused by the loading of the stent onto the catheter balloon in the catheterisation laboratory.

5.2.5.2 FE stent deployment

To replicate the patient-specific stent deployment with FE analysis proved challenging and several approaches were explored. Firstly, Abaqus Explicit was used to run a quasi-static simulation to deploy the stent by means of a contact algorithm between the stent surface and some cuff structures created around the stent strut junctions and displayed in green in Figure 5.8. The displacements measured from the device 3D reconstructions at different times of the procedure and cardiac cycle were imposed to the cuffs.

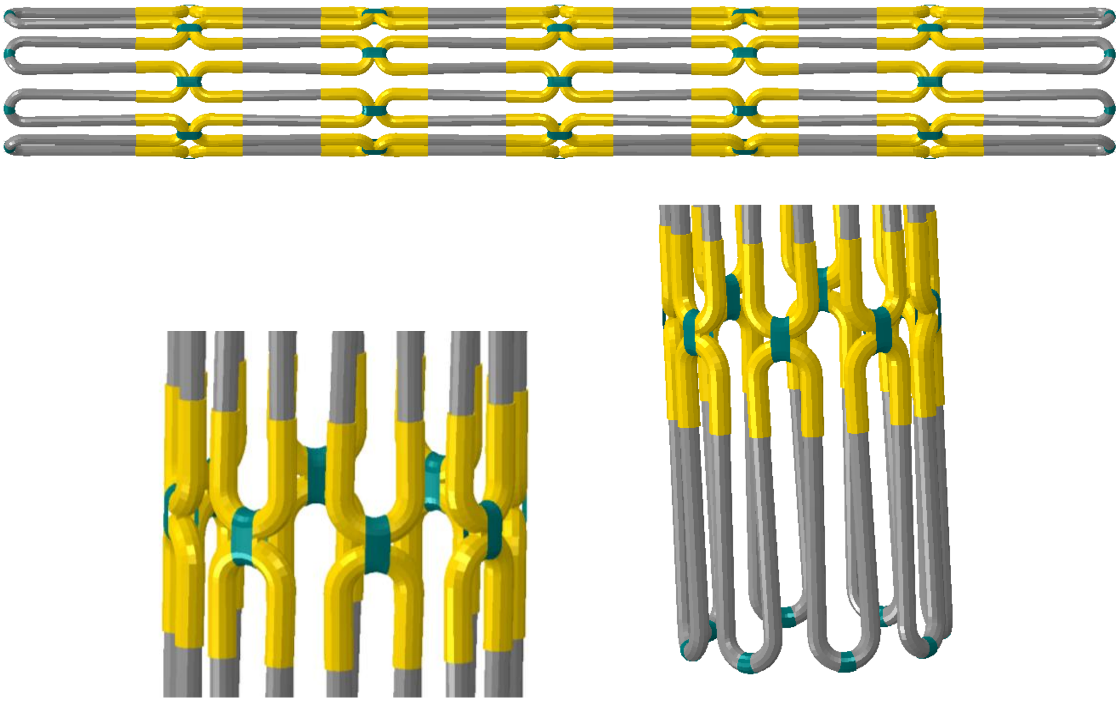

Figure 5.8- FE model of the stent computationally expanded through cuffs (in green) created around the strut junctions.

Plastic, internal and kinetic energy outputs were monitored for these simulations to verify the quasi-static hypothesis: kinetic energy was close to zero and kinetic to internal energy ratio intersected plastic to internal energy ratio below 5%.

Secondly, a load control simulation (Abaqus/Explicit) was used to expand the stent inside a model reproducing the patient's RVOT anatomy (Figure 5.9). This was recreated by connecting the struts of the stent shape, reconstructed from the fluoroscopic images, with a polysurface, and by meshing it with surface elements. Surface elements have no inherent stiffness and can be used to model rigid bodies; they do not enter in the stress calculations, thus requiring less computational time. The RVOT model resulted in a rough-edged structure that could accommodate the stent struts. A contact algorithm was applied between the stent outer surface and the RVOT internal surface, and a loading pressure was applied to the internal surface of the stent for deployment. Slot Abaqus connector elements were added to the model to virtually link every strut junction with their final point on the RVOT surface, thus guiding them through the correct displacement as calculated from the 3D reconstructions.

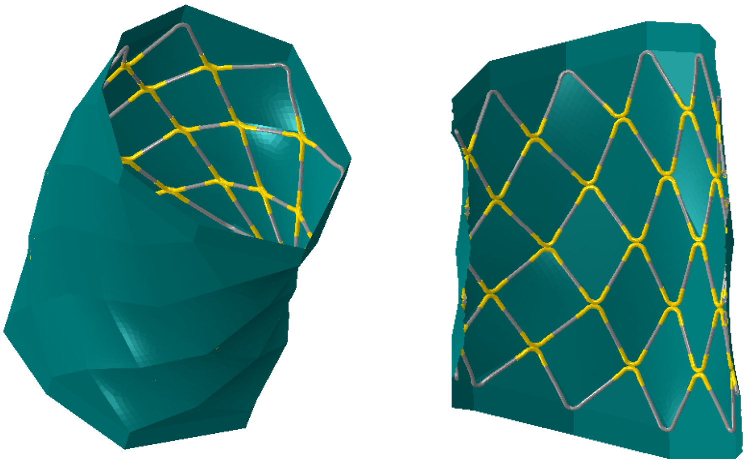

Figure 5.9 - FE model of the stent computationally expanded inside a rough-edged rigid RVOT model, using connector elements.

Thirdly, a shell part as offset from the outer surface elements of the stent model was created and a contact algorithm between the shell and the outer surface of the stent was set up to deploy the stent by applying nodal displacements to the shell (Figure 5.10). This was first tested on a single crown of the stent. The shell was created with an offset of 0.02 mm and with the same material parameters used for the platinum-10% iridium alloy. General contact was imposed between the inner surface of the shell and the outer surface of the stent from the beginning of the simulation, and a Standard method was used. The same idea was then applied to the entire stent.

Figure 5.10 - Stent crown surrounded by a shell, created as a 0.02 mm offset from the external elements of the stent crown.

Finally, nodal displacement boundary conditions were used in Abaqus/Standard to deploy the stent according to the calculated displacements (Figure 5.11). In particular, after a systematic study to select the optimal nodes for these boundary conditions, the displacements calculated from the fluoroscopy reconstruction superimpositions were applied to the central node of the wire sections, for the outer crowns, and of the welding links, for the internal crowns (Figure 5.7b, Figure 5.7c). The simulations included three steps for each patient. First, the stent was expanded from its initial crimped status to the final configuration at the end of balloon inflation. Then, displacements recorded during systole and diastole were replicated.

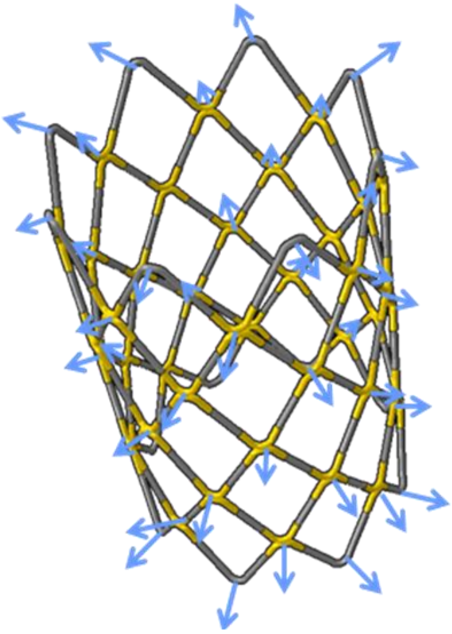

Figure 5.11 - FE model of the stent computationally expanded using nodal displacements boundary conditions.

5.2.6 Stress parameters

The following 13 parameters were analysed for each stent at 10 equally spaced increments during recoil (end of balloon inflation to end of balloon deflation) and during cardiac cycle (systole to diastole):

- Maximum principal stress: maximum, minimum and average values
- Minimum principal stress: maximum, minimum and average values
- Von Mises stress: maximum, minimum and average values
- Stress pressure (i.e. first invariant of stress tensor): maximum, minimum and average values
- Sines equivalent stress for the cardiac cycle step,

  $$\sigma_{sines} = \sqrt{3}\left(\sqrt{J_2}\right)_a + 3\frac{S_e}{S_{ult}}\sigma_{H,m}$$

  where $\left(\sqrt{J_2}\right)_a$ is the amplitude of the mean square root of the second deviatoric stress invariant and $\alpha_{H,m}$ is the hydrostatic pressure, while S_e and S_{ult} are the material strength limit parameters (endurance strength limit and ultimate strength limit respectively). This stress is compared in the Sines criterion with the endurance strength limit (S_e) to assess fatigue performance and the risk of material fracture.

5.2.7 Statistical analysis

The exact location of fractures was detected in the post-PPVI x-rays and attributed to the corresponding strut, cell, section and stent level for every specific patient. Using the binary fractured/ non-fractured outcomes as response variables, previously described clinical or radiographic parameters associated with fracture and the 22 geometrical parameters as explanatory variables, multivariate binary logistic regression analysis was used to estimate their single and combined predictive values for stent fracture. A 95% confidence interval (CI) was considered and a p-value of less than 0.05 was assumed significant. A second similar statistical analysis included the geometrical parameters, and the 13 stress parameters measured in the FE simulations. The likelihood ratio test was performed to gauge the contribution of individual predictors to the resulting models, and the Nagelkerke's R^2 was calculated to assess the appropriateness of the models' fit. In this way the covariates modifying the risk of fracture were identified. The analysis was carried out in the commercial software IBM SPSS Statistics (IBM Corp., USA).

5.3 RESULTS

5.3.1 Reconstruction from fluoroscopy data and Geometrical Parameters

Patient data are summarised in Table 5.2. The in-situ 3D stent geometry from fluoroscopy images was reconstructed for all 42 patients (Figure 5.12) at the 3 time points.

Full elaboration of each set of biplane images took approximately 4 hours. Fractures were not detected immediately after the procedure. Subsequent fractures and their locations are summarised in Table 5.3.

For every patient, at least one strut was selected for calibration purposes, and for those patients where a post-dilatation balloon was used, the maximum difference between the two calibration methods (strut-based and marker-based) was 4.6%. The geometrical parameter results are reported in Table 5.4.

Table 5.2 - Patients' data (average [min, max]) for the fractured and non-fractured group.

	Fractured (n=10)	Non-fractured (n=32)
Age at implant [years]	14 [10, 23]	19[7, 71]
Gender [F/M]	4/6	11/21
BSA [m^2]	1.48 [1.14, 1.90]	1.64 [0.90, 2.20]
Weight [kg]	49.3 [32.9, 70.0]	58.2 [19.1, 106.0]
Pre-stent	4 (40%)	16 (50%)

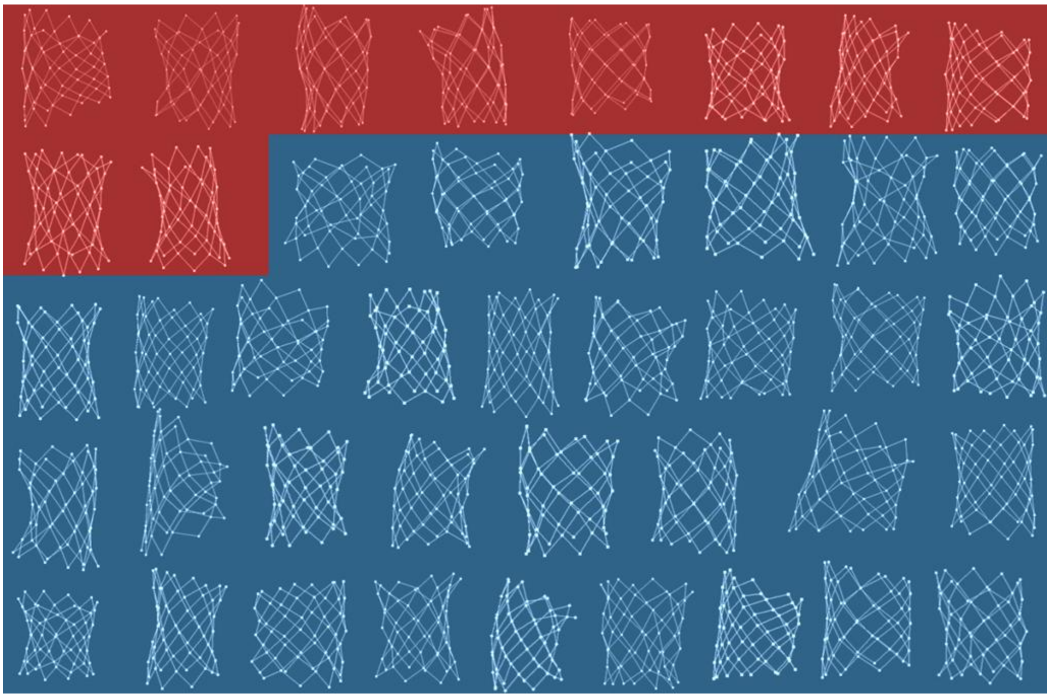

Figure 5.12 - In-situ 3D stent geometry reconstructions of the 42 patients at systole. The red background denotes the stents that underwent fracture, while the blue background is applied to the stents not experiencing fracture in the first year after the implantation.

Table 5.3 - Number of fractured struts at 1, 6, 9 and 12 month (m) follow-up x-ray examination, fracture type and RVOT gradient immediately after PPVI and at 12m follow-up for each patient.

Patient	1m	6m	9m	12m	Fracture type at 1 year**	Fracture progression	Gradient immediately after PPVI	Gradient at 1 year follow-up
1	0	3	NA	8	II	NA	25	NA*
2	0	2	2	2	I	NA	10	21
3	NA	NA	NA	5	II	NA	36	22
4	0	0	0	1	I	NA	19	37
5	0	1	1	1	I	NA	36	25
6	NA	NA	NA	2	I	2 (2 years)	46	57
7	NA	NA	4	NA	I	11 (2 years)	41	43 (2 years)
8	NA	NA	NA	1	I	4 (3 years)	29	29
9	1	1	1	1	I	NA	31	57
10	0	0	NA	1	I	3 (3 years)	22	29

NA- not available

*Difficult imaging window: homograft and PA not well seen

Fracture type classification as in **20

Table 5.4 - Geometrical parameter results (average [min,max]).

	Fractured			Non-fractured		
	Pre-recoil	*Systole*	*Diastole*	*Pre-recoil*	*Systole*	*Diastole*
L [mm]	5.52 [4.89,6.10]	5.52 [4.91,6.06]	5.51 [4.98,6.03]	5.48 [4.42,6.06]	5.50 [4.36,6.12]	5.49 [4.39,6.12]
C_a [-]	1.16 [0.46,3.31]	1.26 [0.55,4.24]	1.26 [0.55,3.85]	1.21 [0.35,3.83]	1.29 [0.37,4.12]	1.29 [0.37,3.99]
C_a^* [mm]	0.72 [-5.43,6.89]	1.19 [-4.14,7.61]	1.16 [-4.39,7.66]	0.97 [-6.17,7.54]	1.39 [-6.25,8.47]	1.44 [-6.39,15.22]
D_{max} [mm]	20.00 [15.61,24.05]	19.93 [14.78,24.77]	19.94 [14.88,24.73]	19.46 [14.43,24.39]	19.19 [13.89,23.90]	19.22 [14.38,24.15]
D_{min} [mm]	18.40 [14.09,22.61]	16.87 [11.87,22.36]	16.68 [11.83,22.32]	17.97 [11.91,22.16]	17.11 [12.24,21.95]	17.04 [12.19,22.17]
D_{std} [mm]	18.98 [14.87,22.40]	18.27 [13.54,22.06]	18.27 [13.40,21.92]	18.50 [13.79,22.45]	17.99 [13.79,22.27]	17.98 [13.67,22.24]
R_a [-]	1.09 [1.02,1.32]	1.20 [1.01,1.88]	1.20 [1.01,1.89]	1.09 [1.01,1.26]	1.13 [1.01,1.54]	1.13 [1.01,1.60]
R_a^* [mm]	1.60 [0.34,5.12]	3.06 [0.18,10.62]	3.08 [0.21,10.73]	1.49 [0.15,4.23]	2.08 [0.19,7.23]	2.18 [0.16,7.73]
L_a [-]	1.19 [1.06,1.38]	1.21 [1.07,1.38]	1.21 [1.06,1.39]	1.21 [1.05,1.35]	1.24 [1.04,1.42]	1.23 [1.04,1.42]
L_a^* [mm]	3.17 [1.16,6.11]	3.29 [1.31,5.87]	3.27 [1.16,5.94]	3.46 [1.00,5.38]	3.71 [0.77,6.13]	3.68 [0.77,6.14]
Max R_a [-]	1.14 [1.04,1.32]	1.32 [1.05,1.88]	1.32 [1.04,1.89]	1.15 [1.06,1.26]	1.20 [1.03,1.54]	1.21 [1.06,1.60]
Min R_a [-]	1.05 [1.02,1.13]	1.09 [1.01,1.29]	1.09 [1.01,1.25]	1.04 [1.01,1.11]	1.07 [1.01,1.28]	1.07 [1.01,1.25]
Aver R_a [-]	1.09 [1.03,1.23]	1.20 [1.03,1.57]	1.20 [1.03,1.58]	1.09 [1.03,1.17]	1.13 [1.02,1.34]	1.13 [1.03,1.37]
Max R_a^* [mm]	2.33 [0.84,5.12]	4.60 [1.10,10.62]	4.62 [0.81,10.73]	2.45 [0.94,4.23]	3.05 [0.53,7.23]	3.21 [0.93,7.73]
Min R_a^* [mm]	0.86 [0.34,2.51]	1.56 [0.18,4.86]	1.61 [0.21,4.34]	0.80 [0.15,2.03]	1.26 [0.19,4.42]	1.27 [0.16,4.54]
Aver R_a^* [mm]	1.60 [0.63,3.93]	3.06 [0.57,7.91]	3.08 [0.53,8.00]	1.49 [0.58,2.97]	2.08 [0.41,5.28]	2.18 [0.55,5.58]
Max C_a [-]	2.12 [1.31,3.31]	2.40 [1.34,4.24]	2.42 [1.37,3.85]	2.08 [1.35,3.83]	2.28 [1.45,4.12]	2.30 [1.46,3.99]
Min C_a [-]	0.65 [0.46,0.83]	0.70 [0.57,0.87]	0.70 [0.55,0.88]	0.66 [0.35,0.99]	0.70 [0.37,1.15]	0.70 [0.37,1.11]
Aver C_a [-]	1.16 [0.91,1.47]	1.26 [1.01,1.59]	1.26 [0.99,1.58]	1.21 [0.89,1.76]	1.29 [0.92,1.81]	1.29 [0.94,1.81]
Max C_a^* [mm]	4.72 [2.04,6.89]	5.21 [2.16,7.61]	5.23 [2.33,7.66]	4.64 [2.29,7.54]	5.15 [2.93,8.47]	5.57 [3.01,15.22]
Min C_a^* [mm]	-3.09 [-5.43,-0.95]	-2.69 [-4.14,-1.08]	-2.70 [-4.39,-0.99]	-3.12 [-6.17,-0.08]	-2.77 [-6.25,1.06]	-2.89 [-6.39,0.80]
Aver C_a^* [mm]	0.73 [-0.84,2.22]	1.19 [-0.10,2.58]	1.16 [-0.24,2.57]	0.96 [-1.25,2.56]	1.39 [-1.00,3.16]	1.44 [-0.88,3.11]

5.3.2 Finite element analysis

5.3.2.1 Mesh sensitivity analysis

The results of the mesh sensitivity analysis performed on the circular cantilever beam are reported in Figure 5.13 and Figure 5.14, the former referring to the elastic field, the latter to the plastic field of the material constitutive behaviour as percentage of difference in stress and displacement with the analytical solution for the elastic field, and with the finest mesh for the plastic field.

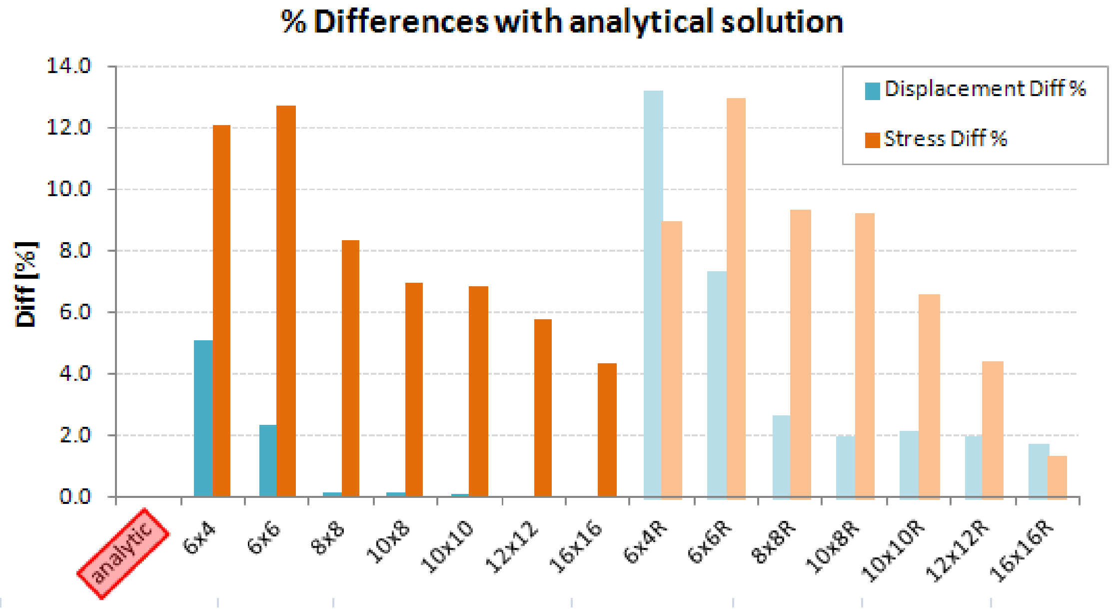

Figure 5.13 - Mesh sensitivity analysis for a cantilever beam in the elastic field: percentage differences in displacement (orange) and stress (blue) between different mesh with the analytic solution. R stands for reduced elements.

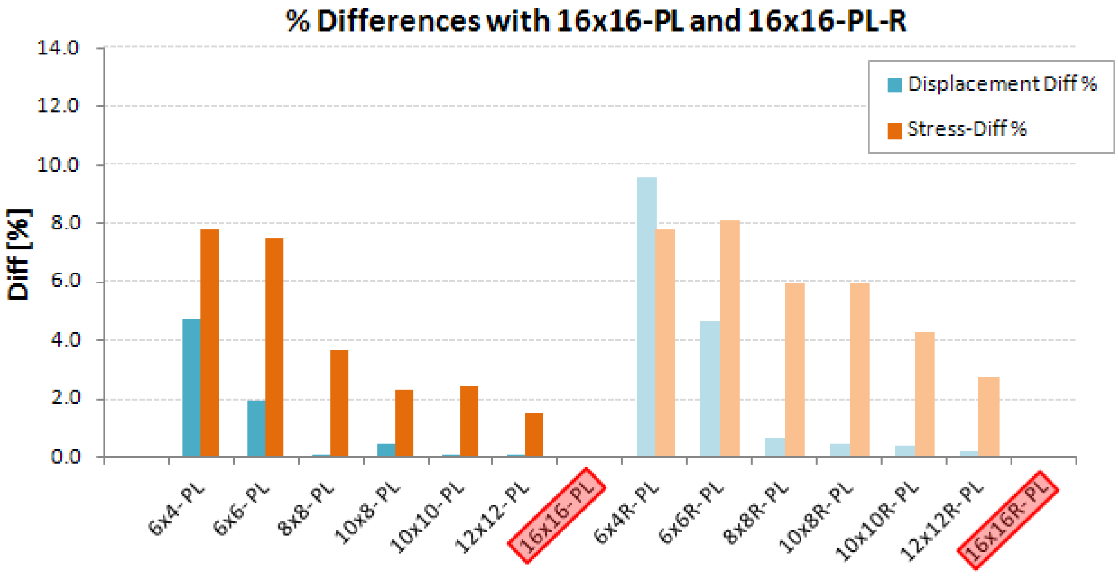

Figure 5.14 - Mesh sensitivity analysis for a cantilever beam in the plastic field: percentage differences in displacement (orange) and stress (blue) between different mesh with the solution from the finest mesh (16x16- PL and 16x16R- PL) . R stands for reduced elements.

In both cases the differences decreased with the increase in the number of elements used to create the mesh of the section. In the elastic field, the largest difference in displacement is obtained with the 6x4 reduced mesh (13.2%), while in terms of stresses is obtained with the 6x6 mesh (13.0%). In the plastic field, the largest difference in displacement is 9.6%, obtained with the 6x4 reduced mesh, while the largest difference in stress is 8.1%, achieved with the 6x6 reduced mesh. In both elastic and plastic fields, the mesh 8x8R presents differences lower than 10% in terms of stress, and 3% in terms of displacement. As the number of elements to mesh the stent geometry with 8x8 elements on the section was 792,640, this mesh type was considered the best compromise between accuracy and computational time, and was therefore chosen to mesh the entire stent.

The additional simulation on the stent entire model comparing a 6x4R mesh and 8x8R mesh showed that the finest mesh produced a stress distribution more uniform than that with the coarsest mesh (Figure 5.15), with also a more uniform deformed stent shape (Figure 5.16).

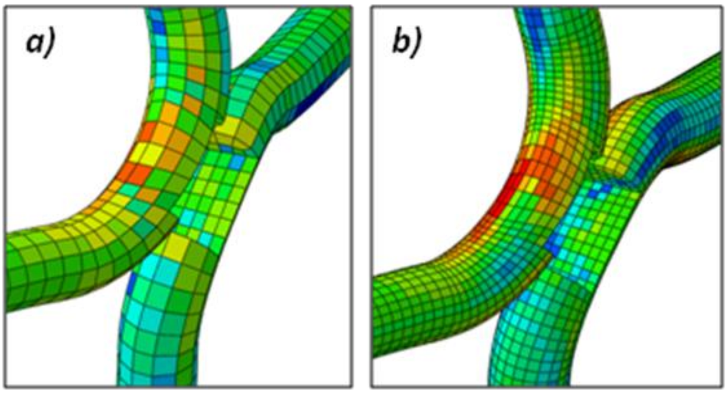

Figure 5.15 - Comparison in the Von Mises stress distribution between the coarsest mesh (a) and the finest mesh (b).

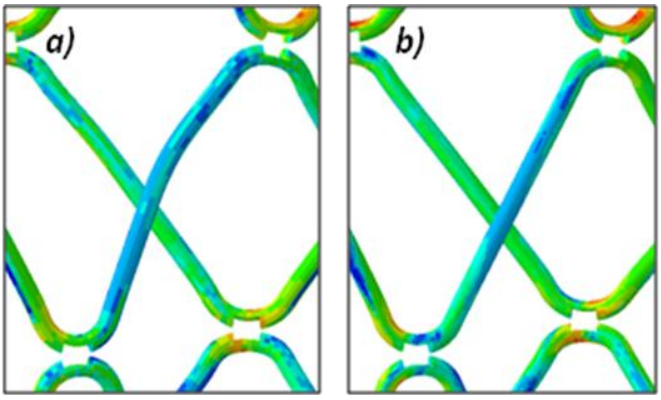

Figure 5.16 - Comparison between the coarsest mesh (a) and the finest mesh (b) in terms of deformed shape.

5.3.2.2 FE stent deployment

The first method tested to deploy the stent according to the patient-specific 3D reconstructions from fluoroscopy images, using cuff structures, resulted in correct final deployment of the stent, but element distortions were present next to the cuffs.

The RVOT surface coupled with a pressure applied to the internal surface of the stent was not a strict enough condition to guarantee the correct deployment of the stent. The addition of the slot connector elements proved to be a good solution to achieve the final patient-specific geometry of the stent, but the elements surrounding the nodes to which the connectors were linked results distorted, thus affecting the stress distribution.

The use of a shell surrounding the stent structure to impose the displacements to the stent was successful in the single crown analysis. However, a problem presented when trying to create a continuous shell around the complex geometry of the full stent with the golden covering and links connecting each crowns.

The displacements applied directly to the nodes of the stent also caused some distortion of the elements surrounding the point of displacement boundary condition. However, this method proved faster, less computationally demanding and without introduction of further simplified hypothesis related to time and energy as in the explicit analysis. Therefore, this was the method selected to expand the patient-specific stents where, to overcome the distortion problem, the set of elements around the displacement nodes were subtracted from the model in the post-processing of the stress results. Fractures at the welding junctions have not been reported for the PPVI stent after the golden reinforcements were introduced; therefore this subtraction was considered acceptable.

The stress parameter results are reported in Table 5.5. The maximum values of the Von Mises and maximum principal stresses were located for every patient in different struts, but always close to the strut junctions, where bending concentrated (Figure 5.17), and always during the cardiac cycle. The minimum value of the minimum principal stress (negative stress) occurred close to the strut junctions, usually where the maximum Von Mises stress was registered. The minimum Von Mises stresses were usually seen in the straight segments (Figure 5.17).

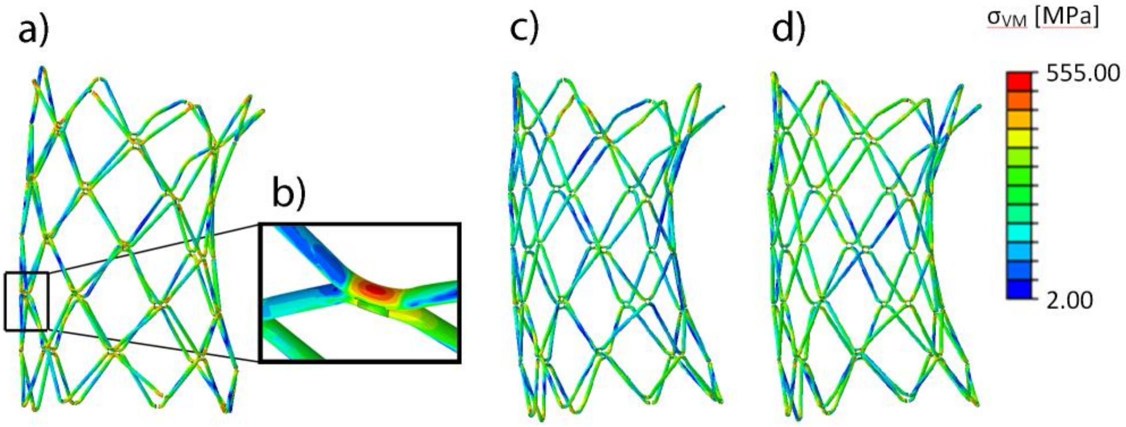

Figure 5.17 - Von Mises stress (σ_{VM}) distribution at the end of the balloon expansion (a), systole (c) and diastole (d) for one patient. Zoom in correspondence of the strut intersection opening to show the elements with highest stress (b).

Table 5.5 - Stress parameter results (average [min,max]).

	Fractured		Non-fractured	
[MPa]	*Recoil*	*Cardiac cycle*	*Recoil*	*Cardiac cycle*
Max Prin Stress, max	607.49 [572.06,655.23]	661.69 [620.77,743.70]	599.03 [548.29,658.22]	636.00 [565.75,769.37]
Max Prin Stress, min	-166.94 [-226.33,-109.74]	-235.92 [-315.25,-163.17]	-143.01 [-189.16,-104.57]	-249.88 [-420.38,-137.09]
Max Prin Stress, aver	113.38 [105.31,119.05]	85.15 [76.20,98.71]	114.93 [110.00,119.39]	85.13 [74.28,110.51]
Min Prin Stress, max	202.37 [139.79,284.64]	206.87 [141.11,345.59]	169.29 [110.99,361.77]	197.65 [120.79, 344.66]
Min Prin Stress, min	-594.88 [-667.39,-495.54]	-664.78 [-723.45,-615.60]	-553.49 [-625.05,-475.40]	-663.71 [-878.97,-571.78]
Min Prin Stress, aver	-90.89 [-94.85,-83.87]	-86.23 [-98.73,-75.35]	-92.19 [-102.83,-88.66]	-85.33 [-111.54,-76.52]
Von Mises Stress, max	580.86 [556.15,615.62]	599.11 [549.45,666.85]	576.48 [531.24,638.52]	598.61 [544.47,691.75]
Von Mises Stress, min	0.57 [0.31,0.86]	0.49 [0.22,0.80]	0.65 [0.24,1.22]	0.68 [0.25,1.15]
Von Mises Stress, aver	195.88 [181.69,202.20]	161.67 [143.59,186.22]	198.56 [191.63,206.46]	161.20 [142.75,210.82]
Stress Pressure, max	319.49 [239.41,399.29]	391.45 [292.31,490.53]	283.09 [232.23,376.17]	400.73 [278.99,609.21]
Stress Pressure, min	-363.19 [-453.17,-272.16]	-359.99 [-473.09,-264.93]	-319.82 [-516.12,-253.70]	-350.78 [-563.03,-244.28]
Stress Pressure, aver	-8.95 [-11.03,-6.77]	0.44 [-0.48,1.47]	-9.05 [-11.61,-4.05]	0.11 [-1.15,1.49]
Sines Stress, max	-	346.47 [299.79,400.25]	-	334.07 [292.20,377.75]
Sines Stress, min	-	-176.01 [-203.40,-150.43]	-	-189.22 [-285.12,-140.26]
Sines Stress, aver	-	77.66 [63.97,90.07]	-	78.43 [64.52,87.31]

5.3.3 Statistical analysis

For the 10 patients with stent fracture, there were a total number of 26 fractures at 1 year follow-up, increasing to 38 when most recent follow-up data were available (Table 5.3). Statistical analysis for all 42 patients was performed using the data from 1 year follow-up and the earliest detected fractures for those patients who experienced this adverse event.

A multivariate logistic regression model using only geometric parameters was fitted to the data, Table 5.6 (-2 Log likelihood= 20.95, Nagelkerke R^2=0.676). Three covariates, all at the stent level, were identified to interact in modifying the risk of fracture: change in the maximum radial asymmetry ΔR_a (Figure 5.18a) and average circumferential asymmetry ΔC_a (Figure 5.18b) after balloon deflation, and change in the maximum circumferential asymmetry ΔC_a during the cardiac cycle (Figure 5.18c).

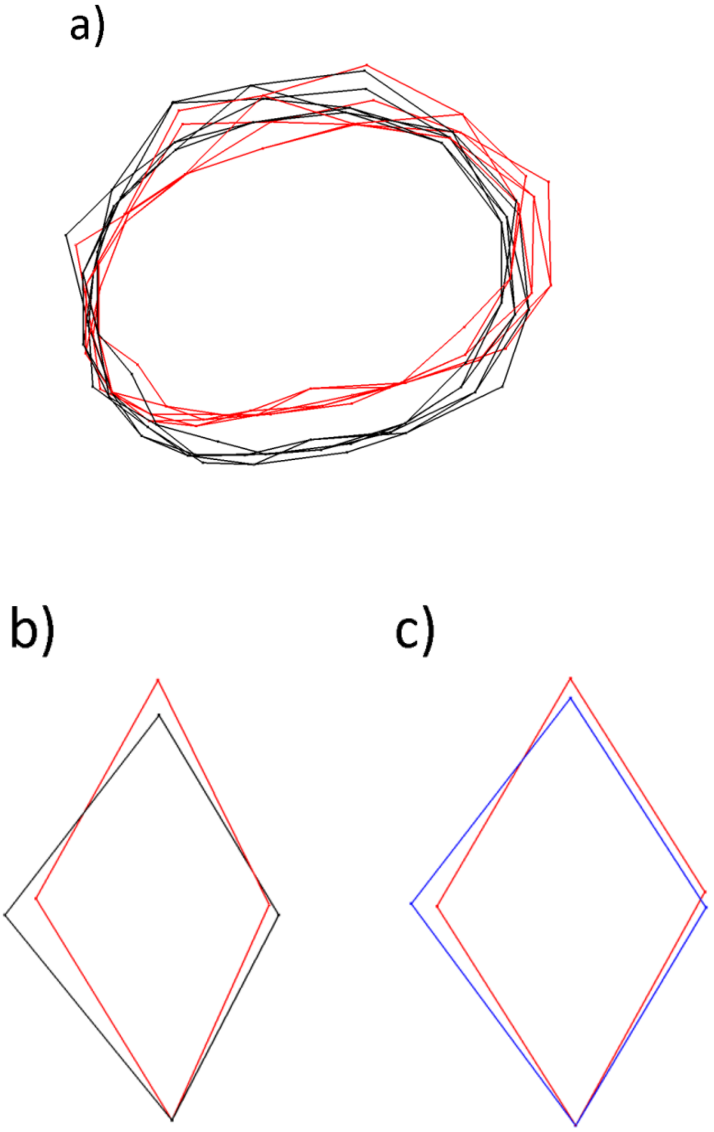

Figure 5.18 - a) Change in the radial asymmetry ΔR_a from the pre-recoil (black) to the systole (red) shown for one patient in the fluoroscopy reconstruction; b) change in the circumferential asymmetry ΔC_a from the pre-recoil (black) to the systole (red) shown for one cell of one patient's stent; c) change in the circumferential asymmetry ΔC_a from the systole (red) to the diastole (blue) shown for one cell of one patient's stent

Table 5.6 - Logistic regression analysis of 42 patients at 1 year following PPVI (geometric predictors only).

Predictor	β	*SE* β	Wald's χ^2	*df*	*p*	Odds Ratio (95% C.I. for OR)
Constant	-5.72	1.82	9.87	1	0.002	NA
ΔR_a max at recoil	-0.51	0.20	6.64	1	0.010	0.950 (0.914-0.988)
ΔC_a max at cardiac cycle	0.35	0.16	4.83	1	0.028	1.419 (1.039-1.940)
ΔC_a average at recoil	0.02	0.001	4.81	1	0.028	1.002 (1.000-1.003)

Test	χ^2	*df*	*P*
Overall model evaluation			
Omnibus tests of Coefficients	25.2	3	<0.00001
Goodness-of-fit test			
Hosmer & Lemeshow	4.36	8	0.823

-2 Log Likelihood= 20.95, Nagelkerke R^2 =0.676, Cox and Snell R^2= 0.451. NA=Not Applicable.

This means that larger changes in cells shape during cardiac cycle (Odds Ratio OR 1.419, p=0.028) and following recoil (OR 1.002, p=0.028) increase the stent fracture probability, while a preserved stent circularity following deployment (OR 0.95, p=0.01) decreases the fracture probability. Fracture happened in 3/10 patients in the cell with maximum change in shape during the cardiac cycle; in 4/10 in the cell next to it; in 2/10 in two cells away from it; and in 1/10 on the opposite side. Furthermore, fracture occurred in the section with maximum change in circularity following the recoil in 7/10 patients, while in the other 3 patients, it happened 2 to 4 sections next to the fractured one. Using this model, a predicted probability score of 0.30 correctly predicted fracture or no fracture in 90.5% of patients, with sensitivity 0.90 (95% CI 0.55-0.98) and specificity 0.91 (95% CI 0.75-0.98), Table 5.7.

Table 5.7 - The observed and the predicted frequencies of fracture for PPVI using geometric predictors only by logistic regression with the cut-off of 0.30.

Observed Fracture	Predicted Fracture No	Predicted Fracture Yes	*%Correct*
No	29	3	90.6
Yes	1	9	90.0
Overall			90.5

Note. Sensitivity =0.90 (C.I. 0.55-0.98), Specificity=0.91(0.75-0.98), False Positive=25.0%, False Negative 3.3%.

By adding the FE simulations results to the explanatory variables, an improved multivariate logistic regression model was produced, Table 5.8 (-2 Log likelihood= 16.68, Nagelkerke R^2 = 0.756). In this model, two covariates (one geometrical and one FE) were found to correctly predict fracture or no fracture in 92.9% of patients, with sensitivity 0.90 (95% CI 0.55-0.98) and specificity 0.94 (95% CI 0.79-0.99), Table 5.9: change in the maximum radial asymmetry ΔR_a after balloon deflation and the minimum values of the minimum principal stresses (negative stress) during recoil. This means that small changes of the cross-sectional shape from circular to elliptical after balloon deflation bear less risk of fracture. Large compressive stresses during balloon deflation are likely to increase the risk of fracture. Importantly, the inclusion of previously described clinical or radiographic parameters did not improve the risk of fracture in either model.

Table 5.8 - Logistic regression analysis of 42 patients at 1 year following PPVI (geometric and finite element predictors).

Predictor	β	*SE* β	Wald's χ^2	*df*	*p*	Odds Ratio (95% C.I. for OR)
Constant	-51.75	21.2	5.96	1	0.015	NA
ΔR_a max at recoil	-0.076	0.03	6.71	1	0.010	0.927 (0.875-0.982)
Min Values of Min Princ Stresses during recoil	-0.078	0.03	5.71	1	0.017	0.924 (0.866-0.986)

Test	χ^2	*df*	*P*
Overall model evaluation			
Omnibus tests of Coefficients	29.4	2	<0.00001
Goodness-of-fit test			
Hosmer & Lemeshow	3.45	8	0.903

-2 Log Likelihood= 16.68, Nagelkerke R^2 =0.756, Cox and Snell R^2= 0.504. NA=Not Applicable.

Table 5.9 - The observed and the predicted frequencies of fracture for PPVI using geometric and finite element predictors by logistic regression with the cut-off of 0.30.

Observed Fracture	Predicted Fracture No	Predicted Fracture Yes	*%Correct*
No	30	2	93.8
Yes	1	9	90.0
Overall			92.9

Note. Sensitivity =0.90 (C.I. 0.55-0.98), Specificity=0.94 (C.I. 0.79-0.99), False Positive=18.2%, False Negative 3.2%.

5.4 DISCUSSION

Fracture is a well-known complication of the PPVI Melody™ stent occurring in up to 25% of patients (**20**; **23**; **102**). This is reflected also by our series of patients (n=42) where 24% of the cases (n=10) experienced fracture in the first year after implantation. However, the reasons for fracture have not been fully identified and the occurrence of this adverse event is likely due to a complex interaction between patient and device factors.

In this study, we categorised and evaluated 3D fundamental geometrical and engineering parameters that could relate to stent fracture. The set of parameters selected takes into account, amongst others, all the clinical risk factors previously identified by Nordmeyer and McElhinney (**20**; **102**): morphological characteristics of the RVOT, presence of a BMS or calcification in the conduit, location of the device in respect to the sternum, stent elastic recoil after balloon deflation, post-PPVI dilatation with a high pressure balloon, and asymmetries in the expanded device. All these influence the stent final geometry and behaviour during balloon deflation and cardiac cycle. The geometry and variation in geometry were fully characterised by dividing the stent in sublevels, while the mechanical effects of each stent final shape and deformation were reflected in the stress distribution.

Multivariate binary logistic regression analysis was used to identify covariates affecting the odds of stent fracture. Two statistical models were developed: the first based only on geometrical parameters alone (derived from clinical fluoroscopy at the time of PPVI) and a second extended model which also included stress information from FE analysis simulations. Both models showed good fit, correctly identifying fracture or no fracture in 90.5% and 92.9% of patients respectively.

The change in the stent section shape after balloon deflation was the most influential variable affecting the odds of stent fracture: the balloon deployment forces the implantation site and therefore the stent toward a cylindrical geometry, which is however lost after balloon deflation due to the recoil of the arterial wall. This makes the stent sections deform to an elliptical shape. The less the shape of a given section of the stent changes, we show the lower the risk of frame fracture. In addition, the data demonstrate that the more the cells' shape changes during arterial recoil and cardiac cycle, the higher is the risk of frame fracture. In general, static asymmetries appeared not to be strongly correlated with fracture, while the dynamics of the implantation site wall highly influences this phenomenon. This is indeed supported by a recent study reporting on balloon-expandable stent implantation in systemic outflow tracts which resulted in fractures in 43% of the cases (**124**). These results are consistent with the clinical findings that pre-stenting, as well as the presence of calcification in the deployment region (less compliant and dynamic), reduces the probability of fracture (**22**; **102**).

However, by describing the mechanical basis of these phenomena in our study, the statistical models are not further improved by their inclusion.

Importantly, our analysis shows that changes in PPVI shape at the time of implantation may help predict stent fracture. This would enable us to define specific follow-up protocols for patients. Using our set statistical criterion, we would categorise 11 patients as high-risk for stent fracture with 9 patients fracturing and 2 not; hence, we would have potentially submitted 2 patients to have stringent follow-up. For the 31 patients we would have placed in the low risk group, 1 patient did have a fracture, but 30 patients would potentially have avoided needless follow-up.

An early, systematic biomedical analysis post device implantation has the potential to accurately risk stratify patients, defining follow-up strategies and possibly reducing expensive follow-up investigations and clinic time. Further work is now required to define what safe follow-up strategies should be used for high and low-risk patients.

5.5 LIMITATIONS

Several important limitations in this study should be considered. Follow-up patient data at 1 year were available in the form of chest x-rays, but no dynamic fluoroscopy images. Despite the excellent radio-opacity of the platinum iridium-alloy, chest x-rays are not always optimal to visualise clearly the presence of a stent fracture, whose number may have been underestimated in this study. The earliest detected fractures were considered for the statistical analysis, but the single first strut to fail could not be identified in 5/10 patients: the presence of a fracture may result in fracture progression to adjacent struts of the stent, thus changing the stent geometry and the stress distribution.

The FE analysis although comprehensive did not include residual stresses caused by the asymmetrical manual crimping of the device onto the delivery catheter and by potential multiple inflations of the post-PPVI dilatation balloon. These residual stresses play an important role in fatigue phenomena but could not be estimated for our patient population.

The proposed models were developed in a relatively small cohort of 42 patients; therefore, they require validation in a prospective cohort, to overcome the inherent possibility of over-fitting in a training data set. However, with this preliminary data we have aimed for simple and parsimonious models, with limited explanatory covariates: 3 in the geometrical model and 2 in the FE model, to reduce the risk of over-fitting.

Finally, the 3D reconstruction process and measurement of the parameters predictors for fracture currently requires technical image processing, unavailable in many clinical environments. Translation of this process to the clinical environment will be aided by automated image processing techniques, in order to create user-friendly tools easily accessible to clinicians.

5.6 CONCLUSIONS

Stent fracture is a common adverse event following Melody™ PPVI and other stent implantation. For this reason, patients require careful follow-up to ensure that device/stent integrity remains. This study highlights that asymmetries in stent section geometry and cells shape, particularly during recoil after balloon deflation, are important variables associated with stent fracture. We have proposed two parsimonious statistical models based on 3D geometrical and stress analysis, to identify whether a PPVI patient is likely to incur a subsequent stent fracture. A model including FE analysis of stress is superior, however, consideration of geometrical information alone performs well, and could be translated to the clinical environment more generally without engineering support. Such models will require prospective validation, but could be used to risk stratify patients and to strategically plan bespoke clinical follow-up.

From the next chapter the background will move from structures to fluids. Different computational methodologies will thus be introduces to study another CHD: the transposition of the great arteries.

CHAPTER 6

THE FLUID DYNAMICS IN THE NEOAORTA OF A TGA PATIENT

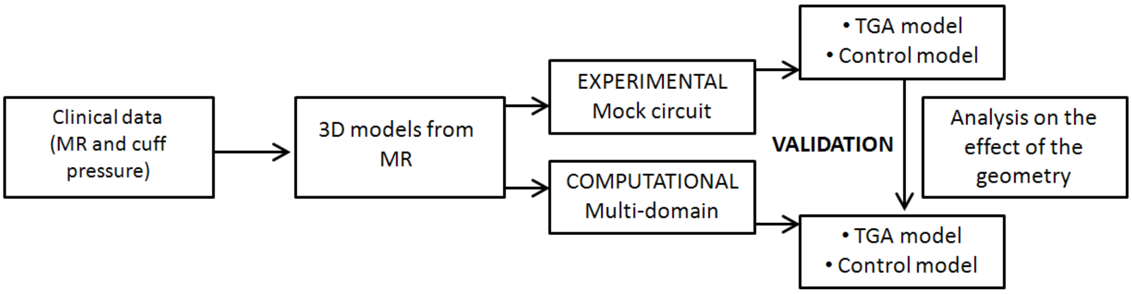

6.1 INTRODUCTION

The studies presented in the previous 2 chapters focused on the development of 2D image analysis techniques and structural simulations to study the problem of stent fracture in PPVI. In this and the following chapter, the research moves to a different clinical problem, the long term complications after ASO in TGA patients (Section 2.5.3), which were analysed using different computational fluid dynamic methodologies. In this chapter, a multi-domain approach including the 3D model of the neoaorta of a patient following ASO was validated against an in-vitro set-up. In the next chapter, this validated methodology further expanded using pure LPN was employed to study the pulmonary circulation in TGA patients who presented unilateral pulmonary artery stenosis.

TGA as explained in Section 2.5 is the most common cyanotic CHD, currently treated with the arterial switch operation. Although ASO restores normal blood flow, several long-term complications can arise and the long-term effects have not been fully appreciated yet, as this procedure was introduced only in the 80s. In particular, the hemodynamics may be affected by anatomical features such as enlarged aortic root and acute aortic arch angulation, typical of TGA repaired by ASO with the Lecompte manoeuvre (Section 2.5.2).

In this chapter, I developed a computational model of the neoaorta of a patient following ASO and of the aorta of a healthy control to assess the local hemodynamics and associated potential complications that arise after ASO compared to those of the normally developed aorta. Different modelling methodologies were explored and validated with in-vitro experiments replicating the same patients’ conditions. The validated numerical model could be used not only to study and compare the local fluid dynamics in different patient-specific morphologies, but also to assess the differences in the same patient if a hypothetical virtual surgery like the spiral operation (Section 2.5.4) could be performed instead of ASO.

6.2 MATERIALS AND METHODS

6.2.1 Patients' selection

One 15-year-old patient with TGA corrected with ASO was selected for the study (1.7 m^2 body surface area (BSA), male). An age and BSA-matched healthy control patient (1.7 m^2 BSA, male) was identified from a list of subjects screened at our Centre for assessment of possible hereditary cardiomyopathy. Both cases had MR investigation: the 2D phase contrast images were used to extract flow-rate information at the level of the sino-tubular junction (Section 3.4.1.1); the 3D whole heart acquisitions were used to reconstruct the 3D anatomy of the patients (Section 3.5.1), including the aortic root, arch and the three brachiocephalic arteries (i.e. innominate, left carotid and left subclavian arteries). Furthermore, in consideration of the experimental study, the access for a pressure catheter was built and positioned in the model at the level of the ascending aorta. Similarly, the inlet (aortic root) and outlets (brachiocephalic vessels and descending aorta) were modified in order to facilitate the connection of the 3D phantom with the mock circulatory system. The resulting geometry was rapid-prototyped with the PolyJet technology (Section 3.6.1) using a transparent and robust resin (Watershed 11122; DSM Somos, Elgin, IL) (Figure 6.1).

Figure 6.1 - Rapid prototyped rigid 3D models of the aortic arch of the TGA (left) and the Control (right) patients.

The transparency of the resin allows to identify the presence of air bubbles in the circuit, thus facilitating de-airing operations, and to control the correct positioning of the pressure catheter in the aortic arch.

6.2.2 Experimental model

A hydraulic circuit consisting of a pulsatile pump, compliance chambers, resistances and an atrial reservoir as explained in Section 3.6.2 was built incorporating the printed 3D phantom, as shown in Figure 6.2 and Figure 6.3. The components of the circuit were carefully chosen to be MR compatible: all the ferromagnetic parts were located in the control room adjacent to the scanner room. As tests were performed inside the MR scanner, water was chosen as the flowing medium for hygiene and safety reasons. Hydraulic seal between the model, the pipes and the compliance chambers was ensured using silicone.

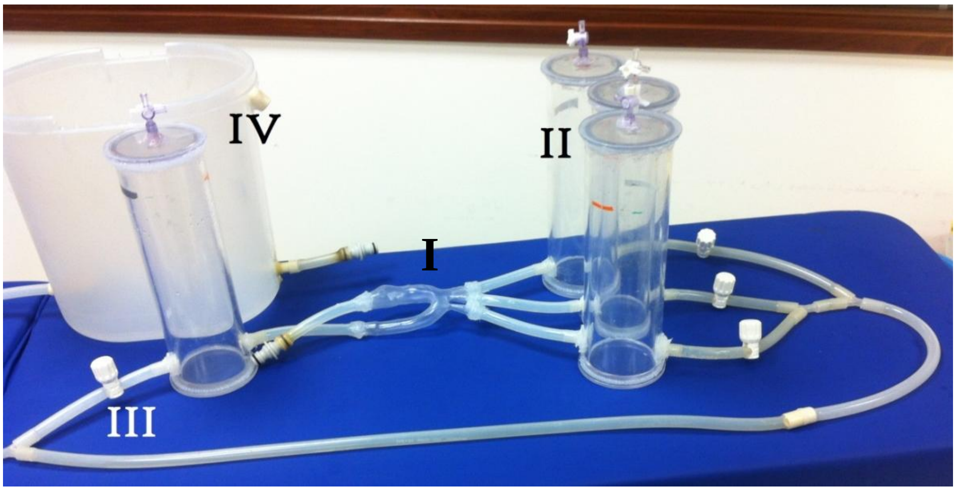

Figure 6.2 - Experimental circuit: I indicates the printed 3D phantom of the patient's aorta, II indicates the compliant chambers, III one of the four taps implementing the resistances, and IV the atrial reservoir.

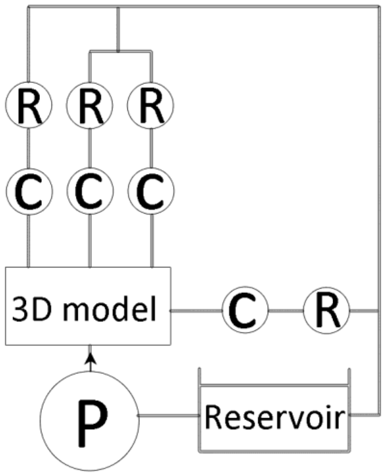

Figure 6.3 - Schematic representation of the circuit: P represents the pulsatile pump, C the compliant chambers, R the non-linear resistances. The arrow indicates the direction of the flow.

Heart rate (HR) and stroke volume (SV) were set in the pump in accordance to the patient's data: HR = 70 bpm and SV = 90 ml. Long braided pipes filled with water were adopted to allow the Harvard pump to sit in the control room.

The pressure range at the inlet of the model was set at 115/60 mmHg, according to cuff pressure data measured in the TGA patient.

The values of the compliances obtained according to the formula in Section 3.6.2 are reported in Table 6.1.

Table 6.1 - Compliance values set at each outlet of the model with patient's mean pressure = 77 mmHg.

	C [m^3/Pa]
Innominate	2.2E-09
Carotid	2.0E-09
Subclavian	2.8E-09
Descending aorta	1.8E-09

Resistances of the downstream district of the circulation were set in order to split the inflow according to the following physiological proportions: 55% in the lower body and

45% in the upper body (of which 15% in the innominate, 10% in the carotid and 20% in the subclavian artery). Characterisation of each resistance was performed using a simplified steady flow circuit (Section 3.6.2) and the resulting data were interpolated with a second-order polynomial equation (Figure 6.4).

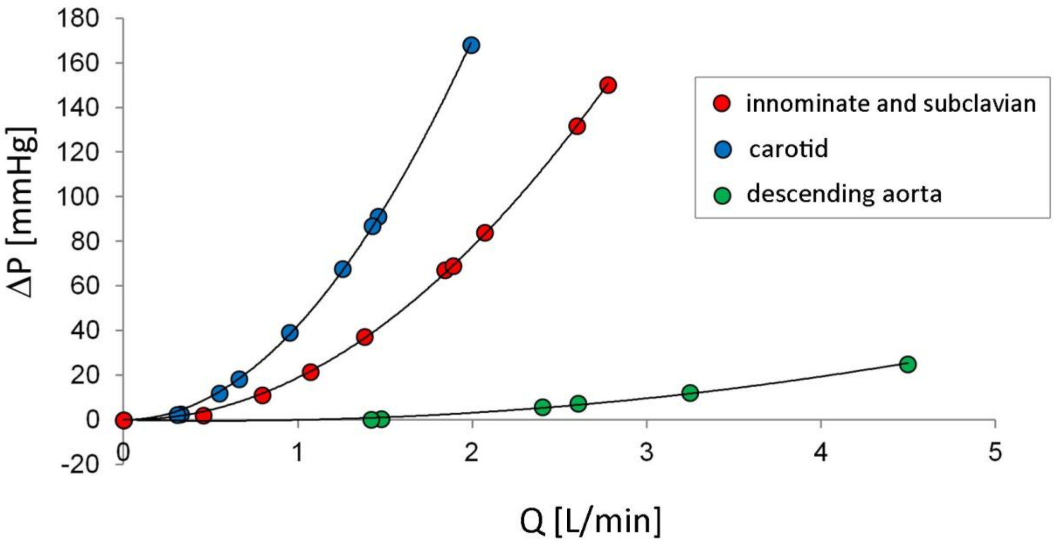

Figure 6.4 - Characteristic curves of the resistances set in the circuit for the carotid (blue), the innominate and subclavian (red), and the descending aorta (green).

All outlets of the 3D model drained to a reservoir representing the atrium, from which the pump intake the working fluid. This chamber was filled with an amount of water suitable to implement a pressure of 9 mmHg (representative of atrial pressure) by the hydraulic head.

The pressure in the aortic arch was measured by means of the high-fidelity factory-calibrated fiber optic catheter Samba Preclin Samba sensor (Section 3.4.2).

6.2.3 In-vitro MR Acquisitions

The 3D model of the TGA patient was assembled in the circuit, and inserted inside the MR scanner. The pump was then turned on, setting the appropriate pressure and flow waveforms. Acquisitions were gated to the pump’s external trigger, via a BNC connection cable.

Firstly, phase contrast data were acquired for 2D quantification of flow at the inlet and at every outlet. The imaging parameter used for the acquisitions were: Venc: 250 cm/s for the outlets and 500 cm/s for the inlet; repetition time/echo time: 29.9/2.18 ms; pixel spacing: 1.17 mm; section thickness: 5 mm; flip angle: 30°.

Then, the 4D (3 spatial dimension and time) acquisitions were performed using two different sequences: a standard sequence (Siemens) and a higher temporal and spatial resolution sequence, of 15 minutes, and 1 hour and 10 minutes respectively. The imaging parameters set for the Standard 4D sequence were: Venc: 200 cm/s; repetition time/echo time: 33.4/2.5 ms; pixel spacing: 2.2 mm; section thickness: 2.2 mm; flip angle: 5°. The imaging parameters set for the High Resolution 4D sequence were: Venc: 200 cm/s; repetition time/echo time: 21.4/3.2 ms; pixel spacing: 2.4 mm; section thickness: 1.2 mm; flip angle: 5°.

The same imaging protocol was adopted for imaging the mock circuit when the TGA 3D model was replaced with the Control 3D model, leaving compliances and resistances to the previously set values.

Flow data were calculated from the phase contrast acquisitions using the imaging software OsiriX (Pixmeo, Geneva, Switzerland), a DICOM viewer designed for navigation and visualisation of multimodality and multidimensional images. Using a plug-in developed in-house at Great Ormond Street Hospital (**125**), it was possible to quantify the instantaneous flow volume at any time during the cardiac cycle through the selected region of interest on the planes scanned. The mean velocity was then obtained dividing the flow by the area of the region of interest.

Flow data extracted from the 4DMR acquisitions were analysed with the Siemens 4D Flow software. A 3D mask containing the region of interest was drawn by a combination of thresholding and segmentation operations. Six planes of interests were drawn perpendicular to the direction of flow to extract flow, velocity and area information: two at the inlet of the model, one in the aortic root, one before and one after the upper branches, and one in the descending aorta. Finally, particle seeds were placed on such planes, to allow the visualisation of particle traces and streamlines across the aortic arch (Figure 6.5).

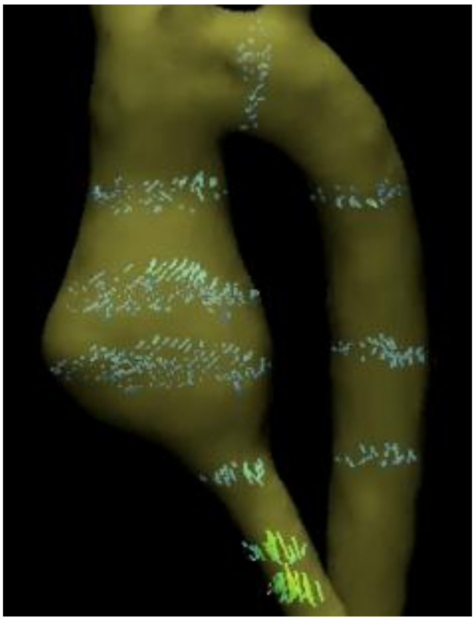

Figure 6.5 -Particle seeds at different locations along the 3D model then used to generate streamlines and pathlines with the Siemens 4D Flow software.

6.2.4 Computational model

The TGA and the Control 3D geometries previously reconstructed from the MR images were used for the computational study. Computational meshes were created with the software ICEM (Ansys Inc., Canonsburg, PA, USA) adopting tetrahedral elements. Five different element sizes were used resulting in five different meshes of around 400000, 500,000, 700,000, 900,000 and 1,200,000 volumes respectively. A sensitivity mesh analysis was conducted on such models to identify the best compromise between accuracy of the results and computational time required by the CFD simulation to converge. The influence of the mesh size was evaluated on the calculated power dissipation index calculated as the difference in energy W entering and exiting the model:

$$W_{dissip} = \left(\frac{1}{2}\rho v_{IN}^2 + P_{IN}\right) \cdot Q_{IN} - \left(\frac{1}{2}\rho v_{OUT}^2 + P_{OUT}\right) \cdot Q_{OUT}$$

where ρ is the fluid viscosity, v is the velocity, P is the pressure, and Q is the volumetric flow-rate at the inlet (IN) face and outlet (OUT) faces (**126**; **127**). This parameter was chosen for the grid independence evaluation as it includes all the type of variables monitored in the simulations (velocities, pressures and flow-rates). Also, an indication of the energy dissipated by the geometry could be a useful parameter to evaluate the performance of different surgical options for treating the same patient. A negligible difference of 1.4% (corresponding to $1{\cdot}10^4$ W) was recorded in the power dissipation index calculated with the 900000 elements and the 1200000 elements meshes, thus the former was chosen for the following analyses.

Ansys Fluent was used to set up and run all the CFD simulations as explained in Section 3.5.2.1. In order to replicate the in-vitro conditions, the fluid used in the simulations was water, considered incompressible and Newtonian, with density ρ=1000 kg/m^3 and viscosity μ=1 cP. The simulations were run under the hypothesis of no gravitational effects, isothermic conditions, with rigid walls and no-slip conditions. The strongest assumption made was the use of a laminar solver. Given the fluid properties, the anatomical dimensions and the flow conditions, the Reynolds number exceeded the laminar limit (i.e. > 1000, **128**) during the systolic peak of the simulations. However, numerical models that can solve accurately the coexistence of laminarity and turbulence have not been fully validated yet and present high computational costs. Thus, in this preliminary study a laminar solver was chosen.

In order to prescribe accurate boundary conditions to the 3D model, a multi-domain approach was employed in this study, by coupling the 3D model of the anatomical part of interest, with a LPN representing the circulation of the patient. In this case, only the systemic circulation was implemented, to replicate the downstream part of the mock circuit. At the inlet of the model, a time-varying velocity function interpolating the experimental flow curve was imposed through a user-defined function (UDF) script. The LPN representing the experimental circuit is shown in Figure 6.6.

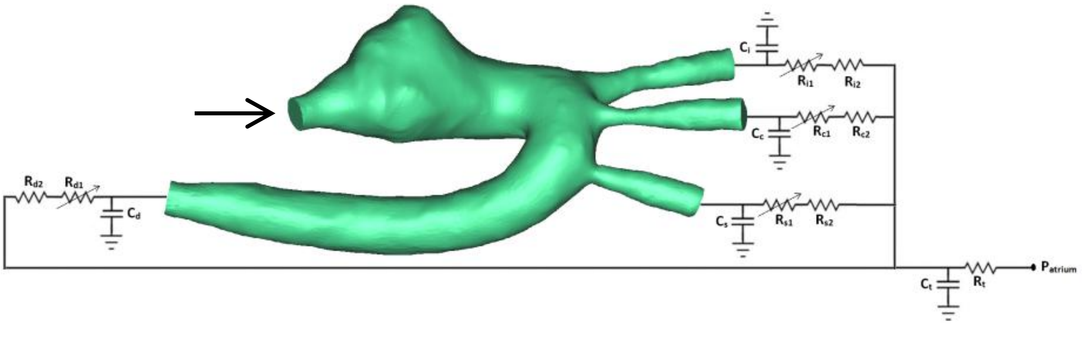

Figure 6.6 - Multi-domain model: coupling between the LPN of the systemic circulation of the patient and the 3D model of TGA patient's aortic arch. The arrow indicates the inlet of the model.

The coupling between the CFD model and the LPN was implemented through pressure and flow information exchanged in correspondence of the boundary faces at the level of the innominate, the carotid, the subclavian and the descending aorta, as explained in Section 3.5.2.3.

The values of the resistances and the compliances were chosen in order to replicate the respective components of the experimental circuit. The non-linear resistance R_1 corresponds to the taps of the mock circuit, and is characterised through the pressure drop-flow relationship obtained during the tap experimental calibration. The other resistances included in the network took into account the distributed and the concentrated pressure drops due to the length of the pipes, the presence of connections, and the sudden variations in diameter at different sections. In particular, the linear resistance R_2 represented the pressure drop caused by the connections of the tubes, while R_t lumped the final part of the tube connecting all outlets to the right atrium reservoir.

The values of the resistances and the compliances are reported in Table 6.2.

Table 6.2 - Value of the parameters chosen to characterise each downstream branch j: non-linear resistances indicated through the pressure drop (ΔP) across the resistance R_{j1} (with Q indicating the volumetric flow-rate); linear resistances R_{j2} to account for the distributed resistances; compliances C_j.

	R_{j1}	**R_{j2}**	**C_j**
	ΔP [Pa]	**[Pa·s/m^3]**	**[m^3/Pa]**
Innominate (*j* = i)	$1.10^{13}\cdot Q^2 - 8.10^{6}\cdot Q$	$5\cdot10^{7}$	$1.88\cdot10^{-9}$
Carotid (*j* = c)	$2.10^{13}\cdot Q^2 - 5.10^{6}\cdot Q$	$1\cdot10^{8}$	$1.98\cdot10^{-9}$
Subclavian (*j* = s)	$1.10^{13}\cdot Q^2 - 8.10^{6}\cdot Q$	$1\cdot10^{7}$	$3.06\cdot10^{-9}$
Descending Aorta (*j* = d)	$8.10^{11}\cdot Q^2 - 1.10^{7}\cdot Q$	$2.5\cdot10^{7}$	$1.48\cdot10^{-9}$
Common Section (*j* = t)	-	$8\cdot10^{7}$	$0.36\cdot10^{-11}$

The ordinary differential equations (ODEs) were resolved through the explicit Euler numerical method, using a time-step Δt of 10^{-4} s.

6.3 RESULTS

6.3.1 Experimental model

The mock circuit proved to be suitable for the representation of the downstream districts of the circulatory system, with pressure and flows in a physiological range. Also, the replacement of the TGA 3D model with the Control model was feasible, without interfering with the settings of the rest of the circuit.

6.3.2 4D-MR Flow

The comparison between the two different 4D flow sequences, Standard and High Resolution respectively, showed no noticeable difference between the outcomes in terms of acquired flow. Both cases were examined against the flows measured with OsiriX from the traditional 2D Cartesian phase-contrast flow acquisitions, which was taken as reference. The High Resolution sequence presented noisier results, and it slightly overestimated the systolic peak at the inlet section of the model, while the Standard sequence slightly underestimated it (Figure 6.7). In terms of mean flow averaged over one cardiac cycle on the inlet of the model, 5.5 L/min were measured with the 2D OsiriX, as well as with the Standard sequence, while with the High Resolution 7 L/min were measured per cardiac cycle. From a qualitative point of view, the images obtained with the High Resolution settings did not provide any additional information when compared with the Standard acquisitions. Figure 6.8 shows the streamlines captured in the two cases in the TGA model. The High Resolution sequence exhibited a noisier background, likely due to compromised signal to noise ratio (SNR), not allowing an accurate mask thresholding for isolating the region of interest. Also, a smaller number of streamlines, not sufficient for an adequate representation of the fluid dynamics in the aortic arch, was noticed.

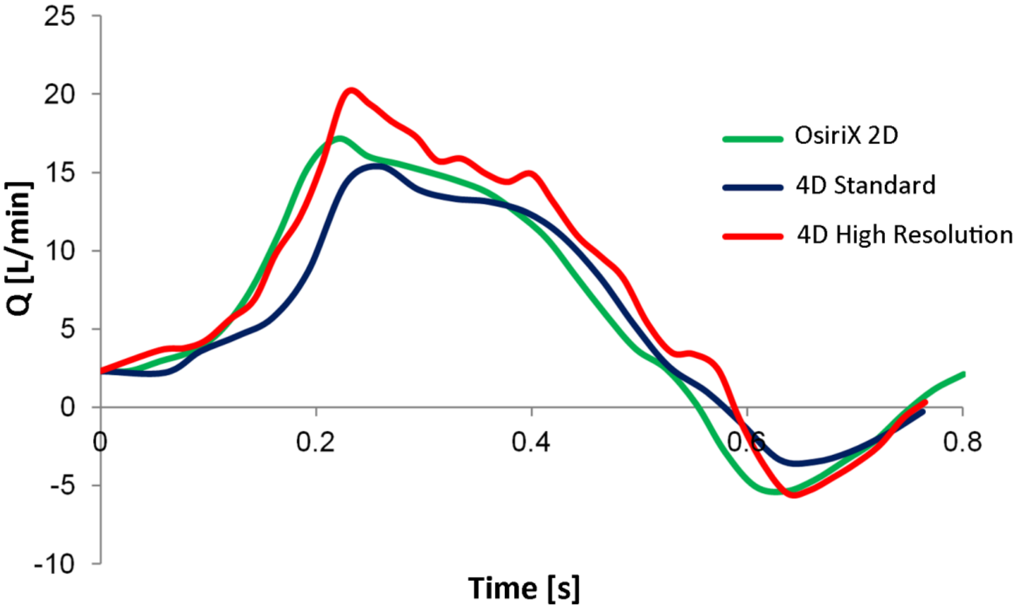

Figure 6.7 - Flows at the inlet of the model acquired with the Standard (blue) and High Resolution (red) 4D Flow sequences, compared with the OsiriX 2D acquisition (green).

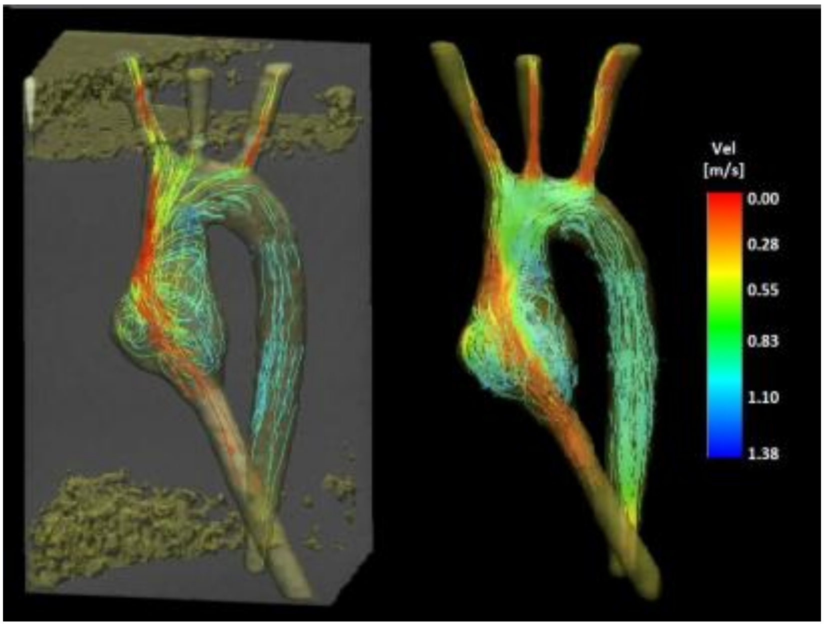

Figure 6.8 - Qualitative comparison of the streamlines of the High Resolution (left) and the Standard (right) 4D flow sequences. The first image shows a noisier background and visibly less number of streamlines than the Standard one.

As a result, the Standard Resolution sequence was adopted also for the test with the Control geometry.

6.3.3 Computational model

In order to understand whether the computational model was able to accurately reproduce the fluid dynamics developed in the mock circuit, data from both tests were compared in terms of flows, pressures and streamlines. The mean flows calculated at every outlet of the TGA and the Control 3D domains are reported in Table 6.3, while the flow-splits among the outlets calculated as a percentage of the inflow are shown in Table 6.4.

Table 6.3 - Mean volumetric flows measured from MR and calculated with the CFD simulations at every outlet of the TGA and the Control model.

	TGA Model		**Control Model**	
	MR [L/min]	**CFD [L/min]**	**MR [L/min]**	**CFD [L/min]**
Innominate	0.92	0.88	0.85	0.9
Carotid	0.54	0.56	0.55	0.59
Subclavian	1.17	1.1	0.9	0.89
Descending Aorta	2.92	3.01	3.2	3.12

Table 6.4 - Flow-split calculated as a percentage of the inflow, measured from MR and calculated with the CFD simulations for every outlet of the TGA and the Control model.

	TGA Model		**Control Model**	
	MR [%]	**CFD [%]**	**MR [%]**	**CFD [%]**
Innominate	16.6	15.8	15.5	16.4
Carotid	9.7	10.1	10.0	10.7
Subclavian	21.1	19.8	16.4	16.2
Descending Aorta	52.6	54.2	58.1	56.7

The results of the computational models were in agreement with the flows measured experimentally, not only in terms of averages over one cardiac cycle, but also in terms of waveforms, as illustrated in Figure 6.9 for the TGA model, and in Figure 6.10 for the Control model.

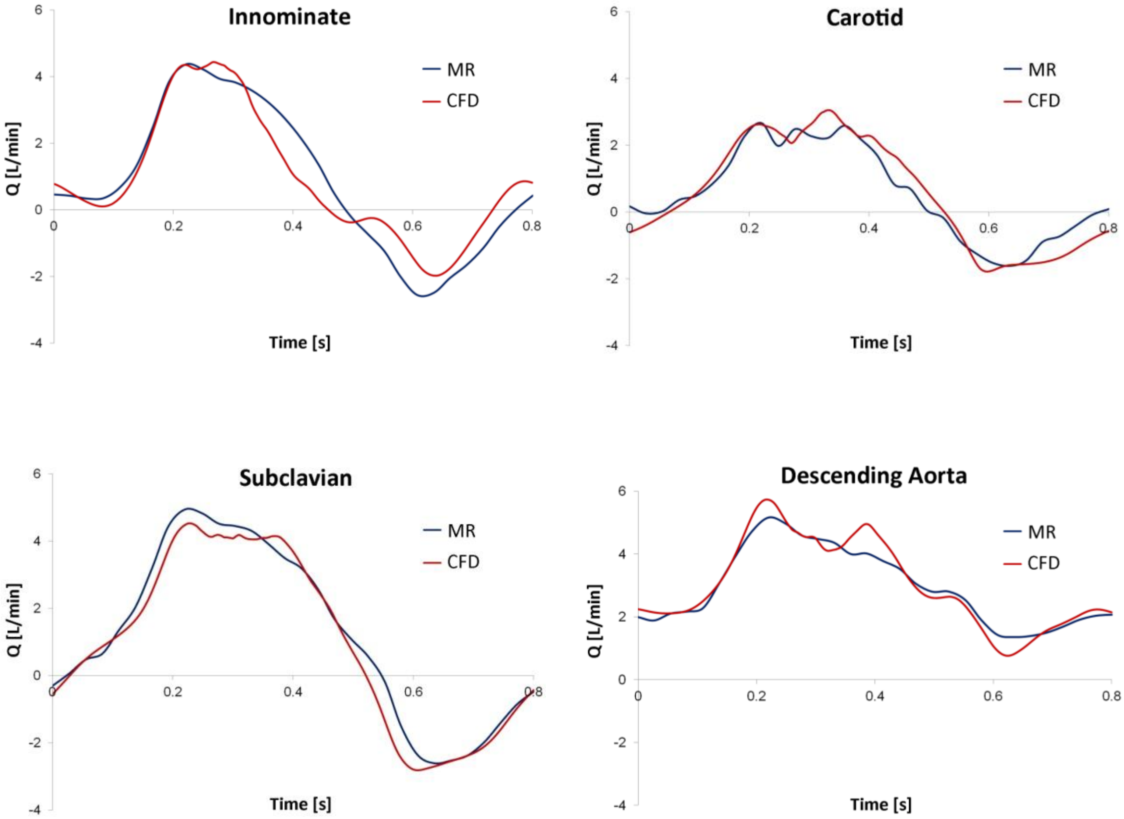

Figure 6.9 - Experimental (blue) and computational (red) volumetric flow-rate waveforms obtained at the outlets of the TGA model over one cardiac cycle (T = 0.8s).

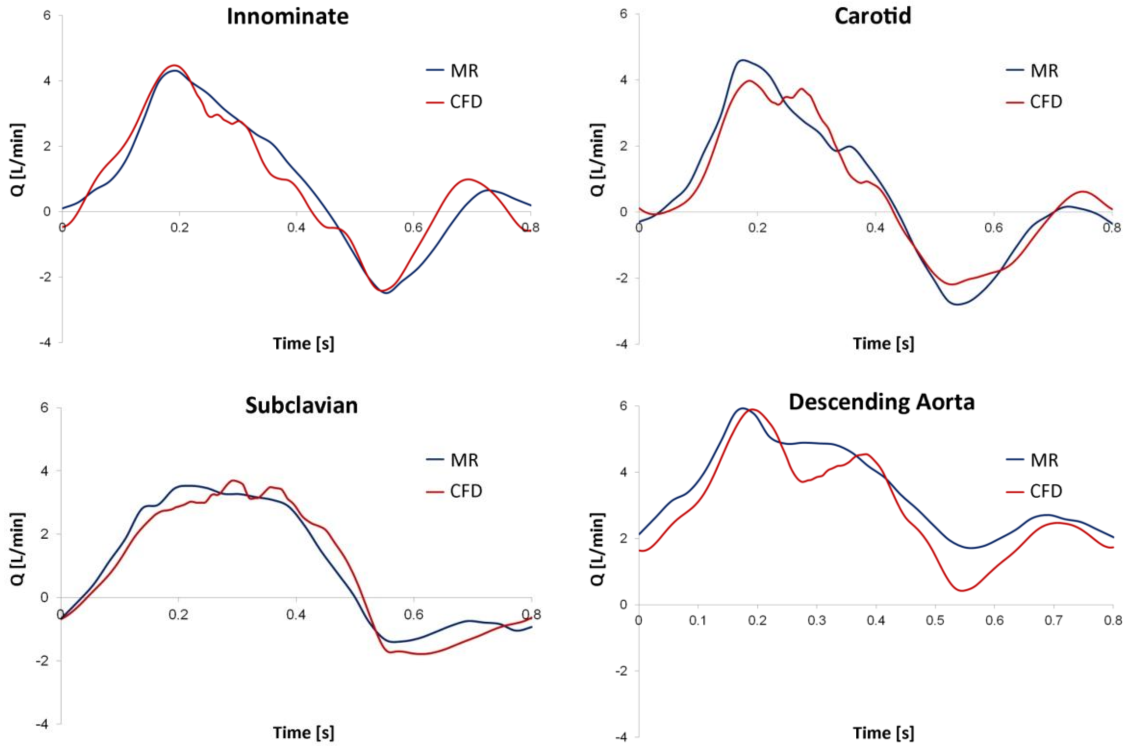

Figure 6.10 - Experimental (blue) and computational (red) volumetric flow-rate waveforms obtained at the outlets of the Control model over one cardiac cycle (T = 0.8s).

The pressure measured experimentally inside the aortic arch was compared with that calculated computationally on a plane specifically created in the geometry at the same level of the dedicated port for the pressure catheter. Figure 6.11 shows the comparison between the experimental (blue) and the computational (red) curves in the TGA model, while in Figure 6.12 the same variables are reported for the Control model.

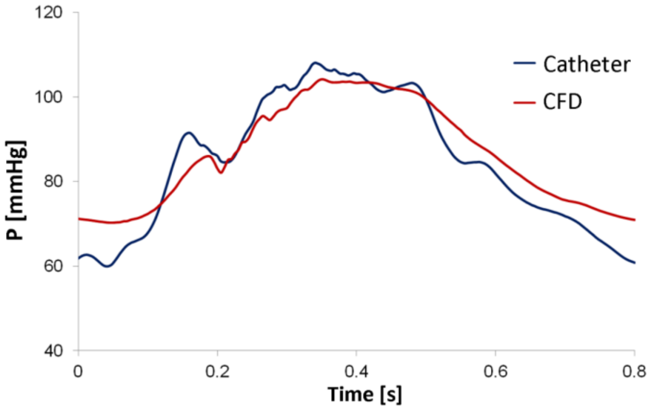

Figure 6.11 - Experimental (blue) and computational (red) pressure waveforms recorded in the aortic arch of the TGA model over one cardiac cycle (T = 0.8s).

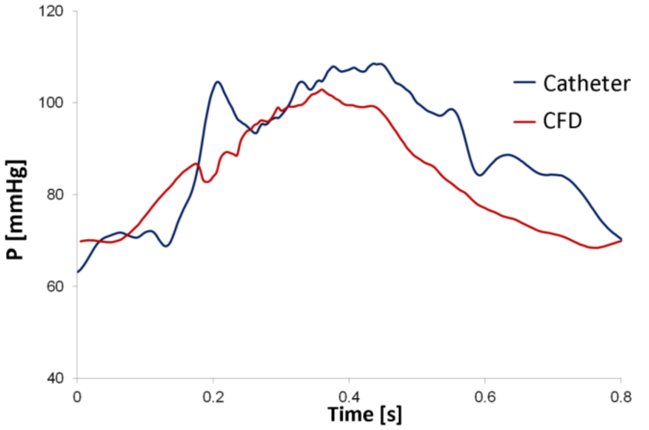

Figure 6.12 - Experimental (blue) and computational (red) pressure waveforms recorded in the aortic arch of the Control model over one cardiac cycle (T = 0.8s).

Satisfactory agreement was noted in terms of pressure tracings and pressure values. In particular, the TGA mean pressure measured experimentally in the aortic arch was 84.6 mmHg, while the one calculated in the CFD analysis was 85.7 mmHg (1.3% difference). For the Control model, the experimental mean pressure was 87 mmHg and the computational pressure value was 83.2 mmHg (4.4% difference).

6.3.4 Qualitative comparison between 4D-Flow and CFD simulations

The velocity streamlines are visualised in both geometries at 4 temporal instants over one cardiac cycle, with both the 4D flow Siemens visualisation software and Fluent in Figure 6.14 to Figure 6.17 for the TGA model, and in Figure 6.18 to Figure 6.21 for the

Control model.The frames considered for the comparison were early systole (t_1=0.1 s), peak systole (t_2=0.2 s), late systole (t_3=0.4 s) and diastole (t_4= 0.6 s), as shown in Figure 6.13.

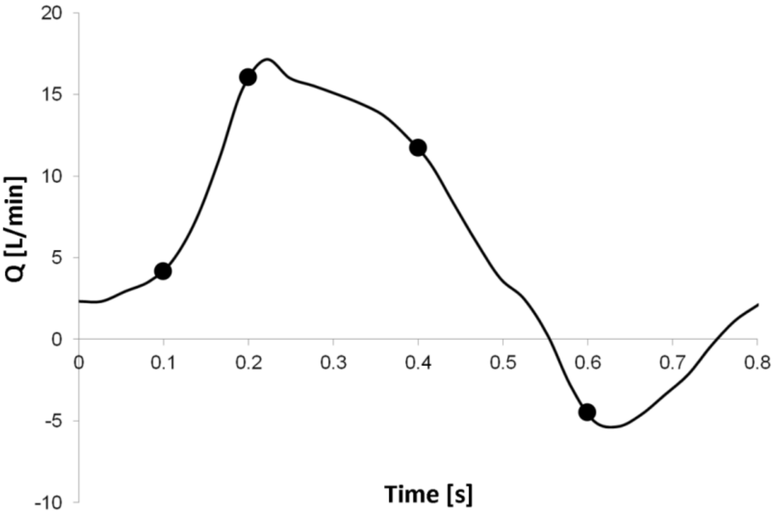

Figure 6.13 - Temporal instants considered for the comparison displayed in the cardiac cycle. : t_1 represents the early systole, t_2 the systolic peak, t_3 the late systole and t_4 the diastole.

A good qualitative agreement was verified between MR and CFD data: the CFD simulation was able to reproduce the same flow jet impinging at the top of the aortic root wall, and the surrounding whirls visible in the 4D flow images. The range of velocities is comparable in both magnitude and distribution. Excellent correspondence was noticed all over the cardiac cycle.

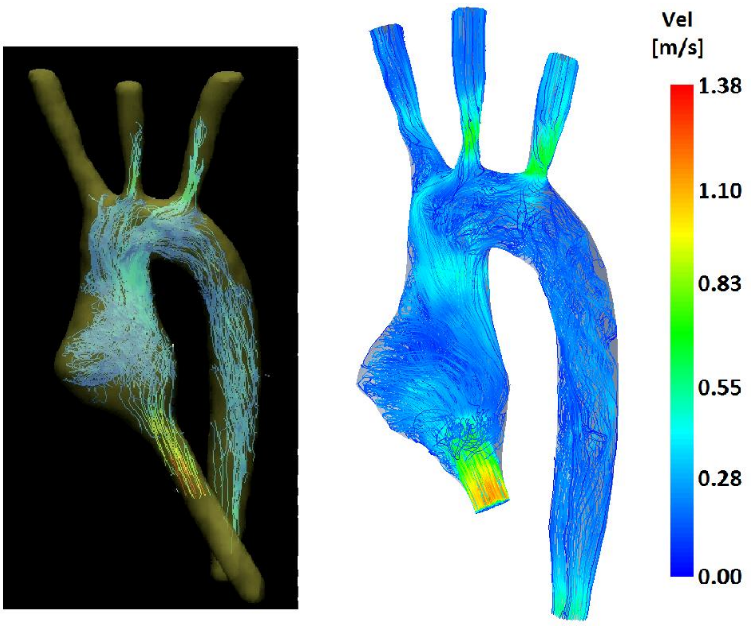

Figure 6.14 - Four-D flow streamlines (left) compared with CFD streamlines (right) at t_1*= 0.1 s (early systole) in the TGA model. The range of velocity is the same for both images.*

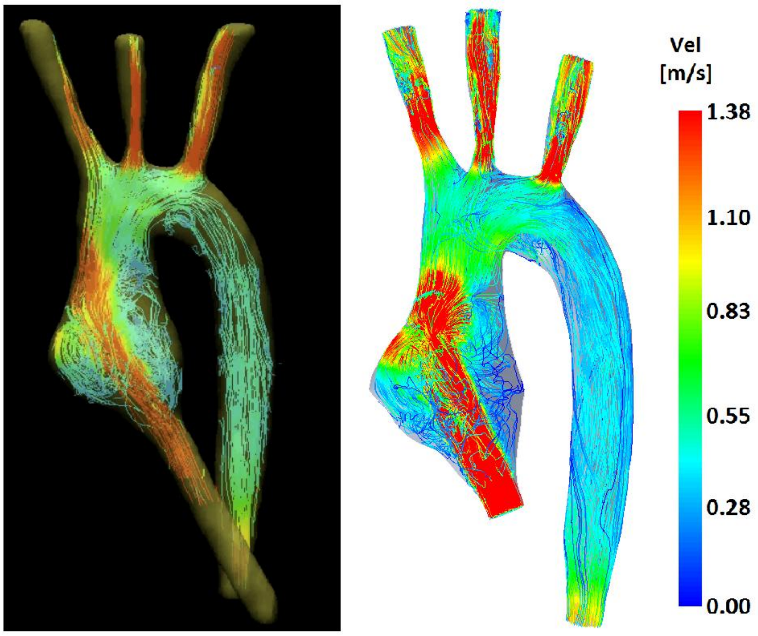

Figure 6.15 - Four-D flow streamlines (left) compared with CFD streamlines (right) at t_2*= 0.2 s (peak systole), in the TGA model. The range of velocity is the same for both images.*

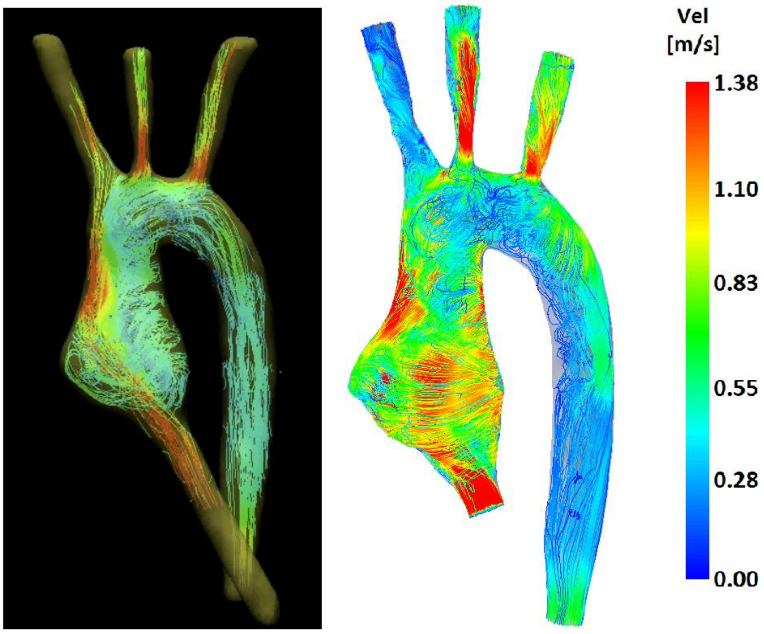

Figure 6.16 - Four-D flow streamlines (left) compared with CFD streamlines (right) at t_3= 0.4 s (late systole), in the TGA model. The range of velocity is the same for both images.

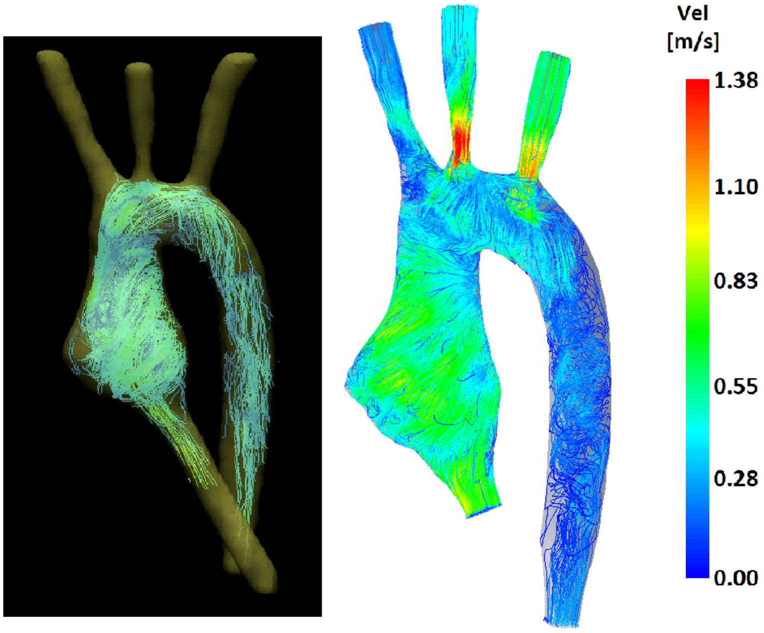

Figure 6.17 - Four-D flow streamlines (left) compared with CFD streamlines (right) at t_4= 0.6 s, (diastole), in the TGA model. The range of velocity is the same for both images.

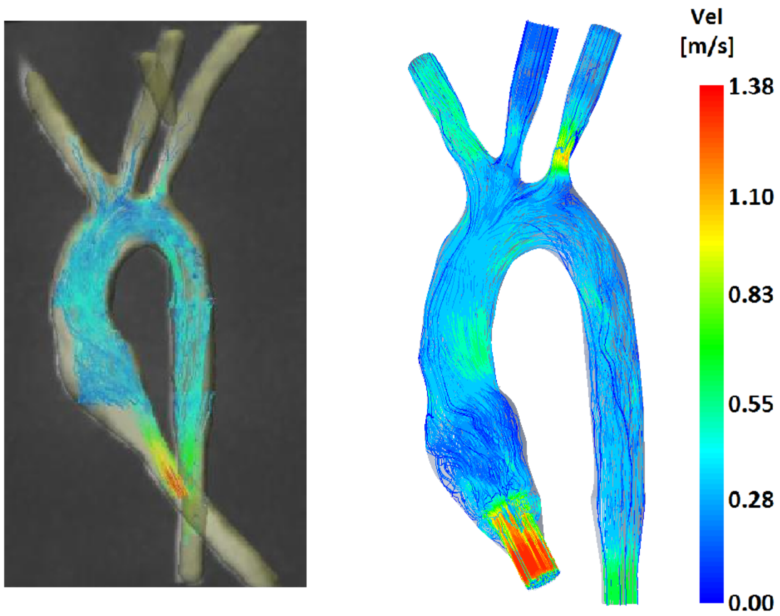

Figure 6.18 - Four-D flow streamlines (left) compared with CFD streamlines (right) at t_1= 0.1 s (early systole) in the Control model. The range of velocity is the same for both images.

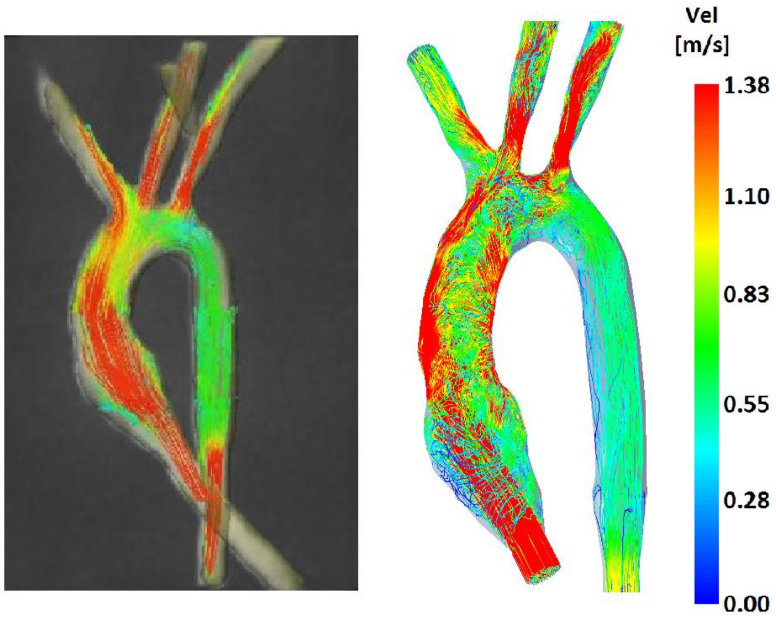

Figure 6.19 - Four-D flow streamlines (left) compared with CFD streamlines (right) at t_2= 0.2 s, (peak systole), in the Control model. The range of velocity is the same for both images.

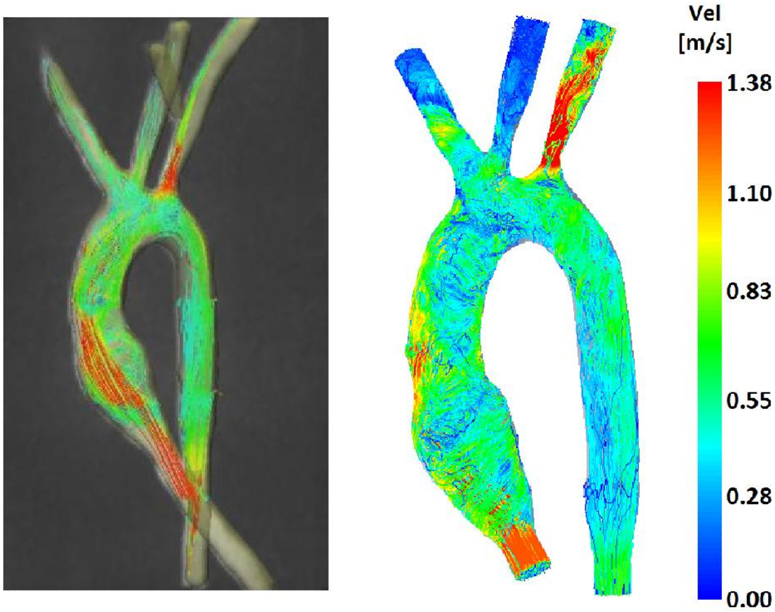

Figure 6.20 - Four-D flow streamlines (left) compared with CFD streamlines (right) at t_3= 0.4 s (late systole), in the Control model. The range of velocity is the same for both images.

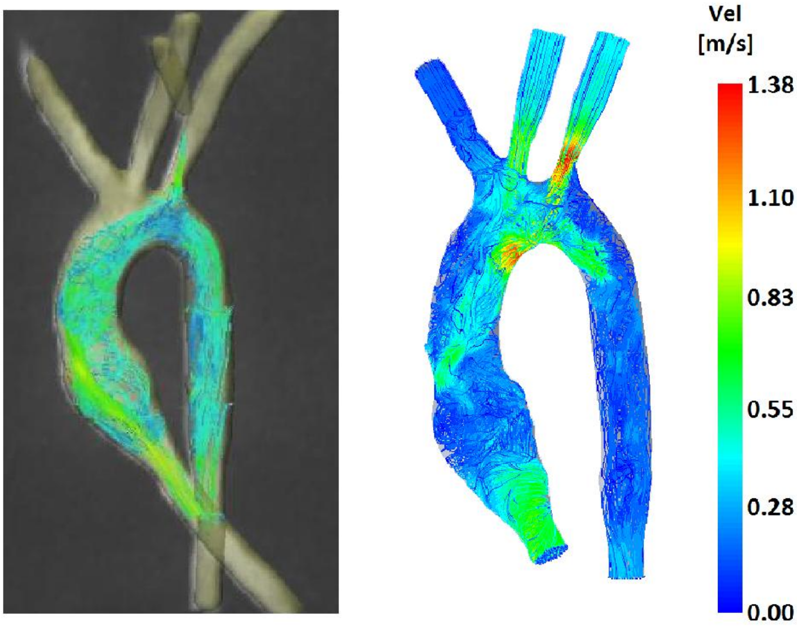

Figure 6.21 - Four-D flow streamlines (left) compared with CFD streamlines (right) at t_4= 0.6 s (diastole), in the Control model. The range of velocity is the same for both images

6.3.5 Comparison between TGA and Control geometries

Given the same inflow and outflow boundary conditions, the solely effects of the arch anatomy was investigated using the CFD approach. Mean flow rates and flow-splits at the outlet faces of both 3D models are reported in Table 6.5, while the waveforms at each outlet are reported in Figure 6.22.

Table 6.5 - Mean flow-rates and flow-splits obtained computationally at every outlet of the TGA and the Control models. Flow-split has been calculated as a percentage of the total inflow.

	Mean Flow Rate [L/min]		**Flow-split [%]**	
	TGA	**Control**	**TGA**	**Control**
Innominate	0.92	0.86	16.6	16.77
Carotid	0.54	0.57	9.7	11.20
Subclavian	1.17	0.87	21.1	16.87
Descending Aorta	2.92	2.83	52.6	55.16

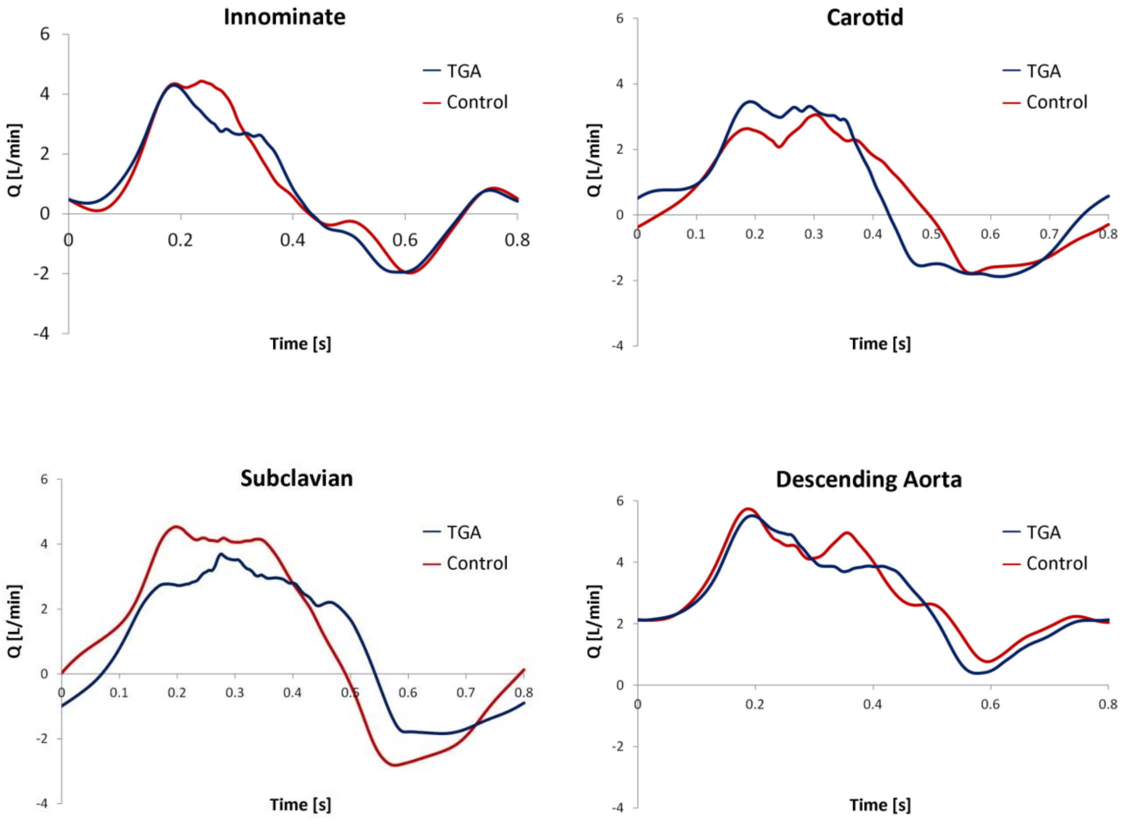

Figure 6.22 - Volumetric flow-rate waveforms obtained computationally at the outlets of the TGA (blue) and the Control (red) models over one cardiac cycle (T = 0.8s).

At all outlets, no substantial difference was noticed in the waveforms between the TGA and the Control model.

A comparison between velocity streamlines in the two different anatomies (with the same inlet flow and outlet LPN) at the four different temporal frames discussed before (0.1 s, 0.2 s, 0.4 s, 0.8 s) is shown in Figure 6.23.

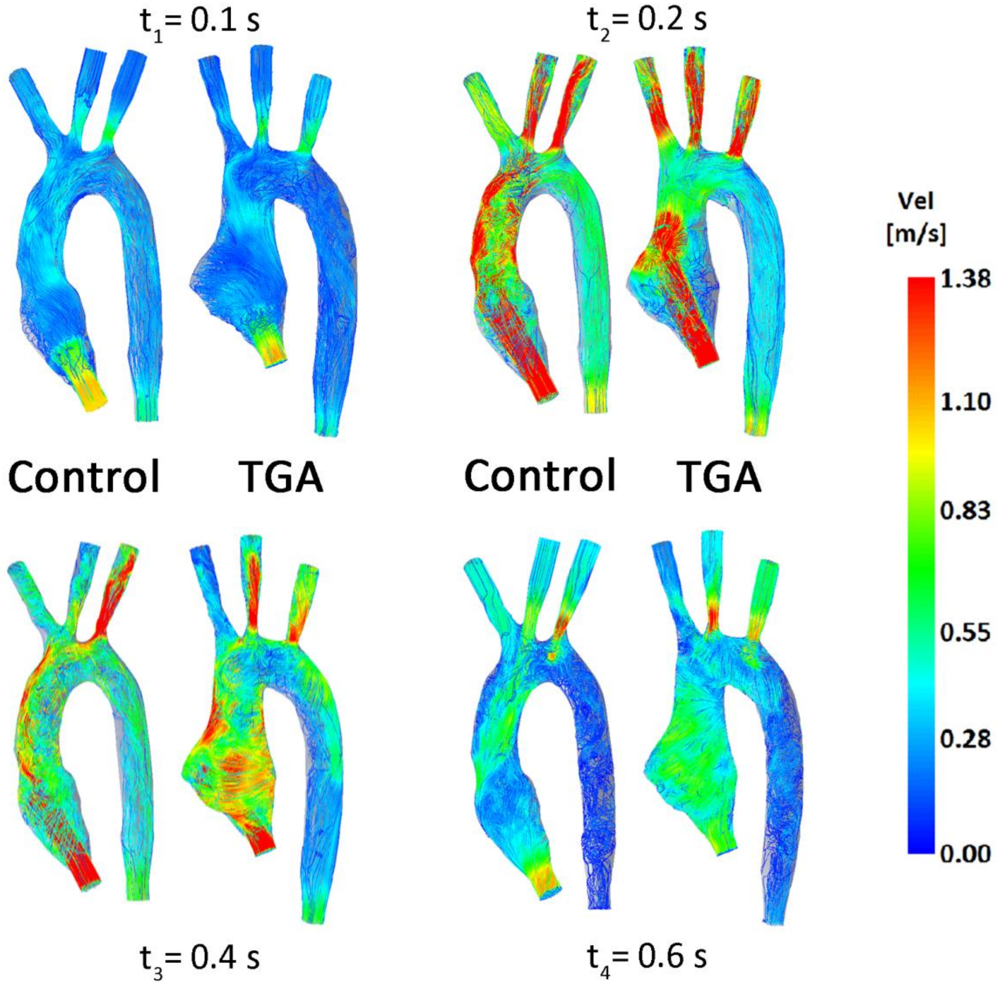

Figure 6.23 - Velocity streamlines in the Control and the TGA anatomies obtained computationally at early systole (t_1=0.1s), at peak systole (t_2=0.2s), at late systole (t_3=0.4s), and at diastole (t_4=0.6s).

At early systole (t_1 = 0.1 s) the velocity started to increase at the inlet of both models, but it was still low in the rest of the arches. In the Control geometry, the majority of the streamlines had a straight path following the geometric shape, while in the TGA the streamlines followed chaotic paths in the enlarged root, recovering a more regular trend in the descending aorta, after the aortic arch.

At peak systole (t_2 = 0.2 s) the geometries showed different behaviours. In the Control model, once again, the streamlines followed the arch. The velocity magnitude remained considerably large also at the level of the upper branches. In the TGA model, a flow jet through the inlet was clearly visible, and, being not directed as the curvature of the geometry, it hit the wall of the enlarged root, losing velocity before reaching the upper branches. Also, whirling streamlines, characterised by lower velocity magnitude, surrounded the main flow jet.

At late systole (t_3 = 0.4 s) what described for the systolic peak was still visible. In particular, higher re-circulation of flow particles around the root were visible for both models.

The diastolic phase (t_4 = 0.6 s) presented, as expected, lower velocities, and it should be noted that the inlet and all outlets except for the descending aorta were characterised by retrograde flow. The enlarged aortic root of the TGA case was perfused by chaotic streamlines.

The velocity vectors (Figure 6.24) at peak systole (t_2 = 0.2 s) showed the TGA model to have a more complex fluid dynamics than the Control model, with presence of secondary flows. While higher velocities in the Control model were clustered in the centre of the root mid-sectional plane, in the TGA model they had a random distribution.

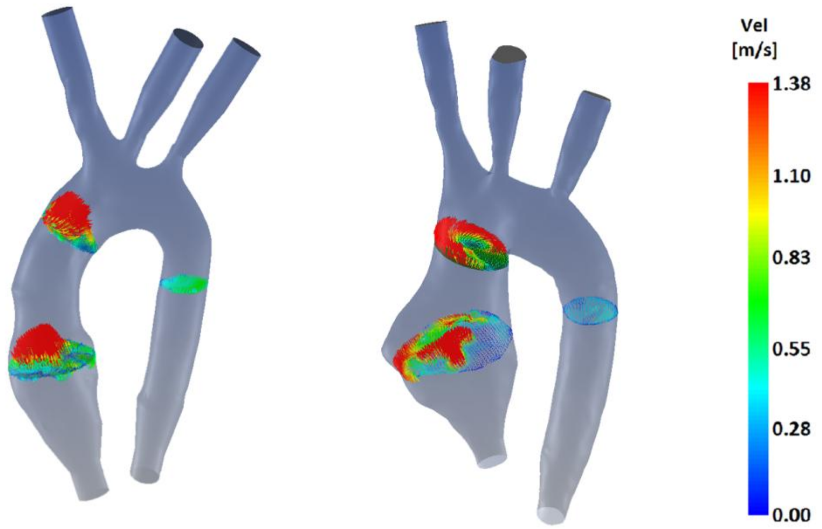

Figure 6.24 - Velocity vectors at peak systole (t_2=0.2s) in the Control (left) and the TGA (right) models.

6.4 DISCUSSION

This study successfully applied a modelling paradigm involving both experimental and computational tools to tackle a complex case of congenital heart disease. Specifically, TGA is a congenital condition presenting a wide range of complications, such as aortic root dilation (**35**), reduced aortic distensibility (**37**) and compromised ventricular-vascular coupling (**41**) on the aortic side, and unilater pulmonary artery stenosis on the pulmonary side (**29**). The full consequences and effects of TGA repaired with ASO are not fully appreciated yet, due to the relatively young age of the patients.

This work focused solely on the aortic side of the problem, using modelling techniques to evaluate the effect of the shape of the neoaorta in this group of patients. Overall, a patient-specific approach was chosen, and a validation study was carried out to demonstrate the reliability of the computational model.

Following from the presented results, a relatively simple and compact mock circuit proved to be an adequate tool to study TGA experimentally. By setting appropriate R and C boundary conditions, the mock circuit was able to accurately reproduce the pathological scenario of interest, at a patient-specific level, according to cuff pressure measurements. The boundary conditions in fact can be easily tuned manually adjusting the stroke volume and the heart rate of the pulsatile pump, the volume of air in the compliant chambers and the extent of closure of the taps used to implement vascular resistances. Moreover, using the manufacturing technique known as rapid prototyping, patient-specific geometries were obtained, and these could be easily mounted into the circuit, implementing patient-specific 3D information. This is important not only because it allows to take into account the variety in aortic morphology between different patients (by testing multiple models), but also because the study focused specifically on the hemodynamics within the neoaorta.

Such hemodynamic features can be appreciated experimentally by taking advantage of the imaging technique known as 4D MR flow (**131**). This requires, first of all, the construction of a MR-compatible mock circuit, which was successfully achieved in this work. 4D MR flow can be very informative in the field of congenital defects, as in cases of Fontan circulation (**132**) as well as bicuspid aortic valve (**133**). The advantage of using this technique, instead of standard 2D acquisitions, is that there is no need to plan flow acquisition prior to acquiring the data, which is collected over a volume of interest.

As a result, this can make the technique time-efficient, especially in those cases where multiple flows need to be planned and acquired (**81**), albeit acquisition time remains a concerns for clinical application of 4D MR flow, especially in children.

Furthermore, the post-processing of a 4D flow dataset gives access to exquisite flow visualisation, including streamlines and particle tracing, over the 3D volume of interest.

Only one study recently applied 4D MR flow to the study of TGA in humans (**134**), however there are several advantages linked to using an in-vitro approach. Firstly, the use of a hydraulic circuit solves problems related to patient's motion, which are of particular concern especially in younger patients and over a long acquisition (15-20 minutes, or more). Moreover, the circuit can be kept inside the scanner for as long as required, and this is useful if multiple acquisitions are necessary. For example, in this study a 1 hour and 10 minute long high spatial and high temporal resolution sequence was performed on the model. The reason to perform this additional scan was to evaluate whether increased resolution provided access to meaningful additional fluid dynamic details, especially in complex geometries, such as TGA. In this work, because of the compromised SNR, it was not possible to get more information than from the standard sequence. This point could be tackled in the future from an MR physics perspective, trying to acquire high resolution sequences without compromising SNR and ongoing work in the MR unit at Great Ormond Street Hospital is evaluating the complexities of 4D flow acquisition. However, as the results of the 'standard' (15 minute) sequence were satisfactorily informative for the hemodynamic problem under investigation, further work in this context was deemed not necessary.

Full datasets were ultimately acquired experimentally for the TGA anatomy and the age-matched healthy control model. In both cases, pressure values were in agreement with cuff pressure readings obtained at the time of the clinical MR scan (Pmean = 80 mmHg). On the other hand, flow distribution between upper and lower body and in the different head and neck vessels was ensured to be realistic but was not set to patient-specific values, as flow data is not acquired in each brachiocephalic vessel in routine clinical scans, so these data were not available.

All the experimental acquisitions of this work were carried out using rigid models. Rigid models are easy to mount and robust. Also, transparency associated with some of the rigid resins used for printing rigid models are important for visualisation studies as particle image velocimetry (PIV) (**101**), albeit not necessary for MR imaging. The disadvantage of using a rigid material, on the other hand, is that it does not take into account the compliant behaviour of the human vessels and the associated recoiling effect in diastole. However, being the computational study designed using 3D rigid-walled models, validation data was successfully provided from the models printed in rigid resin.

As shown in the results, the CFD simulations are in overall good agreement with the experiments. This eventually allows proceeding with a solely computational approach, whether different patient-specific anatomies need to be included in the study. Although it is possible to properly set the boundary conditions also with an experimental approach, a computational approach guarantees their stability. In fact, minor leaks can occur while gathering experimental data, especially over long acquisitions (i.e. multiple scans in the MR). Also, other changes are not straightforward to monitor, e.g. if a solution of water and glycerine were used, its content is prone to changes in viscosity with small changes in temperature.

Computationally, it is also possible to easily undertake parametric studies, simply changing one parameter at a time in order to understand its influence on the fluid dynamics. The only concern in this case is the computational cost of each additional simulation, rather the time associated with re-assembling an experimental rig. It is also possible to extract retrospectively other parameters and values of interest at different locations in the model, not necessarily planned beforehand, while this is not possible in an experimental study. Also, from a modelling point of view, it would be easier to implement non-concentrated resistances, avoiding the use of the taps not able to model the resistances in a physiological way.

In this study two different simulations were performed, the only difference among them being the 3D element in the multi-scale network. This approach is suitable to understand how the geometry alone affects the fluid dynamics, effectively isolating one variable in a complex clinical problem. Indeed, making use of the computational validated methodology, it would be possible to virtually create aortic morphologies resulting from different surgical techniques such as for example the spiral operation (Section 2.5.4), it would be possible to evaluate the potential hemodynamics benefits of each interventional methodology.

Being this a preliminary study, no clinical conclusions can be withdrawn. First of all, the use of water instead of a liquid resembling the blood properties limits the reliability of the results from a diagnostic point of view. This problem could be easily bypassed at this point by running computational simulations with different fluid properties. Also, the absence of a valve at the inlet of the model alters the fluid dynamics reproduced experimentally. The jet flow impinging on the root wall is more likely due to the design of the mock circuit, with a pipe of contained diameter and considerable length connecting the outflow of the pump to the inlet of the 3D model, thus creating a high velocity jet profile. This profile would be limited by using a higher fluid viscosity, and by using a computational model that does not include the extension of the inlet, designed only for experimental purposes.

A more physiological model could give additional and reliable information on the fluid dynamics and on the wall shear stress distribution on the wall. The risk of having high WSS is potential mechanical damage of the inner wall of the vessel (**135**; **136**), which could in turn weaken the vessel and possibly initiate a lesion. The combination of these two factors may have an impact in long-term pathologies, in particular the development of aortic dilatation (**137**). This effect, added to the already enlarged root of TGA patients because of the surgical operation, may leads to structural failure of the vessels. For this reason, a computational study investigating such variables could help the clinicians in a better understanding of the ASO drawbacks, and eventually, in the development of different surgical approaches.

Interesting would be the comparison of the in-vitro results with both a CFD model using a laminar solver and one using a turbulent solver, to better simulate the systolic peak characterised by high Reynolds numbers. Amongst the others, the k-ω model could be chosen as literature studies (**56**; **129**; **130**) suggest that to be suitable for modelling flows where both transitional and turbulent regimes may occur.

Finally, the compliant behaviour of the wall was not taken into account in this study, neither experimentally or computationally. CFD simulations assumed rigid vessel walls, so different distensibility was not an issue. Admittedly, such variations in vessel compliance have been reported also at young ages (**138**), but these are not as meaningful as much more significant changes in distensibility occurring later on in life. Fluid structure interaction approaches could overcome this limitation, but accurate patients' vessel wall material properties should be known.

6.5 CONCLUSIONS

The fluid dynamics of a patient who underwent treatment for TGA and that of a healthy subject were successfully modelled experimentally, and afterwards replicated computationally using a multi-domain approach. The mock circulatory system, which included a rapid prototyped patient-specific 3D element for both the TGA and the control case was tuned according to clinical data. CFD simulations coupled with a LPN properly tuned in order to exactly replicate the conditions of the experiments were performed, thus using the experimental data to validate the computational models. Computational results were in good agreement with their experimental counterpart, showing that a multi-domain approach provides a reliable methodology for hemodynamics evaluations in complex patient-specific models. In the next chapter, the CFD and LPN modelling techniques developed and validated in this study are applied and integrated into an innovative framework for better understanding of unilateral pulmonary artery stenosis hemodynamics.

CHAPTER 7

UNILATERAL PULMONARY ARTERY STENOSIS IN TGA PATIENTS

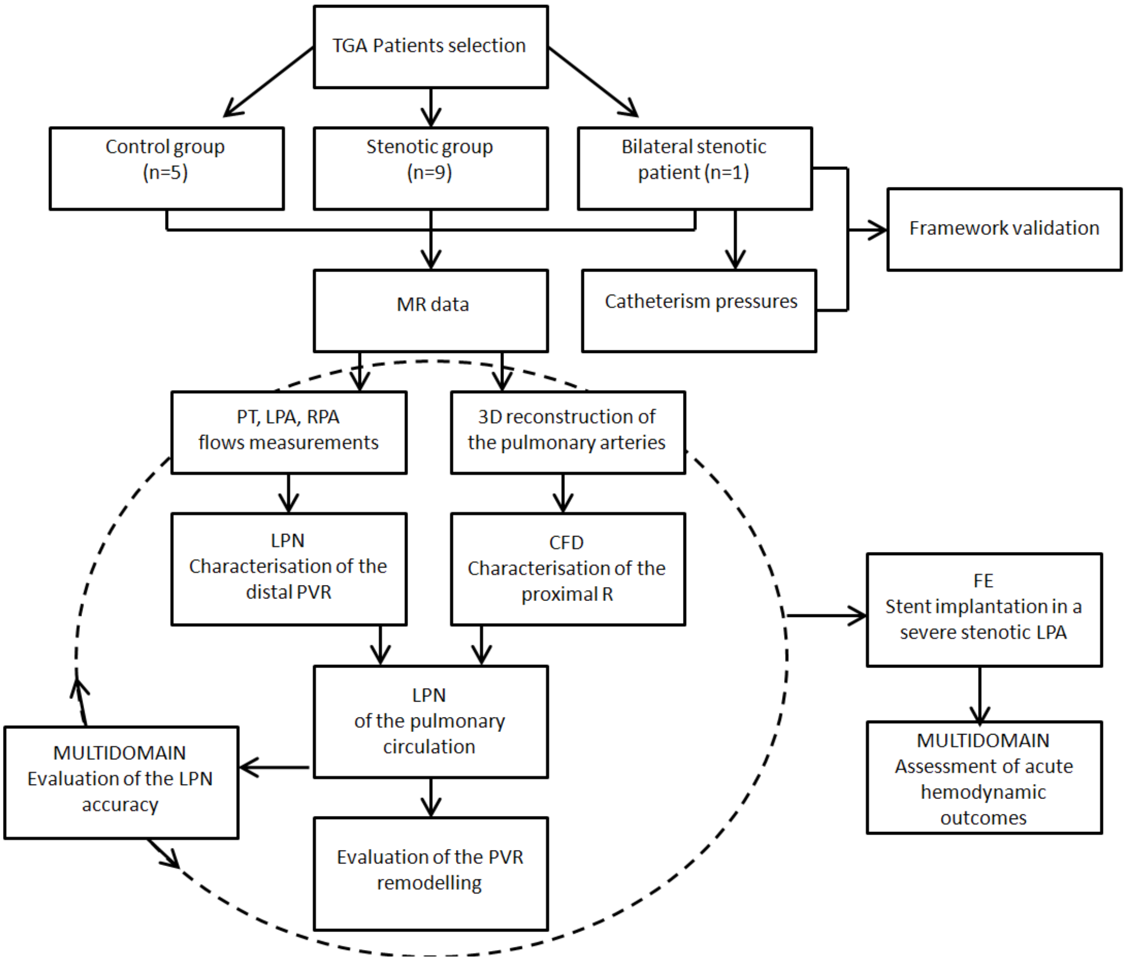

7.1 INTRODUCTION

In the previous chapter, I created a multi-domain model coupling a 3D volume of the region of interest to an open LPN representing the reminder of the circulation. This methodology, applied to model the aorta of a TGA patient and of a control subject, was validated against in-vitro experiments and provided important information on the local hemodynamics. In this chapter, I propose to employ the validated computational methodology to further develop engineering tools that would enhance our understanding of patient-specific general hemodynamic conditions. In particular, LPNs were used to model the pulmonary circulation and study another complication of TGA patients after ASO: stenosis of the branch pulmonary arteries (**139**). Typically, during surgery the left pulmonary artery (LPA) of the patient is forced to lengthen in order to allow the anastomosis of the pulmonary trunk (PT) to the RVOT (Figure 7.1b-d). This complication is usually associated with reduced flow to the affected lung and thus abnormal differential pulmonary blood flow. The preferred therapeutic option is balloon angioplasty (with or without stenting) which improves pulmonary blood flow to the affected lung by reducing the resistance to flow caused by the narrowed artery lumen (Figure 7.1a). However, there are cases in which angioplasty or stenting has little effect on clinical symptoms.

In some patients, the expected relationship between stenosis and reduced pulmonary blood flow does not hold true, and there is equal flow split to both lungs despite the clear presence of an anatomical stenosis. One currently accepted explanation for this phenomenon takes into account the remodelling of the peripheral pulmonary vascular resistances (PVR) which counteracts the presence of the stenosis, thus readjusting the flow split to physiological levels. Raised contralateral PVR may balance the effects of the unilateral stenosis and explain the poor results after relieving of this stenosis by balloon/stenting procedure on clinical symptoms.

Further studies assessing the complex haemodynamics of unilateral pulmonary stenosis should be carried out to enhance our understanding of this phenomenon and improve treatment outcomes. The reference standard method is cardiac catheterisation; however, such an invasive test is not warranted in patients who do not undergo angioplasty/stenting.

Non-invasive imaging modalities, such as cardiovascular MR can be particularly useful in the diagnosis and management of these patients, as it provides both anatomical and flow distribution data to develop patient-specific computational models. Therefore, in this study, I propose to combine MR data and computational models to study patients with unilateral pulmonary artery stenosis in order to assess PVR remodelling and acute hemodynamic outcomes of stenting procedure, with no need for additional invasive measurements.

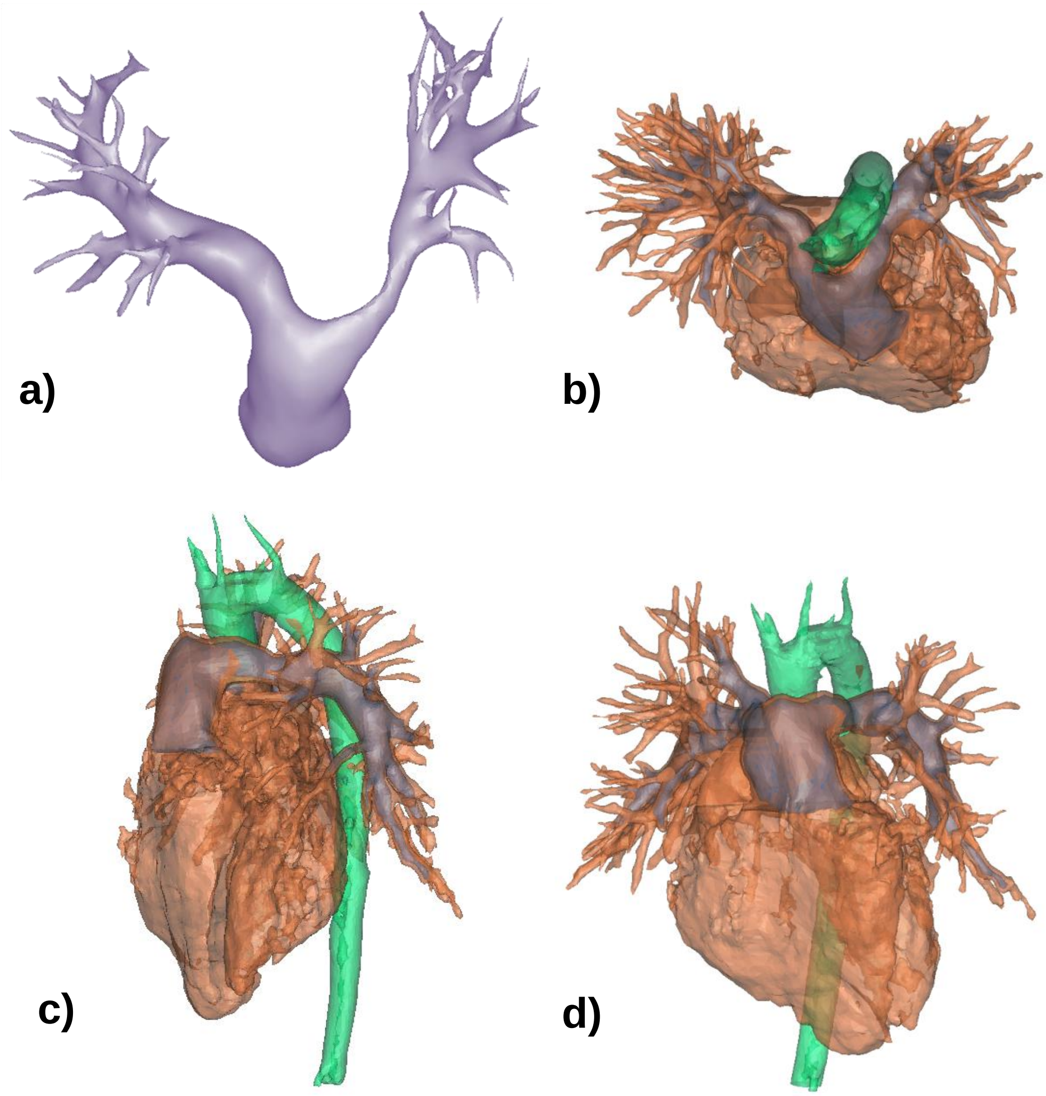

Figure 7.1 - 3D volume rendering of the cardiac structures in a TGA patient corrected by ASO. Presence of a unilateral branch pulmonary artery stenosis in the left side (a). Relationship between pulmonary artery (blue) and aorta (green) showed in (b,c,d)- top and lateral views.

7.2 MATERIALS AND METHODS

MR scans from TGA patients after ASO were used to reconstruct the patient-specific 3D pulmonary tree anatomy and acquire pulmonary blood flows. Different modelling techniques were strategically employed to quantify the hemodynamic effects of the stenosis, the amount of peripheral PVR remodelling and the acute outcomes of stenting procedure in a patient with severe LPA obstruction. 3D CFD analyses were used to characterise the proximal LPA and RPA resistances. A 0D LPN was set up to simulate, with low computational costs, the pulmonary tree circulation of each patient. Peripheral PVR and compliances were tuned in the LPN until the flows in the computational model matched the known MR flow data in the branches for each patient. Finally, a FE simulation was carried out to obtain the lumen of the stenotic branch vessel after virtual stenting procedure, and to analyse the resulting fluid dynamics after stenosis relief.

7.2.1 Patient population and MR imaging

Fifteen patients who underwent ASO for correction of TGA were retrospectively selected from our Centre database according to the following criteria: i) cardiovascular MR scan performed in the second decade of life, ii) MR images with voxel size < 2mm and no visible artefacts, iii) continuity in the inflow-outflow PA balance from MR flow data measurements (differences <7% of the inflow considered acceptable), and iv) no pulmonary hypertension.

The MR 3D whole heart sequence was used to reconstruct the blood volume of PT, LPA and right pulmonary artery (RPA) before further branching (Section 3.5.1) (Figure 7.2).

Patients were divided in 2 groups, according to the presence/absence of pulmonary stenosis as stated in the clinical MR report: control group CG (n=5) of patients with no pulmonary artery stenosis; and stenotic group SG (n=9) which comprised patients diagnosed with LPA unilateral stenosis (n=9). An additional patient with bilateral pulmonary stenosis (BPS) was included in the study to validate the developed methodology as he underwent diagnostic cardiac catheterisation 16 months after MR examination as part of his clinical assessment.

The degree of stenosis for SG and BPS was quantified from the 3D anatomical reconstruction as:

$$\%\mathrm{Stenosis} = \left(1 - \frac{D_{stenosis}}{D_{vessel}}\right) * 100$$

where $D_{stenosis}$ is the diameter at the narrowest section of the vessel and D_{vessel} is the diameter of the vessel downstream the narrowing, with the diameters derived from the cross-sectional area of the sections of interest. Stenoses ≤10% were considered absent/trivial, between 10% and 40% mild/moderate, and ≥40% severe (Table 7.1) (**140**).

Inflow (PT) and outflows (pulmonary branches) were calculated from MR phase contrast velocity mapping images (Section 3.4.1.1, Table 7.1). LPA flows ranging from 40% to 50% of the total pulmonary flow are considered physiological due to the different morphology of the left and right lung (**141**). Therefore, 5 out of 9 SG patients (SG3, SG4, SG5, SG8 and SG9) had expected reduced flow to the left lung due to the LPA stenosis, while the other 4 presented balanced flow split – even slightly higher flow towards the LPA – despite the presence of the stenosis.

Average age at scan was 16 years (12-18 years) for CG and 14 years (9-18 years) for SG, while the average body surface area (BSA) was 1.76 m^2 (1.44-2.00 m^2) for CG and 1.56 m^2 (1.10-2.00 m^2) for SG (Table 7.1).

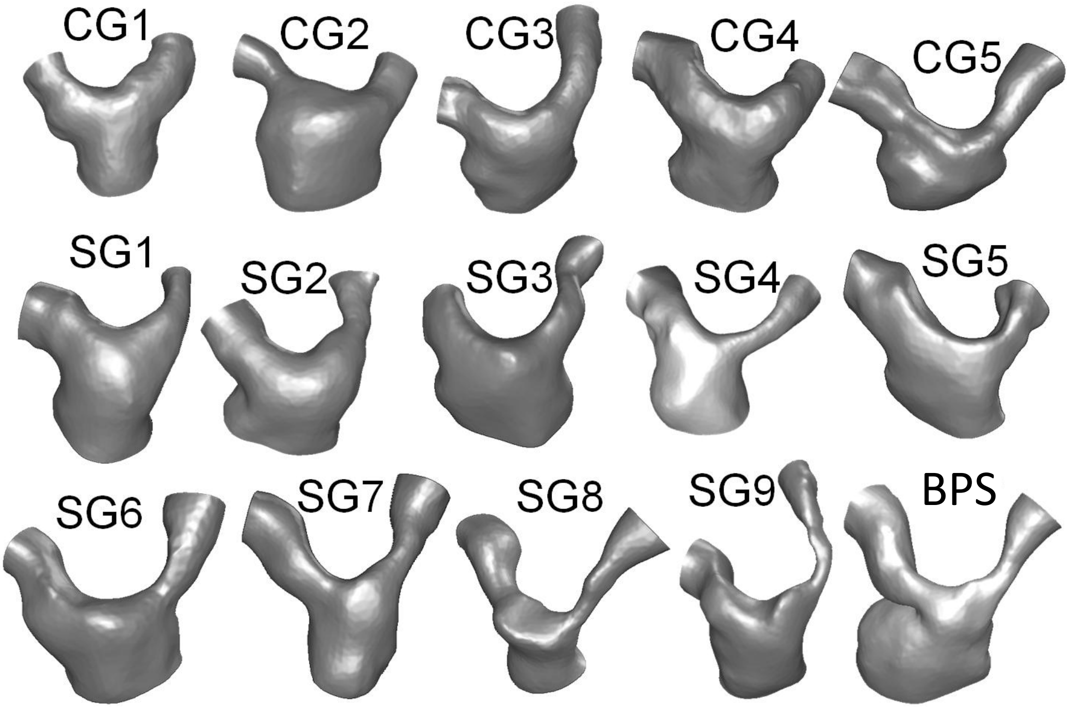

Figure 7.2 - Volume rendering of PT, LPA and RPA for each patient included in the cohort.

Table 7.1 - Patients population and categorisation according to the presence/absence of stenosis.

Patient ID	**Gender**	**Age at scan [yrs]**	**BSA [m^2]**	**LPA Stenosis degree [%]**	**LPA Stenosis classification**	**LPA:RPA flow split**
CG1	F	18	1.88	-	-	43:57
CG2	M	12	1.44	-	-	46:54
CG3	M	17	2.00	-	-	50:50
CG4	F	16	1.60	-	-	52:48
CG5	M	16	1.90	-	-	54:46
SG1	F	18	1.38	7	Trivial	53:47
SG2	M	11	1.10	23	Mild-moderate	43:57
SG3	M	16	1.68	39	Severe	31:69
SG4	M	15	1.80	40	Severe	38:62
SG5	F	13	1.35	44	Severe	33:67
SG6	F	14	1.93	58	Severe	50:50
SG7	F	13	1.70	60	Severe	52:48
SG8	M	17	2.00	65	Severe	35:65
SG9	M	9	1.14	70	Severe	38:62
BPS	M	14	1.91	53 (RPA 59)	Severe (RPA: Severe)	52:48

7.2.2 Lumped parameter network

A schematic representation of the open-loop LPN used to model the pulmonary circulation is shown in Figure 7.3, where R_{RPA} and R_{LPA} represent the two proximal pulmonary branch resistances, while the downstream arterial circulation and the venous circulation are modelled with a 2-element Windkessel blocks respectively on each side of the bifurcation.

R_{RPA} and R_{LPA} were obtained through hydraulic characterisation as described in the following paragraph (equations 1 or 2) using stand-alone 3D CFD analyses.

Allometric equations from literature (**126**; **142**) were adopted to set the relationship between peripheral arterial resistance (R_a) and venous resistance (R_v) for each pulmonary side (R = right, L = left) $\frac{R_{Ra}}{R_{Rv}} = \frac{R_{La}}{R_{Lv}} = 0.3$ and between total equivalent resistances and compliances $\frac{C_{Rtot}}{C_{Ltot}} = \left[\frac{R_{Rtot}}{R_{Ltot}}\right]^{-0.75}$, with R_{Rtot} and R_{Ltot} = total equivalent resistances for the right and left side respectively, and C_{Rtot} and C_{Ltot} = total equivalent compliances for the right and left side respectively.

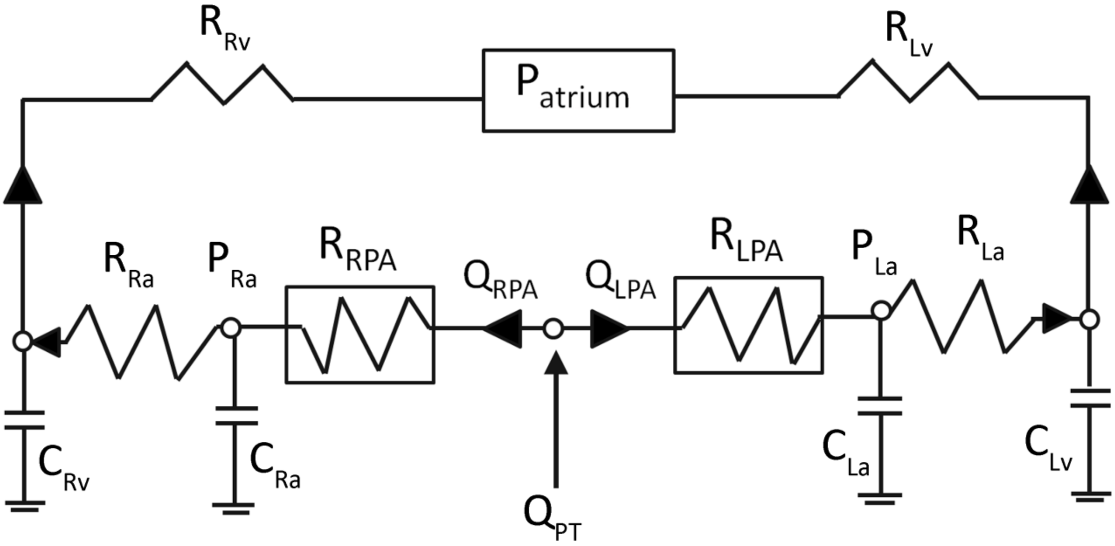

Figure 7.3 - Schematic representation of the open-loop LPN used to model the pulmonary circulation of the TGA patients.

LPN simulations were set-up and compiled as indicated in Section 3.5.2.2. Twenty cardiac cycles were simulated per analysis, with the last used in the post-processing of the results.

7.2.3 Characterisation of the proximal resistances R_{RPA} and R_{LPA}

A CFD model was created for each patient from the 3D MR reconstructed anatomy. A tetrahedral grid mesh with 800,000 volumes (0.5 mm element size) was chosen after a sensitivity analysis and an adaptive mesh refinement was further implemented (**126**; **127**). The blood was assumed to be Newtonian and incompressible (density $\rho = 1060$ kg/m^3 and viscosity $\mu = 0.003$ Pa·s). CFD simulations were performed using the discretisation schemes and the convergence criteria indicated in Section 3.5.2.1 with the software Ansys Fluent. For unsteady simulations, a time-step of 10^{-4} s was applied, and 4 cardiac cycles per analysis were simulated to ensure stable computational solution.

The main aim of this study was to evaluate the flow distribution between RPA and LPA, with no specific focus on the local fluid dynamics; therefore, a laminar solver was adopted despite the risk of turbulence generation during the systolic peak in severe stenoses.

Stand-alone CFD steady simulations were carried out to characterise the 3D model of the pulmonary branches in terms of hydraulic resistances by inputting 6 different constant flows (0 to 10 l/min), representative of the patients' flow range, at the inlet, and a constant pressure of 8 mmHg, matching the left atrial pressure, at each outlet.

Pressure drops ΔP, measured in each branch as P_{PT}-P_{LPA} and P_{PT}-P_{RPA}, were plotted versus the flow Q streaming in the branch (Q_{LPA} and Q_{RPA}), and either a linear relationship (equation 1) or a second degree polynomial relationship (equation 2) was used to interpolate the obtained data points:

$$\Delta P_{branch} = R_{branch} Q_{branch} \qquad \text{(equation 1)}$$

$$\Delta P_{branch} = a Q_{branch}^{2} + b Q_{branch} \qquad \text{(equation 2)}$$

The coefficient R_{branch} or the coefficients a and b defined the proximal branch resistances in every patient and the characteristic curves were used in the LPN.

The results were further validated using unsteady simulations which are more computationally expensive, but account for the dynamic effects in the bifurcation. In these analyses, the time-varying flows measured from patients' MR were imposed as boundary conditions at the inlet and at the right outlet of each model, and a constant pressure of 8 mmHg was set at the left outlet.

7.2.4 Peripheral PVR remodelling

A first set of LPN simulations was run to quantify the flow split based on pure anatomical consideration when assuming that there is no remodelling of the peripheral PVRs and compare this with the measured flow split from MR.

A split between the peripheral resistances R_{Ltot} and R_{Rtot} = 55:45 was considered physiological (**141**) to account for the different lung morphology, and total peripheral PVR was assumed = 1 WU. The difference between the flow-split obtained in the hypothesis of no peripheral remodelling and the real flow-split measured from MR was adopted as index of the amount of remodelling experienced by the patient.

7.2.5 Characterisation of the peripheral parameters

In the LPN, the characteristic curves derived from the CFD analyses were implemented for R_{LPA} and R_{RPA}, and the peripheral parameters were tuned by changing the percentage ratio between the total right and left resistances, in order to obtain the MR flow split and curves of the patient at the outlets of the model. The time-variant patient PT flow was imposed at the inlet of the each model.

Six simulations were performed for all patients by varying the total peripheral PVR between 1 and 10 WU (1, 2, 4, 6, 8, 10 WU) to account for physiological and mild hypertensive scenarios (**143**; **144**; **145**; **146**). The total compliance of the circuit was maintained in a physiological range, estimated around 2 ± 1.1 mL/mmHg (**126**; **142**; **147**).

The tuning of resistances and compliances was considered achieved when the difference between the flow split generated by the LPN and that measured from MR was $\leq 1\%$. The values of the pressures distally to the LPA (P_{La}) and RPA (P_{Ra}) obtained from the LPN were compared to physiological values to evaluate the effects of the choice of total peripheral PVR.

In addition, pulmonary artery pressures were available for BPS who underwent diagnostic catheterisation. These data were used to calculate the patient's peripheral left and right PVR as follows:

$$R_{Ltot} = \frac{\Delta P_L}{Q_{LPA}} = \frac{(P_{La} - P_{atrium})}{Q_{LPA}} = 1.65\,WU$$

$$R_{Rtot} = \frac{\Delta P_R}{Q_{RPA}} = \frac{(P_{Ra} - P_{atrium})}{Q_{RPA}} = 2.08\,WU$$

with P_{La} = 14 mmHg and P_{Ra} = 15 mmHg pressures measured downstream the left and right stenoses respectively. These resistances were compared to those obtained from the tuning process of the network created for the BPS patient, and the LPN resulting pressures P_{La} and P_{Ra} distal to the stenosis were compared with the patient's data, in both cases: when the newly calculated peripheral resistances were inputted in the LPN, and when the LPN was blindly tuned.

Once the parameters for the peripheral circulations were assessed to reproduce each patient's real flow-split, the proximal resistances R_{RPA} and R_{LPA} were replaced in the LPN with the realistic 3D geometry of the bifurcation (multi-domain analysis coupling 3D and 0D elements) to validate the LPN model of the 3D hydraulic characterisation.

7.2.6 Simulation of the stenting procedure

A virtual stenting procedure was performed in a patient with severe LPA stenosis (SG7) using Abaqus Explicit. The previously developed computational model of the CP stent with 6 crown (Section 5.2.5) was modified into a 3-crown stent and was expanded using a uniform pressure (1.0 Pa) in the patient-specific reconstructed LPA anatomy (arterial wall surface) to relieve the stenosis (Figure 7.4a-b). The patients' arterial wall was modelled as a shell with 11,360 triangular elements with reduced integration (S3R) and linear-elastic material properties from literature (E=0.7 MPa; ν=0.25) (**41**; **150**). A contact algorithm was activated between the outer surface of the stent and the inner surface of the LPA.

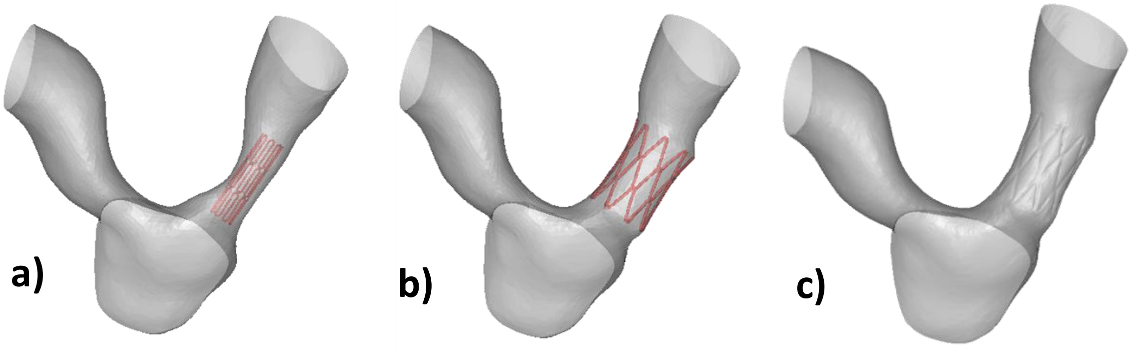

Figure 7.4 - Simulation of stenting procedure for patient SG7: FE stent expansion in the narrowed LPA (a and b), and extraction of the resulting blood volume after stenting (c).

The resulting blood volume with no LPA stenosis was extracted (Figure 7.4c) and remeshed with tetrahedaral elements of the same size of the non-stented volume (0.5 mm element size) to run a new CFD analysis in order to characterise the new R_{LPA} and R_{RPA} after stenting. These new values were inputted in the LPN representing the patient without changing the peripheral resistances and compliances to assess the acute hemodynamic outcomes of the stenting procedure.

7.3 RESULTS

7.3.1 Characterisation of the proximal resistances R_{RPA} and R_{LPA}

The coefficients of the pressure drop equations (equations 1 and 2) over each branch were estimated for each patient. Both branches of the 5 CG patients were best represented through linear relationships. 5 out of 9 SG patients were modelled with one linear (RPA) and one non-linear (LPA) relationship, while in the other 4 and in BPS, both branches were represented with non-linear equations.

In the stenotic vessels, the same non-linear equation best-fitted the results of both the steady and the unsteady simulation. In the non-stenotic branches, the unsteady simulations showed the presence of a hysteretic cycle, due to inertial effects, with a width proportional to the diameter of the vessel. Values of inertia L, estimated from $\Delta P = L\frac{dQ}{dt}$, were in good agreement with literature data (**126**; **148**). In steady simulations, the inertial effects are not included, but it emerged that the best-fitter was located in the centre of the hysteretic loop of the unsteady results (Figure 7.5 and Figure 7.6). Satisfactory results were obtained without the inclusion of the inertial parameter in the LPN; therefore, the inertial contribution in the networks was discarded to reduce computational time.

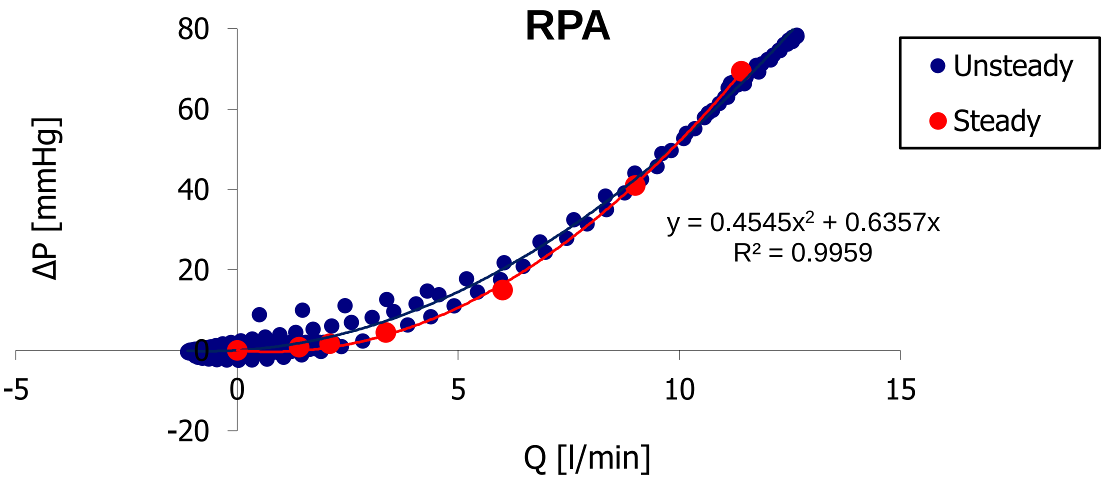

Figure 7.5 - Characterisation of the hydraulic resistances for the BPS patient: results of steady and unsteady simulations superimposed for the RPA.

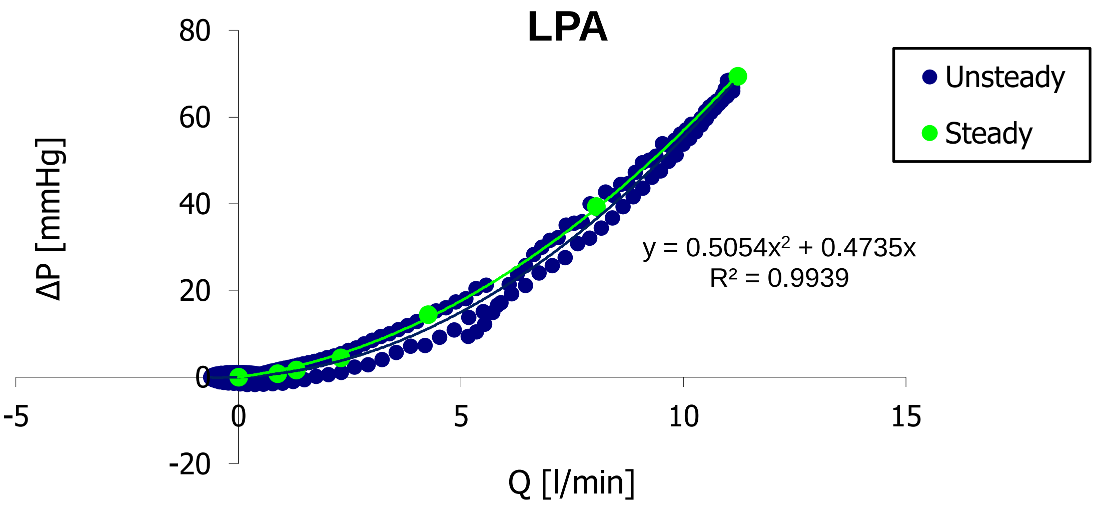

Figure 7.6 – Characterisation of the hydraulic resistances for the BPS patient: results of steady and unsteady simulations superimposed for the LPA.

7.3.2 Peripheral PVR remodelling

The difference between the flow resulting from the LPN simulations in the hypothesis of no remodelling and the patients' flow measured from MR in SG cases is depicted in Figure 7.7. The LPN left artery flow was lower than the measured flow meaning that if there was no change in the peripheral PVR, the flow to the stenotic LPA should be lower due to the presence of the unilateral stenosis as expected. In two patients, SG3 and SG5, the estimated left flow was slightly higher than the measured one (2% and 7% respectively), suggesting that some peripheral remodelling may occur even in the opposite direction, thus further unbalancing the flow split. However, such small differences may also be ascribed to errors in flow measurements.

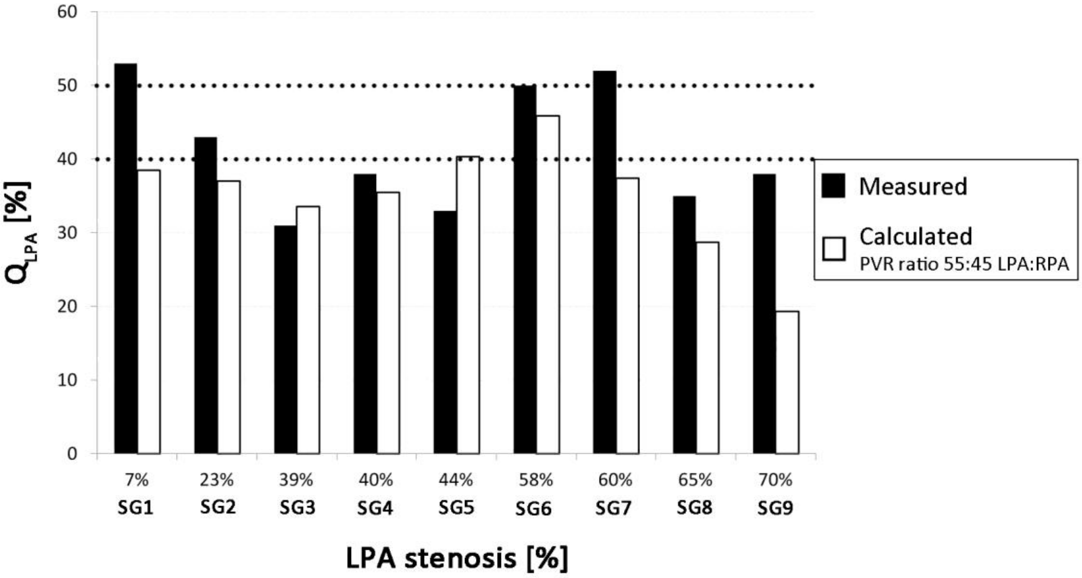

Figure 7.7 - Flow-split calculated as percentage of flow going to the LPA. Comparison between the flow split clinically measured (black bars) and the flow-split obtained from the LPN simulation in the hypothesis of no remodelling with PVR ratio set to 55:45 between LPA:RPA (white bars). Patients ordered according to the increasing degree of LPA stenosis. The range of physiological flow-split values is highlighted by the black horizontal dotted lines.

7.3.3 Characterisation of the peripheral parameters

The six LPN simulations with varying total peripheral PVR, showed, as expected, that with the increase of the total resistance, the contribution of the geometry on the flow-split become less important. The percentage resistance imposed on the left side to obtain the desired flow-split is reported as a function of the chosen total PVR, for the CG and SG patients in Figure 7.8 and Figure 7.9 respectively. In the CG patients, the branch resistances slightly changed with increasing PVR, but in general, from 2 WU, the geometry did not have an influence on the flow split. In the SG group of patients, a more complex behaviour arose. Indeed, in one of these patients – that with the most severe degree of stenosis (SG9, 70%) – it was not possible to reach the measured flow-split for low values of PVR, as the geometry completely overcame the effect of the peripheral resistances in the determination of the flow-split. Although the trend of the remaining eight patients was similar to that of CG, some differences were noticed: in some cases (SG2, SG3, SG4, SG5 and SG6), the measured flow split was reached with PVR almost balanced between the two branches also for low total PVR; in other patients (SG1, SG7 and SG8), the resistance distribution between right and left side to reach the desired flow split was particularly asymmetric at low PVR. At higher levels of PVR (>4 WU), the percentage of resistance on the left side tended to be equal to the value that the left resistance would assume if the 3D geometry was symmetric (Figure 7.9).

In terms of pressure, with the increase of total PVR, the pressures raised in both branches as shown in Figure 7.10 for CG and Figure 7.11 for SG.

The hypothesis of total PVR ≥ 4 WU was discarded as the resulting mean pressures from the simulations were physiologically unacceptable (**48**; **143**). In addition, for SG9, the flow-split was reached for a minimum of total PVR = 2 WU with physiological resistance distribution between LPA and RPA, but this total PVR was not sufficiently low to determine acceptable values of pressure.

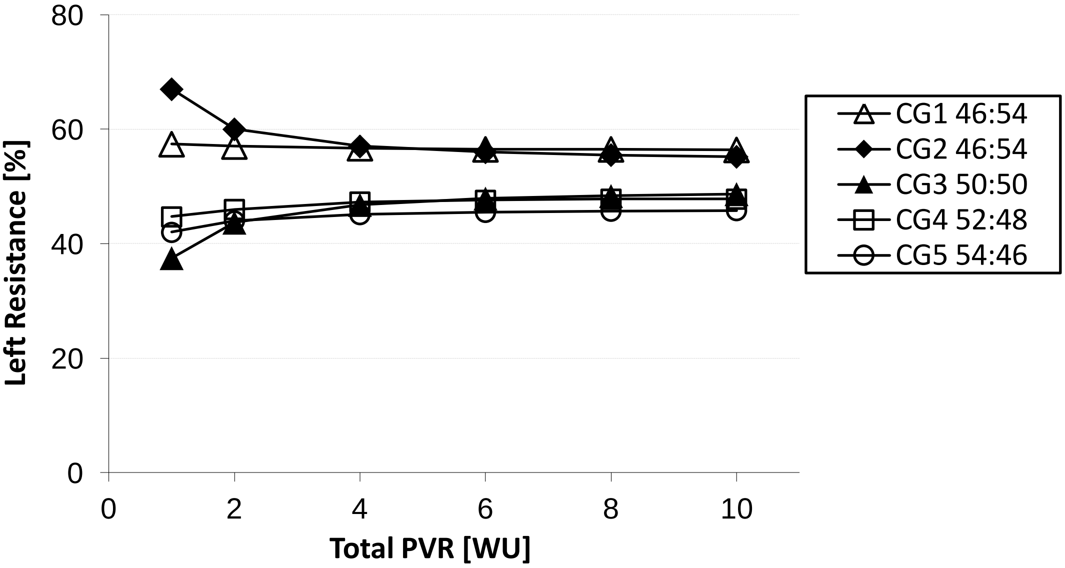

Figure 7.8 - Control patients: percentage resistance imposed on the left side to obtain the desired flow-split reported as a function of the chosen total PVR.

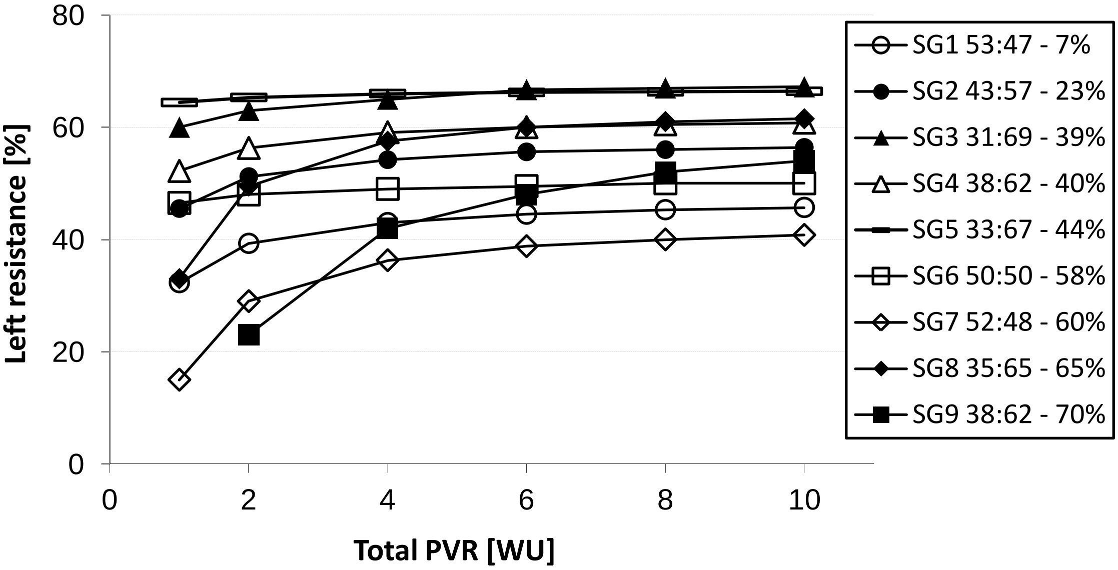

Figure 7.9 - Stenotic patients: percentage resistance imposed on the left side to obtain the desired flow-split reported as a function of the chosen total PVR. In the legend, the LPA stenosis degree is reported for every patient.

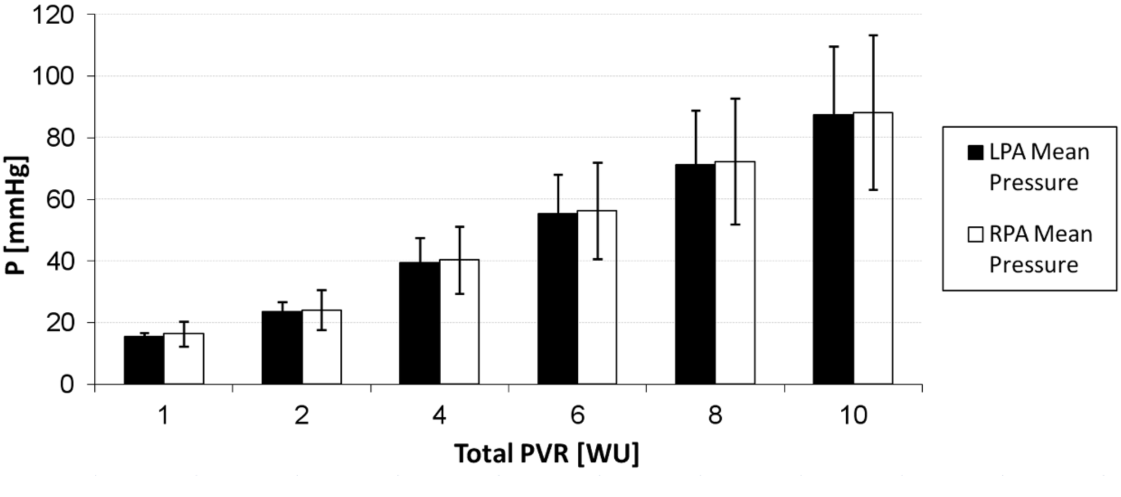

Figure 7.10 - Mean and systolic pressure obtained at LPA and RPA as function of total distal PVT averaged over the control group.

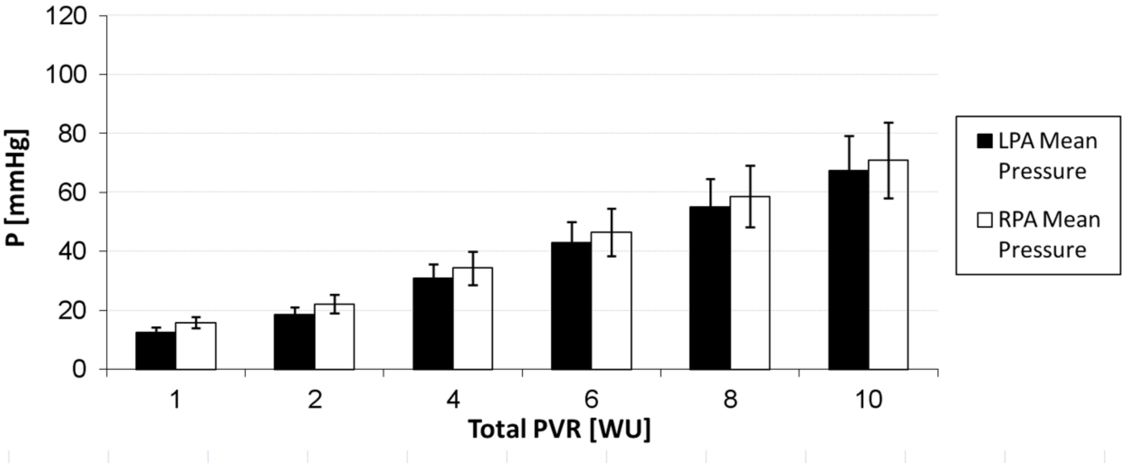

Figure 7.11 - Mean and systolic pressure obtained at LPA and RPA as function of total distal PVT averaged over the stenotic group.

For BPS (Table 7.2), the flow-split obtained with peripheral resistances of the network calculated from the catheterisation pressure data was 51:49 in favour of the LPA, equal to a difference of 1% with the clinical data (52:48) (Figure 7.12 and Figure 7.13). Clinical mean pressures were satisfactorily approximated by the LPN obtained by blindly tuning the parameters: for total distal PVR = 1 WU, P_{La} and P_{Ra} averaged over one cardiac cycle resulted both equal to 15 mmHg, while the pressures measured from catheterism were 14 mmHg at both sides. The LPN with peripheral resistances calculated from the catheterisation satisfactorily approximated the clinical mean pressures in both the left and right branch (6.7 and 7.1% of difference respectively). Systolic peaks were slightly overestimated in the LPN by 3 mmHg in the LPA and 2 mmHg in the RPA, while diastolic pressures were underestimated by 5 mmHg for the LPA and 4 mmHg in the RPA.

Table 7.2 - Flow split and pressure at LPA and RPA of the BPS patient: clinical measurements are compared with the LPN values obtained in case of blind tuning of the peripheral resistances and in case of peripheral resistances imposed from catheterisation pressure data.

	Clinical data	**LPN with tuned peripheral R (PVR=1 WU)**	**LPN with calculated peripheral R**
Q_{LPA} [%]	52	52	51
Q_{RPA} [%]	48	48	49
P_{LA} [mmHg]	14 (24/12)	15 (28/7)	14 (27/7)
P_{RA} [mmHg]	15 (23/12)	15 (29/7)	13 (25/8)

Results from multi-domain simulations were compared with the respective LPN simulations, ensuring the correct representation of the fluid dynamics in the bifurcations, in terms of flow-splits (Table 7.3), of pressures (Table 7.4), and of flow curves (Figure 7.12 and Figure 7.13). The maximum % difference between the flow-splits averaged over one cardiac cycle obtained with the LPN and the multi-domain models was 6% for SG3. The pressure values obtained (Table 7.4) were within a physiological range (**48**; **143**).

Table 7.3 - Comparison of the flow split between LPA and RPA obtained (i) clinically, (ii) with the LPN simulation and (iii) with the correspondent multi-domain (MD) simulation for the stenotic patients.

	Measured LPA flow [%]	**LPN LPA flow [%]**	**MD LPA flow [%]**
SG1	53	53	49
SG2	43	43	40
SG3	32	31	37
SG4	38	37	36
SG5	33	33	29
SG6	50	50	48
SG7	52	52	48
SG8	35	35	37
SG9	38	38	36
BPS	52	52	52

Table 7.4 - Comparison of LPA and RPA pressures obtained with the LPN simulation and with the correspondent multi-domain (MD) simulation for the stenotic patients.

	LPA pressure [mmHg]		**RPA pressure [mmHg]**	
	LPN	**MD**	**LPN**	**MD**
SG1	12 (22/8)	11 (21/8)	15 (38/8)	15 (42/2)
SG2	12 (21/6)	12 (21/5)	14 (33/5)	14 (33/5)
SG3	14 (27/7)	15 (33/7)	17 (38/7)	16 (36/7)
SG4	15 (34/7)	14 (29/8)	18 (52/7)	18 (46/8)
SG5	13 (24/6)	13 (22/6)	13 (26/6)	14 (28/7)
SG6	16 (30/7)	18(37/6)	18 (34/6)	20 (42/5)
SG7	11 (16/6)	11 (16/7)	17 (36/5)	18 (36/4)
SG8	9 (14/7)	10 (17/5)	19 (48/6)	21 (56/3)
SG9	12 (21/7)	14 (25/7)	30 (100/5)	34 (106/8)
BPS	15 (28/7)	14 (28/8)	15 (29/7)	15(30/8)

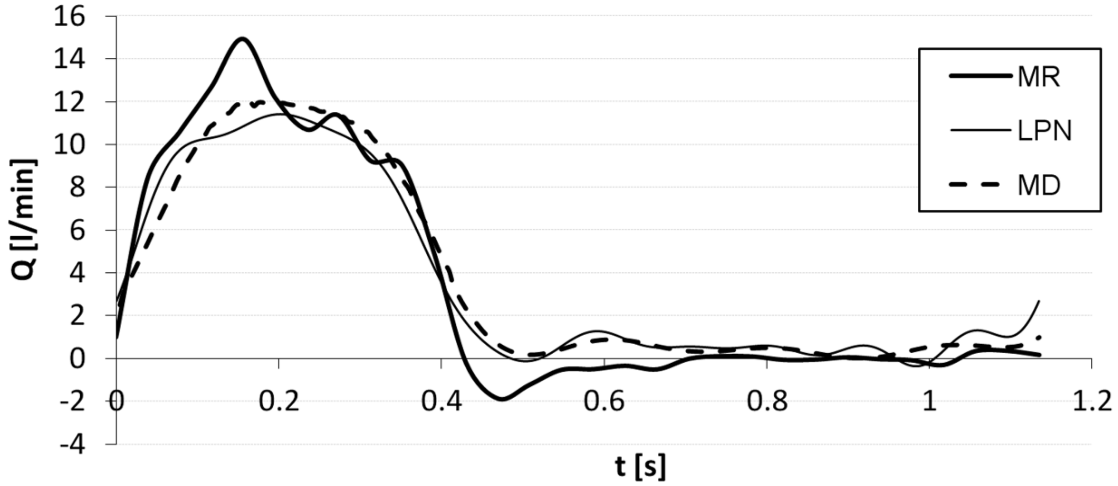

Figure 7.12 - Flow curve in the LPA of the BPS case. Comparison between the measured clinical flow, the LPN simulated flow and the one obtained with a multi-domain (MD) simulation.

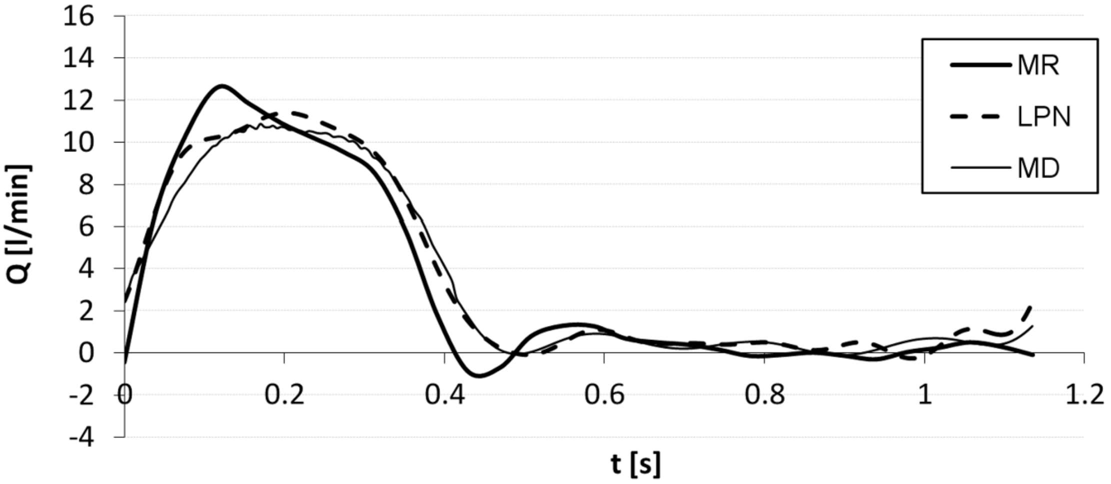

Figure 7.13 - Flow curve in the RPA of the BPS case. Comparison between the measured clinical flow, the LPN simulated flow and the one obtained with a multi-domain (MD) simulation.

7.3.4 Computational Stenting

The stent was successfully expanded in SG7's LPA to fully relieve the stenosis. The newly patent proximal LPA and the proximal RPA resistances were characterised and inputted in the LPN of the patient representing the pre-stenting peripheral circulation. The new flow-split between right and left pulmonary artery was unbalanced towards the LPA (68%) while the pre-stenting flow split was 52:48 in favour of the LPA, which denoted a more balanced condition despite the presence of the stenosis.

7.4 DISCUSSION

In this work, the fluid dynamics that develops in the pulmonary circulation of TGA patients after ASO was studied using clinical MR images and computational tools. Two groups of patients, with and without LPA stenosis, were analysed and compared. In addition, a patient with bilateral pulmonary artery stenosis was included in the study as a validation case for the proposed methodology since he underwent diagnostic catheter procedure a few months after the MR examination. The adopted computational methodology allowed for patient-specific characterisation and quantification of peripheral vascular resistances thus helping our understanding of unilateral pulmonary artery stenosis hemodynamics.

The morphological reasons for the development of LPA stenosis as a result of ASO in TGA patients are well known, and are connected to the Lecompte manoeuvre that requires pulling of the LPA to anastomose the PT to the RVOT when the aorta is moved posteriorly (**42**). However, the hemodynamic physiology that develops in the presence of such stenosis has not been fully investigated. Indeed, the discrepancy between expected unbalanced flows in the pulmonary branches due to the presence of a stenosis and the effective measured flow distribution, which in some cases results balanced, has not yet been explained. The widely accepted hypothesis for this phenomenon is that remodelling has occurred in the peripheral resistances of the pulmonary bed, but only invasive pressure measurements could validate this hypothesis.

A methodology involving patient-specific LPN and CFD simulations based on MR data was developed in this study to overcome the difficulty in acquiring pressure data invasively while still trying to explain the hemodynamics in unilateral pulmonary artery stenosis. Patient-specific geometries of the main and proximal left and right pulmonary arteries were reconstructed from MR data. Steady-state CFD simulations were set up to characterise the hydraulic resistances of the proximal pulmonary system; hence, an LPN was adopted to represent the full pulmonary circulation and characterise the range of peripheral resistances in every patient using only MR derived flow data. Finally, stenting implantation was virtually simulated in a severely stenotic LPA to assess the immediate post fluid dynamic outcomes of such intervention.

Patients with no stenosis (CG) behaved as expected in the computational analyses showing little influence of the proximal geometry on the flow split for any total PVR. In the stenotic patients (SG), increased total PVR resulted in a decreased effect of the stenosis, differently for each patient. The BPS case demonstrated that the developed framework was able to capture the hemodynamics of these patients, as the simulated pressures and resistances were in the correct range for that patient.

Numerical simulations allowed first to evaluate the difference between the measured MR flows and the flow split that should be expected if no remodelling occurred in the patients. Clearly, results highlighted the amount of peripheral pulmonary vasculature remodelling necessary to explain the unexpected clinically measured flow-split

Ballooning and/or stenting of arterial stenoses are conventional treatments to relieve the obstruction in most vasculature sites in order to decrease the pressure drop across the stenosis and re-establish good flow. However, in the setting of unilateral pulmonary artery stenosis treatment remains controversial, as in some cases balanced flow distribution between the PAs is measured despite the presence of the severe obstructions. Timing of intervention may also present an important factor to consider in the long term management of these patients. Indeed, stenting simulation in a patient with severe stenosis but well balanced flow split showed how the morphological relief of the obstruction worsened the hemodynamic conditions in the immediate post-operative scenario.

Peripheral pulmonary vascular remodelling in pulmonary artery stenosis has not been fully explained yet. Thus, it is not well known whether such phenomenon is related to vasodilatation of the lung vasculature in the stenotic side, vasoconstriction of the contra lateral side, or a combination of the previous two adaptation mechanisms. The model developed in this work is purely mechanical, not accounting for any cellular level information and cannot also distinguish between these two phenomena. .

In a patient with severe stenosis, it was not possible to identify the correct parameters to simulate the in-vivo hemodynamic conditions. A source of error for the proposed methodology was individuated in the 3D reconstruction of the PAs at the level of the narrowing. Indeed, for this patient, the voxel size of the MR images was comparable to the dimension of the LPA vessels in the obstruction area (1.5 x 1.5 x 1.5 mm voxel size vs 3.4mm vessel diameter) therefore introducing a potential error in the proximal resistance characterisation which uses the 3D CFD model. To investigate the influence of the reconstruction process on the fluid dynamic outcomes, the geometries should be re-analysed by changing the threshold selected to calculate the 3D volume.

7.5 CONCLUSIONS

The fluid dynamics in the pulmonary system of a cohort of patients who underwent ASO, presenting the long term complication of pulmonary branch stenosis, was successfully modelled using CFD, LPN and multi-domain simulations. In particular, CFD analyses were used to set-up patient-specific pure LPNs, and multi-domain simulations were performed to confirm the accuracy of these pure LPN models. The integration of the above mentioned tools allowed the estimation of the peripheral PVR remodelling in the cohort of patients by using only non-invasive MR measurements. The workflow was verified simulating a patient case with pressures known from catheterisation.

Furthermore, a virtual stent implantation in one patient with LPA severe stenosis was carried out, allowing the evaluation of the acute post-operative outcomes after stenosis relief.

In the next chapter, the framework here developed for the creation of patient-specific LPNs from steady-state CFD simulations, and for the evaluation of the fluid dynamic outcome after a stent implantation will be applied for the modelling of a clinical case of CoA. In particular, the model presented in the next chapter was created to the purpose of helping the clinicians in deciding size and position for a safe stent expansion in the patient's aorta, accounting for the effects the stenosis relief will have on the patient's hemodynamics.

CHAPTER 8

COMPUTATIONAL MODEL OF CoA STENTING: A PATIENT-SPECIFIC CASE

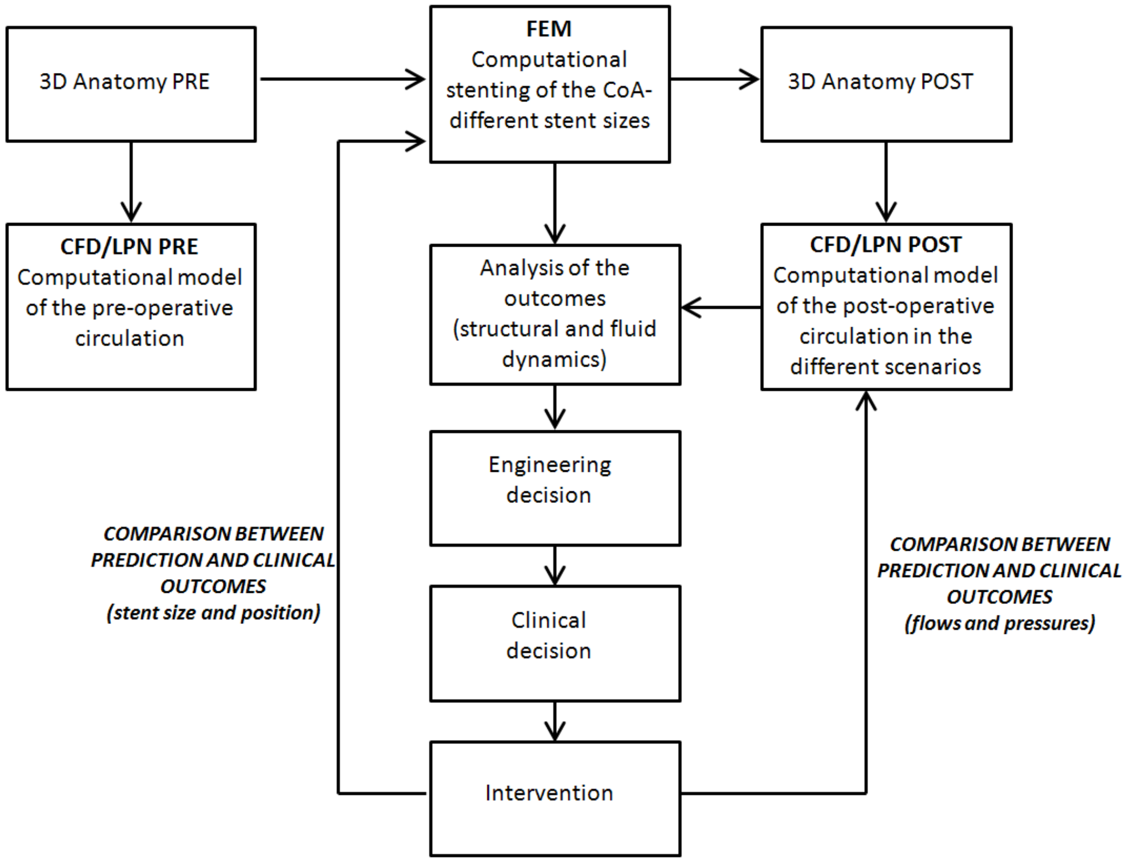

8.1 INTRODUCTION

The study presented in this chapter integrates all the different modelling techniques applied in the previous Chapters (from 4 to 7) with the aim of creating a model to guide treatment in a patient with recurrent CoA (Section 2.6). Several image analysis methodologies (MR, CT, fluoroscopy and echo) discussed in Chapter 3 are adopted in this study to develop the 3D model of the patient's aorta, and to derive the patient-specific boundary conditions to be applied to the computational models. The approach introduced in the previous chapter for the hydraulic characterisation of the 3D geometry through CFD analyses is used for the creation of a LPN representative of the anatomy of interest. FE simulations are utilised as in Chapters 5 and 7 to virtually expand a stent, in this case up to different final diameters in order to assess the optimal interventional strategy for this specific patient.

In literature, computational studies have investigated the hemodynamics in CoA anatomies not only to understand physiology and pathogenesis occurring at the diseased zone, but also to predict the effects of different treatments. In this context, models of patient-specific anatomies have been aiming at providing better understanding of long term morbidity and outcomes of current treatments. CFD analyses have replicated realistic conditions including geometric characteristics, physiological boundary conditions, and compliance of arterial walls. According to the state of the art, not all these factors could be implemented in a single model. However, CFD analyses have already offered better insights of specific scenarios. For example, the study by LaDisa et al, focused on the patho-physiology of CoA, and showed the differences between control subjects and different surgically repaired cases of CoA in terms of wall shear stresses distributions. The results showed that in addition to any pre-existing alterations in vascular function, locations involving the surgical correction are often those associated with potentially deleterious alterations in indices of WSS (**149**). In this scenario, another study by LaDisa's group investigated less invasive treatments as the percutaneous implant of stent. CFD analyses were focused on understanding the impact of different stent types on blood flow patterns in the descending thoracic aorta. The results highlighted greater WSS along the posterior wall of the descending thoracic aorta distal to the stents as well the anterior wall exposed to low WSS, generally associated with the onset and progression of cardiovascular disease (**149**).

However, to the best of my knowledge, in literature there are no prospective studies in which a developed computational methodology has been applied to predict the results of an intervention and support the clinician decision making process for a specific patient case. This step is usually complicated by the need for a validated and computationally demanding framework on one side and reduced time-frame combined with difficulties of translating the available clinical data towards the model, on the other. In this chapter, I report the results of the application of the patient-specific methodologies that I have developed during my PhD project to optimise the treatment strategy for a patient with CoA.

8.2 MATERIALS AND METHODS

8.2.1 Patient's clinical history

The patient is a 19-year-old male with native CoA and aberrant right subclavian artery (ARSA) originating in correspondence of the narrowing (Figure 8.1).

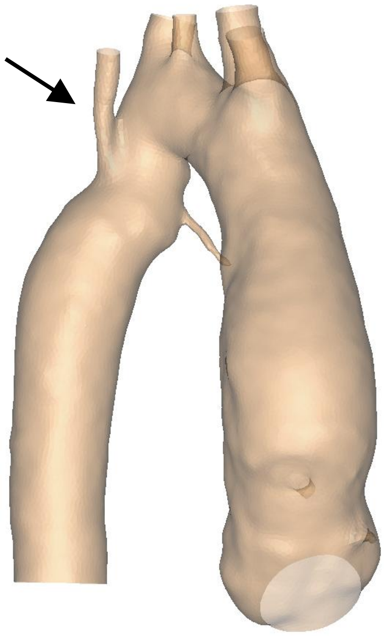

Figure 8.1 - 3D rendering of the patient's aorta with the origin of the aberrant right subclavian artery indicated by the arrow.

The coarctation was first treated in 2001 with a Palmaz P308 stent (Johnson & Johnson Interventional Systems Co., Warren, NJ) successfully implanted to relieve the pressure gradient. In 2007, the patient underwent a first re-dilatation of the bare metal stent that reduced the peak systolic pressure gradient across the stent from 13 to 8 mmHg. In 2011, follow-up catheter examination showed recurrent obstruction (9 mmHg gradient) and the formation of a small aneurysm in the proximal portion of the stent (Figure 8.2). The risk of aneurysm rupture prevented the clinician to further re-dilate the stent and insertion of a covered stent was discussed, but postponed after further investigations because of the ARSA origin positioned in the distal portion of the Palmaz stent. After this catheterisation procedure, additional image assessment was carried out including a CT scan to allow full anatomical understanding of the relationships between the bare metal stent, the aneurysm and the ARSA origin, and an MR investigation to assess the hemodynamics.

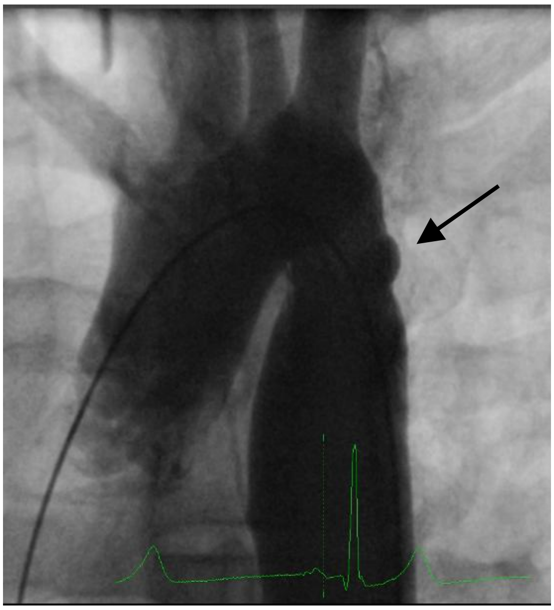

Figure 8.2 - Aortogram showing the presence of an aneurysm indicated by the arrow.

The CT parameters were the following: pixel size = 0.799 x 0.799 mm with slice increment = 0.499 mm; scanning parameters: 100 kV and 145.3 effective mAs per rotation.

MR imaging was performed and analysed as explained in Section 3.4.1.1. In particular, 2D phase contrast MR images for flow measurements were acquired at the following planes (Figure 8.3): in the sino-tubular junction (STJ), in the ascending aorta (AA), at all brachio-cephalic branches originating from the aortic arch (the right common carotid (RCC) artery, the left common carotid (LCC) artery, the left vertebral (LVERT), the left subclavia (LSUB), the ARSA) and in the descending aorta (DA), soon after the stent position and at the level of the diaphragm (DIAG). Flow averaged over one cardiac cycle in the AA was 5.25 l/min (distributed according to the following proportion in the other vessels: RCC = 8.84%, LCC = 3.79%, LVERT = 1.73%, LSUB=4.65%, ARSA = 9.52% and DA=71.47%).

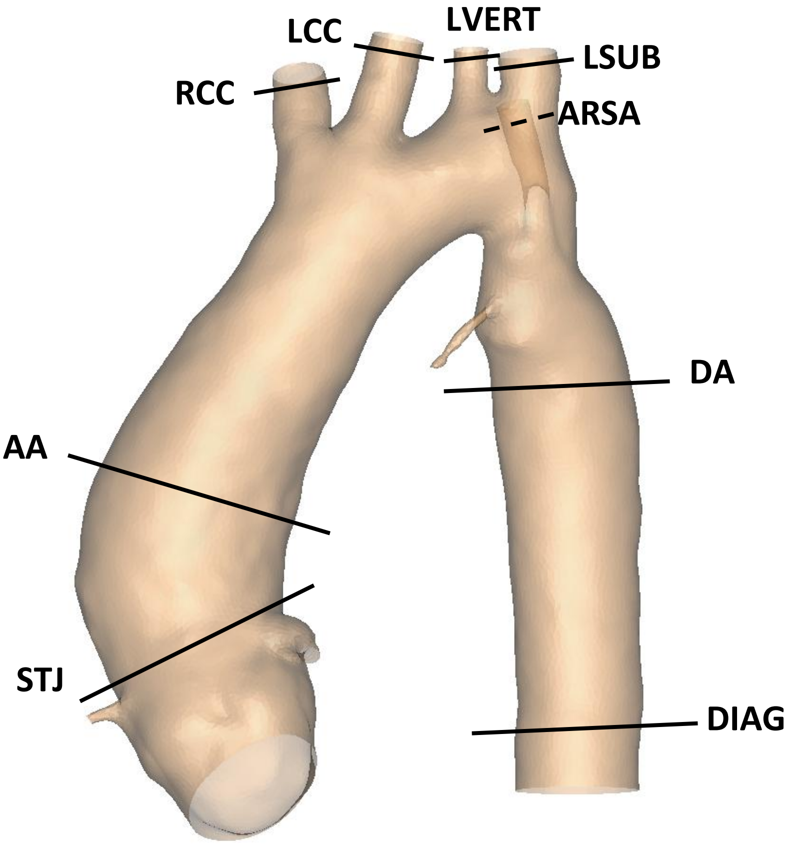

Figure 8.3 - Diagram of the planes set for the MR flow acquisitions in the patient's aorta.

The additional image information allowed the development of a patient-specific modelling framework which together with the set of conventionally acquired clinical data, gave confidence to the cardiologists to treat the patient with the insertion of a covered stent. The intervention was performed under general anaesthesia and angiographic guidance. Pressures were measured in the aortic arch, descending aorta, ARSA, and across the treated CoA before and after the intervention.

After 3 months, MR follow-up was performed to assess the hemodynamic conditions.

8.2.2 Patient-specific model

The interventional cardiologists at our Centre planned to implant a covered CP stent inside the CoA region to relieve the stenosis and cover the aneurysm, without obstructing the origin of the ARSA. They asked for advice from the engineering team working in the Unit to work out the optimal deployment diameter for the covered stent in order to achieve those results. Therefore, in less than two weeks from when the additional image assessment was performed to the time of intervention, I implemented a patient-specific model which aimed i) to identify and predict the optimal stent size in order to achieve an optimal compromise between gradient relief, aneurysm treatment and ARSA origin patency, thus helping the cardiologist in the decision making process; and ii) to compare the results of the modelling prediction with the real outcomes of the actual procedure in the patient, in order to evaluate the ability of the developed framework in predicting realistic clinical outcomes.

Prior to the new procedure, clinically acquired image data were used to set-up both structural and CFD analyses (Figure 8.4). Previous catheterisation fluoroscopy images, CT and echo data were used to build the 3D computational model of the implantation site prior to the procedure; the hemodynamic boundary conditions for this model were set up using information acquired from pre-procedural MR and catheterism examinations. Following stent implantation, the procedural and follow-up data were used to compare the real outcomes with the model results in order to assess the modelling framework accuracy. In particular, stent size and position were verified using the procedural fluoroscopy images – the in-vivo CP stent geometry was reconstructed from the biplane fluoroscopy images as described in Section 4.2.1.3 – flow distribution and flow waveforms using the follow-up MR images, and pressures using the catheterisation data.

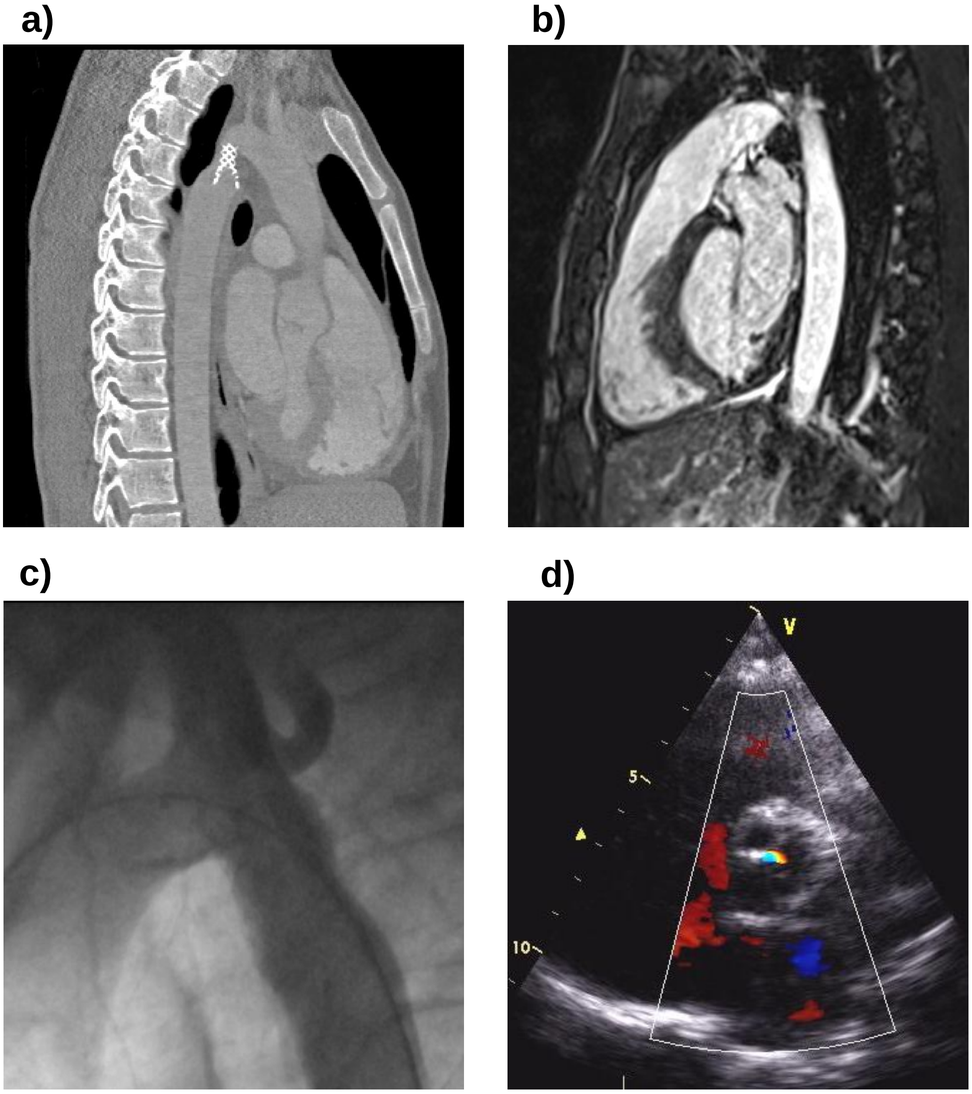

Figure 8.4 - Imaging data available to set-up the computational model: a) CT, b) MR, c) fluoroscopy, and d) echo data.

8.2.3 Anatomical model

Segmentation of the CT images was performed with Mimics (Section 3.5.1) to create the 3D geometry of the patient’s aorta and indwelling bare metal stent. Previous fluoroscopy and echo images were used to guide the reconstruction of the stenotic site, as ingrowth tissue was not visible from the CT images (Figure 8.5). In particular, echo measurements at the level of the narrowing highlighted a peak velocity (v) of 3.6 m/s, which was used to estimate the cross-sectional lumen area in this portion of the vessel.

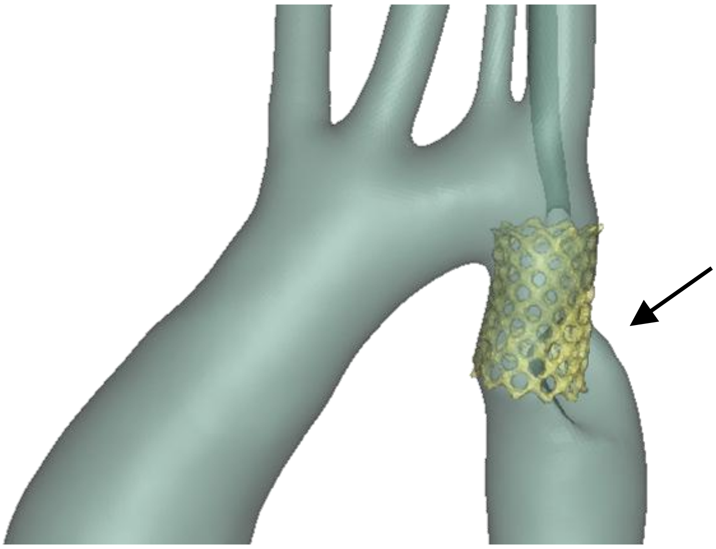

Figure 8.5 - 3D model of the patient's aorta with the previously implanted Palmaz stent reconstructed from CT images. The tissue growth inside the stent is indicated by the arrow.

A 3D rapid prototyped model was printed (Figure 8.6) to aid the clinicians understand the 3D complex morphology and gain confidence in the interventional procedure. The model was built using a transparent and robust resin (Watershed 11122; DSM Somos, Elgin, IL) for the aortic wall, and an opaque rigid Nylon for the inner stent.

Figure 8.6 - 3D rapid prototyped plastic model of the anatomy prior to the new stent implantation.

8.2.4 Computational models

The workflow of the modelling techniques used in this patient-specific study is summarised in Figure 8.7. An LPN strategy was adopted to predict in the available timeframe the overall hemodynamics resulting from the expansion of the stent to different sizes. The pre-intervention 3D model of the patient was first characterised using CFD analyses. An extended LPN was created to account for the downstream circulation and characterised using the pre-implantation MR patient flow information. The stent was implanted in the 3D geometry using FE simulations to obtain the post-implantation lumen geometry for each of the tested expansion size. This new 3D volume was fluid dynamically characterised using CFD and the information inserted in the pre-implantation LPN.

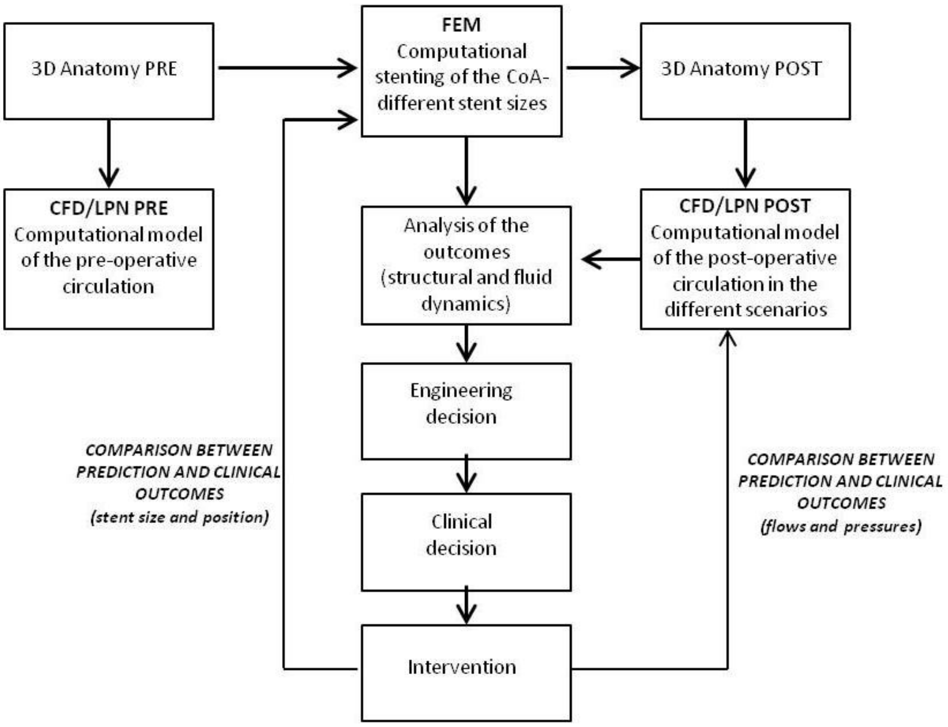

Figure 8.7 - Workflow adopted for the implementation of the computational model to be used in order to provide an answer to the specific clinical question related to the feasibility of the procedure.

CFD simulations of the hemodynamics before and after the stent implantation were carried out using Ansys Fluent with the discretisation schemes and the convergence criteria indicated in Section 3.5.2.1. The vessels of the 3D model were assumed to be rigid, and a no-slip condition was imposed at the walls. For the unsteady simulations a time-step of 10^{-4} s was applied, and five cardiac cycles were performed to ensure stability in the calculated solutions. The blood was modelled as a Newtonian fluid with a density ρ of 1060 kg/m^3 and a viscosity μ of 0.003 Pa·s.

LPN equations were set-up as discussed in Section 3.5.2.2, and in order to guarantee a stable solution twenty cardiac-cycles were simulated, selecting the last one for post-processing the results.

8.2.4.1 Fluid dynamic model pre-intervention

The 3D pre-operative anatomy was modified for the CFD simulations by adding cylindrical flow extensions to the outlets to assure a fully developed flow at those sections, in order not to force the chosen boundary conditions. Different tetrahedral element meshes were built using an adaptive mesh refinement to increase the accuracy of the solution in the regions of larger pressure variations. A sensitivity analysis was performed to select the optimal mesh that compromised between solution accuracy and computational time. The decision was based on the evaluation of the power dissipation index, calculated as in Pennati 2011 (**126**), in steady-state CFD analyses: the flow-rate measured from MR data in the ascending aorta, averaged over one cardiac cycle, was imposed at the inlet of the model, while the MR calculated flow split, averaged over one cardiac cycle, was imposed at the outlets. A mesh of 910,329 volumes was finally selected to run the simulations.

In order to characterise the geometric resistances to the blood flow, a set of CFD steady simulations was carried out imposing 8 different velocities (0.05, 0.1, 0.2, 0.3, 0.5, 0.7, 0.8, 0.9 m/s) at the inlet of the aorta, and a zero pressure condition at all outlets. Pressure drops (ΔP) were measured in every simulation between the aortic inlet and the aortic arch, and between the aortic arch and all outlets. Such pressure drops were divided by the flow-rate (Q) streaming through every branch. Plotting the results of all simulations in a pressure drop-flow graph, the data points were interpolated with either a linear or a second order polynomial equation (Section 7.2.3), to characterise the hydraulic behaviour of the whole 3D geometry for different flow-rates.

The obtained equations were then used to implement a LPN representative of the pre-operative 3D aortic anatomy of the patient (Figure 8.8).

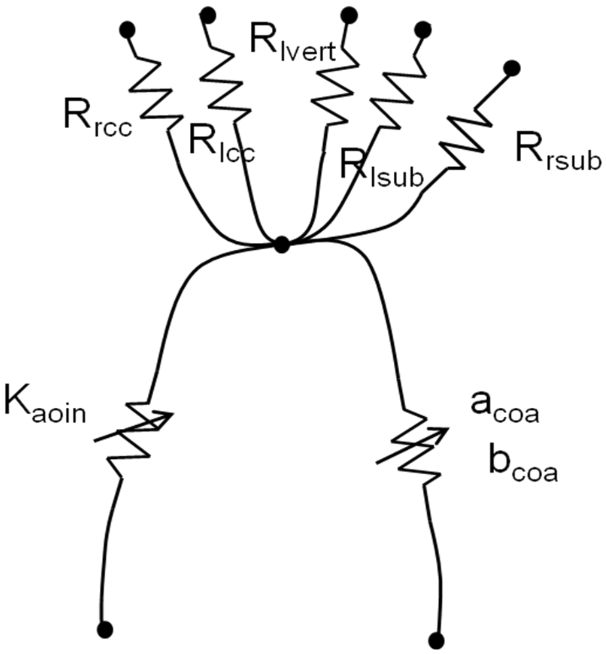

Figure 8.8 - LPN representation of the 3D pre-operative aortic arch of the patient.

The equivalence between the 3D CFD and the LPN representation of the aortic arch and upper branches was verified by performing a time-variant simulation with equal boundary conditions with both models. The patient's pre-operative aortic flow, as measured from MR was imposed at both inlets, while a zero-pressure was imposed at all outlets. The results were then compared in terms of flow distribution, flow waveforms at the outlets and mean pressure.

The LPN model was then expanded to simulate the whole pre-operative systemic circulation of the patient with the addition of 2 two-element (RC) Windkessel blocks per branch, representative of the arteriosus and venous systemic compartments. All branches were connected to the right atrium with 5 mmHg constant pressure (Figure 8.9). The resistive and compliant parameters were tuned in order to achieve the same flow split and flow curves at the outlets of the patient, when the patient's inflow was imposed at the inlet of the LPN model.

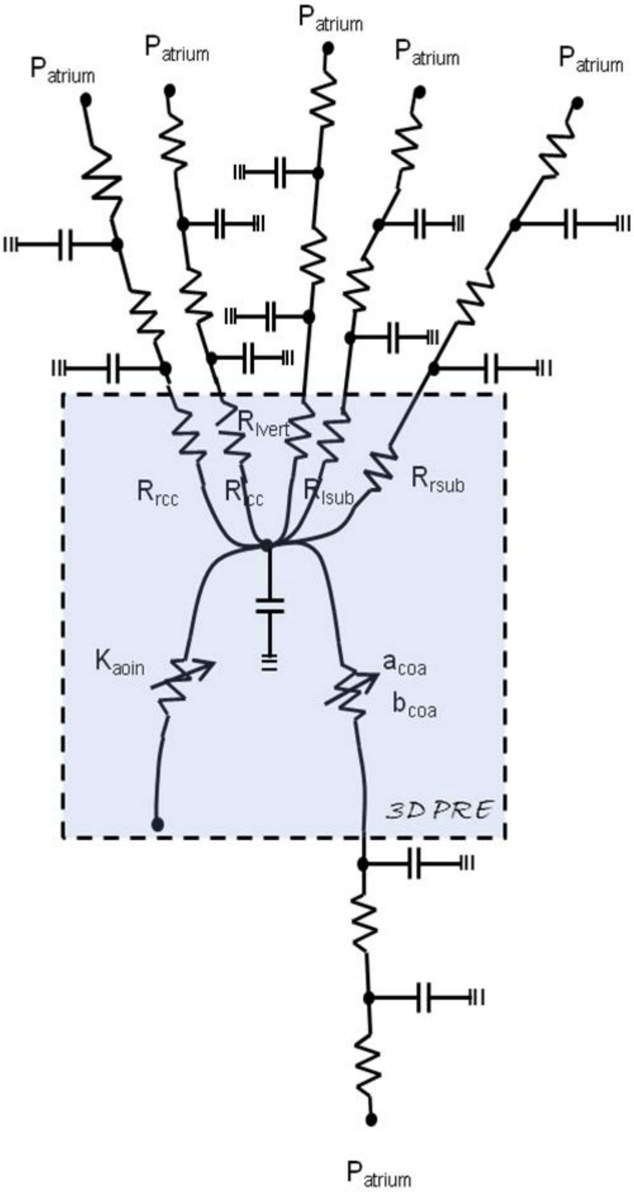

Figure 8.9 - LPN of the systemic circulation of the patient prior to the procedure.

8.2.4.2 Finite element model of the intervention

A computational model resembling a crimped covered CP stent was built including 5 platinum-iridium rings and Gore-Tex® graft (Figure 8.10a). Two-dimensional beam elements were used to mesh the stent (2,464 beams), while membrane elements were adopted for the graft (23,008 quadrilateral elements). In this study, the beam elements were adopted to model the stent because of their fast computational time response compared to solid elements (**150**). The geometry of the Palmaz stent in-situ, was obtained from the CT reconstruction, and a FE mesh of such deployed stent was created with 2,017 beam elements (Figure 8.10b). The arterial wall model interacting with the stents was built using 41,199 triangular shell elements. In addition, an angioplasty balloon model (diameter = 3.5 mm) was created using surface elements to be kept inflated in the ARSA during the implantation of the covered stent to further protect the patency of the ARSA origin according to the protocol planned by the clinicians for the procedure (Figure 8.11). The material models and parameters adopted for the different FE structures are reported in Table 8.1.

Table 8.1 - Material properties used for the FE simulation.

	Material	Model	E [MPa]	ν [-]
CP stent	Platinum-Iridium	Elasto-plastic	224000	0.37
CP graft	Gore-Tex®	Elastic	500	0.3
Palmaz stent	Stainless Steel	Elastic	193000	0.3
Wall (**150**)	Artery	Elastic	0.7	0.25
Balloon (ARSA)	Nylon	Elastic	450	0.45

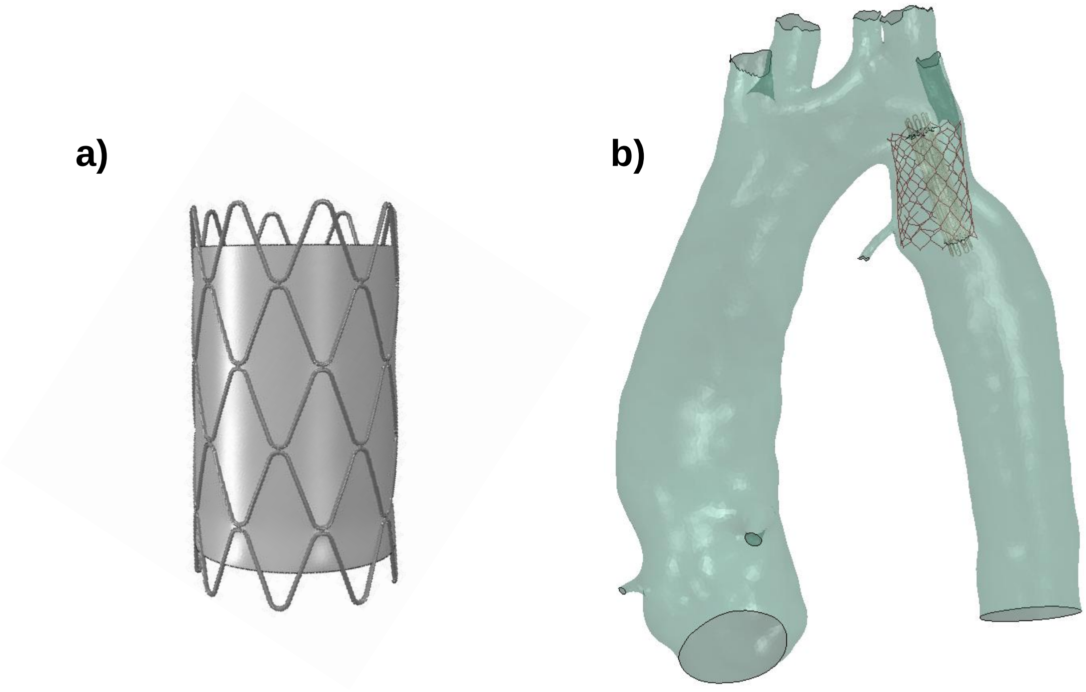

Figure 8.10 - Computational model of the covered stent (a) to be implanted inside the patient's aorta (b).

The covered CP stent implantation procedure was simulated using Abaqus/Explicit. Quasi-static conditions were verified: values of kinetic energy were 5% times lower than the internal energy according to Abaqus Simulia user's manual. Contact constraints were imposed i) between the outer surface of the CP stent and graft, and the inner surface of the Palmaz stent and of the arterial wall; and ii) between the outer surface of the balloon, and the inner surface of the ARSA and the outer surface of the CP stent and graft.

The balloon was first inflated in the ARSA using 0.05 Pa of pressure and kept inflated throughout the implantation of the covered CP stent. This was positioned inside the 3D CoA patient-specific model in correspondence to the Palmaz stent landmark following the interventional cardiologist guidance. Pressure loads (0.004, 0.020, 0.032, and 0.040 Pa) were applied to the internal surface of the stent/graft to achieve four different expansion diameters, 14, 16, 18, and 20 mm.

The following quantities of interest were considered: device configuration at the end of the stent expansion relatively to the origin of the ARSA and to the aneurysm; stress distribution on the arterial wall to evaluate whether an adequate contact was achieved between device and vessel.

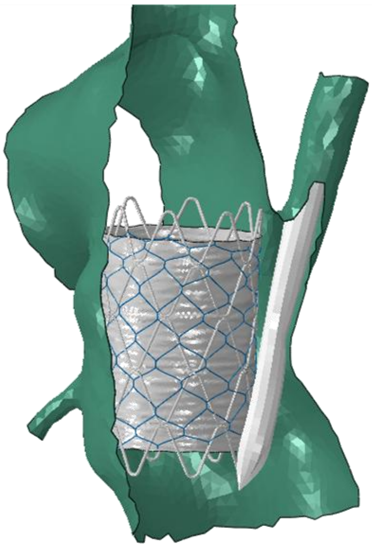

Figure 8.11 - Computational model of the stent expansion. Highlighted in this figure is the balloon inflated in the ARSA to assure its patency after the covered stent implantation.

8.2.4.3 Fluid dynamic model post-intervention

The geometries resulting from the FE simulations were then used to build a CFD 3D model of the resulting post-operative lumen anatomy including the arterial wall and the graft (Figure 8.12). Stent struts were discarded in this lumen mesh creation as their influence in the flow distribution and pressure drop across the treated coarctation was considered small.

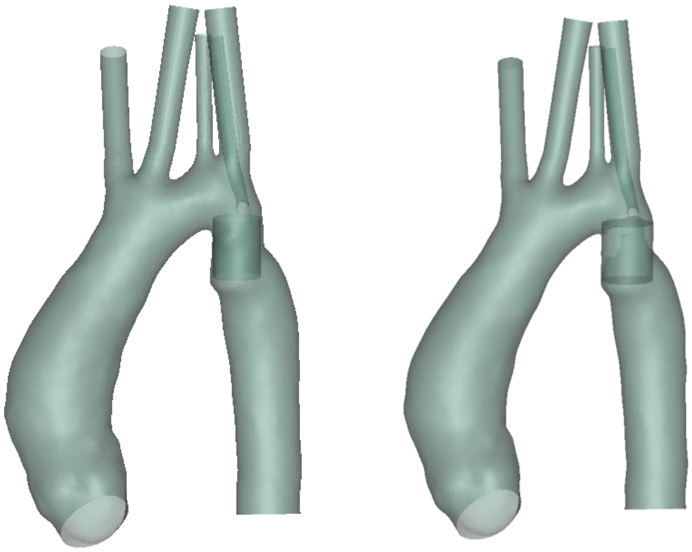

Figure 8.12 - CFD models of the post-operative anatomies derived from the FE simulations after the covered stent implantation at 16 mm (left) and 18 mm (right).

The blood volume was meshed with over 910,000 tetrahedral elements with increased accuracy in the regions of higher pressure difference. A wall condition was assigned to the surface of the graft not allowing blood-flow through it. As previously explained for the pre-operative geometry (Section 8.2.4.1), the 3D post-operative lumen anatomies were characterised hydraulically through a set of steady-state simulations. The same eight inflow velocities conditions as the pre-procedural simulations were imposed to both inlets, and a zero-pressure condition was applied to all outlets. The ratio between pressure drop and flow streaming through each branch allowed the mathematical equations describing the 3D geometries to be inferred. Particular attention was given to the ARSA, to evaluate if the graft was obstructing its perfusion.

From this set of simulations a LPN was created for each post-operative aorta, and a time-variant simulation was run applying the same boundary conditions (patient’s pre-operative flow-rate applied to the inlets and zero-pressure at all outlets) to both the CFD and LPN models, to check the correspondence of flow waveforms and flow distribution. Finally, under the hypothesis of no remodelling of the peripheral vasculature after the intervention, the extended LPN of the pre-operative systemic circulation was modified to represent the post-operative scenarios: the equations representative of the pre-operative aorta were replaced with the new equations derived for the post-operative aortas. Outcome fluid dynamic differences between the expansion sizes of the covered stent were evaluated in terms of percentage of the total flow going to the ARSA and to the lower body, and the pressure gradient across the treated CoA.

8.3 RESULTS

8.3.1 Anatomical model

The 3D reconstruction of the patient's anatomy allowed the full assessment of the patient's morphological characteristics with aneurysm size and position in relation to the previously implanted stent and origin of ARSA. It also allowed identification of the presence of fractures in the Palmaz stent, which was not recognised before (Figure 8.13).

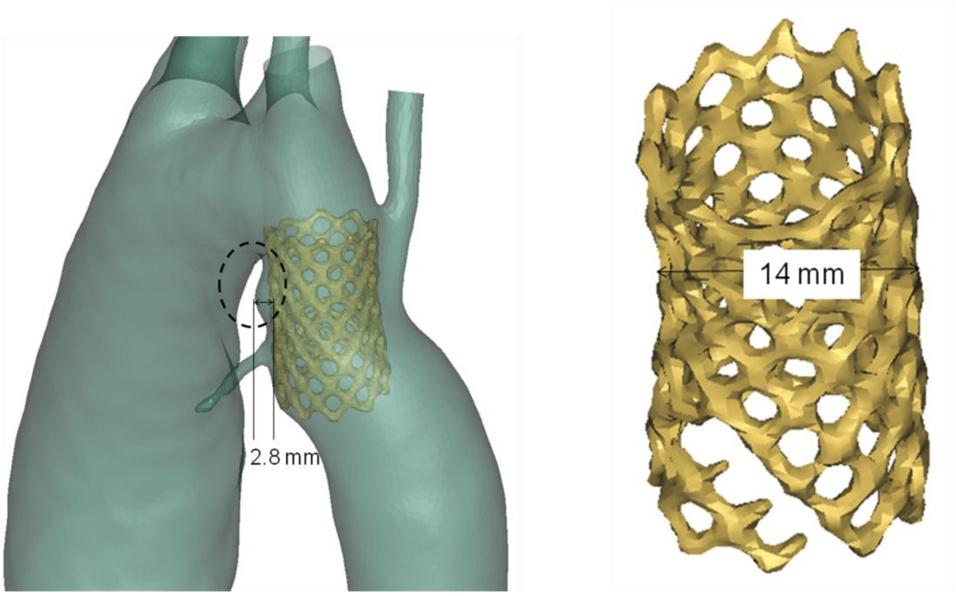

Figure 8.13 - 3D reconstruction of the patient's anatomy with the previously expanded Palmaz stent. To be noted the aortic aneurysm (left) and the stent fractures (right).

8.3.2 Computational models

8.3.2.1 Fluid dynamic model pre-intervention

The pressure drop and flow data obtained from the steady-state simulations were used for the 3D hydraulic characterisation: the ΔP/Q data obtained for the upper branches (RCC, LCC, LVERT, LSUB and ARSA) were interpolated through linear relationships ($\Delta P=R\cdot Q$), while the ascending and descending parts of the aorta (AA and CoA) were modelled through second order polynomial equations ($\Delta P=K\cdot Q^2$ and $\Delta P=a\cdot Q^2+ b\cdot Q$ respectively). The coefficients of such equations are reported in Table 8.4.

The equivalence between the 3D CFD model of the aorta and the LPN of the aorta prior to the operation was confirmed by the results of the time-variant simulations run imposing the same boundary conditions to both models: Figure 8.14 and Table 8.2 report a comparison between flow waveforms and flow-split obtained with both models.

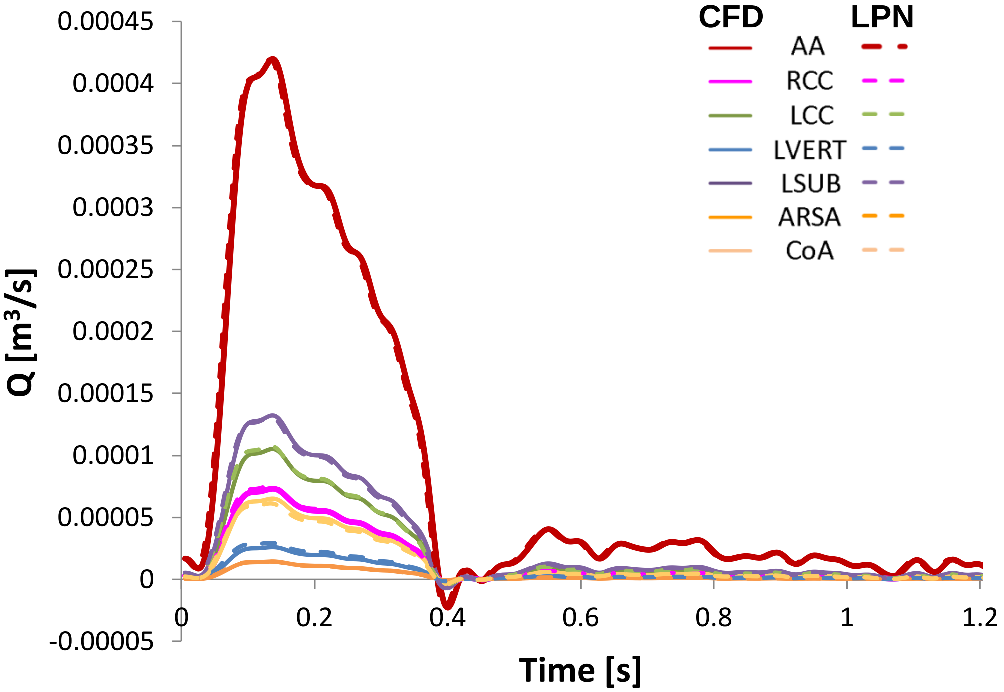

Figure 8.14 - Comparison between the flows obtained with the CFD (solid line) and the LPN (dotted line) models of the pre-operative aorta.

Table 8.2 – Flow split in the outlets of the aorta in terms of percentages of the total inflow for the CFD and the LPN models of the pre-operative patient's aorta.

PRE-OP AORTA	**CFD**	**LPN**
Q_{RCC} [%]	16.9	17.97
Q_{LCC} [%]	24.91	25.59
Q_{LVERT} [%]	6.51	7.02
Q_{LSUB} [%]	32.08	31.13
Q_{ARSA} [%]	3.44	3.43
Q_{CoA} [%]	16.18	14.87

The extension of the LPN model allowed the modelling of the full systemic circulation whose parameters were tuned to obtain the representation of the patient's fluid dynamics. The comparison between the model and the patient's flow data at all outlets and at the inlet are reported in Figure 8.15, while the flow splits are reported in Table 8.3. The pressure difference measured across the CoA in the LPN was 8.27 mmHg, while that measured in-vivo was 9 mmHg.

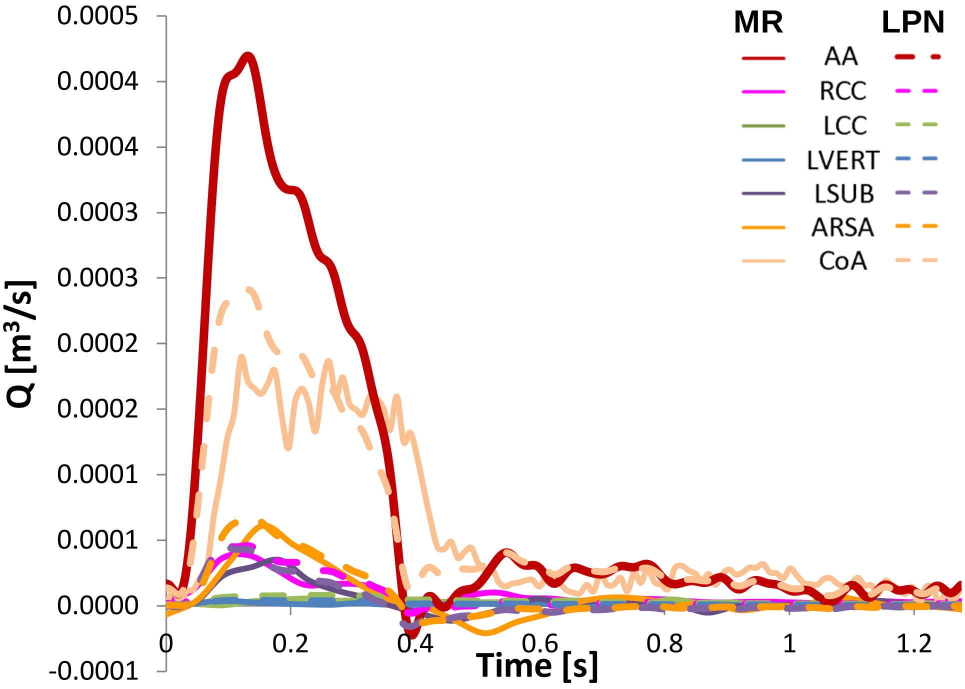

Figure 8.15 - Flow comparison at the inlet and outlet sections between the LPN model (dotted line) of the systemic pre-operative circulation and the pre-operative MR data of the patient (solid line).

Table 8.3 - Flow split in the outlets of the aorta in terms of percentages of the total inflow as measured from the patient's MR and as calculated from the LPN model of the whole systemic circulation before the procedure.

PRE-OP SYSTEMIC	**MR**	**LPN**
Q_{RCC} [%]	8.84	9.71
Q_{LCC} [%]	3.79	2.95
Q_{LVERT} [%]	1.73	1.2
Q_{LSUB} [%]	4.65	4.87
Q_{ARSA} [%]	9.52	9.24
Q_{CoA} [%]	71.47	72.03

8.3.2.2 Finite element model of the intervention

The final aortic configuration obtained after deployment of the CP covered stent in the four different sizes is shown in Figure 8.16 in two different perspectives (i.e. lateral and sagittal views). Observing these configurations, it is possible to note how the CP stent expanded at 14 mm did not achieve contact around the entire structure, while the stent opened at 20 mm obstructed the origin of the ARSA. Contrarily, both sizes 16 and 18 mm showed a good contact with the arterial wall with no risk of obstruction of ARSA. Stress distribution is reported in Figure 8.17 for the 16 and 18 mm cases, where the areas at higher contact are highlighted.

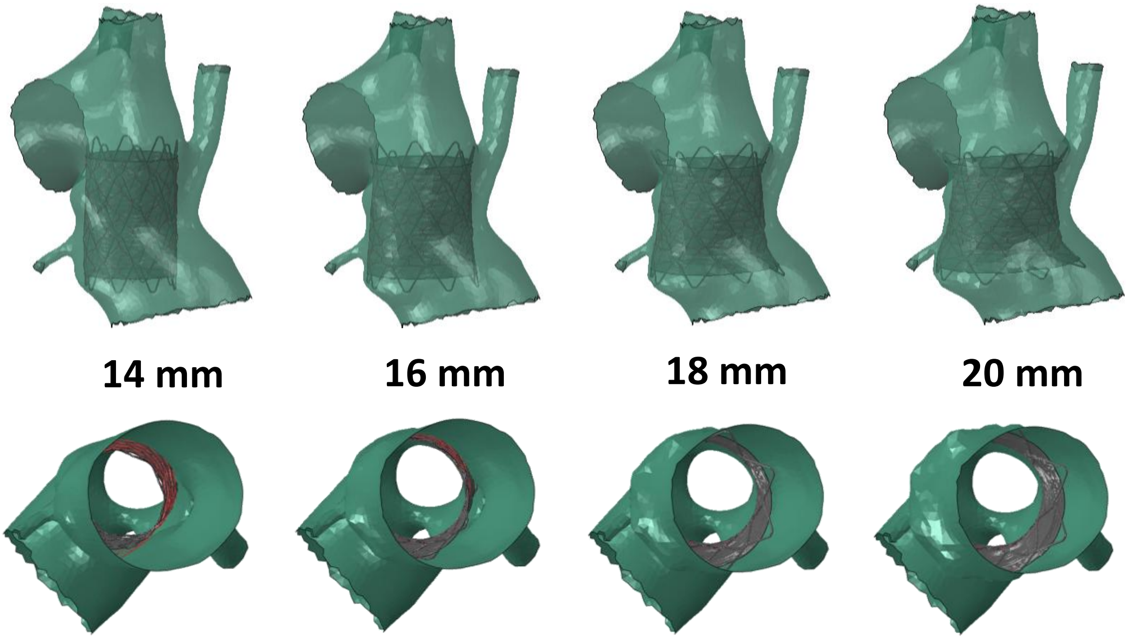

Figure 8.16- FE expansion of the covered stent at four different sizes. Lateral (upper panel) and sagittal (lower panel) views.

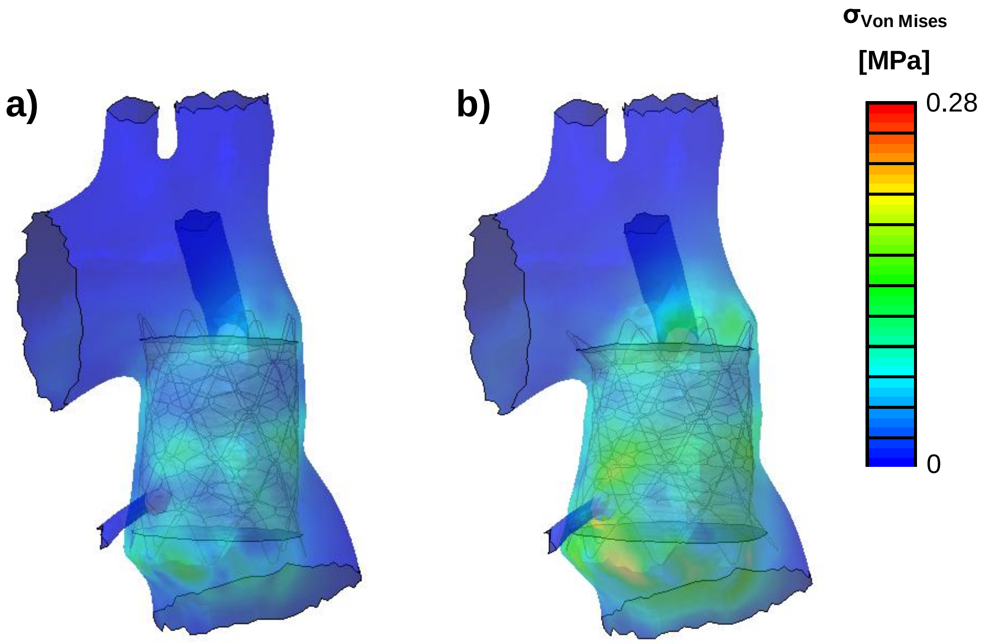

Figure 8.17 – Von Mises stress distribution on the arterial wall after the stent expansion at 16 mm (a) and 18 mm (b).

8.3.2.3 <u>Fluid dynamic model post-intervention</u>

The interpolation functions for the data extracted through the steady-state simulations with the two post-procedure 3D models (16 and 18 mm) resulted to be linear for the five upper branches (RCC, LCC, LVERT, LSUB and ARSA), and of the second order for the ascending (AA) and the descending aorta (CoA). The coefficients of such equations are reported in Table 8.4.

The comparison between the outcomes obtained with the CFD post-procedure aortic models and the corresponding LPNs showed a satisfactory agreement in the flow curves (Figure 8.18 for the 16 mm model and Figure 8.19 for the 18 mm model) and flow splits (Table 8.5). The maximum percentage difference between LPN and CFD in terms of flow split was equal to 3.05% in the 16 mm model at the left subclavian artery and to 3.51% in the 18 mm model at the descending aorta.

Table 8.4 - Resistance parameters set in the pre and post-operative LPN models of the aorta.

	PRE-OP	POST-OP 16mm	POST-OP 18mm
R_{RCC} [Pa/m^3/s]	8.40 E+06	6.68E+06	6.30E+06
R_{LCC} [Pa/m^3/s]	5.90 E+06	4.20E+06	4.7E+06
R_{LVERT} [Pa/m^3/s]	2.15E+07	2.15E+07	2.00E+07
R_{LSUB} [Pa/m^3/s]	4.85E+06	4.10E+06	4.44E+06
R_{ARSA} [Pa/m^3/s]	4.4 E+07	7.50E+07	6.75E+07
a_{CoA} [Pa/(m^3/s)^2]	9.0E+09	8.20E+09	7.90E+09
b_{CoA} [Pa/m^3/s]	9.80E+06	1.04E+05	7.40E+04

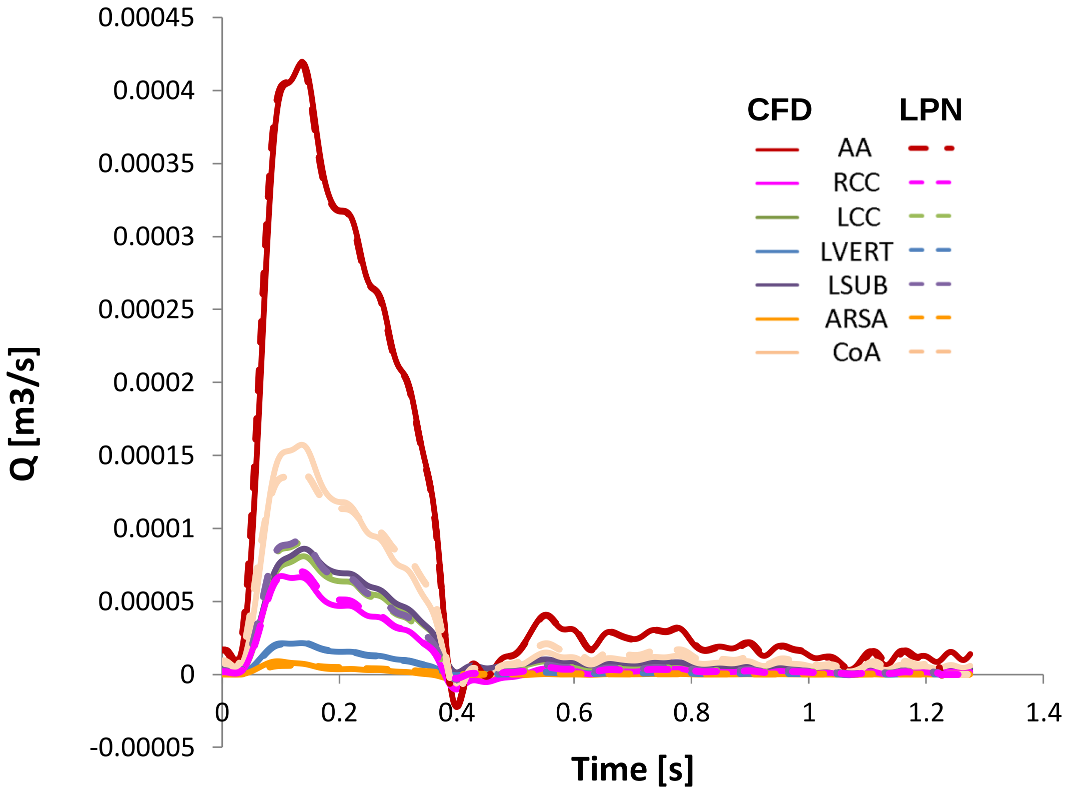

Figure 8.18 - Flow comparison at the inlet and outlet sections between the LPN model (dotted line) and the CFD model (solid line) of the post-operative aorta with the stent expanded at 16 mm of diameter.

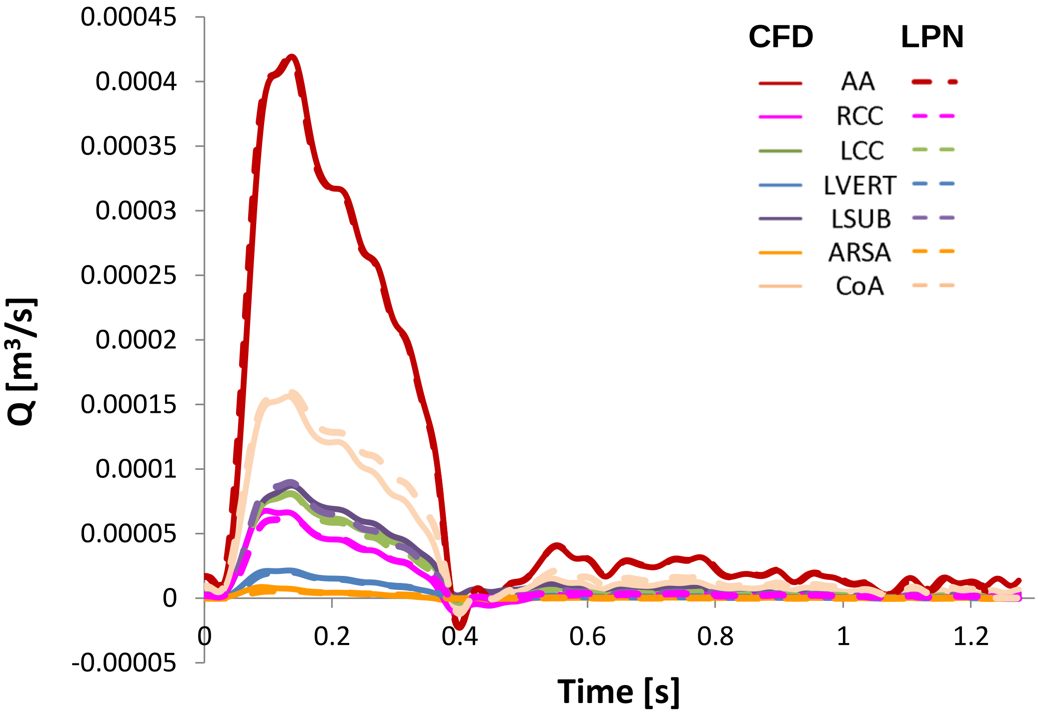

Figure 8.19 - Flow comparison at the inlet and outlet sections between the LPN model (dotted line) and the CFD model (solid line) of the post-operative aorta with the stent expanded at 18 mm of diameter.

Table 8.5 - Flow split in the outlets of the aorta in terms of percentages of the total inflow for the CFD and the LPN models of the aorta after stent implantation at 16 and 18 mm.

	16 mm		**18 mm**	
POST-OP AORTA	**CFD**	**LPN**	**CFD**	**LPN**
Q_{RCC} [%]	13.94	15.25	13.54	13.90
Q_{LCC} [%]	19.97	19.59	19.42	17.77
Q_{LVERT} [%]	4.67	4.74	4.50	4.47
Q_{LSUB} [%]	23.02	19.97	22.01	19.73
Q_{ARSA} [%]	1.10	1.36	1.21	1.30
Q_{CoA} [%]	37.3	39.09	39.32	42.83

The LPN simulations of the complete post-procedural systemic circulation showed negligible differences between the 16 and the 18 mm stent expansions. In the former case, 5.48% of the total inflow during 1 cardiac cycle was directed to the ARSA and

72.69% to the lower body; the latter case presented 5.36% and 73.08% going to the ARSA and the descending aorta respectively (Table 8.6).

The pressure gradient across the treated CoA was reduced to 1.91 mmHg in case of a 16 mm stent expansion and to 1.81 mmHg in case an 18 mm stent was implanted.

Following the results of the FE and LPN simulations, a deployment of the covered CP stent between 16 and 18 mm diameter was suggested to the interventional cardiologist for the procedure.

Table 8.6 - Flow split in the outlets of the aorta in terms of percentages of the total inflow for the CFD and the LPN models of the whole systemic circulation after the stent implantation at 16 and 18 mm.

POST-OP SYSTEMIC	**LPN 16 mm**	**LPN 18 mm**
Q_{RCC} [%]	8.75	8.49
Q_{LCC} [%]	4.91	4.88
Q_{LVERT} [%]	1.82	1.73
Q_{LSUB} [%]	6.35	6.46
Q_{ARSA} [%]	5.48	5.36
Q_{CoA} [%]	72.69	73.08

8.3.3 Intervention

The procedure was successfully carried out according to the planned strategy. The interventional cardiologists implanted a CP covered device expanded inflating an 18 x 45 mm balloon-in-balloon system to a final diameter of 16 mm (Figure 8.20a). This size was in the range suggested by the modelling analyses.

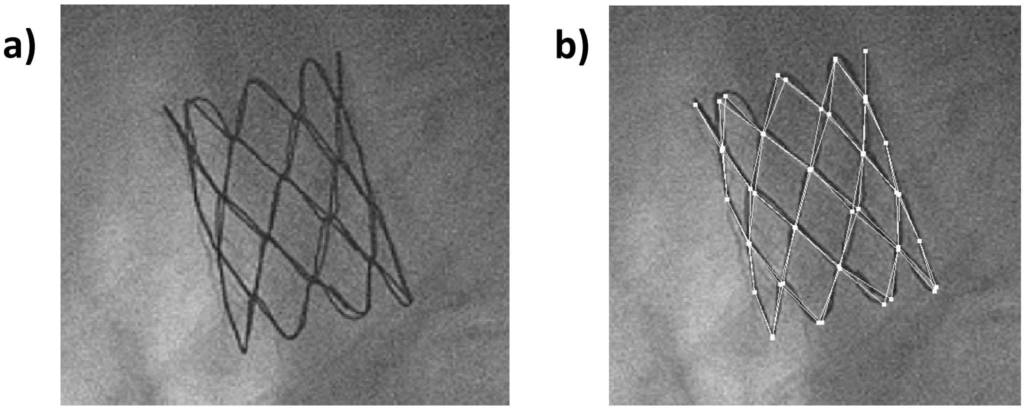

Figure 8.20 - Fluoroscopy image of the covered stent implanted in the patient with a 16 mm diameter size (a), and 3D in-situ reconstruction with the biplane fluoroscopy method.

The procedural biplane fluoroscopy images were processed to obtain the 3D geometry and position of the CP stent in-situ (Figure 8.20b). In the axial direction, the maximum distance between the vertexes of the stent in the 16 mm computational prediction and in the reality was 2.5 mm. In terms of diameter, the difference between the two cases varied between 2.3 % and 6.1% measured respectively in the proximal and distal ring (Figure 8.22). The ARSA remained patent after stenting also thanks to the presence of an Opta Pro 7 x 20 mm balloon inflated in the subclavian artery during the covered stent implantation. Repeated angiograms showed good perfusion of the ARSA and across the stented CoA, as predicted by the computational analyses. Neither extravasations nor dissections were noted, and the patient remained stable throughout the all procedure. Catheter measurements before stent implantation showed no significant pullback pressure gradient between the ascending and the descending arch, while 15 mmHg pullback gradient was recorded across the existing CoA stent. The pressures obtained after the covered stent positioning, under general anaesthesia, were 65/42/52 mmHg (max/min/mean) in the ascending aorta, and 69/40/51 mmHg in descending aorta. The gradient from pull back measurement across the device was reduced to approximately 1 mmHg.

The CFD model was able to predict the reduction in pressure difference across the coarctation and the perfusion of the ARSA after covered stent implantation. However, the post-operative LPN was not able to fully capture the flow split as measured from the post-operative MR flow data (Table 8.7 and Figure 8.21). The maximum difference was recorded in the left subclavian artery: 2.92% of the total inflow from MR measurements vs. 6.25% from the LPN predictive model.

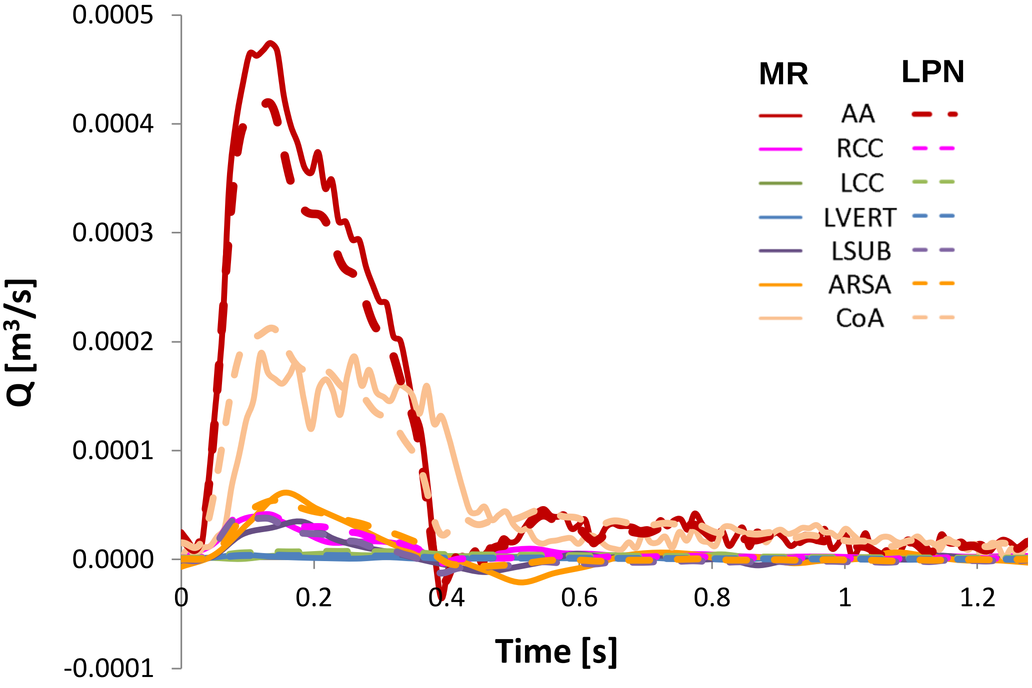

Figure 8.21 - Flow comparison at the inlet and outlet sections between the LPN model prediction (dotted line) and the patient's MR data (solid line) of the post-operative systemic circulation.

Table 8.7 - Flow split in the outlets of the aorta in terms of percentages of the total inflow for the LPN models of the whole systemic circulation after the stent implantation at 16 and the post-operative patient's MR data.

POST-OP SYSTEMIC	**MR**	**LPN 16 mm**
Q_{RCC} [%]	8.93	8.75
Q_{LCC} [%]	7.56	4.91
Q_{LVERT} [%]	3.44	1.82
Q_{LSUB} [%]	2.92	6.35
Q_{ARSA} [%]	4.12	5.48
Q_{CoA} [%]	73.03	72.69

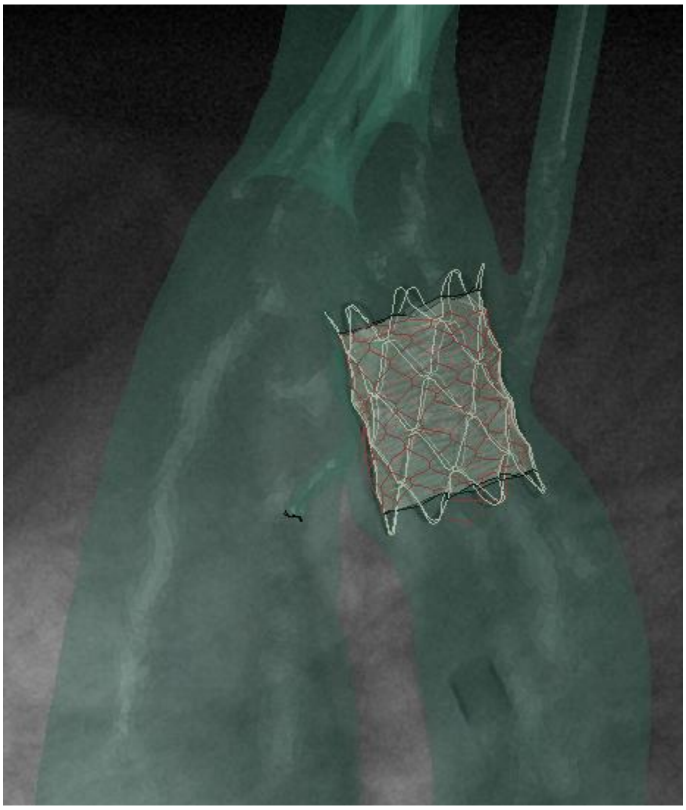

Figure 8.22 - Superimposition of the computational FE results and the angiographic images taken after the intervention.

8.4 DISCUSSION

In this study, a patient-specific modelling methodology was developed to help clinicians select a successful strategy for the treatment of a patient with recurrent CoA. This work showed the benefits of integrating modelling techniques into patient's conventional clinical assessment to support the clinical care team and optimise treatment in complex cases.

The various engineering modelling techniques adopted in this work provided different information to the clinicians improving their confidence in the procedure. The 3D reconstruction and the physical rapid prototyping model of the patient's anatomy fully informed the interventional cardiologists on the 3D spatial relationships between the indwelling stent, the ARSA, the aneurysm and the rest of the descending aorta. Computational models allowed testing different scenarios in a virtual reality that realistically replicated the patient's condition. The results of the virtual procedures could be not only visualised in 3D, but also quantified, thus enabling an extensive comparison between the different procedural options to highlight the optimal stenting approach. The computational modelling techniques included FE analyses that were used to identify the most favourable stent deployment diameter for this specific CoA patient and to define aneurysm treatment, and fluid dynamic simulations with 3D CFD models and LPN equivalent systems, which confirmed that favourable hemodynamic outcomes would be achieved with the FE indicated stent size i.e. patency of the ARSA and pressure drop reduction across the narrowing.

The modelling results were presented and discussed during the multidisciplinary meeting along with the rest of the conventional clinical assessment carried out for the patient, and formed part of the decision for this patient's care. The study was also presented to the patient/parents before treatment and in the discharge letter here reported, underlying how the modelling framework was considered useful by the clinicians:

"We had some expert help from our engineers who created a rapid prototyping three-dimensional model of his aorta and indwelling stent, and we were able to see the relations of his indwelling stent to his aberrant subclavian and his descending aorta. We were also able to ask the engineers to perform computer modelling using computational analysis, and they showed that there would be room to insert an 18 mm covered stent whilst protecting the origin of the right subclavian with a small balloon. In fact, we moved forward and performed that yesterday, and it went very well. Following the procedure, the gradients from pull back of 15 mmHg across the stent was reduced to approximately 1 mmHg."

Importantly, in this patient-specific case, the computational models were all based on available clinical data routinely acquired prior to the intervention. The 3D geometry was reconstructed from CT images integrated with fluoroscopy angiograms and echo data. Fluid dynamics boundary conditions were set using MR derived flows and catheterisation data. However, patient's data were collected using the different imaging modalities over a year time. For example, in terms of pressure, a gradient of 9 mmHg was used in the implementation of the pre-operative model based on the last catheterisation available before the procedure, which however was dated back to about one year before the CT and MR assessment. At the time of cover stent implantation, the pressure gradient was increased up to 15 mmHg, showing progression of the occlusion in the region of the CoA.

The modelling results were compared with the procedural and follow-up clinical data to evaluate the reliability of the developed computational framework in predicting stenting outcomes. FE results differed by a maximum of 6.1% in terms of expansion diameter compared to the real stent expansion as reconstructed from fluoroscopy images. Fluid dynamic outcomes were in satisfactory agreement with the values of pressures measured during the catheterisation at the end of the procedure, and the flows from follow up MR. The largest difference between computationally predicted and real flows was registered in the left subclavian artery (3.4%). Once again, it must be considered the timing of post-operative MR examination that was performed three months after the intervention. In this period, the patient’s vascular resistances may have remodelled, adapting to the new flow regime and consequently the flow distribution among the vessels could have changed accordingly.

In the light of translating results of computational analyses to meet clinical needs, some modelling simplifications were adopted in order to translate computational analysis results to clinical inputs and effectively meet clinical needs such as the limited time for producing the requested results. LPNs were preferred to multi-domain simulations as their computational time is conspicuously reduced. This approach did not allow for visualisation of the local fluid dynamics, but the parameters of interest to answer the clinical question were still represented. The definition of the LPN through CFD 3D model characterisation and peripheral parameter tuning was time consuming but, once set up, presented the advantage of allowing very fast simulation of several different scenarios by tuning of a limited number of parameters. With regards to FE simulations, a beam formulation was preferred to the conventional solid element formulation to model the stent structures. Also in this case, fast simulation response was favoured over accuracy of the results in terms of stress distribution in the stent. The FE analysis was designed to predict the final configuration of the stented aorta and obtain the lumen after the procedure to use as an input in the CFD 3D model, which could be achieved with the use of beams to model the stent. An accurate 3D distribution of stress parameters which could be used to evaluate the stent mechanical performance is not provided by beam elements, but this evaluation was not required.

8.5 CONCLUSIONS

The case study presented in this chapter has allowed me to apply most of the image methodologies and engineering tools that I have analysed, developed, tested, and validated during my PhD programme to support clinicians in treatment planning for a specific patient, and has shown how engineering models can be successfully applied to real prospective clinical cases.

The key aspects for successful patient-specific modelling emerged from this work:

- Access to a wide range of clinical data
- Use of fast and validated engineering methodologies
- Strong collaboration between clinicians and engineers.

CHAPTER 9

CONCLUSIONS and FUTURE WORK

9.1 OVERVIEW

The overall aim of this work was the application of engineering tools to clinical practice in the sphere of patient-specific modelling. During my PhD, I was in the privileged position of working in an engineering team based in the Cardiorespiratory Unit of Great Ormond Street Hospital for Children. Hence, this Thesis is the result of a continuous close collaboration between engineers on one side and clinicians on the other, sharing ideas, better understanding the mutual skills and needs, exchanging advices, influencing each other decisions, with the common objective of delivering better solutions to the patients and improve healthcare.

The general idea of this Thesis was to provide an overview of the current methodologies available to the bioengineers to build patient-specific models and frameworks in the cardiovascular field, to verify their accuracy and to validate them. From this, the work has found application of such tools to a few clinical areas of interest and cases to answer specific clinical questions in the context of congenital heart disease.

Cornerstone of the research was to comply with the principles of translational research, “from bench-to-bedside”: this approach leads directly from computational models and laboratory experiments through clinical research to patient care. Such research does not require to produce extremely complex models, but rather adaptable, simpler and faster tools that have practical benefits and can be used to improve the clinician’s delivery of patient care. For this reason, some of the modelling methodologies implemented in this Thesis privileged clinical applicability to complexity, according to the needs and the time available to set-up the models.

Exemplar application of translational research is the patient-specific model required by the clinicians to support their decision-making process presented in Chapter 8. The time available to set-up the model was less than two weeks. Therefore, fast computational approaches were needed to solve the problem and answer the clinical question in a timely manner. In this case, the clinical question was related to the feasibility of an interventional procedure to relieve the pressure drop experienced by a patient across his previously stented CoA. Complications were represented by the presence of an aneurysm and of the origin of the subclavian artery at the location of the implantation site. The clinical decision was to deploy a new covered stent inside the previous one to treat the aneurysm, but this intervention had the risks of covering the access to the aberrant subclavian artery of the patient, originating at the level of the CoA. Hence, the question of the clinicians regarded the position and the best size for the covered stent to be deployed in order to relieve the pressure drop, cover the aneurysm, and leave the subclavian artery patent. The engineering approach in this case was to reconstruct the pre-operative 3D anatomy of the patient's aorta from clinically acquired images; to use 3D CFD steady-state analysis to derive hemodynamic information on the studied pre-operative geometry then converted in a fast 0D LPN; to simulate with FE method and a fast beam element formulation the stent deployment at different sizes; to convert these post-operative anatomies in LPNs (through CFD simulations) in order to investigate the fluid dynamic outcomes of the different interventional choices, and finally select the best compromise between pressure drop release and vessel perfusion. In this case, a positive outcome resulted from the modelling approach, as the clinicians, driven by the engineering results, successfully treated the patient.

Engineering tools not only can be helpful in the clinical decision-making process, but they could also provide useful information on how to understand specific phenomena and subsequently tailor follow-up for each patient. An example of this is the study conducted on the patient population of 42 individuals who underwent PPVI, reported in Chapter 5. This case was different from the previous in terms of modelling choices, as time was not an issue. Aim of this research was the individuation of those factors responsible for PPVI stent fracture, and the implementation of a statistical model able to identify the risk of device failure for a specific patient just using imaging information routinely acquired during the procedure. The statistical rule created on a cohort of 42 patients used in-situ stent geometrical parameters and their variation measured during the deployment and the cardiac cycle. The geometry of the expanded stent in-situ was derived by means of a newly tested approach that allows the 3D stent to be reconstructed from biplane fluoroscopy images. Such reconstruction process and its accuracy were validated in Chapter 4. Also, fluoroscopy imaging outcomes were compared to those of other static imaging methods, such as micro-CT, CT and stereo-photogrammetry (however limited by its exclusive in-vitro usage). Also, Chapter 4 assessed the biplane fluoroscopy method for capturing dynamic deformations of a stent. Indeed, its accuracy was compared with that of 4DCT, confirming the value of this new approach. Therefore, patient-specific stent deformation can be extracted from fluoroscopy acquisitions and imposed to the FE model of a stent to realistically replicate the deployment history and in-situ loading conditions. Outcomes of these simulations can provide valuable information on the stresses experienced by the device not only during implantation but also from a fatigue point of view. The statistical model developed only on geometrical parameters successfully predicted the stent fracture in 90% of the analysed patients. While the combination of geometrical parameters and FE results permitted the implementation of a statistical model with 93% of accuracy in stent fracture prediction for each patient.

Moving to the fluid dynamic issues, the research presented in Chapter 7 successfully addressed a clinical question raised by the clinicians during MR investigation of the pulmonary system in patients with TGA corrected with ASO. Indeed, ASO is often associated with stenosis of one of the two pulmonary arteries, typically the LPA. Examining patients with unilateral stenosis, it was observed that some cases presented substantially unbalanced blood flow between the stenotic side and the non-stenotic one, as expected. In other cases, however, LPA and RPA flows were relatively balanced, despite the presence of a moderate or even severe stenosis. One currently accepted hypothesis for this takes into account the remodelling of the distal pulmonary vascular resistances (PVR) which counteracts the presence of the stenosis, readjusting the flow split towards more physiological levels. Thus, a model was created to evaluate this hypothesis and eventually estimate the amount of remodelling using anatomical imaging information and flows obtained from MR. A multi-domain approach was used, in which the 3D anatomy of the PAs of 15 TGA patients after ASO was coupled to a patient-specific LPN representative of the distal pulmonary circulation. Also, the consequences on the flow distribution when treating the unilateral stenosis with a stent implantation despite the presence of a physiological flow split was investigated, by integrating the CFD solution with a FE simulation.

Most of the fluid dynamic numerical methodologies utilised in the study of Chapter 7 where first tested and validated in the research presented in Chapter 6 using an in-vitro set-up. A computational model of the neoaorta following ASO and of an healthy control was used to validate the multi-domain approach and to compare the local fluid dynamics in the two different anatomies. The mock circuit was purposely designed for this experiment choosing MR-safe and compatible components, as it was planned to be MR scanned to acquire 4DMR flows on the patient-specific aortas, physically reproduced through the rapid-prototyping technique. The in-silico model was set to reproduce exactly the same boundary conditions applied in-vitro. Velocity pathlines, flows and pressures inside the 3D aorta were compared in the two cases, and satisfactory results obtained.

9.2 FUTURE WORKS

The research presented in this Thesis has covered a broad range of topics, using different engineering tools, demonstrating how they can be used to address clinical questions. Modelling of a dynamic and complex system such as the human being, constantly under regulation by the nervous system, and with a large number of closed loop feedbacks, is tricky and demanding. Important simplifications and assumptions have to be made in case data are missing or unclear to compensate for this. In addition, for easiness of representation, the compartment of interest is usually isolated, not accounting for the influences exerted by all the other systems.

The rapid technological advancements already allowed the science of computational modelling to improve remarkably over the past few years, and this increase in computational power and speed is expected to continue. New modelling tools will thus become available, opening to new methodological opportunities in less computational time. At the same time, technological improvements will affect the clinical parameter acquisition techniques, for example for routinely performed imaging techniques that are gaining increasing resolution with faster acquisitions.

In this section, I will identify general limitations of the models previously presented that need improvement and further development, also in view of the potential technological advancements above mentioned.

9.2.1 Process automation

One of the major issues in patient-specific modelling is that several manual steps in the workflow are required, from anatomy reconstruction to the generation of the results. The automation of these mechanisms is desirable to speed up the process and to reduce operator bias. The 3D stent reconstruction from biplane fluoroscopy images reported in Chapter 4 and used in Chapter 5 could remarkably benefit from such improvement because the currently manually performed reconstruction requires long operator’s times.

Automatic reconstructions would allow not only to use the statistical model for stent fracture prediction immediately after device implantation, but also to analyse considerably more frames during stent implantation and cardiac cycle (Section 4.4). Acquisition of a know phantom with the same parameter settings for table and fluoroscopy arms as those used during the procedure would allow to automate the reconstruction process and an algorithm to perform this is already under development.

Another framework step which would benefit from automation is the reconstruction of the 3D anatomical models from medical imaging. Current image post-processing programs are constantly improving, but manual corrections to refine the volumes or their automatically generated meshes are still required to obtain the correct patient-specific morphology and a mesh accurate enough for numerical simulations. In both cases, operator's experience plays an extremely important role, which better automated reconstructing and meshing functions could reduce.

9.2.2 In-vitro compliant model and FSI

Certainly, one aspect to take into consideration for further studies is the compliant behaviour of the physiological vessels for fluid dynamic analyses. While gross differences in flow split or mean pressures are not expected, a compliant model, both in-vitro and in-vivo, reproducing realistic distensible behaviour would be helpful to study local hemodynamics.

A first attempt towards this was carried out in the in-vitro study described in Chapter 6; however, the material chosen for manufacturing the compliant TGA model did not withstand physiological pressures for the whole time needed for a full MR acquisition. The material (i.e. TangoPlus) suffered structural failure at the arch, so different materials are currently being evaluated. Silicone-based compounds may represent a valid alternative in this regard.

Computationally, if significant differences are observed experimentally between a rigid and a compliant model, it would be possible to simulate such compliant behaviour also numerically, by means of fluid-structural interaction (FSI) simulations. One problem typically related to this methodology is the lack of information of patient-specific vessels' material properties. In the first instance, this issue could be bypassed by using an artificial material which experimentally reproduced the compliant behaviour of the vessel considered. In this way the elastic characteristic would be known, facilitating the FSI simulations.

The fluid dynamics models presented in Chapter 7 and 8 would also benefit from the reproduction of compliant vessels but again the estimation of the in-vivo vessels' properties is not straightforward, and it usually changes along the vessel. For this reason, it must be carefully evaluated when adding compliant characteristics to the simulations is necessary and when it might add further important uncertainties to the model.

9.2.3 Evaluation of in-vivo material properties

The patient-specific anatomy is now usually easy to create but, as mentioned in the previous paragraph, the patient-specific in-vivo material parameters are still missing. Large variations from individual to individual are present, especially in the CHD population, and therefore they cannot be considered the same for all (**74**) to create predictive patient-specific models (see the stent implantation modelled in Chapter 7 and Chapter 8). This could have been also a problem for the FE simulation performed to study the covered stent insertion in the CoA patient of Chapter 8. However, in this case, a metallic stent was already present in the region of implantation; therefore the response to the new stent deployment depended by the combination of the properties of the previously implanted stent and the vessel which were thus playing a less important role.

Several methods have been proposed in literature to overcome this problem combining numerical and experimental approaches (**151**; **152**). In our team, we are working on imaging techniques such as 4DCT and 4DMR that could be employed to identify the 3D temporal deformations of different vessel regions throughout the cardiac cycle, which synchronised with pressure information inside the vessel, would allow an indirect estimation of the distensibility for each patient.

9.2.4 Inlet/Outlet velocity boundary conditions

4D MR flow is a novel imaging technique that could be used not only to validate a computational model, as shown in Chapter 6, but also to set more accurate velocity boundary conditions. In fact, using these data, it is possible to acquire all inlet and outlet information simultaneously and also extract the x, y and z velocity components in time in each of the voxels of one section. Imposing these values to each corresponding element of the mesh at the inlet of the computational model, instead of the spatial average as typically done, could allow a more detailed characterisation of the complex fluid dynamics, e.g. whirling and recirculation in the aortic root. However, the time required for the simulations would considerably increased, while the flow split and overall pressure distribution would not be affected by this different approach. A first attempt was performed in the study presented in Chapter 6, using 2D Cartesian flow acquisitions, in order to explore the methodological aspects. To reduce the high computational cost a coarsen mesh (300,000 elements) was considered, but this was not fine enough for this complex simulation. Therefore, convergence was not reached and further studies are required, taking advantage in the future of more powerful calculation machines.

9.3 CONCLUSION

The use of computational modelling is nowadays integrated in many industrial processes, and is also considered a mandatory step for the development and optimisation of a medical device, before FDA approval. What is not yet established is the systematic use of computational modelling into the clinical environment. This Thesis has shown possible applications and potentialities of computational engineering tools to address specific clinical questions. The models here presented do not intend to give any sort of "dogma" or ineluctable rule to the clinicians, but they represent an additional tool that could be used in the decision making process. Several steps need to be improved before a patient-specific model could be adopted as a clinical standard of care, and at the moment the bottleneck lies in the manual executions these models require to be implemented, in the need for model standardisation, and systematic validation (**74**), in the time sensitivity, and sometimes in the lack of the necessary clinical data such as material properties. Once all these technical problems are solved, the final difficulty will consist in the integration of such models in the clinical workflow. Researchers are already putting lots of efforts in trying to overcome these limitations, and, in my opinion, key to the success of patient-specific modelling is the establishment of a multidisciplinary team, with clinicians and engineers working together to enhance patient healthcare.

BIBLIOGRAPHY

1 - Anderson RN, Smith BL. Deaths: leading causes for 2001. *National Vital Statistics Report;* 52(9): 1-85. 2003.

2 - Bruneau BG. The developmental genetics of congenital heart disease. *Nature;* 451(21): 943:948. 2008.

3 - Macmahon B, Mckeown T, Record RG. The incidence and life expectation of children with congenital heart disease. *British Heart Journal;* 15(2):121-129. 1953.

4 - Ntsinjana H, Hughes ML, Taylor AM. The role of cardiovascular magnetic resonance in pediatric congenital heart disease. *Journal of Cardiovascular Magnetic Resonance;* 13(1): 51:1-20. 2011.

5 - de Leval MR. Right heart bypass operations. *In: Stark J, de Leval MR. Surgery for Congenital Heart Defects, W.B. Saunders Company (eds);* 565-585. 1992.

6 - Mitsuno M, Nakano S, Shimazaki Y, Taniguchi K, Kawamoto T, Kobayashi J, Matsuda H, Kawashima Y. Fate of right ventricular hypertrophy in tetralogy of Fallot after corrective surgery. *American Journal of Cardiology;* 72(9):694-698. 1993.

7 - Lutter G, Ardehali R, Cremer J, Bonhoeffer P. Percutaneous Valve Replacement: Current State and Future Prospects. *The Annals of Thoracic Surgery;* 78: 2199-2206. 2004.

8 - Khambadkone S, Bonhoeffer P. Nonsurgical Pulmonary Valve Replacement: why, when and how? *Catheterization and Cardiovascular Interventions;* 62(3):401-408. 2004.

9 - Pavcnik D, Wright KC, Wallace S. Development and Initial Experimental Evaluation of a Prosthetic Aortic Valve for Transcatheter Placement – work in progress. *Cardiovascular Radiology;* 183: 151-154. 1992.

10 - Bonhoeffer P, Boudjelmine Y, Saliba Z, Hausse AO, Aggoun Y, Bonnet D, Sidi D, Kachaner J. Transcatheter implantation of a bovine valve in pulmonary position: a lamb study. *Circulation;* 102: 813-816. 2000.

11 - Lutter G, Kuklinski D, Berg G, von Samson P, Martin J, Handke M, Uhrmeister P, Beyersdorf F. Percutaneous aortic valve replacement: An experimental study. I. Studies on implantation. *Journal of Thoracic and Cardiovascular Surgery;* 123(4):768-776. 2002.

12 - Boudjemline Y, Bonhoeffer P. Percutaneous implantation of a valve in the descending aorta in lambs. *European Heart journal;* 23(13):1045-1049. 2002.

13 - Pavcnik D, Uchida BT, Timmermans HA, Corless CL, O'Hara M, Toyota N, Moneta GL, Keller FS, Rosch J. Percutaneous bioprosthetic venous valve: a long-term study in sheep. *Journal of Vascular Surgery;* 35(3):598-602. 2002.

14 - Bonhoeffer P, Boundjemeline Y, Saliba Z, Merckx J, Aggoun Y, Bonnet D, Acar P, Le Bidois J, Sidi D, Kachaner J. Percutaneous replacement of pulmonary valve in a right-ventricle to pulmonary-artery prosthetic conduit with valve dysfunction. *The Lancet;* 356 (9239):1403-1405. 2000.

15 - Cribier A, Eltchaninoff H, Bash A, Borenstein N, Tron C, Bauer F, Derumeaux G, Anselme F, Laborde F, Leon MB. Percutaneous transcatheter implantation of an aortic valve prosthesis for calcific aortic stenosis: first human case description. *Circulation*; 106(24):3006-3008. 2002.

16 - Vahanian A, Acar C. Percutaneous valve procedures: what is the future? *Current Opinion in Cardiology;* 20(2):100-106. 2005.

17 - Cheatham JP. Stenting of Coarctation of the Aorta. *Catheterization and Cardiovascular Interventions;* 54:112-125. 2001.

18 - Capelli C, Taylor AM, Migliavacca F, Bonhoeffer P, Schievano S. Patient-specific reconstructed anatomies and computer simulations are fundamental for selecting medical device treatment: application to a new percutaneous pulmonary valve. *Philosophical Transactions Series A, Mathematical, Physical and Engineering Sciences;* 368(1921):3027-3038. 2010.

19 - Schievano S, Taylor AM, Capelli C, Coats L, Walker F, Lurz P, Nordmeyer J, Wright S, Khambadkone S, Tsang V, Carminati M, Bonhoeffer P. First-in-man implantation of a novel percutaneous valve: a new approach to medical device development. *EuroIntervention;* 5(6):745-50. 2010.

20 - Nordmeyer J, Khambadkone S, Coats L, Schievano S, Lurz P, Parenzan G, Taylor AM, Lock JE, Bonhoeffer P. Risk Stratification, Systematic Classification, and Anticipatory Management Strategies for Stent Fracture After Percutaneous Pulmonary Valve Implantation. *Circulation;* 115:1392-1397. 2007.

21 - Nordmeyer J, Coats L, Lurz P, Lee TY, Derrick G, Rees P, Cullen S, Taylor AM, Khambadkone S, Bonhoeffer P. Percutaneous pulmonary valve-in-valve implantation: a successful treatment concept for early device failure. *European Heart Journal;* 29(6):810-815. 2008.

22 - Nordmeyer J, Lurz P, Khambadkone S, Schievano S, Jones A, McElhinney DB, Taylor AM, Bonhoeffer P. Pre-stenting with a bare metal stent before percutaneous pulmonary valve implantation: acute and 1-year outcomes. *Heart;* 97(2):118-123. 2011.

23 - Fleming GA, Hill KD, Green AS, Rhodes JF. Percutaneous pulmonary valve replacement. *Progress in Pediatric Cardiology;* 33:143-150. 2012.

24 - Lincon CR, Lima R, Rigby ML. Anatomic correction of simple transposition of the great arteries during the neonatal cardiovascular transition. *Archives of disease in childhood;* 59(7):673-675. 1984.

25 - Kalogeropoulos AP, Geogiopoulou VV, Giamouzis G, Pernetz AA, Anadiotis A, Mc Connell M, Lerakis S, Butler J, Book WM, Martin RP. Myocardial deformation imaging of the systemic right ventricle by two-dimensional strain echocardiography in patients with D-transposition of the great arteries. *The Hellenic Journal of Cardiology;* 50:275-282. 2009.

26 - Warnes CA. Transposition of the great arteries. *Circulation;* 114:2699-2709. 2006.

27 - Allen HD, Driscoll DJ, Shaddy RE, Feltes TF. Moss & Adams' Heart Disease in Infants, Children, and Adolescents, 7th Edition. *By Lippincott Williams & Wilkins, Philadelphia, PA, USA*. 2008.

28 - Planche C, Lacour-Gayer F, Serraf A. Arterial switch. *Pediatric Cardiology;* 19:297-307. 1998.

29 - Shrivastava S, Tadavarthy SM, Fukuda T, Edwards JE. Anatomic causes of pulmonary stenosis in complete transposition. *Circulation;* 54:154-159. 1976.

30 - Senning A. Surgical correction of transposition of the great vessels. *Surgery;* 45:966-80. 1959.

31 - Mustard WT, Keith JD, Trusler GA. The surgical management of transposition of great arteries. *Journal of Thoracic Cardiovascular Surgery;* 48:953-8. 1964.

32 - Kostantinov IE, Alexi-Meskishvili VV, Wiliams WG, Freedom RM, Vam Praagh R. Arterial switch operation: past, present, and future. *The Annals of Thoracic Surgery;* 77:2250-8. 2004.

33 - Jatene AF, Fontes VF, Souza LCB. Anatomic correction of transposition of the great arteries. *Journal of Thoracic Cardiovascular Surgery;* 83:20-6. 1982.

34 - Cohen MD, Johnson T, Ramrakhiani S. MRI of surgical repair of transposition of the great vessels. *American Journal of Roentgenology;* 194:140-160. 2010.

35 - Ntsinjana H, Biglino G, Steeden JA, Schievano S, Taylor AM. Mechanical and morphological properties of the aortic root and arch late after arterial switch operation for transposition of the great arteries. *Journal of Cardiovascular Magnetic Resonance;* 14(Suppl 1):P115. 2012.

36 - Mavroudis C, Steward RD, Backer CL, Rudra H, Vargo P, Jacobs ML. Reoperative techniques for complications after arterial switch. *The Annals of Thoracic Surgery;* 92:1747-55. 2011.

37 - Grotenhuis HB, Ottenkamp J, Fontein D, Vligen HW, Westenberg JJM, Kroft LJM, Roos A. Aortic elasticity and left ventricular function after arterial switch operation: MR imaging – initial experience. *Radiology;* 249(3):801-809. 2008.

38 - Co-Vu J, Glinde S, Bartz PJ, Frommelt PC, Tweddell CJS, Earing MG. Long-term outcomes of the neoaorta after arterial switch operation for transposition of the great arteries. *The Annals of Thoracic Surgery;* 95(5): 1654-1659. 2013.

39 - Agnoletti G, Ou P,Celermajer DS, Boudjemline Y, Marini D, Bonnet D, Aggoun Y. Acute angulation of the aortic arch predisposes a patient to ascending aortic dilatation and aortic regurgitation late after the arterial switch operation for transposition of the great arteries. *Journal of Thoracic Cardiovascular Surgery;* 135(3):568-72. 2007.

40 - Ou P, Celermajer DS, Raisky O, Jolivet O, Buyens F, Herment A, Sidi D, Bonnet D, Mousseaux E. Angular (Gothic) aortic arch leads to enhance systolic wave reflection, central aortic stiffness, and increased left ventricular mass late after aortic coarctation repair: evaluation with magnetic resonance flow mapping. *Journal of Thoracic Cardiovascular Surgery;* 135:62-8. 2008.

41 - Biglino G, Verschueren P, Zegels R, Taylor AM, Schievano S. Rapid prototyping compliant arterial phantoms for in-vitro studies and device testing. *Journal of Cardiovascular Magnetic Resonance;* 15:2. 2013.

42 - Prifti E, Crucean A, Bonacchi M, Bernabei M, Murzi B, Luisi SV, Vanini V. Early and long term outcome of the arterial switch operation for transposition of the great arteries: predictors and functional evaluation. *European Journal of Cardio-Thoracic Surgery;* 22: 864-873. 2002.

43 - Nakanishi T, Matsumoto Y, Seguchi M, Nakazawa M, Imai Y, Momma K. Balloon angioplasty for postoperative pulmonary artery stenosis in transposition of the great arteries. *Journal of the American College of Cardiology;* 22: 859-66. 1993.

44 - Formigari R, Santoro G, Guccione P, Giamberti A, Pasquini L, Grigioni M, Ballerini L. Treatment of pulmonary artery stenosis after arterial switch operation: stent implantation vs. balloon angioplasty. *Catheterization and Cardiovascular Interventions;* 50: 207-211. 2000.

45 - Baumbach GL, Heistad DD, Siems JE. Effect of sympathetic nerves on composition and distensibility of cerebral arterioles in rats. *Physiology;* 416:123-140. 1989.

46 - Mulvany MJ. Vascular remodelling of resistance vessels: can we define this? *Cardiovascular Research;* 41:9-13. 1999.

47 - Bakker ENTP, Matlung HL, Bonta P, deVries CJ, vanRooijen N, vanBavel E. Blood flow-dependent arterial remodelling is facilitated by inflammation but directed by vascular tone. *Cardiovascular Research;* 78:341-348. 2008.

48 - Tulloh RMR. Congenital heart disease in relation to pulmonary hypertension in paediatric practice. *Paediatric respiratory reviews;* 6:174-180. 2005.

49 - Bakker ENTP, Pistea P, Spaan JAE, Rolf T, deVries CJ, vanRooijen N, Candi E, vanBavel E. Flow-dependent remodelling of small arteries in mice deficient for type tranglutaminase: possible compensation by macroohage-derived factor XIII. *Circulation Research;* 99: 86-92. 2006.

50 - Yin Z, Wang Z, Zhu H, Zhang R, Wang H, Li X. Experimental study of effect of Fontan circuit n pulmonary microcirculation. *Asian Cardiovascular and Thoracic Annals;* 14:183-188. 2006.

51 - Chiu IS, Wang JK, Wu MH. Spiral arterial switch operation in transposition of the great arteries. *Journal of Thoracic Cardiovascular Surgery;* 134:1050:1052. 2002.

52 - De Mey S, Segers P, Coomans I, Verhaaren H, Verdonck P. Limitations of Doppler echocardiography for the post-operative evaluation of aortic coarctation. Journal of Biomechanics; 34:951-960. 2001.

53 - Brickner ME, Hillis LD, Lange RA. Congenital heart disease in adults. *The New England Journal of Medicine;* 342(4):256-263. 2000.

54 - Hamdan M. Coarctation of the aorta: a comprehensive review. *Journal of the Arab Neonatology Forum;* 3:5-13. 2006.

55 - Krishnam AM, Tomasian A, Malik S, Desphande V, Laub G, Ruehm SG. Image quality and diagnostic accuracy of unenhanced SSFP MR angiography compared with conventional contrast enhanced MR angiography for the assessment of thoracic aortic diseases. *European Radiology;* 20(6):1311-1320. 2010.

56 - Keshavarz-Motamed Z, Kadem L. 3D pulsatile flow in a curved tube with coexisting model of aortic stenosis and coarctation of the aorta. *Medical Engineering & Physics;* 33:315-324. 2011.

57 - Lantz J, Ebbers T, Engvall J, Karlsson M. Numerical and experimental assessment of turbulent kinetic energy in an aortic coarctation. *Journal of Biomechanics;* 46:1851-1858. 2013.

58 - Prada F, Carretero J, Mortera C, Velasco D. Balloon Angioplasty in a 1200-Gram Premature Infant with Critical Aortic Coarctation. *Revista Espanola de Cardiologia;* 63:741-743. 2010.

59 - Itu L, Puneet S, Ralovich K, Mihalef V, Ionasec R, Everett A, Ringel R, Kamen A, Comaniciu D. Non-Invasive Hemodynamic Assessment of Aortic Coarctation: Validation with In Vivo Measurement. *Annals of Biomedical Engineering;* 41(4):669-681. 2013.

60 - Seifert BL, DesRochers K, Ta M, Giraud G, Zarandi M, Gharib M, Sahn DJ. Accuracy of Doppler methods for estimating peak-to-peak and peak instantaneous gradients across coarctation of the aorta: an in vitro study. *Journal of the American Society of Echocardiography;* 12:744-753. 1999.

61 - Hom J, Ordovas K, Reddy GP. Velocity-encoded Cine MR Imaging in Aortic Coarctation: Functional Assessment of Hemodynamic Events. *RadioGraphics;* 28:407-416. 2008.

62 - Sadiq M, Rehman AU, Qureshi AU, Qureshi SA. Covered Stents in the Management of Native Coarctation of the Aorta – Intermediate and Long-Term Follow-Up. *Catheterization and Cardiovascular Interventions;* 8(4):511-518. 2013.

63 - Tanous D, Benson LN, Horlick EM. Coarctation of the aorta: evaluation and management. *Current Opinion in Cardiology;* 24:509-515. 2009.

64 - Lock JE, Niemi T, Burke BA, Einzig S, Castaneda-Zuniga WR. Transcutaneous angioplasty of experimental aortic coarctation. *Circulation;* 66:1280-1286. 1982.

65 - Ringel RE, Gauvreau K, Moses H, Jenkins KJ. Coarctation of the Aorta Stent Trial (COAST): study design and rationale. *American Heart Journal;* 164(1):7-13. 2012.

66 - Krasemann T. Treatment for coarctation of the aorta: where are we and where do we go from here? *Interventional Cardiology;* 3(5):531-533. 2011.

67 - Mortazaeian H, Moghadam MYA, Ghaderian M, Davary PN, Meraji M, Mohammadi AS. Evaluation of Exercise-Induced Hypertension Post Endovascular Stenting of Coarctation of Aorta. *The Journal of Teheran University Heart Center;* 5(3):137-140. 2010.

68 - Forbes TJ, Kim DW, Turner DR, Holzer R, Amin Z, Hijazi Z, Ghasemi A, Rome JJ, Nykanen D, Zahn E, Cowley C, Hoyer M, Waight D, Gruenstein D, Javois A, Foerster S, Kreutzer J, Sullivan N, Khan A, Owada C, Hagler D, Lim S, Canter J, Zellers T, CCISC Investigators. Comparison of surgical, stent, and balloon angioplasty treatment of native coarctation of the aorta: an observational study by the CCISC (Congenital Cardiovascular Interventional Study Consortium). *Journal of the American College of Cardiology;* 58(25):2664-2674. 2011.

69 - Ford A. Modeling the environment, *2nd Edition, Island Press*. 2009.

70 - Frigg R, Hartmann S. Models in Science. *The Stanford Encyclopedia of Philosophy (Fall 2012 Edition), Edward N. Zalta (ed.),* URL = <http://plato.stanford.edu/archives/fall2012/entries/models-science/>. 2012.

71 - Box GEP, Draper NR. Empirical Model-Building and Response Surfaces, *Wiley*. p. 424. 1987.

72 - Science Learning Hub- The University of Waikato). *(http://www.sciencelearn.org.nz/Contexts/The-Noisy-Reef/Science-Ideas-and-Concepts/Scientific-modelling)*

73 - Black M. Models and Metaphors. Studies in Language and Philosophy. *Ithaca, New York: Cornell University Press.* 1962.

74 - Neal ML, Kerckhoffs R. Current progress in patient-specific Modelling. *Briefings in Bioinformatics;* 11(1):111-126. 2009.

75 - Bogaert J, Dymarkowsky S, Taylor AM. Clinical cardiac MRI. *Heidelberg: Springer-Verlag ed.* 2005.

76 - Anderson RH, Razavi R, Taylor AM. Cardiac anatomy revisited. *Journal of Anatomy;* 205(3):159-177. 2004.

77 - Razavi RS, Hill DL, Muthurangu V, Miquel ME, Taylor AM, Kozerke S. Three-dimensional magnetic resonance imaging of congenital cardiac anomalies. *Cardiology in the Young;* 13(5):461-465. 2003.

78 - Sorensen TS, Korperich H, Greil GF, Eichhorn J, Barth P, Meyer H, Pedersen EM, Beerbaum P. Operator-independent isotropic three-dimensional magnetic resonance imaging for morphology in congenital heart disease: a validation study. *Circulation;* 110(2):163-169. 2004.

79 - Schievano S, Taylor AM, Capelli C, Lurz P, Nordmeyer J, Migliavacca F, Bonhoeffer P. Patient specific finite element analysis results in more accurate prediction of stent fractures: application to percutaneous pulmonary valve implantation. *Journal of Biomechanics;* 43(4):687-693. 2010.

80 - Taggart DP, Hadjinikolas L, Hooper J, Albert J, Kemp M, Hue D, Yacoub M, Lincoln JC. Effects of age and ischemic times on biochemical evidence of myocardial injury after pediatric cardiac operations. *Journal of Thoracic Cardiovascular Surgery;* 113(4):728-735. 1997.

81 - Nordmeyer A, Berger F, Kuehne T, Riesenkampff. Flow-sensitive four-dimensional magnetic resonance imaging facilitates and improves the accurate diagnosis of partial

anomalous pulmonary venous drainage. *Journal of Magnetic Resonance Imaging;* 32:677-683. 2010.

82 - Uribe S, Bachler P, Valverde I, Crelier GR, Beerbaum P, Tejos C, Irarrazaval P. Hemodynamic assessment in patients with one-and-a-half ventricle repair revealed by four-dimensional flow magnetic resonance imaging. *Pediatric Cardiology;* 34(2):447-451. 2013.

83 - Mahnken AH. CT Imaging of Coronary Stents: Past, Present, and Future. *ISRN Cardiology;* ID:139823. 2012.

84 - Lim HB, Hur G, Kim SY, Kim YH, Kwon SU, Lee WR, Cha SJ. Coronary Stent Fracture: Detection with 64-Section Multidetector CT Angiography in Patients and in Vitro. *Radiology;* 249(3):810-819. 2008.

85 - Sherwin SJ, Peiro J. Finite difference, finite element and finite volume methods for partial differential equations. *Handbook of materials modeling, Editor(s): Yip, Berlin, Springer;* Pages:1-30, ISBN:9781402032875. 2005.

86 - Dhatt G, Lefrançois E, Touzot G. Finite Element Method. *ISTE Ltd John Wiley & Sons, Great Britain;* 2012.

87 - Clough RW. The finite element method after twenty-five years: a personal view. *Computers & Structures;* 12:361-370. 1980.

88 - Symposium on the use of computers in civil engineering laboratorio national de engenharia civil, Lisbon, Portugal. 1962.

89 - Cook RD. Concepts and applications of finite element analysis. *Willey;* 2007.

90 - ASTM F2514 .Standard Guide for Finite Element Analysis (FEA) of Metallic Vascular Stents Subjected to Uniform Radial Loading. 2008.

91 - Guidance for Industry and FDA Staff - Non-Clinical Engineering Tests and Recommended Labeling for Intravascular Stents and Associated Delivery Systems. January 2005.

92 - Anderson JD. Computational Fluid Dynamics: The Basic with Applications. *McGraw Hill, Inc.;* 1995.

93 - Coveney P, Diaz V, Hunter P, Viceconti M. The virtual physiological human. *Interface Focus;* 1(3):281-473. 2011.

94 - Laganà K. Multiscale mathematical models for biofluidynamic applications. *PhD Thesis, Politecnico di Milano;* 2002.

95 - Migliavacca F, Balossino R, Pennati G, Dubini G, Hsia TY, de Leval MR, Bove EL. Multiscale modelling in biofluid dynamics: application to reconstructive paediatric cardiac surgery. *Journal of biomechanics;* 39:1010-1020. 2006.

96 - Quarteroni A, Veneziani A. Analysis of a geometrical multiscale model based on the coupling of ODE and PDE for blood flow simulations. *Multiscale Modeling & Simulation;* 1:173-195. 2003.

97 - Skalak R. Synthesis of a complete circulation. *In Cardiovascular fluid Dynamics (DH Bergel ed.); Vol.2 Ch.19 - Academic Press*. 1972.

98 - Vismara R, Laganà K, Migliavacca F, Schievano S, Coats L, Taylor AM, Bohnoeffer P. Experimental setup to evaluate the performance of percutaneous pulmonary valved stent in different outflow tract morphologies. *Artificial Organs;* 33(1):46-53. 2009.

99 - Biglino G, Giardini A, Baker C, Figliola RS, Hsia TY, Taylor AM, Schievano S. In vitro study of the Norwood palliation: a patient-specific mock circulatory system. *ASAIO Journal;* 58:25-31. 2012.

100 - Quarteroni A, Ragni S, Veneziani A. Coupling between lumped and distributed models for blood flow problems. *Computing and Visualization in Science;* 4:111-124. 2001.

101 - Ibrahim D, Broilo TL, Heitz C, De Oliveira MG, De Oliveira HW, Nobre SMW, Dos Santos Filho JHG, Silva DN. Dimensional error of selective laser sintering, three-dimensional printing and PolyJetTM models in the reproduction of mandibular anatomy. *Journal of Cranio-Maxillofacial Surgery;* 37:167-173. 2009.

102 - McElhinney DB, Cheatham JP, Jones TK, Lock JE, Vincent JA, Zahn EM, Hellenbrand WE. Stent Fracture, Valve Dysfunction, and Right Ventricular Outflow Tract Reintervention After Transcatheter Pulmonary Valve Implantation Patient-Related and Procedural Risk Factors in the US Melody Valve Trial. *Circulation-Cardiovascular Interventions;* 4(6):602-614. 2011.

103 - Orminston JA, Webster MW, Webber B, Stewart JT, Ruygrok PN, Hatrick RI. The "Crush" Technique for Coronary Artery Bifurcation Stenting: Insights From Micro-Computed Tomographic Imaging of Bench Deployments. *Journal of the American College of Cardiology: cardiovascular interventions;* 1(4):351-357. 2008.

104 - Poerner TC, Ludwig B, Duda SH, Diesing P, Kalmar G, Suselbeck T, Kaden JJ, Borggrefe M, Haase KK. Determinants of Stent Expansion in Curved Stenotic Lesions: An In Vitro Experimental Study. *Journal of Vascular and Interventional Radiology;* 15: 727-735. 2004.

105 - Conti M, Van Loo D, Auricchio F, De Beule M, De Santis G, Verhegghe B, Pirrelli S, Odero A. Impact of Carotid Stent Cell Design on Vessel Scaffolding: A Case Study Comparing Experimental Investigation and Numerical Simulations. *Journal of Endovascular Therapy;* 18:397-406. 2011.

106 - Leipsic J, Gurvitch R, LaBounty TM, Min JK, Wood D, Johnson M, Ajlan AM, Wijesinghe N, Webb JG. Multidetector Computed Tomography in Transcatheter Aortic Valve Implantation. *Journal of the American College of Cardiology: cardiovascular imaging;* 4(4):416-429. 2011.

107 - Ionescu M, Metcalfe RW, Cody D, Valdivia y Alvarado M, Hipp J, Benndorf G. Spatial Resolution Limits of Multislice Computed Tomography (MS-CT), C-arm-CT, and Flat Panel-CT (FP-CT) Compared to MicroCT for Visualization of a Small Metallic Stent. *Academic Radiology;* 18(7):866-875. 2011.

108 - Connolley T, Nash D, Buffiere J-Y, Sharif F, McHugh PE. X-ray micro-tomography of a coronary stent deployed in a model artery. *Medical Engineering & Physics;* 29:1132-1141. 2007.

109 - Narracott AJ, Hose DR, Lawford PV, Gunn J. Measurement of the symmetry of in vitro stent expansion: a stereo-photogrammetric approach. *Journal of Medical Engineering and Technology;* 27(2):59-70. 2003.

110 - Russ C, Gessat M, Falk V, Szekely G. Rapid Prototyping of Silicone-based Phantom Models for Stent Simulation Validation. *MICCAI - Stent'12, 1st MICCAI Workshop on Computer Assisted Stenting*. 2012.

111 - Bouguet, Camera Calibration Toolbox for Matlab, Retrieved 2008, http://www.vision.caltech.edu/bouguetj/calib_doc/. Retrieved September , 2010.

112 - Zwierzak I, Fenner JW, Narracott AJ. Strain Measurement in an Elastic Material under Large Deformation Using Optical Reconstruction Methods. *International Conference on Advancements of Medicine and Health Care through Technology IFMBE Proceedings*. 120-123. 2011.

113 - Liu P, Willis A, Sui Y. Stereoscopic 3D Reconstruction using Motorized Zoon Lenses within an embedded system. *Image Processing: Machine Vision Applications II;* SPIE-IS&T-465:7251-72510W-1.

114 - Zwierzak I, Fenner JW, Narracott AJ. Three dimensional optical reconstruction method for stent geometry characterisation; data validation using micro CT technique. *VPH2012, London, UK.* 2012.

115 - Alp NJ, Alia ZA, Channona KM. Models for studying coronary artery stenting. *Drug Discovery Today: Disease Models;* 3(3):297-303. 2006.

116 - Gijsen FJH, Migliavacca F, Schievano S, Socci L, Petrini L, Thury A, Wentzel JJ, van der Steen AFW, Serruys PWS, Dubini G. Simulation of stent deployment in a realistic human coronary artery. *BioMedical Engineering OnLine;* 7(23). 2008.

117 - Migliavacca, F., L. Petrini, M. Colombo, F. Auricchio, and R. Pietrabissa, Mechanical behavior of coronary stents investigated through the finite element method. Journal of Biomechanics, 2002. 35(6): p. 803-811

118 - Auricchio F, Conti M, De Beule M, De Santis G, Verhegghe B. Carotid artery stenting simulation: From patient-specific images to finite element analysis. *Medical Engineering & Physics;* 33:281-289. 2011.

119 - Lurz P, Schuler PK, Muthurangu V, Schievano S, Khambadkone S, Derrick G, Bonhoeffer P, Taylor AM. Percutaneous Pulmonary Valve Implantation for Right Ventricular Outflow Tract Obstruction Enhances Cardiac Response to Exercise by Improved Bi-ventricular Stroke Volume. *Circulation;* 120(18):S608-S608. 2009.

120 - Schievano S, Capelli C, Young C, Lurz P, Nordmeyer J, Owens C, Bonhoeffer P, Taylor AM. Four-dimensional computed tomography: a method of assessing right ventricular outflow tract and pulmonary artery deformations throughout the cardiac cycle. *European Radiology;* 21(1):36-45. 2011.

121 - Mishell JM, Vakharia KT, Ports TA, Yeghiazarians Y, Michaels AD. Determination of adequate coronary stent expansion using StentBoost, a novel fluoroscopic image processing technique. *Catheterization and Cardiovascular Interventions;* 69(1):84-93. 2007.

122 - Zeng DH, Boutsianis E, Ammann M, Boomsma K, Wildermuth S, Poulikakos D. A study on the compliance of a right coronary artery and its impact on wall shear stress. *Journal of Biomechanical Engineering-Transactions of the Asme*. 130(4). 2008.

123 - Schievano S, Petrini L, Migliavacca F, Coats L, Nordmeyer J, Lurz P, Khambadkone S, Taylor AM, Dubini G, Bonhoeffer P. Finite Element Analysis of Stent Deployment: Understanding Stent Fracture in Percutaneous Pulmonary Valve Implantation. *Journal of Interventional Cardiology;* 20:546-554. 2007.

124 - Porras D, McElhinney DB, Del Nido P, Lock JE, Meadows J, Marshall AC. Clinical and stent-related outcomes after transcatheter or operative placement of bare-metal stents in the ventricular septum or subvalvar systemic outflow tract. *Circulation: Cardiovascular Interventions;* 5:570-581. 2012.

125 - Steeden JA. Rapid Phase-contrast Magnetic Resonance Imaging Using Spiral Trajectories and Parallel Imaging. *UCL PhD Thesis, London.* 2011.

126 - Pennati G, Corsini C, Cosentino D, Hsia TY, Luisi VS, Dubini G, Migliavacca F. Boundary conditions of a patient specific fluid dynamics modelling of cavopulmonary connections: possible adaptation of pulmonary resistances results in a critical issues for a virtual surgical planning. *Interface Focus;* 1:297-307. 2011.

127 - Low HT, Chew YT, Lee CN. Flow studies on atriopulmonary and cavopulmonary connections of the Fontan operations for the congenital heart defects. *Journal of Biomedical Engineering;* 15:303-307. 1993.

128 - Ryval J, Straatman A.G, Steinman DA. Two-Equation Turbulence Modeling of Pulsatile Flow in a Stenosed Tube. *ASME Journal of Biomechanical Engineering;* 126:625–635. 2004.

129 - Varghese SS, Frankel SH. Numerical modeling of pulsatile turbulent flow in stenotic vessels. *Journal of Biomechanical Engineering;* 125:445-460. 2003.

130 - Ghalichi F, Deng X, De Champlain A, Douville Y, King M, Guidoin R. Low Reynolds number turbulence modeling of blood flow in arterial stenoses. *Biorheology;* 35(4-5):281-294. 1998.

131 - Meierhofer C, Schneider EP, Lykol C, Hutter A, Martinoff S, Markl M, Hager A, Hess A, Stern H, Fratz S. Wall shear stress and flow patterns in the ascending aorta in patients with bicuspid aortic valves differ significantly from tricuspid aortic valves: a prospective study. *European Heart Journal of Cardiovascular Imaging*; 14(8): 797-804. 2012.

132 - Valverde I, Nordmeyer S, Uribe S, Greil G, Berger F, Kuehne T, Beerbaum P. Systemic-to-pulmonary collateral flow in patients with palliated univentricular heart physiology: measurement using cardiovascular magnetic resonance 4D velocity acquisition. *Journal of Cardiovascular Magnetic Resonance;* 14:25. 2012.

133 - Barker AJ, Markl M, Burk J, Lorenz R, Bock J, Bauer S, Schulz-Menger J, von Knobelsdorff-Brenkenhoff. Bicuspid aortic valve is associated with altered wall shear stress in the ascending aorta. *Circulation: Cardiovascular Imaging;* 5:457-466. 2012.

134 - Hsiao A, Lustig CM, Alley MT, Murphy MJ, Vasanawala SS. Evaluation of valvular insufficiency and shunts with parallel-imaging compressed-sensing 4D phase-contrast MR imaging with stereoscopic 3D velocity-fusion volume-rendered visualization. *Radiology;* 265(1). 2012.

135 - Chien S, Li S, Shyy JYJ. Effect of mechanical forces on signal transuction and gene expression in endothelial cells. *Hypertension;* 1:162-169. 1998.

136 - Shyy JYJ. Mechanotransduction in endo thelial responses to shear stress. *Biorheology;* 38:109-117. 2001

137 - Poltem D. A review: Hemodynamics of cerebral aneurysm with matethematical modelling. *International Mathematical Forum;* 54:2687-2693. 2012.

138 - Voges I, Jerosch-Herold M, Hedderich J, Pardun E, Haur C, Gabbert DD, Kramer HH, Rickers C. Normal values of aortic dimensions, distensibility and pulse wave velocity in children and young adults. *Journal of Cardiovascular Magnetic Resonance;* 14(1):O55. 2012.

139 - Beek FJ, Beekman RP, Dillon EH, Mali WP, Meiners LC, Kramer PP, Meyboom EJ. MRI of the pulmonary artery after arterial switch operation for transposition of the great arteries. *Pediatric Radiology;* 23(5):335-340. 1993.

140 - Muthurangu V, Taylor AM, Hegde SR, Johnson R, Tulloh R, Simpson JM, Qureshi S, Rosenthal E, Baker E, Anderson D, Razavi R. Cardiac magnetic resonance imaging after stage I Norwood operation for hypoplastic left heart syndrome. *Circulation;* 112:3256-3263.2005.

141 - Giardini A, Khambadkone S, Taylor AM, Derrick G. Effect of abnormal pulmonary flow distribution on ventilatory efficiency and exercise capacity after arterial switch operation for transposition of the great arteries. *American Journal of Cardiology;* 106:1023-1028. 2010.

142 - Muthurangu V, Atkinson D, Sermesant M, Miquel ME, Hegde S, Johnson R, Andriantsimiavona R, Taylor AM, Baker E, Tulloh R, Hill R, Razavi RS. Measurement of total pulmonary arterial compliance using invasive pressure monitoring and MR flow quantification during MR guided cardiac catheterization. *American Journal of Physiology - Heart and Circulation Physiology;* 289:H1301-H1306. 2005.

143 - Kind T, Faes TJC, Vonk-Noordegraaf A, Westerhof N. Proportional relations between systolic, diastolic and mean pulmonary artery pressure are explained by vascular properties. *Cardiovascular engineering and technology;* 2:15-23. 2010.

144 - Lankhaar JW, Westerhof N, Faes TJC, Gan CTJ, Marques KM, Boonstra A, van der Berg FG, Postmus PE, Vonk-Noordegraaf A. Pulmonary vascular resistance and compliance stay

inversely related during treatment of pulmonary hypertension. *European Heart Journal;* 29:1688-1695. 2008.

145 - Lambermont B, Gérard P, Detry O, Kolh P, Potty P, Defraigne JO, D'Orio V, Marcelle R. Comparison between three- and four-element windkessel models to characterize vascular properties of pulmonary circulation. *Archives of Physiology and biochemistry;* 150(7):625-632. 1997.

146 - Lieber BB, Li X, Grant BJB. Beat by beat changes of viscoelastic and inertial properties of the pulmonary arteries. *Journal of Applied Physiology;* 76(6): 2384-2355. 1994.

147 - Presson RG, Audi S, Hanger CC, Zenk GM, Sidner RA, Linehan JH, Wagner WW, Dawson CA. Anatomic distribution of pulmonary vascular compliance. *Journal of Applied Physiology;* 84:303-310. 1998.

148 - Kilner PJ, Balossino R, Dubini G, Babu-Narayan SV, Taylor AM, Pennati G, Migliavacca F. Pulmonary regurgitation: the effects of varying pulmonary artery compliance, and of increased resistance proximal or distal to the compliance. *International Journal of Cardiology;* 133:157-166. 2009.

149 - LaDisa JFJ, Taylor CA, Feinstein JA. Aortic coarctation: recent developments in experimental and computational methods to assess treatments for this simple condition. *Progress in Pediatric Cardiology*; 30(1):45-49. 2010.

150 - Capelli C, Bosi GM, Cerri E, Nordmeyer J, Odenwald T, Bonhoeffer P, Migliavacca F, Taylor AM, Schievano S. Patient-specific simulations of transcatheter aortic valve stent implantation. *Medical & Biological Engineering & Computing*; 50:183-192. 2012.

151 - Oomens CWJ, Ratingen MRV, Janssen JD, Kik JJ, Hendriks MA. A numerical-experimental method for a mechanical characterization of biological materials. *Journal of Biomechanics;* 26:617. 1993.

152 - Hendriks FM, Brokken D, Van Eemeren J, Oomens CW, Baaijens FP, Horsten JB. A numerical-experimental method to characterize the non-linear mechanical behaviour of human skin. *Skin Research and Technology;* 9:274–283. 2003.

List of publications arising during this thesis

Original peer reviewed articles directly related to this work

Zwierzak I*, Cosentino D*, Narracott AJ, Bonhoeffer P, Diaz-Zuccarini V, Fenner JW, Schievano S. Three-dimensional measurement of in vivo and in vitro stent geometry and deformation: challenges and progress. *The International Journal of Artificial Organs*; under review.

Cosentino D*, Zwierzak I*, Schievano S, Diaz-Zuccarini V, Fenner JW, Narracott AJ. Uncertainty assessment of imaging techniques for the 3D reconstruction of stent geometry. *Medical Engineering & Physics;* under review

Cosentino D, Quail M, Pennati G, Capelli C, Bonhoeffer P, Diaz-Zuccarini V, Taylor AM, Schievano S. Geometrical and stress analysis of Melody percutaneous pulmonary valves: risk factors for stent fracture. *Circulation: Cardiovascular Interventions;* under review.

Cosentino D, Capelli C, Derrick G, Taylor A, Schievano S. Patient-Specific models to support interventional procedures: a case study of aortic coarctation. In preparation.

Cosentino D, Pennati G, Bavo A, Tanda G, Quail M, Migliavacca F, Diaz-Zuccarini V, Taylor AM, Schievano S. Patient-specific evaluation of pulmonary vascular resistances after corrected transposition of the great arteries. In preparation.

Original peer reviewed articles not directly related to this work

Baker C, Corsini C, Cosentino D, Dubini G, Pennati G, Migliavacca F, Hsia T-Y. Effects of Pulmonary Artery Banding and Retrograde Aortic Arch Obstruction on the Hybrid Palliation of Hypoplastic Left Heart Syndrome. *The Journal of Thoracic and Cardiovascular Surgery;* in press. 2013.

Capelli C, Biglino G, Petrini L, Migliavacca F, Cosentino D, Bonhoeffer P, Taylor A. Finite Element Strategies to Satisfy Clinical and Engineering Requirements in the Field of Percutaneous Valves. *Annals of Biomedical Engineering;* 40(12):2663:2673. 2012.

Biglino G, Capelli C, Binazzi A, Reggiani R, Cosentino D, Migliavacca F, Bonhoeffer P, Taylor A, Schievano S. Virtual and real bench testing of a new percutaneous valve device: a case study. *EuroIntervention*; 8:120-128. 2012.

Hsia TY, Cosentino D, Corsini C, Pennati G, Dubini G, Migliavacca F. Use of mathematical modeling to compare and predict hemodynamic effects between hybrid and surgical Norwood palliations for hypoplastic left heart syndrome. *Circulation*; 124(11 Suppl):S204-210. 2011.

Pennati G, Corsini C, Cosentino D, Hsia TY, Luisi VS, Dubini G, Migliavacca F. Boundary conditions of patient-specific fluid dynamics modelling of cavopulmonary connections: possible adaptations of pulmonary resistances results in a critical issue for a virtual surgical planning. *Interface Focus*; 1:297-307. 2011.

Corsini C, Cosentino D, Pennati G, Dubini G, Hsia TY, Migliavacca F. Multiscale models of the hybrid palliation for hypoplastic left heart syndrome. *Journal of Biomechanics*; 44(4): 767-770. 2011.